

Electronic Thesis and Dissertation Repository

---

7-29-2020 10:00 AM

## Effects of corner radii on wind tunnel testing of low-rise buildings

Kytin Kwan, *The University of Western Ontario*

Supervisor: Kopp, Gregory A., *The University of Western Ontario*

A thesis submitted in partial fulfillment of the requirements for the Master of Engineering Science degree in Civil and Environmental Engineering

© Kytin Kwan 2020

Follow this and additional works at: <https://ir.lib.uwo.ca/etd>



Part of the [Civil and Environmental Engineering Commons](#)

---

### Recommended Citation

Kwan, Kytin, "Effects of corner radii on wind tunnel testing of low-rise buildings" (2020). *Electronic Thesis and Dissertation Repository*. 7096.

<https://ir.lib.uwo.ca/etd/7096>

This Dissertation/Thesis is brought to you for free and open access by Scholarship@Western. It has been accepted for inclusion in Electronic Thesis and Dissertation Repository by an authorized administrator of Scholarship@Western. For more information, please contact [wlsadmin@uwo.ca](mailto:wlsadmin@uwo.ca).

## Abstract

Wind effects on buildings are commonly studied by testing 3D printed building models in a wind tunnel. A challenge with 3D printing is that the edges of these models may not be perfectly sharp, but rounded with a radius of curvature,  $R$ . It is well known that when edges are significantly rounded, the aerodynamics of the building can be altered (Robertson, 1991; Mahmood 2011), leading to inaccurate predictions of full-scale surface pressures and wind loads. However, there is presently no guidance on model edge radii prescribed in wind tunnel testing standards such as ASCE 49-12. The objective of the present study is to define a practical limit for edge curvature, beyond which, separating flow behaviour is no-longer representative of flow around a sharp-edged bluff body.

To investigate the effect of edge radii on the separating and reattaching flow, a wind tunnel study was conducted on a generic low-rise building. Models of the building were constructed in four scales (1:200, 1:100, 1:50 and 1:25), each with five non-dimensional radii,  $R/H$ , where  $H$  is the model height. In total, twenty model configurations were tested in similar upstream flow conditions. It was found that pressure coefficients in regions of separated flow were most sensitive to changes in  $R/H$ . Changes in the pressure distributions with  $R/H$  suggest that the increased curvature weakens and suppresses the vortices near model edges responsible for severe suction. These changes in the pressure distributions in these regions lead to changes in area-averaged pressure coefficients and overall uplift coefficients.

The change in pressure distributions appeared to be a continuous function of  $R/H$ . As a result, differences in the pressure distributions may continue to appear as  $R/H$  continues to decrease. Thus, it is suggested that the edges of the wind tunnel models ought to be as sharp as possible. However, within the limitations of measurement uncertainty in the current experimental setup, it was determined that discrepancies in pressure distributions may continue to be discernable up to  $R/H=1.3\%$ . Therefore, it is proposed that edge radii of wind tunnel models should not exceed  $R/H = 1.3\%$  to ensure similarity of model-scale and full-scale results.

## Keywords

Wind loads, bluff-body aerodynamics, wind tunnel testing, 3D printing

## Lay Summary

Wind effects on buildings are commonly studied by testing scaled, 3D printed building models in a wind tunnel. As the wind tunnel operates, pressure taps across the model surfaces measure surface pressures which are used to predict full-scale wind loads. A challenge with 3D printed models is that the edges may not be perfectly sharp, but rounded with a radius of curvature,  $R$ . It is well known that when edges are significantly rounded, the aerodynamics of the building can be altered (Robertson, 1991; Mahmood 2011), leading to inaccurate predictions of full-scale wind loads. However, there is presently no guidance on model edge radii prescribed in wind tunnel testing standards such as ASCE 49-12. The objective of the present study is to define a practical limit for edge curvature, beyond which, the aerodynamics and predicted wind loads have significantly changed.

To investigate the effect of edge radii, a wind tunnel study was conducted on a generic low-rise building. Models of the building were constructed in four scales (1:200, 1:100, 1:50 and 1:25), each with five non-dimensional radii,  $R/H$ , where  $H$  is the model height. In total, twenty model configurations were tested. It was found that surface pressures in regions near model edges are most sensitive to changes in  $R/H$ . These changes in the surface pressures subsequently lead to discrepancies in the predicted wind loads.

The change in surface pressures appear to be a continuous function of  $R/H$ . As a result, differences in the pressure distributions may continue to appear as continues to decrease and, thus, it is suggested the edges of wind tunnel ought to be as sharp as possible. However, within the limitations of measurement uncertainty in the current experimental setup, it was determined that discrepancies in pressure distributions may continue to be discernable up to  $R/H = 1.3\%$ . As a result, it is proposed that edge radii of wind tunnel models should not exceed  $R/H = 1.3\%$  to ensure similarity of model-scale and full-scale results.

## Acknowledgments

First, I would like to thank my supervisor, Prof. Kopp for his continual support throughout my work. His guidance has been invaluable in my studies and career, and has helped me further my understanding of experimental fluid mechanics. It has certainly been a pleasure working with Prof. Kopp, and his mentorship has both deepened my passion for the field of wind engineering and has challenged me to continue learning.

Sincere thanks also goes to Dr. Chieh-Hsun Wu, Emilio Hong, Aaron Jaffe, Yitian Guo, Anant Gairola, Osmany Hernández Cruz, Mahbub Hossain Tanjil , Matt Vandewiel, Mark Chorostecki and Charissa Ong. Without their long, and often late, hours in the tunnel, the testing for this project would not have been possible. Additionally, I would like to thank Dr. Chieh-Hsun Wu for his support with MATLAB and guidance during the analysis of the wind tunnel data.

I would also like to thank the Boundary Layer Wind Tunnel Laboratory technicians, especially Anthony Burggraaf, for all their help during the experiments and for being available whenever things went awry. Additionally, I'd like to thank all of the BLWTL staff who, during my time during my time as an engineering assistant, inspired me to pursue studies in wind engineering.

Lastly, I would like to thank all my family and friends for their unconditional support during this degree.



# Table of Contents

Abstract .....	ii
Lay Summary .....	iii
Acknowledgments.....	iv
Table of Contents .....	v
List of Tables .....	viii
List of Figures .....	x
Nomenclature .....	xv
Chapter 1: Introduction .....	1
1.1 Separating and reattaching flow around a sharp-edged bluff body .....	3
1.1.1 Influence of Reynolds number .....	4
1.1.2 Influence of free stream turbulence .....	5
1.1.3 Influence of rounded edges .....	7
1.2 Objectives .....	11
Chapter 2: Experimental Approach .....	12
2.1 Model Design.....	12
2.1.1 Building Size.....	12
2.1.2 Tap Layout .....	14
2.1.3 Edge radii sizing .....	16
2.1.4 Building Sign Conventions .....	19
2.2 Flow simulation .....	23
2.2.1 Terrain Simulation .....	24
2.2.2 Exposure Selection.....	25
2.3 Data Acquisition .....	29
2.4 Data Analysis .....	30
Chapter 3: Uncertainty Analysis .....	33

3.1	Introduction.....	33
3.2	Approach.....	34
3.2.1	Elemental error.....	34
3.2.2	Uncertainty of $C_pH$ .....	35
3.2.3	Standard Error of $r$ th order statistical moments.....	36
3.2.4	Nominal values for uncertainty estimates.....	38
3.3	Results.....	41
3.4	Discussion of uncertainty estimates.....	45
3.5	Summary of findings.....	49
Chapter 4: Spatial pressure coefficient distributions .....		50
4.1	Introduction.....	50
4.2	Normal flow directions .....	50
4.2.1	M1 and M2 Midline Results .....	52
4.2.2	M3 Midlines.....	55
4.2.3	Discussion.....	57
4.2.4	Fluctuating pressure coefficient spectra.....	62
4.2.5	Possible flow mechanisms .....	64
4.3	Oblique flow directions.....	64
4.3.1	Roof contours.....	65
4.3.2	Pressures along the roof edges.....	67
4.3.3	Discussion.....	69
4.4	Summary of findings.....	77
Chapter 5: Area-Averaged Pressure Coefficients and Uplift.....		78
5.1	Introduction.....	78
5.2	Calculation method .....	78
5.3	Results.....	83

5.3.1	Area-averaged pressure coefficients .....	83
5.3.2	Uplift coefficient .....	87
5.4	Discussion .....	89
5.4.1	Influence of edge curvature .....	89
5.4.2	Influence of model scale .....	91
5.4.3	Influence of tap resolution and tributary area .....	93
5.5	Summary of findings.....	95
Chapter 6:	Conclusions .....	97
6.1	Summary of findings.....	97
6.1.1	Point pressure coefficients .....	97
6.1.2	Area-averaged pressure coefficients .....	97
6.2	Definition and limit of edge radius .....	98
6.3	Future work.....	98
6.3.1	Repeating experiments.....	99
6.3.2	Flow visualization.....	99
6.3.3	Investigating the effects of free stream turbulence .....	99
6.3.4	Investigating potential Reynolds number effects.....	100
6.3.5	Application of proposed limit to high-rise buildings.....	101
References	.....	102
Appendices	.....	110
Curriculum Vitae	.....	192

## List of Tables

Table 2-1 Selected Building Sizing .....	12
Table 2-2 Survey of various low-rise building wind tunnel studies .....	13
Table 2-3 Survey of metal panel cladding systems .....	17
Table 2-4 Studies of bluff bodies with curved edges.....	18
Table 2-5 Wind tunnel model configurations .....	18
Table 2-6 BLWT II Dimensions .....	24
Table 2-7 Summary of selected profiles .....	28
Table 2-8 Sample times of wind tunnel tests .....	30
Table 3-1 Sources of Elemental Error .....	34
Table 3-2 Mean of standard errors of $C_p H$ statistical moments .....	38
Table 3-3 Nominal $C_p D$ used for determination of $w C_p H$ .....	41
Table 3-4 $w C_p H$ determined using various methods .....	43
Table 3-5: Nominal values of variables used in uncertainty estimation.....	46
Table 3-6: Influence of various terms in Method C.....	47
Table 4-1 Comparison of stagnation points .....	52
Table 4-2 Differences in $C_p D_{max}$ in M1 (values beyond uncertainty in red).....	60
Table 4-3 Differences in $C_p D_{max}$ in M2 (differences beyond uncertainty in red) .....	60
Table 4-4 Comparison of $C_p max_{c2}$ at $x/W = 0.1$ .....	74
Table 4-5 Comparison of $C_p max_{c2}$ at $x/W = 0.23$ .....	74

Table 5-1 Average tributary area,  $A_i/H2$ , per tap configurations and model regions ..... 80

Table 5-2 Tap and tributary area configurations and their applicability to model scales,  
denoted with  $\times$  ..... 80

## List of Figures

Figure 1-1 Separating and reattaching flow on a generic sharp-edged bluff body (from Akon and Kopp, 2016).....	3
Figure 1-2 Conical vortices at oblique wind directions (from Holmes, 2015). .....	4
Figure 1-3 Comparison of a sharp (left) and curved (right) building corner. ....	8
Figure 1-4 Flow around curved (left) and sharp (right) eave (from Robertson,1991).....	9
Figure 1-5 Mean $C_p$ along roof with curved and sharp eaves (from Robertson , 1991). .....	9
Figure 1-6 Flow visualization of corner vortices with increasing edge curvature (R in mm, from Mahmood 2011). .....	10
Figure 1-7 Mean $C_p$ plotted by roof corner at oblique wind angles (from Mahmood, 2011). Note that $H$ was 40mm, so $R = 10\text{mm}$ corresponds $R/H = 25\%$ . “50501” refers to tap location on the TTU WERFL building. ....	10
Figure 2-1 Definition of building dimensions ( $L>W$ ). .....	12
Figure 2-2 Example of 1:200 (left) and 1:100 (right) model roof tap layout. ....	15
Figure 2-3 1:100 wall tap layout. ....	16
Figure 2-4 Visualization of edge radii considered .....	19
Figure 2-5 Azimuth $\theta$ sign convention. ....	19
Figure 2-6 Lines of taps located on models. ....	20
Figure 2-7 M1 and M2 midline sign convention (side view). ....	20
Figure 2-8 M3 midline sign convention (plan view). ....	21
Figure 2-9 Tap lines in red for pressures at oblique angles (plan view).....	21

Figure 2-10 Approximation of conical vortex axis angle, $\phi_c$ , using the location of the maximum $C_pH$ , $lc$ , observed along a tap lines (in red).....	22
Figure 2-11 (1) Middle roof, (2) roof corner and (3) wall regions examined for area averaging.....	23
Figure 2-12 Red spires and 15" barrier.....	24
Figure 2-13 Typical wind tunnel setup for 1:50 scale model and Open 15 exposure. ....	25
Figure 2-14 Velocity spectra of the selected profiles at model roof height $z = H$ .....	27
Figure 2-15 Non dimensional mean velocity profile of selected profiles where (×) indicate measurements and – represent fitted profile. ....	28
Figure 3-1 $C_pH$ at $R/H = 0.3\%$ plotted along the M1 midline on (a) roof and (b) leeward wall.....	38
Figure 3-2 Mean velocity measured $1H$ above the center of models at a $90^\circ$ azimuth .....	39
Figure 3-3 $C_pD$ at $R/H = 0.3\%$ plotted along the M1 midline on (a) S2 roof and (b) S3 leeward wall.....	40
Figure 3-4 $C_pH$ on M1 roof at $R/H = 0.3\%$ with $wC_pH$ determined from (a) Method A (b) Method B (c) Method C.....	44
Figure 3-5 $C_pH$ on M1 roof at $R/H = 0.3\%$ with $wC_pH$ determined from (a) Method A (b) Method B (c) Method C.....	44
Figure 4-1 Mean $C_p$ on a surface mounted cube in turbulent flow (from Castro and Robins, 1977). ....	51
Figure 4-2 Results for 1:25 models along M1 for (a) to (c) mean, (d) to (f) RMS, and (g) to (i) peak $C_pH$ .....	53
Figure 4-3 Results for 1:25 models along M3 for, (a) to (d) mean, (e) to (h) RMS, and (i) to (l) peak $C_pH$ .....	56

Figure 4-4 Definitions of $CpD_{max}$ and $ls$ .	58
Figure 4-5 (a) M1 $CpD_{max}$ and (b) M1 $ls$	59
Figure 4-6 (a) M2 $CpD_{max}$ and (b) M2 $ls$	59
Figure 4-7 Normalized fluctuating pressure coefficient and velocity spectra on M1 of 1:25 models at (a) $S2/L = 0.16$ and (b) $S2/L = 0.5$ .	62
Figure 4-8 Contours of 1:25 models at $\theta = 45^\circ$ with various $R/H$ for, (a) to (e) mean, (f) to (j) RMS and, (k) to (o) peak $CpH$ .	66
Figure 4-9 Mean $CpH$ along longest roof edge at $\theta = 45^\circ$ at (a) $x/L = 0.01$ , (b) $x/L = 0.10$ and (c) $x/L = 0.23$ .	68
Figure 4-10 RMS $CpH$ along longest roof edge at $\theta = 45^\circ$ at (a) $x/L = 0.01$ , (b) $x/L = 0.10$ and (c) $x/L = 0.23$ .	68
Figure 4-11 Peak $CpH$ along longest roof edge at $\theta = 45^\circ$ at (a) $x/L = 0.01$ , (b) $x/L = 0.10$ and (c) $x/L = 0.23$ .	68
Figure 4-12 Mean $CpH$ along roof edge at oblique angles at $x/L=0.23$ and $R/H=0.3\%$ .	69
Figure 4-13 Mean $CpD$ along roof edge at oblique angles at $x/L=0.23$ and $R/H=0.3\%$ .	70
Figure 4-14 Definition of $Cpc_{max1}$ along $x/W = 0.01$ .	70
Figure 4-15 Definition of $Cpc_{max2}$ and $lc$ along $x/W = 0.1$ .	71
Figure 4-16 $Cpc_{max1}$ at $x/W = 0.01$ at $45^\circ$ azimuth.	72
Figure 4-17 $CpD$ at $x/W= 0.01$ near the roof corner for $R/H = 0.3\%$ .	73
Figure 4-18 $Cpc_{max2}$ at (a) $x/W = 0.1$ and (b) $x/W = 0.23$ .	74
Figure 4-19 $lc$ at (a) $x/W = 0.1$ and (b) $x/W = 0.23$ .	75
Figure 4-20 $\phi c$ at (a) $x/W = 0.1$ and (b) $x/W = 0.23$ .	75



Figure 4-21 Turbulence intensity above roof corner with varying radii at $\theta = 45^\circ$ where $R$ is in mm and $H= 40\text{mm}$ (from Mahmood, 2011). .....	76
Figure 5-1 Tributary area example for a tap at a roof corner.....	79
Figure 5-2 Tap locations and tributary areas on roof corner using (a) “A” Configuration, (b) “B” Configuration and (c) “C” Configuration. Tap locations are denoted with + and boundaries of $A_{tot}$ considered are shown in bold lines. ....	81
Figure 5-3 Tap locations and tributary areas on the middle of roof edge using (a) “A” Configuration, (b) “B” Configuration and (c) “C” Configuration. Tap locations are denoted with + and boundaries of $A_{tot}$ considered are shown in bold lines. ....	82
Figure 5-4 Tap locations and tributary areas on wall using (a) “A” Configuration, (b) “B” Configuration and (c) “C” Configuration. Tap locations are denoted with + and boundaries of $A_{tot}$ considered are shown in bold lines.....	82
Figure 5-5 Tap location and tributary areas for determination of uplift using (a) "A" Configuration and (b) "B" Configuration. ....	83
Figure 5-6 1:25 $C_{pavg}$ using configuration A of (a) to (c) roof corner , (d) to(f) middle of roof edge and, (g) to (i) wall. ....	84
Figure 5-7 1:25 $C_{pavg}$ using configuration C of, (a) to (c) roof corner , (d) to(f) middle of roof edge and, (g) to (i) wall. ....	85
Figure 5-8 (a) Mean, (b) RMS and (c) Peak $CFZ$ from 1:25 model using configuration “A”. .....	88
Figure 5-9 (a) Mean, (b) RMS and (c) peak $CFZ$ of 1:25 Model using configuration "B". ...	88
Figure 5-10 $r$ of 1:25 using “C” tributary areas at(a) roof corner, (b) middle of roof edge and (c) wall. ....	90
Figure 5-11 $r_{min}$ of 1:25 using “C” tributary areas at(a) roof corner, (b) middle of roof edge and (c) wall. ....	90

Figure 5-12 (a) $r^-$ and (b) $r_{min}$ of $CFZ$ from 1:25 models using "A" tributary areas.....	91
Figure 5-13 Comparison of (a) $r^-$ and (b) $r_{min}$ at the roof corner with $R/H=2.5\%$ and "B" tributary areas.....	92
Figure 5-14 Comparison of (a) $r$ and (b) $r_{min}$ of $CFZ$ with $R/H = 20\%$ at various model scales. ....	92
Figure 5-15 $2.45m^2$ area on windward roof corner of 1:25 models considered. ....	93
Figure 5-16 $C_p H$ contours ° roof corner of 1:25 models at $\theta = 45^\circ$ and "A" taps (+) and "B" taps ( $\times$ ) with (a) $R/H= 0.3\%$ , (b) $R/H = 2.5\%$ and (c) $R/H = 5\%$ . ....	94
Figure 5-17 (a) Mean, (b) RMS and (c) peak $C_{pavg}$ determined on $2.45m^2$ roof corner at $\theta = 45^\circ$ on a 1:25 model. ....	94
Figure 5-18 $7.85m^2$ area on windward roof corner of 1:25 models considered. ....	95
Figure 5-19 (a) Mean, (b) RMS and (c) peak $C_{pavg}$ determined on $7.85m^2$ roof corner at $\theta = 45^\circ$ on a 1:25 model. ....	95
Figure 6-1 Distance of stagnation point to separation point $S$ on (a) a low-rise building (side view) and (b) a high-rise building (plan view). ....	101

## Nomenclature

$A_i$	Tributary area
$A_{tot}$	Total area of surface
$B_x$	Bias limit of variable x
$C_{FZ}$	Uplift coefficient
$C_p$	Pressure coefficient
$Cp_{avg}$	Area-averaged pressure coefficient
$Cp_b$	Base pressure coefficient
$Cp_{cmax}$	Maximum mean $Cp_D$ observed along tap line in oblique flow direction
$Cp_D$	Pressure coefficient normalized by base pressure coefficient
$\overline{Cp_{Dmax}}$	Maximum mean $Cp_D$ observed along tap line in normal flow directions
$Cp_H$	Pressure coefficient referenced to mean roof height velocity
$Cp_{pkgi}$	Peak pressure coefficient within time-series segment
$Cp_{ref}$	Pressure coefficient referenced to reference height velocity
$d$	Distance from roof origin to tap corner line
$f$	frequency
$f_s$	Sampling frequency
$H$	Building height
$I_u, I_v$	Longitudinal and lateral turbulence intensity
$Je$	Jensen number
$L$	Building depth
$L_C$	Cutoff length scale for quasi-steady model
$L_{ux}$	Integral length scale
$l_c$	Location of maximum mean suction on roof at a 45 degree azimuth
$l_s$	Approximated reattachment length
$n$	Number of samples
$p$	Surface pressure
$p_0$	Static pressure
$R$	Radius of edge curvature
$\bar{r}, r_{min}$	Ratios of mean and peak area-averaged pressure coefficients
$Re$	Reynolds number
$R_{uu}$	Spatial correlation coefficient of fluctuating velocity
$S$	Distance from stagnation point to separation point
$S1, S2, S3, S4$	Distance along tap midline from leading edge
$Sp(f)$	Power spectral density of fluctuating pressure coefficient
$Su(f)$	Power spectral density of fluctuating velocity
$S_x$	Precision limit of variable x
$T$	integral time scale
$T_s$	Sampling time
$t$	Student t value
$\bar{U}$	Mean velocity
$\overline{U_H}$	Mean roof height velocity

$U_{ref}$	Reference velocity
$u_*$	Friction velocity
$W$	Building width
$w_x$	Uncertainty of variable a variable $x$
$z$	Height from wind tunnel floor
$z_0$	Roughness length
$\alpha$	Gumbel distribution scale factor
$\theta$	Azimuth of wind direction
$\kappa$	Karman constant
$\nu$	Kinematic fluid density
$\rho$	Fluid density
$\sigma_u$	RMS of fluctuating velocity
$\phi_c$	Vortex axis angle
$d\tau$	Time step
$v$	Gumbel distribution location parameter

## Chapter 1: Introduction

In building design, wind effects must be considered. The most common way to study wind effects is through a pressure or loading study in a boundary layer wind tunnel. During these studies, a scaled model of a building is constructed and placed in the wind tunnel. As the wind tunnel operates, pressure taps located throughout the model surfaces measure pressures using a pressure-scanning module connected through plastic tubing. The pressures are measured across the model surfaces simultaneously as a series of pressure coefficient time histories,

$$C_p(t) = \frac{p(t) - p_0}{\frac{1}{2} \rho U_{ref}^2} \quad (1-1)$$

where  $p(t)$  is the surface pressure time history at a give tap,  $p_0$  is the static pressure,  $\rho$  is the fluid density and  $U_{ref}$  is a reference velocity (Flay, 2013). These pressure coefficients can then be used to predict full-scale wind-induced loads and structural responses (Holmes, 2015)

To accurately simulate wind effects in a wind tunnel, both building shape and flow conditions need to be properly scaled. Building shape is scaled by achieving geometric similarity. In other words, the body dimensions of the full-scale building and the model in all three coordinates have the same linear scale ratios (White, 2009).

Flow conditions on the other hand, are scaled by matching the behaviour of the turbulent boundary layer upstream of the building, namely the velocity profile and turbulence characteristics. One approach linking the flow and building is through Jensen number similarity (Holmes, 2015) , where the Jensen number is defined as

$$Je = \frac{H}{z_0} \quad (1-2)$$

$H$ , being the building height, and  $z_0$  being the roughness length, which is dependent on upstream terrain. Similarity of the flow and building scales require that

$$(Je)_p = (Je)_m \quad (1-3)$$

where subscripts  $p$  and  $m$  denote prototype and model, respectively. In this approach to flow scaling,  $z_0$  represents all features of the atmospheric boundary layer, including the velocity profile and turbulence characteristics.

Perfect similarity in building shape and flow conditions is difficult to achieve. Mismatches in scaling are thought to cause discrepancies between  $C_p$ 's measured at different scales, as has been reported in literature. A wind tunnel study on a low-rise building model by Stathopoulos and Surry (1983) found that at three different model scales (1:500, 1:250 and 1:100), local peak  $C_p$ 's were underestimated by up to 30% as scale increased. However, it appears that discrepancies in data are possibly due to mismatches upstream flow conditions as they report a mismatch in both  $Je$  and roof height turbulence intensity at the different model scales.

Even with better matching of upstream turbulence, peak pressures estimated in wind tunnel studies may still underestimate full-scale findings. A study on pressures around a residential structure showed that a better match in roof height turbulence intensity and turbulent length scales produces close agreement in both full-scale and model-scale mean and root mean square, RMS,  $C_p$ 's (Liu, et al., 2009). However, model-scale peak pressures still tend to underestimate full-scale measurements. The authors did not discuss the underlying cause of discrepancies, but suggests that it may be related to a difference in skewness of the full-scale and model-scale  $C_p$  measurements. Hoxey et al. (1998) suggest discrepancies between full-scale and model-scale pressures maybe due to a mismatch in Reynolds number, which alters vortex behaviour at roof eaves.

The causes of the discrepancies in  $C_p$  with model scale are not yet fully explained in literature but is thought to be related primarily to mismatches in scaling parameters and the subsequent effect on separating and reattaching flow behaviour. The nature of separating and reattaching flow behaviour is further discussed in the following sections, as are the possible sources of mismatches and their effects.

## 1.1 Separating and reattaching flow around a sharp-edged bluff body

As flow approaches a building surface, it separates at the building corners and reattaches further downstream on the surface (if the building is long enough) to form a separation bubble, as shown in Figure 1-1. At the corner, the boundary layer separates to form a separated shear layer, which is a thin region of flow that exhibits high shear and vorticity (Holmes, 2015). These separated shear layers roll up to form vortices that shed downstream. The vortices produced by the separated shear layer create extreme suction on building surfaces beneath the vortex core (Tieleman et al.2001).

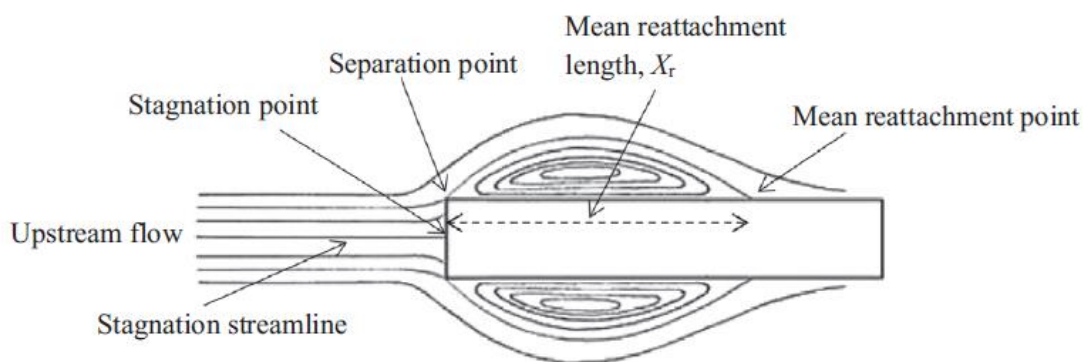


**Figure 1-1 Separating and reattaching flow on a generic sharp-edged bluff body (from Akon and Kopp, 2016).**

For high-rise buildings, these vortices are typically the strongest along the edges of the building walls. However, for low-rise buildings, the strongest vortices and greatest suction are on the roof, as most of the oncoming flow is directed up and over the top of the building. As flow approaches a low-rise building with a flat or low-pitched roof, it separates at the roof edges and, if the roof is large enough, flow reattaches further downstream on the roof (Kopp, 2013). At wind directions normal to walls, flow separates at the windward eave and high suction is observed on the windward portion of the roof. However, at oblique angles, as shown in Figure 1-2, incident cornering winds produce a pair of conical vortices at the roof corner (Holmes, 2015). The vortices produce high

suctions along lines extending from the corner of the building and that are located below the axis of the conical vortices (Tieleman, Surry, & Lin, 1994).

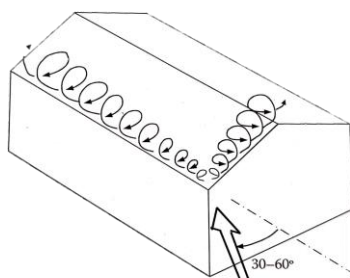


**Figure 1-2 Conical vortices at oblique wind directions (from Holmes, 2015).**

The magnitude and spatial distribution of  $C_p$  across the building surface are highly influenced by the separating and reattaching flow. However, the behaviour of the separated shear layer is highly dependent on parameters used for scaling. At least three scaling parameters are known to have significant influence:

1. Reynolds number
2. Free stream turbulence (turbulence intensity and length scale)
3. Edge radius

As a result, mismatches in scaling parameters may alter separated shear layer behaviour and can subsequently produce discrepancies in  $C_p$  magnitudes and spatial distributions.

### 1.1.1 Influence of Reynolds number

Typically speaking, flow can be scaled through dynamic similarity where length, time and force scale ratios match in both model and full scale (White, 2009). Dynamic similarity can be achieved by matching the Reynolds numbers, defined as

$$Re = \frac{\overline{U_H} H}{\nu} \quad (1-4)$$

such that

$$Re_p = Re_m \quad (1-5)$$



where  $\overline{U}_H$  is the mean velocity at mean roof height,  $H$  is mean roof height,  $\nu$  is kinematic viscosity of the fluid and subscripts  $p$  and  $m$  denote prototype and model, respectively.

For curved bodies, such as a two-dimensional circular cylinder, the separation point and subsequent flow behaviour around the body are highly sensitive to  $Re$  (Achenbach, 1968). As flow behaviour changes, the resultant surface pressure distribution changes as well, and thus a match in  $Re$  would be necessary to produce similar  $C_p$  distributions across the surface.

However, on sharp-edged bluff bodies such as buildings, the separation point is fixed at the body corners. It is commonly believed that since the separation point is fixed, the resultant aerodynamic characteristics and surface pressures are invariant with  $Re$  (Larose and D'Auteuil, 2006; Irwin, 2008). Subsequently,  $Re$  similarity is often relaxed in wind engineering applications, and testing standards such as ASCE 49-12 prescribe wind tunnel tests to be conducted beyond  $Re = 1.1 \times 10^4$  to avoid Reynolds number effects in test results (ASCE 49-12, 2012). Though the separation point is fixed on sharp-edged bluff bodies, the  $C_p$  measured on surfaces near flow reattachment may still exhibit  $Re$  effects. A study by Hoxey et al. (1998) observed that a reduction in  $Re$  by one order of magnitude caused a reduction in mean  $C_p$  by 0.25 in roof regions where flow reattached after separating at the windward eave. It is suggested that the reduction in  $C_p$  is a result of longer separation bubble at higher  $Re$  (Hoxey et al., 1997) and that the behaviour of the trailing edge of the separation bubble may be  $Re$  sensitive (Hoxey et al., 1998).

### 1.1.2 Influence of free stream turbulence

Free stream turbulence must also be matched to ensure similarity in tests. One of the most important turbulence parameters is the streamwise turbulence intensity,

$$I_u = \frac{\sigma_u}{\overline{U}} \quad (1-6)$$

where  $\sigma_u$  and  $\bar{U}$  are the RMS of the fluctuating component of streamwise fluid velocity and mean streamwise velocity, respectively (Cao, 2013).

As free stream turbulence is introduced into upstream flow and approaches the body, it becomes stretched and distorted by the mean flow field around the body (Bearman, 1972). The distorted turbulence interacts with separated shear layers to enhance turbulent mixing, increasing fluid entrainment and causing separated flow to reattach closer to the separation point (Gartshore, 1973). Numerous studies on sharp-edged bluff bodies have observed that as  $I_u$  increases in the upstream flow, the separated flow reattaches closer to the separation point, thereby producing smaller separation bubbles. (Hillier and Cherry, 1981; Kiya and Sasaki 1983; Akon and Kopp, 2016).

Furthermore, increased freestream turbulence produces larger fluctuating surface pressures. Fluctuating pressures are linked to the development and growth of the separated shear layer (Cherry, et al., 1984; Saathoff and Melbourne, 1997) which is enhanced as  $I_u$  and turbulence length scale  $L_{ux}$  are increased (Hillier & Cherry, 1981) as defined below

$$L_{ux} = \int_0^{\infty} R_{uu}(x) dx \quad (1-7)$$

where  $R_{uu}$  is the spatial correlation coefficient of the fluctuating velocity  $u$  in the stream-wise direction  $x$  (Cao, 2013). The enhanced growth of the separated shear layers accelerates vortex production and maturation which results in larger peak suction on building surfaces (Tieleman, 2003), which occur much closer to the edge (Morrison & Kopp, 2018).

For conical vortices, vertical turbulence intensity  $I_v$  is also a pertinent parameter. Quick changes in vertical wind direction can change the location of conical vortex (Wu et al., 2001). As a result, discrepancies in  $I_v$  may alter the peak suction distribution on the roof produced by conical vortices.

The various scales of turbulence in flow also need to be considered, as turbulence at different scales are responsible for different aspects of separated shear layer behaviour.

According to Saathoff and Melbourne (1997), small-scale, high frequency turbulence enhances shear layer rollup, thereby enhancing vortex shedding frequency. Conversely, large-scale, low frequency turbulence enhances vortex maturation, producing stronger vortices and consequently greater surface suction. Scaling the turbulence content in the upstream flow is typically achieved by matching the non dimensional turbulence spectrum, across all non dimensional turbulence frequencies,

$$\frac{f S_u(f)}{\bar{U}}, \frac{f H}{\bar{U}} \quad (1-8)$$

where  $f$  and  $S_u(n)$  are frequency and spectral density function, respectively (Holmes, 2015).

Ideally, the non-dimensional turbulence spectra of flow at various model scales ought to match at all frequencies, but in practice, this can be difficult to achieve. Large scale, low frequency turbulence that is used with small model scales (say 1:500) may not be reproducible at larger model scales (such as 1:20), as these eddies when scaled up would be larger than the tunnel itself (Asghari Mooneghi et al., 2016; Wu and Kopp, 2018). As a result, it is possible that at larger model scales, some large-scale turbulence will be missing in the flow. Missing large-scale turbulence would reduce vortex maturation, and in turn reduce the magnitude of peak pressure coefficients on the building surface (Tieleman, 2003).

### 1.1.3 Influence of rounded edges

Building models used for wind tunnel testing are typically 3D printed using fused deposition modelling (FDM) which allows these models to be produced relatively easily and quickly. However, a challenge to 3D printing is that a 3D printer may not be able to capture small building details, namely the sharp corner edges (Comminal et al., 2019). Since 3D printing involves layering a continuous bead of material, corners where two building faces intersect may be slightly curved with a radius,  $R$ , whereas in full-scale, the radius of these corners would be smaller (i.e.  $R \rightarrow 0$ ) as illustrated in Figure 1-3.



**Figure 1-3 Comparison of a sharp (left) and curved (right) building corner.**

The size and accuracy of corner radii produced by 3D printing is dependent on bead width (Ghareghpagh et al., 2019) and tool path of the nozzle (Comminal et al., 2019) which can vary by printer. It is possible that the smallest corner radii producible by a given 3D printer will not be small enough to ensure geometric similarity at the building edges. In other words:

$$\left(\frac{R}{H}\right)_m > \left(\frac{R}{H}\right)_p \quad (1-9)$$

Models lacking a sufficiently sharp corner can pose a significant issue in wind tunnel testing, as a change edge geometry can alter the behaviour of the separated shear layer. If the radius of curvature on the edge of a bluff body is sufficiently large, flow may remain attached around the body. Subsequently, the lack of flow separation will alter the pressures on the surface.

A full-scale study conducted on a low-rise building with a sharp and curved eaves showed that the flow did not seem to separate nor recirculate when the eave was curved (Robertson, 1991), as shown in Figure 1-4. The suppression of flow separation prevented or weakened vortex production in the separated shear layer, resulting in reduced mean  $C_p$  near the leading edge, as shown in Figure 1-5. Due to its ability to suppress or weaken vortices on the roof, rounded roof edges have been explored as a method to mitigate high suction on roofs (Surry and Lin 1995; Kopp et al., 2005; Dong et. al. 2019).

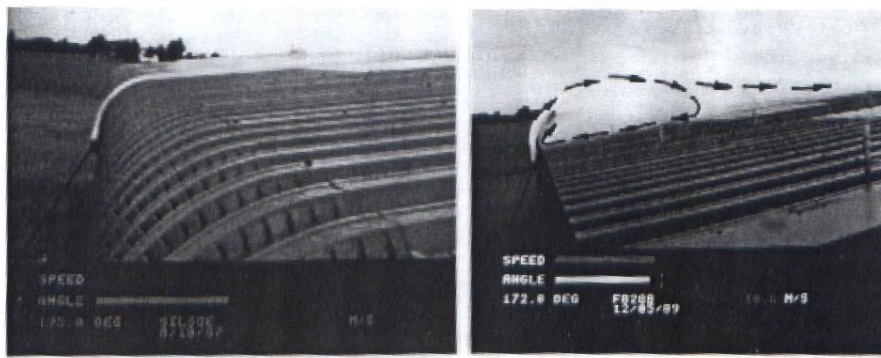


**Figure 1-4 Flow around curved (left) and sharp (right) eave (from Robertson,1991).**

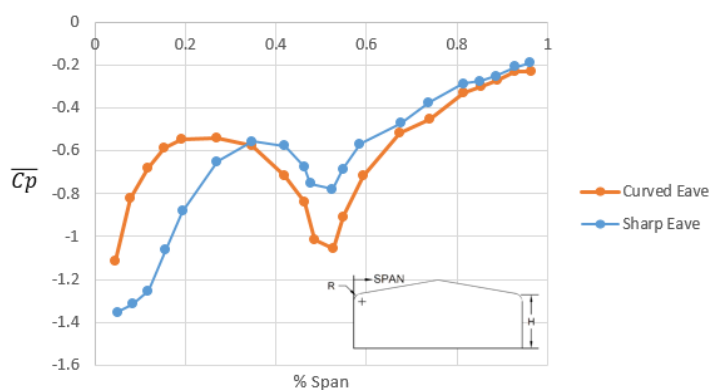


**Figure 1-5 Mean  $C_p$  along roof with curved and sharp eaves (from Robertson , 1991).**

Flow visualization by Mahmood (2011) shows that rounded roof edges have similar effects on conical vortices. As shown in Figure 1-6, conical vortices at the corner of the roof become smaller and weaker as  $R$  increases. Eventually as  $R$  was increased to  $R/H = 25\%$ , conical vortices at the corner disappeared altogether. Mean  $C_p$ 's along the leading edge of the roof at oblique wind directions, are shown in Figure 1-7. Important to note is that Mahmood (2011) reports their sharpest edge to be  $R = 0$  mm , though the actual edge radius might be slightly larger due to manufacturing limitations. As shown in Figure 1-7, similar to  $C_p$ 's in Figure 1-5, mean suctions are reduced as the edge radius increases, which is likely attributed to the suppression of vortex production.

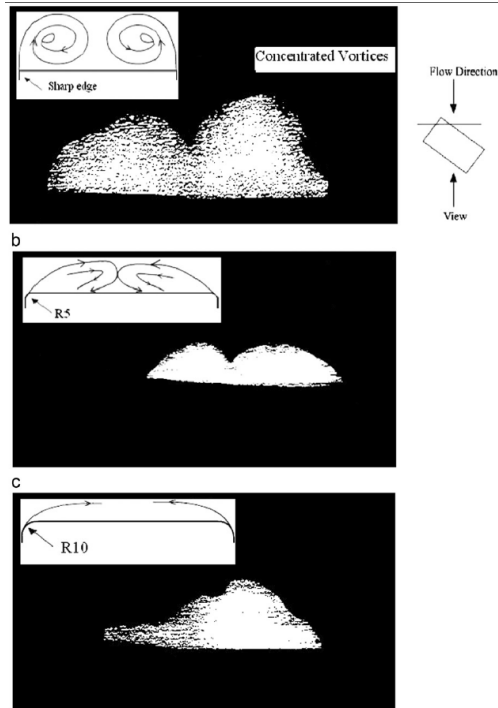


**Figure 1-6 Flow visualization of corner vortices with increasing edge curvature ( $R$  in mm, from Mahmood 2011).**

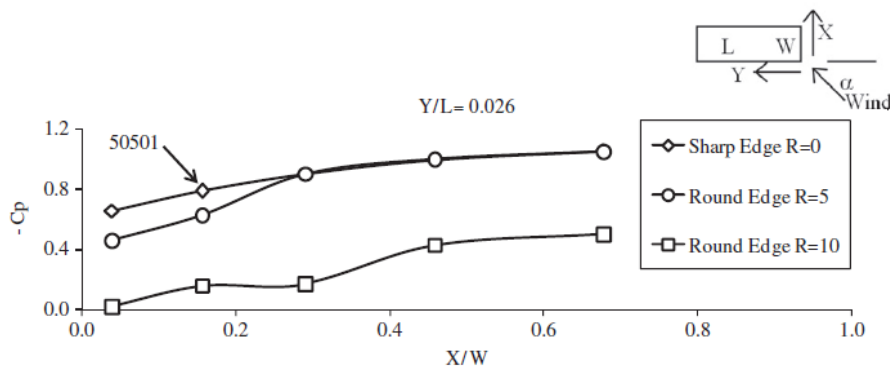


**Figure 1-7 Mean  $C_p$  plotted by roof corner at oblique wind angles (from Mahmood, 2011). Note that  $H$  was 40mm, so  $R = 10\text{mm}$  corresponds  $R/H = 25\%$ . “50501” refers to tap location on the TTU WERFL building.**

The mechanisms that weaken and suppress vortex production are not entirely clear. One potential explanation is that as that  $R$  increases, the separated shear layer remains closer to the body surface. A study on a flat plate with a semicircular nose has shown that as  $Re$

increased (in this case,  $Re$  is defined using  $R$  as a characteristic length), the separated shear layer was increasingly forced to curve in the stream-wise direction (Ota, Asano, & Okawa, 1981). In other words, as  $R$  increases, the separated shear layer may remain closer to the roof and may reattach further upstream than would be expected in a sharp-edged case. The smaller distance between the roof and the shear layer may reduce the size of the vortices produced, thereby reducing suction experienced near roof edges.

## 1.2 Objectives

It is clear from literature that a sufficiently curved edge can weaken or suppress vortex generation and subsequently reduce pressures experienced on a body surface. The concern in wind tunnel testing is that if the edges on a 3D printed model are curved due to manufacturing limitations, vortices produced around model edges may be weaker than what would be expected of a sharp-edged building at full-scale. As a result, pressures and subsequently design wind loads determined from a study conducted on a building model with curved edges may be underestimated in these situations.

There are presently no guidelines in wind tunnel testing standards such as ASCE 49-12 to prescribe a limit on the edge radii of wind tunnel models. Consequently, the objective of this thesis is to determine a practical limit for edge radii curvature, beyond which, separating flow behaviour is no longer representative of flow around a sharp-edged bluff body.

To evaluate the effects of edge radii, a generic low-rise building was tested at the Boundary Layer Wind Tunnel Laboratory. Models of the building were constructed in four model scales and five edge non-dimensional radii,  $R/H$ , leading to twenty model configurations. Pressures on the roof of the model were analyzed to evaluate the effect of edge radii on separating flow behaviour at both normal and oblique wind directions. Significant changes to pressure results were defined as differences in pressures which exceed the measurement uncertainty of the pressure measurement system. The smallest edge radius that produced differences beyond measurement uncertainty was determined as the limit to edge radius.

## Chapter 2: Experimental Approach

A wind tunnel pressure study was conducted on generic low-rise buildings at the Boundary Layer Wind Tunnel Laboratory at the University of Western Ontario. Models of the building were constructed at four different scales that are commonly used for testing low-rise buildings (1:200, 1:100, 1:50 and 1:25). Edges on the models were interchangeable in order to vary edge radii and a total of five edge radii were tested at each scale, making for a total of twenty test configurations. Flow conditions in the wind tunnel were selected with the aim of simulating similar turbulence content at each model scale.

### 2.1 Model Design

#### 2.1.1 Building Size

The generic building that was tested was sized based on three parameters: the prototype building height,  $H_p$ , the plan aspect ratio  $L/W$  and the wall aspect ratio  $W/H$ . The selected size is summarized in Table 2-1. A generic building design was determined by surveying a variety of low-rise building studies as summarized in Table 2-2. The subscript  $p$  and  $m$  denote prototype and model. Dimensions of the buildings are defined in Figure 2-1.

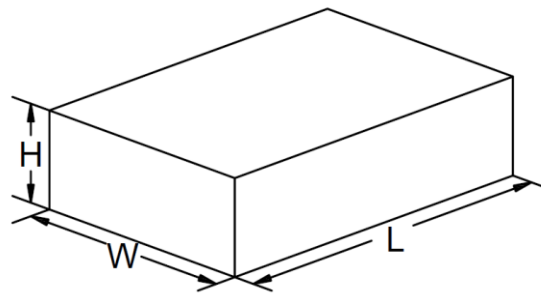


**Figure 2-1 Definition of building dimensions ( $L > W$ ).**

**Table 2-1 Selected Building Sizing**

$H_p$ [m]	$W/H$	$L/W$	$L/H$
4	2.5	1.5	3.75



Table 2-2 Survey of various low-rise building wind tunnel studies

Study	Scale	$H_m$ [m]		$H_p$ [m]		W/H		L/W	Roof Slope
		Min	Max	Min	Max	Min H	Max H		
<b>Dong et al. 2019</b>	200	0.20	-	40.00	-	3.00	-	3.00	-
<b>Shao et al. 2018</b>	200	0.03	-	5.00	-	2.00	-	2.00	4:12
<b>Duthinh et al. 2017</b>	100	0.12	-	12.00	-	1.00	-	1.58	1:12
<b>Akon and Kopp 2016</b>	-	0.08	-	-	-	2.31	-	1.56	-
	-	0.24	-	-	-	2.21	-	1.42	.
<b>Wu and Kopp 2016</b>	50	0.08	-	4.00	-	2.29	-	0.44	10°
<b>Kim and Tamura 2014</b>	50	0.10	-	5.00	-	1.00	-	1.00	-
<b>Mahmood 2011</b>	100	0.04	-	4.00	-	2.28	-	1.51	-
<b>Fritz et al. 2008</b>	150	0.04	0.065	6.10	9.80	5.02	6.20	1.99	2.39°
	200	0.03	0.049	6.10	9.80	5.02	6.20	1.99	2.39°
<b>Wu and Sarkar 2006</b>	1	4.00	-	4.00	-	2.28	-	1.51	-
<b>Ho et al. 2005</b>	100	0.04	0.12	3.60	12.19	6.78	2.00	1.56	1:48 -1:2
	100	0.04	0.12	3.60	12.19	3.58	1.06	1.48	1:12
	100	0.04	0.12	3.60	12.19	13.56	4.00	1.56	1:12
	100	0.04	0.12	3.60	12.19	10.17	3.00	0.63	1:12
<b>Kopp, Surrey and Mans 2005</b>	50	0.09	-	4.60	-	6.76	-	1.49	-
<b>Surry and Lin 1995</b>	50	0.08	-	3.90	-	2.35	-	1.48	1:60
<b>Robertson 1991</b>	1	4.14	-	4.14	-	3.12	-	1.86	10°
<b>Stathopoulos and Surry 1983</b>	500	0.01	-	4.90	-	4.98	-	1.25	1:12
	250	0.02	-	4.90	-	4.98	-	1.25	1:12
	100	0.05	-	4.90	-	4.98	-	1.25	1:12

The various geometric parameters have different effects on the pressure distribution across surfaces. The prototype height,  $H_p$  is important as the magnitude of the area-averaged pressures, and subsequent loads, are a function of building height (Kopp & Morrison, 2018). To ensure that results of roof pressure coefficients are comparable to other low-rise building studies, an  $H_p$  of 4 m was selected, as it has been commonly used in literature and approximately relates to a one story building. Additionally, based on Table 2-2,  $L/W$  was selected to be 1.5 as it has been commonly used in many studies.

The aspect ratio of the wall with the smallest breadth,  $W/H$ , is also important as it significantly affects the  $C_p$  distribution on the roof, namely the reattachment length of separated flow on the centreline (Akon & Kopp, 2016). For a flow where wind direction is normal to a building wall, wind flows up the wall and separates as it reaches the roof and then reattaches downstream. Due to flow separation, the region located upstream of the mean reattachment point experiences high magnitudes of  $C_p$  and large spatial variation as shown previously in Figure 1-5 . The span where the majority of the significant spatial variation of peak  $C_p$  occur within a distance of  $H$  from the leading edge (Kopp & Morrison, 2018). To ensure that the reattachment lengths and surface areas affected by high suction comparable to other low-rise building studies, a wall aspect ratio of 2.5 was selected, which was within the range of aspect ratios examined in Table 2-2.

### 2.1.2 Tap Layout

Taps were placed across the walls and roofs of the building models. On the roof, taps were laid out in an evenly spaced grid so that pressure contours can be produced to observe the effects of flow separation. Taps on the roof of the 1:200 model were spaced by 12.5mm in order to have a line of taps on the middle of the roof, and so that these taps could be in identical locations across the other model scales as shown in Figure 2-1. When model scales increased and where space allowed, tap density was increased, with a focus on building edges and corners where pressures change rapidly.

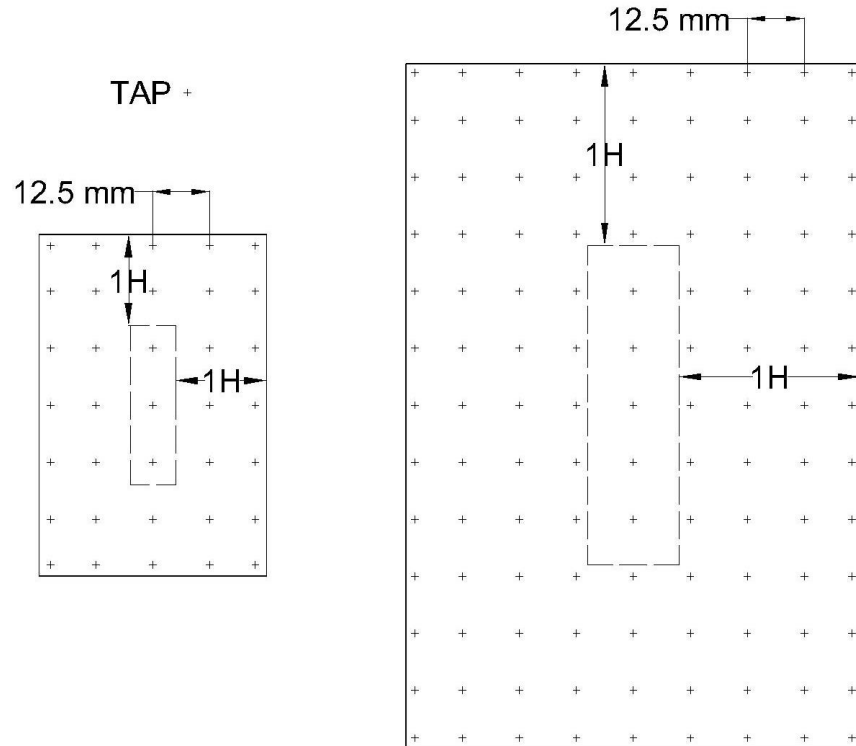


**Figure 2-2 Example of 1:200 (left) and 1:100 (right) model roof tap layout.**

The goal of the present roof tap layout was to have geometric similarity of tap locations across all model scales so that direct comparison of pressure and uplift coefficients is possible. However, in retrospect, tap density should have been increased on the 1:200 model. As noted by Kopp and Morrison (2018), the largest changes in pressures distributions occur within a distance of  $1H$  from the roof edges. Since only two rings of taps are present within this region on the 1:200 model, it is possible that tap layouts at smaller model scales may not have fully captured the rapid change in pressure distribution.

Taps along wall surfaces also have a minimum spacing of 12.5mm to have taps in identical location between model configurations; however, tap resolution is not as high. The focus of the present study is primarily on the roof, and since many models were tested, a lower tap density on walls reduces instrumentation and testing time. Where possible, the tap resolution is increased near wall and roof edges to capture rapid changes in pressures. Where the edge itself was large enough, some taps are placed on the

building edge. The wall tap layout for a 1:100 wall is shown below in Figure 2-3. Tap layouts of all models are included in Appendix A.

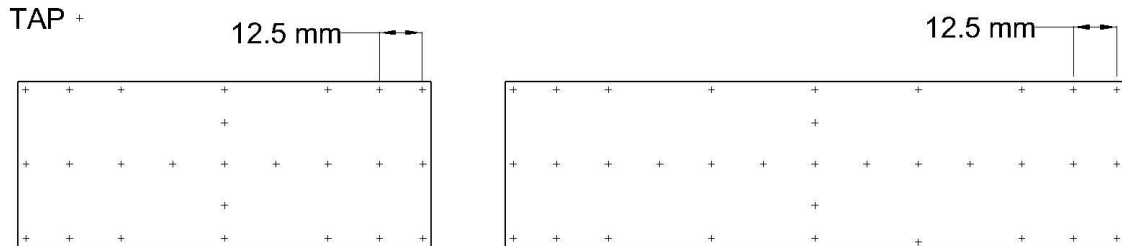


**Figure 2-3 1:100 wall tap layout.**

### 2.1.3 Edge radii sizing

In the present study, edge radius is presented as a ratio,  $R/H$ . Model height  $H$  was chosen as a non-dimensionalizing parameter since both length scales are associated with the separation bubble length because:

1. As edge radius  $R$  is sufficiently large, flow remains attached around the building edge. Therefore, it is presumed that as  $R$  increases, the separation bubble on the roof ought to shrink.
2. Roof regions which experience high suctions are within the separation bubble, and the size of these regions are related to the building height (Kopp & Morrison, 2018).

Given the relations of  $R$  and  $H$  with the size of the separation bubble, the parameter  $R/H$  may be directly proportional to separation bubble size as is further discussed in Chapter 4. Thus, low-rise buildings with similar  $R/H$  ought to experience similar separated flow behaviour if the free stream turbulence and building aspect ratios are the same, as previously discussed in section 1.1.2.

The smallest  $R/H$  was 0.3% . This edge radii is the combination of the smallest controllable edge radius producible through 3D printing at the University Machine Services and the height of the smallest model at 1:200 scale. Wind tunnel models were constructed using an EOS 3D printer whose smallest controllable radius is 0.0635 mm.

The sharpest model configuration is somewhat similar to the edge radii of buildings in full-scale. In building construction, various materials may be used for cladding, including sheet metal, masonry and glass. Measurements of edge curvature on masonry and glass cladding components was difficult to find. The most detailed information on edge radius available was for composite metal cladding systems made of bended sheet metals. A survey of the edge radii of metal cladding systems was conducted by examining CAD drawings from four manufacturers, which are in Appendix B, seem to vary between 1.2 to 5 mm, as summarized below in Table 2-3. When applied to the present building dimensions, this would result in a full – scale  $R/H$  of 0.03% to 0.125%.

**Table 2-3 Survey of metal panel cladding systems**

Manufacturer	Radius of Curvature [mm]	
	Parapet	Wall Corner
Atas International Inc.	1.6	5
Vicwest	1.2	3.2
Alucobond	1.6	1.6
Centria	3.9	3.9

The radius on the sharpest models ( $R/H = 0.3\%$ ) is one order of magnitude greater than the sharpest edge reported at full-scale, should the building use metal cladding. However, as will be further examined below, it is not expected that local pressures will change significantly below  $R/H = 0.3\%$ , so this value is representative of a “sharp” edge.

The larger  $R/H$  that were selected were based on  $R/H$  which had been shown to significantly alter flow and surface pressures in other low-rise building/ bluff body aerodynamics studies, as summarized in Table 2-4. Based on the review of literature, changes to flow structure and surface pressure distributions tend to appear at  $R/H > 10\%$  in both smooth and turbulent upstream flows. Also to note is that detailed model manufacturing information were not reported in most studies. The exception was the study by Carssale et al. (2014) who report a dimensional tolerance of 0.1% of cylinder width ranging from 50-150mm.

**Table 2-4 Studies of bluff bodies with curved edges**

Study name	Geometry	Scale	$H_m$ [m]	R/H		Model Material
				Min	Max	
Dong et al. 2019	Low -rise bldg.	200	0.2	0% <sup>1</sup>	18%	Not reported
van Hinsberg et al. 2017	Square Cyl.	n/a	0.06	16%	29%	Stainless steel
Wang and Gu 2015	Various rect. Cyl.	n/a		0% <sup>1</sup>	15%	Organic glass
Carassale et al. 2014	Square Cyl.	n/a	0.05 to 0.15	0%	13%	Aluminum
Mahmood 2011	TTU Bldg..	100	0.04	0% <sup>1</sup>	25%	Plexiglas
Surry and Lin 1995	TTU Bldg..	50	0.078	10%	-	Acrylic
Robertson 1991	Silsoe Bldg..	1	5.3	12%	-	Sheet metal
Cooper 1985	Trucks	10 to 4		0% <sup>1</sup>	25%	Not reported
Delany and Sorensen 1953	Square Cyl.	n/a	0.03 to 0.3	2%	33%	Lacquered wood
	2:1 Rect. Cyl.	n/a	0.015to .15	4%	50%	

To minimize the number of edge radii,  $R$ , considered, five  $R/H$  ranging from 0.3% to 20% were considering, varying each by a factor of 2. A summary of all model configurations considered is provided in Table 2-5. A visual representation of the model radii being considered is shown in Figure 2-4.

**Table 2-5 Wind tunnel model configurations**

Scale	$H_m$ [mm]	$W_m$ [mm]	$L_m$ [mm]	$R_m$ [mm]				
				R/H = 0.3%	R/H = 2.5%	R/H = 5%	R/H = 10%	R/H = 20%
1:25	160	400	600	0.508	4	8	16	32
1:50	80	200	300	0.254	2	4	8	16
1:100	40	100	150	0.127	1	2	4	8
1:200	20	50	75	0.0635	0.5	1	2	4

<sup>1</sup>Edge geometry reported as “Sharp”, actual edge radius nor manufacturing tolerances were provided.

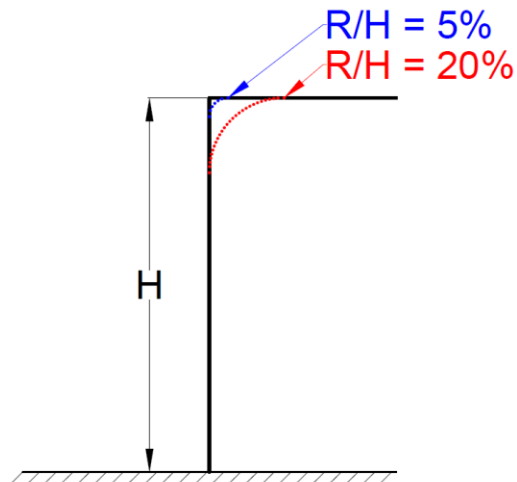


**Figure 2-4 Visualization of edge radii considered**

### 2.1.4 Building Sign Conventions

Due to symmetry, the models are tested at azimuths,  $\theta$ , from 0 to 90° in 5° increments as defined by Figure 2-5.

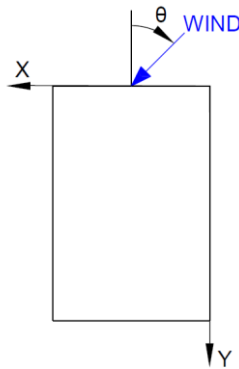


**Figure 2-5 Azimuth  $\theta$  sign convention.**

To observe the effect of edge radii in normal flow directions, three lines of taps are included around the middle model walls and roof as defined below in Figure 2-6. The purpose of these lines is to capture the separating flow behaviour in normal wind directions.

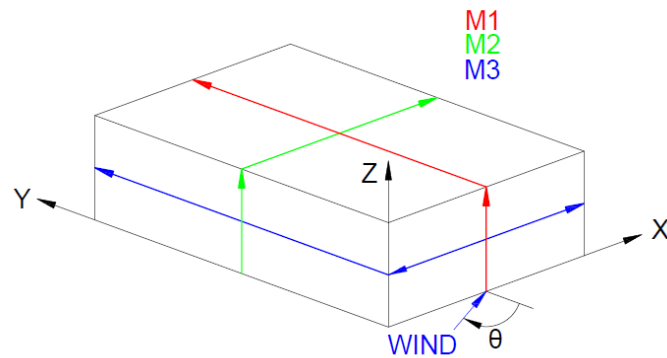


**Figure 2-6 Lines of taps located on models.**

Midlines are divided based on building surface. The location of the tap on the surface is denoted as  $S$ , whose origin differs based on surface. On plots for pressure distributions,  $S$  is normalized by the length of the surface. For midlines M1 and M2, surfaces S1, S2 and S3 refer to the windward wall, roof and leeward wall, respectively, as shown in Figure 2-7. The origin for tap locations on each surface is denoted by red arrows.

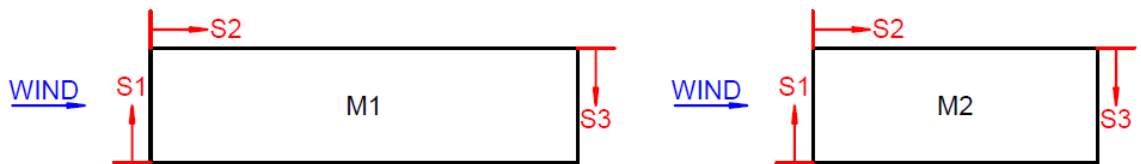


**Figure 2-7 M1 and M2 midline sign convention (side view).**

The sign convention for M3 is shown in Figure 2-8. S1 refers to the windward wall, S2 and S4 are the side walls and S3 is the leeward wall.



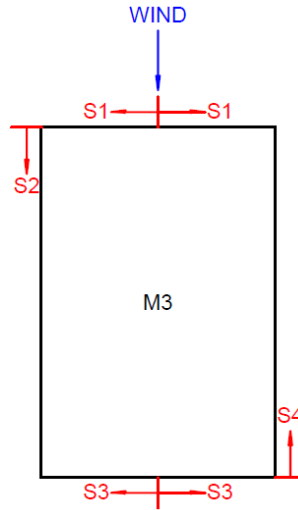


**Figure 2-8 M3 midline sign convention (plan view).**

Additionally, lines of taps along the longest roof edges were used to observe high suction produced by conical vortices, these lines of taps as well the sign convention for tap locations is shown in Figure 2-9. Tap coordinates were normalized using building plan dimensions, i.e.,  $y/L$  and  $x/W$ . Important to note is that the origin of this sign convention is located at the roof corner where the edge curvature of the roof edge intersect.

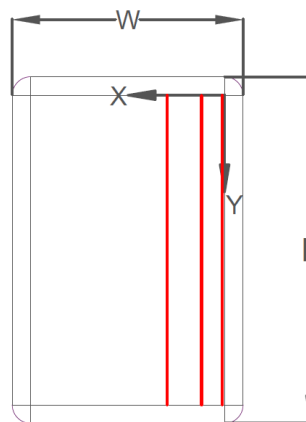


**Figure 2-9 Tap lines in red for pressures at oblique angles (plan view).**

As previously discussed, the axis of rotation of the conical vortex is located along a ray extending from the roof corner, and offset from the roof edge by an angle,  $\phi_c$ . The

location of the conical vortex core can be estimated by the location of the maximum mean pressure coefficient on the roof (Banks, Meroney, Sarkar, Zhao, & Wu, 2000). As shown in Figure 2-10, the location of the maximum pressure coefficient along a given tap line is denoted by  $l_c$  and the location of the conical vortex axis may be estimated with  $\phi_c$ , where:

$$\phi_c = \tan^{-1}\left(\frac{d}{l_c}\right) \quad (2-1)$$

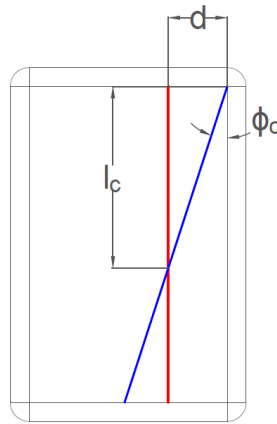


**Figure 2-10 Approximation of conical vortex axis angle,  $\phi_c$ , using the location of the maximum  $\overline{Cp_H}$ ,  $l_c$ , observed along a tap lines (in red).**

Effects of edge radius on area-averaged  $Cp$ 's and overall uplifts are examined in Chapter 5. Three building regions are considered for area averages: the middle of the windward roof edge, the windward roof corner, and the windward wall, as shown in Figure 2-11. Area-averaged pressure coefficients for the middle of the roof (1) and wall (3) are examined at a  $0^\circ$  azimuth flow direction, while values at the roof corner were examined at a  $45^\circ$  azimuth. Pressures and forces acting normal and away from building surfaces are presented as negative values.

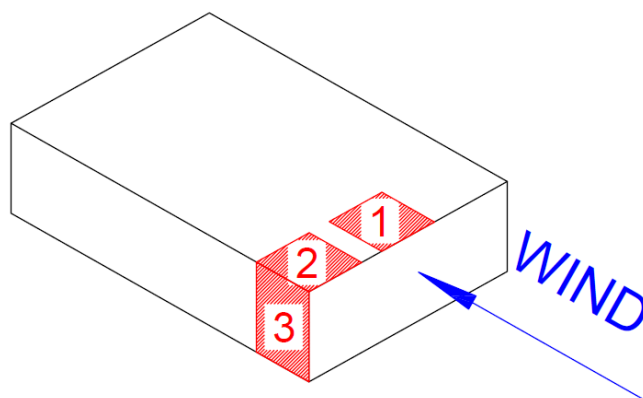


**Figure 2-11 (1) Middle roof, (2) roof corner and (3) wall regions examined for area averaging.**

## 2.2 Flow simulation

In order for surface pressures to be comparable between models of different scales, the upstream flow characteristics need to be similar. To ensure similarity, a wind tunnel setup must be selected such that the flow produced is similar across the chosen model scales in terms of turbulence spectra, mean velocity profiles and turbulence intensity at roof height.

## 2.2.1 Terrain Simulation

Wind tunnel testing was conducted in BLWT II at the Boundary Layer Wind Tunnel Laboratory, 1:25 and 1:50 scale models were tested in January 2019 while 1:100 and 1:200 models were tested in May 2019. The dimensions of the wind tunnel are shown below in Table 2-6.

**Table 2-6 BLWT II Dimensions**

<b>Tunnel Length</b>	39 m
<b>Width</b>	3.36 m
<b>Inlet Height</b>	1.85 m
<b>Outlet Height</b>	2.5 m

Upstream flow conditions can be controlled using roughness blocks along the fetch of the tunnel and spires and barriers at the tunnel inlet, as shown in Figure 2-12. Six standard configurations and their resultant flows were considered to find flow that would be similar at the chosen model scales. Details of the selected configurations are in Appendix C.



**Figure 2-12 Red spires and 15" barrier.**

A typical test setup is shown in Figure 2-13. Building models were set on the wind tunnel turntable. A standard 1.22 m radius proxy board was placed around the models and fastened to the turntable by screws. Seams around model base and proxy board were sealed with tape to prevent “jetting” during testing.

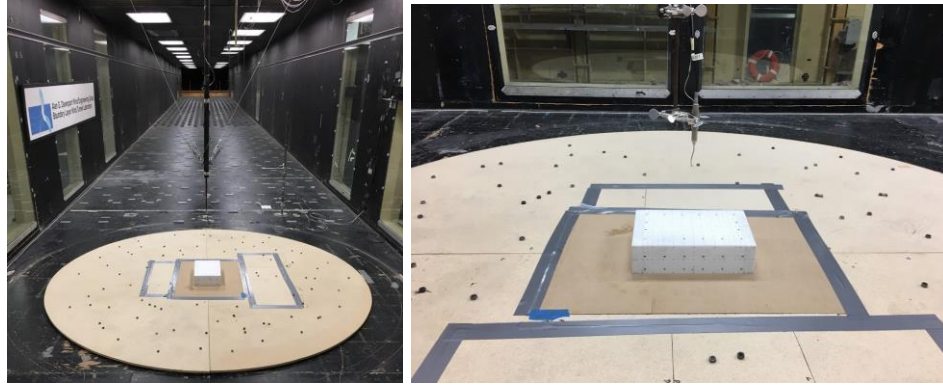


**Figure 2-13 Typical wind tunnel setup for 1:50 scale model and Open 15 exposure.**

### 2.2.2 Exposure Selection

Free stream turbulence greatly affects the aerodynamic behaviour of sharp-edged bluff bodies, as discussed in section 1.1.2. Turbulence can be described to contain a spectrum of eddies producing velocity fluctuations at various frequencies and length scales (Cao, 2013). In the context of flow around bluff bodies, the content of the turbulence spectrum can be separated into two categories: small-scale and large-scale turbulence. Small-scale turbulence is related to high frequency eddies which affect the aerodynamic behaviour of bluff bodies by interacting with shear layer roll-up in separating and reattaching flow (Tieleman 2003, Lander et al. 2016). Large-scale turbulence has larger eddies producing low frequency fluctuations which can be considered quasi-steady (Asghari Mooneghi et al., 2016) but can affect the maturation of vortices form in separated flow (Tieleman, 2003). The turbulence content can be described using the non-dimensional power spectral density and frequency as:

$$\frac{f S_u(f)}{\sigma_u^2}, \quad \frac{fH}{\bar{U}} \quad (2-2)$$

As discussed, large-scale turbulence is difficult to replicate, and may be missing in wind tunnel simulations at larger model-scales. Since small-scale turbulence is primarily responsible for the separating and reattaching flow behaviour, it is sufficient to only match the small-scale, high frequency portion of the non-dimensionalized turbulence spectra to ensure aerodynamic similarity (Asghari Mooneghi et al., 2016). Discrepancies

in large-scale turbulence content can be later accounted for by a quasi-steady (QS) model if needed (Wu & Kopp, 2018; Asghari Mooneghi et al., 2016). However, this approach was not used in the present study, so the focus in exposure selection was on matching the high frequency portion of the spectra as closely as possible. Subsequently, only mean and RMS pressure coefficients are used to define a suitable  $R/H$  in the present work.

In order to compare spectra between wind profiles for various model scales, the stream-wise velocity time history was examined at the model height. Streamwise velocity time histories were measured using a Cobra probe sampling all three velocity components at 625 Hz for 3 minutes. Spectra were estimated using segments of 2048 samples with 50% overlap. No filter was applied to velocity measurements

The most important portion of the spectra to match was the portion which could not be corrected for using a QS model. The rationale was that, if for some reason, turbulence spectra conditions in the wind tunnel are difficult to match, we could at least match the high frequency portion at which the QS model cannot correct for. According to Wu and Kopp (2018) difference in spectra for length scales larger than  $L_c = 5H$  could be accounted for by a QS model. As a result, using the mathematical manipulation below, a non-dimensionalized cut-off frequency,  $f_c$ , was defined, above which, the streamwise turbulence spectra ought to match,

$$L_c = 5H ; \Delta T_c = \frac{5H}{\bar{U}} = \frac{1}{f_c} \quad (2-3)$$

$$f_c = \frac{\bar{U}}{5H} \text{ or } \frac{f_c H}{\bar{U}} = 0.2 \quad (2-4)$$

where  $\Delta T_c$  is a time scale and thus velocity  $\bar{U}$  can be defined as  $\bar{U} = L/\Delta T_c$  where  $L$  is a length scale

After comparing six different wind tunnel profiles at four roof heights, the best match that could be made in the spectra at  $z = H$  is shown in Figure 2-14. The selected spectra show a reasonable match above  $\frac{fH}{\bar{U}} > 0.1$ , meaning that the small-scale turbulence content similar. However, it is evident that the integral scales are different amongst the

simulations and that there is a mismatch in the low-frequency portion of the spectra. As a result, direct comparison of peak pressure coefficients between different model scales is not possible.

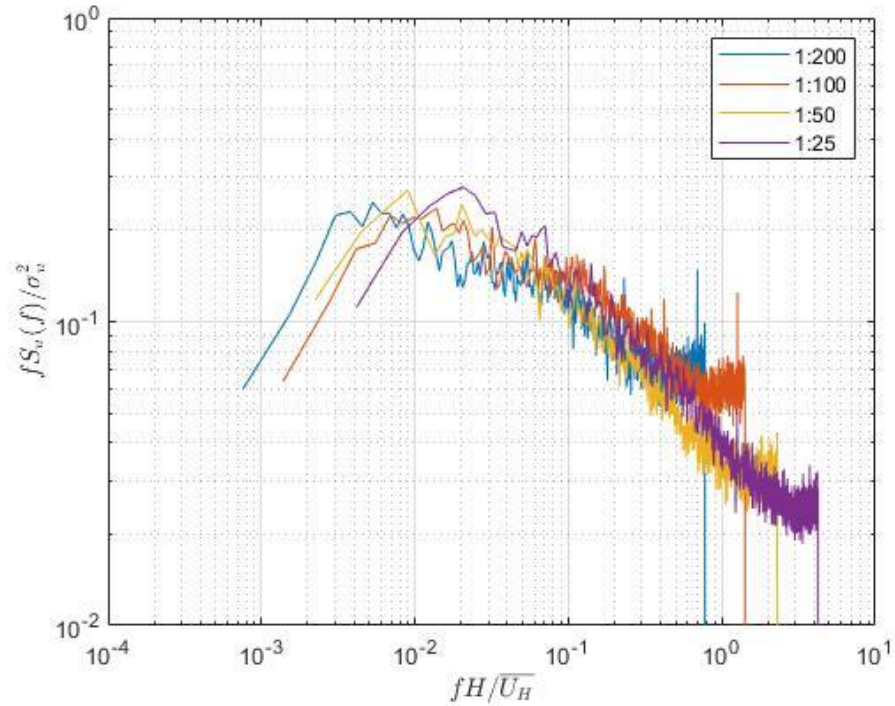


**Figure 2-14 Velocity spectra of the selected profiles at model roof height  $z=H$ .**

Non-dimensional mean velocity profiles of these selected exposures also match reasonably, as shown in Figure 2-15. Important to note is that measurements of the profile below the 1:200 model height (2cm) were not made as the probe was getting very close to the tunnel floor. For the sake of comparison and to address the missing velocity measurements at smaller model scales, a logarithmic mean velocity profile was fitted to data, defined as

$$\bar{U}(z) = \frac{u_*}{\kappa} \ln\left(\frac{z}{z_0}\right) \quad (2-5)$$

where  $u_*$  and  $\kappa$  are the friction velocity and Karman constant ( $\approx 0.4$ ), respectively (Cao, 2013).

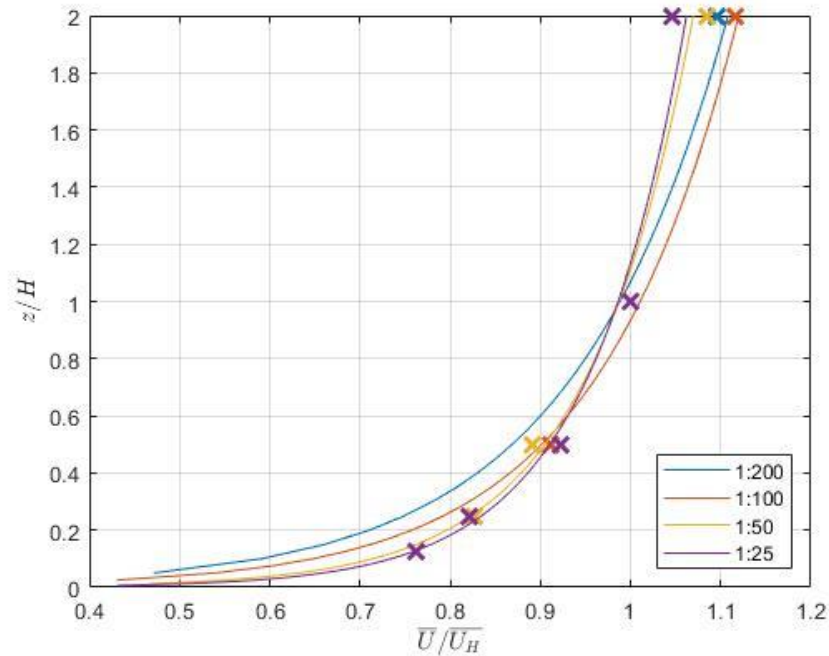


**Figure 2-15 Non dimensional mean velocity profile of selected profiles where (×) indicate measurements and (–) represent fitted profile.**

Roof height streamwise and vertical turbulence intensities,  $I_u$  and  $I_v$ , respectively are presented below in Table 2-7. It can be seen that there is a reasonable match in  $I_u$  amongst the chosen model scales. Some differences are observed in  $I_v$  which may affect peak pressure distributions along the roof at oblique wind directions (Tieleman, Reinhold, & Hajj, 2001), although peaks are not a focus in the present study.

**Table 2-7 Summary of selected profiles**

Scale	1:200	1:100	1:50	1:25
$\overline{U}_H$ [m/s]	8.05	8.83	10.86	11.78
$I_u(H)$ [%]	15.5	14.4	16.1	14.1
$I_v(H)$ [%]	9.4	8.6	12.2	10.9
$Re_H$	$1.1 \times 10^4$	$2.4 \times 10^4$	$5.8 \times 10^4$	$1.3 \times 10^5$
<b>Blockage Ratio</b>	0.01%	0.1%	0.2%	0.8%



$Re_H$  was not held constant in order to observe any potential  $Re_H$  dependencies in pressure coefficients.  $Re_H$  sensitivity could provide another way to evaluate a limit on  $R/H$ , since pressure coefficients around a sharp-edged bluff body are thought to be invariant with  $Re_H$  above  $10^4$ . Also, blockage ratios were fairly small so no corrections were made for blockage effects

As can be seen, there are slight differences in the profiles, which is always a challenge in such experiments, especially with limited degrees of freedom for the roughness elements in the test section.

## 2.3 Data Acquisition

Pressure coefficients were measured using electronic pressure scanners. Pressure taps connected to electronic pressure scanners via approximately 2' of 1/16" ID plastic tubing. Restrictors were added to the tubing, resulting in negligible attenuation or distortion of surface pressure fluctuations with frequencies up to about 200 Hz (Ho et al., 2005). For the estimation of pressure spectra, a 200 Hz low-pass filter was applied to pressure time histories to address distortions in pressure fluctuations above 200Hz. Similar to velocity spectra, the pressure spectra at select tap locations were determined using segments of 2048 samples with 50% overlap.

In the present study, pressure coefficients were sampled at 625 Hz to match the Cobra probe sampling rate. Additionally, static pressure used to determine the zero output of the scanners are taken from the Pitot static tube at the reference height and fed directly to all pressure scanners during calibration.

Due to different model scales and mean velocities at the roof height, sampling times varied between model scales. The sampling rate and sampling duration were determined using the non-dimensionalized sampling time

$$\frac{T_s \overline{U_H}}{H} \quad (2-6)$$

where  $T_s$ ,  $U_H$  and  $H$  are sample time, mean roof height velocity and model height respectively. Typical sampling duration,  $T_s$ , for 1:50 scale low-rise testing is 3 minutes (180 s). A non-dimensional sampling time was determined for the 1:50 scale configurations which was then used to determine a sampling time for other model scales. The selected sampling rates and durations are summarized in Table 2-8.

**Table 2-8 Sample times of wind tunnel tests**

Scale	$H$ [m]	$U_H$ [m/s]	$f_s$ [Hz]	$T_s$ [s]	$\frac{(f_s)^{-1}\overline{U_H}}{H}$	$\frac{T_s\overline{U_H}}{H}$
1:200	0.02	8.0	625	60	0.64	$2.4 \times 10^4$
1:100	0.04	8.83	625	120	0.35	$2.6 \times 10^4$
1:50	0.08	10.86	625	180	0.22	$2.4 \times 10^4$
1:25	0.16	11.78	625	300	0.12	$2.2 \times 10^4$

A wire-stayed mast is attached to the tunnel ceiling to place a cobra probe  $1H$  above the center of the roof of every model. The cobra probe measured 3D velocity at 625 Hz simultaneously with pressure measurements so that a QS model could be applied later, following Wu and Kopp (2018). Vibrations in the cobra probe and mast were of concern; however, no vibrations were visually observed during testing.

Wind tunnel tests were conducted for the 1:200,  $R/H = 0.3\%$  and 1:25,  $R/H = 0.3\%$  models with and without the mast in place. No differences in mean and RMS  $Cp$ 's were observed for tests with and without the mast at 1:25 scale. However, a slight scalar offset was observed with 1:200 data, though it is within measurement uncertainty, which will be further discussed in Chapter 3. Subsequently, it was assumed that the mast posed no blockage issues. Pressure coefficients measured on the roof with and without the mast are shown in Appendix D.

## 2.4 Data Analysis

The mean and the standard deviation of pressure coefficients were primarily used to evaluate effects of varying edge radii. For a given pressure coefficient time history of  $n$  samples, the mean pressure coefficient is defined as

$$\overline{Cp_H} = \frac{\sum_{i=1}^n Cp_{Hi}}{n} \quad (2-7)$$

Fluctuating pressures were characterized by the standard deviation of the pressure coefficient time history defined as

$$\widetilde{Cp_H} = \left[ \frac{\sum_{i=1}^n (Cp_{Hi} - \overline{Cp_H})^2}{n-1} \right]^{\frac{1}{2}} \quad (2-8)$$

Peak values of  $Cp$ ,  $Cp_{max}$  and  $Cp_{min}$ , are important as they estimate the critical wind loads which a building may experience. Since there is a mismatch in integral length scales, peak pressure coefficients from tests at different model scales could not be directly compared nor used as a way to evaluate a suitable  $R/H$ . However, peak values from tests in the same model scale could still be compared and used to observe  $R/H$  effects since upstream flow conditions are identical.

In the present study, peak pressure coefficients were determined using a Gumbel distribution estimated with the Lieblein best linear unbiased estimator method (Lieblein, 1974), as this is a common extreme value estimation method in wind engineering (Gavanski et al., 2016).

To evaluate the peak pressure coefficient at given tap, the  $Cp_H$  time history was divided into 30 equally sized segments. The largest instantaneous  $Cp_H$  sampled within each of these segments,  $Cp_{pk_{gi}}$ , are then recorded, ranked in ascending order and assigned estimators  $a_i$  and  $b_i$ . The Lieblein BLUE estimators used in the present analysis were determined by Hong et al. (2013) for 30 peaks ( $n_{pk_g} = 30$ ). The estimators and  $Cp_{pk_{gi}}$  were then combined to determine the scale factor,  $\alpha$ , and the location parameter,  $u$ , of the Gumbel distribution

$$\alpha = \sum_i^{n_{pk_g}} Cp_{pk_{gi}} b_i \quad (2-9)$$

$$u = \sum_i^{n_{pk_g}} Cp_{pk_{gi}} a_i \quad (2-10)$$

These parameters are used to determine the cumulative Gumbel distribution function  $F(Cp_{Hmin})$  for peak suctions,

$$F(Cp_{Hmin}) = \exp(-\exp(-\alpha(Cp_{Hmin} - u))) \quad (2-11)$$

For the present application, the 80% fractile peaks , i.e. ( $F(Cp_{Hmin}) = 0.8$ ), were compared which was found by rearranging the equation 2-11 into

$$Cp_{Hmin} = (-\log(-\log(0.8)) \alpha) + u \quad (2-12)$$

## Chapter 3: Uncertainty Analysis

### 3.1 Introduction

The present study seeks to investigate the effect of edge radii on surface pressures. To be confident that observed changes to surface pressures are due to changes in aerodynamic behaviour and not measurement uncertainty, an uncertainty analysis must be conducted.

Pressures on the model surfaces are measured by pressure taps connected to solid state pressure scanners by plastic tubing. The measurements directly from the scanners are represented as  $Cp_{ref}$ ,

$$Cp_{ref}(t) = \frac{p(t) - p_0}{\frac{1}{2} \rho \bar{U}_{ref}^2} \quad (3-1)$$

where  $p(t)$  is the instantaneous surface pressure,  $p_0$  is the static pressure,  $\rho$  is air density,  $\bar{U}_{ref}$  is the mean reference velocity measured by a Pitot-static tube in the wind tunnel, 57 inches above the tunnel floor.

For measured values to be comparable, pressure coefficients were re-referenced to roof height velocities using

$$Cp_H(t) = Cp_{ref}(t) \left( \frac{\bar{U}_{ref}}{\bar{U}_H} \right)^2 \quad (3-2)$$

where  $Cp_H(t)$  is the instantaneous pressure coefficient referenced to roof height and  $\bar{U}_H$  is the mean velocity measured at the model roof height.

The purpose of the uncertainty analysis is to determine the uncertainty bounds,  $w_{Cp_H}$ , related to the measurement of  $Cp_H$ . In other words, the aim is to determine how large the difference between two  $Cp_H$  measurements must be in order to be confidently unattributed to measurement uncertainty.

## 3.2 Approach

The determination of  $w_{Cp_H}$  involves a three step process, which follows prior work by Quiroga (2006):

1. Determination of the elemental error of each variable used to calculate  $Cp_H$
2. Determination of overall uncertainty of  $Cp_H$
3. Incorporation of uncertainty associated with statistical moments of  $Cp_H$

### 3.2.1 Elemental error

Various devices and systems are used to measure  $Cp_{ref}$  and velocities ( $U_{ref}$  and  $U_H$ ), each of which introduces uncertainty into the measurement of  $Cp_H$ . These uncertainties are elemental errors, which include uncertainty from equipment and well as variability in testing conditions. To determine  $w_{Cp_H}$ , the elemental errors must first be identified and categorized as either:

1. A bias limit,  $B$ , - systematic uncertainty that is unchanged between tests
2. A precision limit,  $S$ , – random error that varies between tests

Sources of elemental error in the wind tunnel pressure measuring system at BLWT II were identified by Quiroga Diaz (2006) and are presented in Table 3-1.

**Table 3-1 Sources of Elemental Error**

<b><math>Cp_{ref}</math></b>			
<b>Error Source</b>	<b>Reference</b>	<b>Value</b>	<b>Type</b>
Scanner Accuracy	Quiroga Diaz (2006)	0.0305[ $Cp_H$ ]	Bias
Scanner Thermal Zero Shift	Quiroga Diaz (2006)	0.0305[ $Cp_H$ ]	Precision
Thermal Stability	Quiroga Diaz (2006)	0.00061[ $Cp_H$ ]	Precision
A/D Converter Accuracy	Quiroga Diaz (2006)	0.0073[ $Cp_H$ ]	Precision
A/D Converter Repeatability	Quiroga Diaz (2006)	0.0073[ $Cp_H$ ]	Precision
Terrain	Mans et al. (2002)	0.04[ $Cp_H$ ]	Bias
Tap Dimension	Shaw (1960)	0.01[ $Cp_H$ ]	Bias
Tap Burrs	Arts et al. (1994)	0.006[ $Cp_H$ ]	Bias
Tap Angle	Erwin (1964)	0.001[ $Cp_H$ ]	Bias
<b>Velocity (<math>U_{ref}, U_H</math>)</b>			
Cobra Probe Accuracy	TFI (n.d.)	0.5 [m/s]	Bias

Errors associated with static pressures are assumed to be accounted for by pressure scanner uncertainties, since during calibration, static pressures from the Pitot static tube are fed directly to scanners to provide the static reference (Quiroga Diaz, 2006). Another source for errors in static pressures may be misalignment of the pitot but are omitted since these errors are negligible within a misalignment of  $\pm 20^\circ$  (Quiroga Diaz, 2006).

The bias and precision uncertainty for each variable used to determine  $Cp_H$  in equation 3-2, are combined to find the overall bias and precision limit for that given variable. This is done through a root sum squared method (Coleman & Steele, 2009), for a variable,  $x$ ,

$$B_x = (\sum B_{x,i}^2)^{\frac{1}{2}}; S_x = (\sum S_{x,i}^2)^{\frac{1}{2}} \quad (3-3)$$

The overall uncertainty for  $x$  is determined by combining the bias and precision limit using

$$w_x = [B_x^2 + (tS_x)^2]^{\frac{1}{2}} \quad (3-4)$$

where  $t$  is a Student  $t$  value, dependent on degrees of freedom. Since time histories of pressure coefficients measured at taps exceed 30 samples,  $t = 1.96$  for a 95% confidence level (Wheeler & Ganji, A.R., 1996).

### 3.2.2 Uncertainty of $Cp_H$

$Cp_H$  is a function of multiple variables; thus, to determine the uncertainty of  $Cp_H$ , uncertainties of the constituent variables must be combined. Consider the general case of a quantity,  $R$ , which is a function of multiple variables, i.e.,

$$R = f(x_1, x_2, \dots, x_n) \quad (3-5)$$

The uncertainty of the result  $R$ ,  $w_R$ , such that the uncertainty bounds of  $R$  are  $\pm w_R$  (Wheeler & Ganji, A.R., 1996), is,

$$w_R = \left[ \sum_{i=1}^n \left( w_{x_i} \frac{\partial R}{\partial x_i} \right)^2 \right]^{\frac{1}{2}} \quad (3-6)$$

where  $w_{x_i}$  is the uncertainty associated with the variable  $x_i$ .

Applying the equation above to equation 3-2 for  $w_{Cp_H}$ , the expression becomes

$$w_{Cp_H} = \left[ \left( w_{Cp_{ref}} \frac{\bar{U}_{ref}^2}{\bar{U}_H^2} \right)^2 + \left( w_{U_{ref}} \frac{2Cp_{ref}\bar{U}_{ref}}{\bar{U}_H^2} \right)^2 + \left( w_{U_H} \frac{-2Cp_{ref}\bar{U}_{ref}^2}{\bar{U}_H^3} \right)^2 \right]^{\frac{1}{2}} \quad (3-7)$$

Substituting terms from equation 3-2, and following the manipulation by Quiroga Diaz (2006), the expression simplifies to

$$w_{Cp_H} = \left[ \left( w_{Cp_{ref}} \left( \frac{Cp_H}{Cp_{ref}} \right) \right)^2 + \left( w_{U_{ref}} \left( \frac{2Cp_H}{\bar{U}_{ref}} \right) \right)^2 + \left( w_{U_H} \left( -\frac{2Cp_H}{\bar{U}_H} \right) \right)^2 \right]^{\frac{1}{2}} \quad (3-8)$$

$$\frac{w_{Cp_H}}{Cp_H} = \left[ \left( \frac{w_{Cp_{ref}}}{Cp_{ref}} \right)^2 + \left( 2 \frac{w_{U_{ref}}}{\bar{U}_{ref}} \right)^2 + \left( -2 \frac{w_{U_H}}{\bar{U}_H} \right)^2 \right]^{\frac{1}{2}} \quad (3-9)$$

Clearly,  $w_{Cp_H}$  is dependent on nominal the values of the variables. Since these variables may differ between model scales ( $Cp_H$ ,  $Cp_{ref}$  and  $\bar{U}_H$ ),  $w_{Cp_H}$  will also differ between scales.

### 3.2.3 Standard Error of $r^{th}$ order statistical moments

Typically,  $Cp_H$  is presented as a first or second order statistical moment (mean and RMS, respectively). The uncertainty involved in determining these statistical moments can be accounted for in  $w_{Cp_H}$  as a standard error for an  $r^{th}$  order moment,  $Var[m_r]$ . The standard error associated with the statistical moment is then combined with  $w_{Cp_H}$  to determine the uncertainty of the mean and RMS  $Cp_H$ .

$$w_{m_r} = [w_{Cp_H}^2 + tVar[m_r]]^{\frac{1}{2}} \quad (3-10)$$

A set of independent samples is required to determine standard error (Benedict & Gould, 1996). A  $Cp_H$  time history from a typical tap is used as the sample set. However, samples



from the time history may not be independent since surface pressures at a fixed location in separated and reattaching flow are temporally correlated (Cherry, Hillier, & Latour, 1984). To obtain a set of independent  $Cp_H$  values from the time history, the autocorrelation function,  $R_{xx}$ , and integral time scale,  $T$ , were determined from the time history of interest with

$$T = \int_0^b R_{xx} d\tau \quad (3-11)$$

where  $b$  is the time step where the first occurrence of the down crossing of  $R_{xx}$  past zero occurs and  $d\tau$  is time step.

Multiple samples taken within the integral time scale cannot be considered independent, since within this time period,  $R_{xx} > 0$ . A set of independent samples was then formed by taking consecutive samples from the time history, that are separated by a time  $T$ . When applied to all model configurations, the size of the independent sample sets,  $n$ , exceeded 1000, which is suitable for determining the standard error of statistical moments of turbulent quantities (Benedict & Gould, 1996).

Second and fourth order statistical moments were determined from the independent sample set and used to estimate the standard error using (Stuart & Ord, 1994)

$$Var[\overline{Cp_H}] = \left(\frac{m_2}{n}\right)^{\frac{1}{2}} \quad (3-12)$$

$$Var[\widetilde{Cp_H}] = \left[\frac{1}{n} \frac{(m_4 - m_2^2)}{4m_2}\right]^{\frac{1}{2}} \quad (3-13)$$

Mean results determined for each model scale is presented below in Table 3-2.

**Table 3-2 Mean of standard errors of  $Cp_H$  statistical moments**

SCALE	$Var[\overline{Cp_H}]$	$Var[\overline{Cp_H}]$
1:200	0.011	0.009
1:100	0.005	0.004
1:50	0.007	0.006
1:25	0.005	0.005

### 3.2.4 Nominal values for uncertainty estimates

In equation 3-9, nominal values for  $p_H$ ,  $U_{ref}$  and  $U_H$  are required to determine  $w_{Cp_H}$ . Nominal values of  $\overline{U}_{ref}$  and  $\overline{U}_H$  were taken as the mean reference and roof height velocities measured by Cobra probes. For nominal values of  $Cp_H$ , a normalized pressure coefficient  $Cp_D$  was used due to account for an observed scalar offsets in  $Cp_H$  results.

When examining data, for a given  $R/H$  across different scales, a scalar offset was observed in the  $\overline{Cp_H}$  profile on surfaces affected by to separated flow behaviour, namely the roof and leeward wall. An example of this observation is shown below for the M1 midline in Figure 3-1.

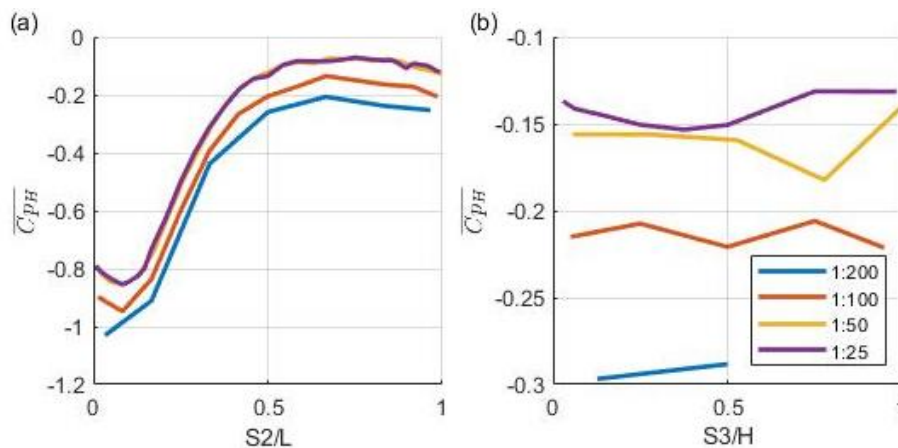


**Figure 3-1  $\overline{Cp_H}$  at  $R/H = 0.3\%$  plotted along the M1 midline on (a) roof and (b) leeward wall.**

The magnitude of  $\overline{Cp_H}$  increases slightly as the scale diminishes, and this trend persists on the leeward wall of all model configurations. The trend could be due blockage effects, since the frontal area of the models vary significantly with scale. However, as shown in Table 2-7, the blockage ratios are well below the recommended limit of 5% (ASCE 49-

12), and these differences in mean pressure coefficients are within the uncertainty estimates which will be later discussed.

Upon examining the mean velocity measured  $1H$  above the model roof during testing, it is possible that the offset is due to a slight mismatch in the mean velocity profile. As shown in Figure 3-2. The mean velocity measured above the model increases slightly with model scale. Subsequently, blockage effects are expected to be negligible, and it is more likely that these offsets are due to measurement uncertainty in the static pressure or a slight mismatch in the mean velocity profile.

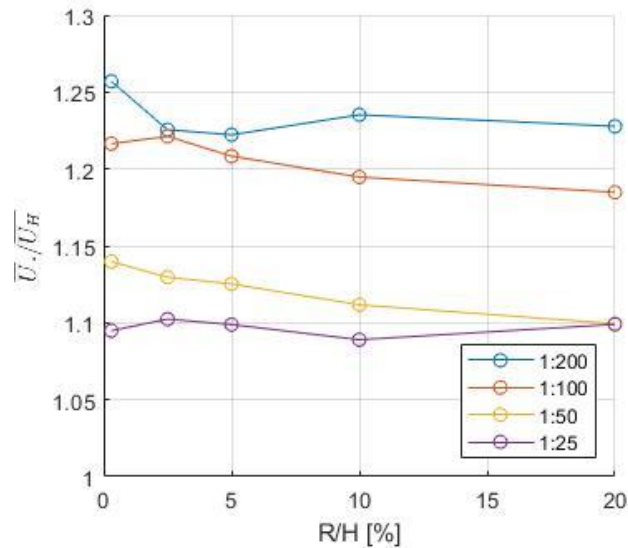


**Figure 3-2 Mean velocity measured  $1H$  above the center of models at a  $90^\circ$  azimuth**

In order to compare findings between different model scales and address the scalar offset,  $\overline{Cp_H}$  is normalized by a base pressure coefficient  $Cp_b$ , producing a parameter,

$$Cp_D(t) = Cp_H(t) - Cp_b \quad (3-14)$$

Base pressure was taken as the average  $\overline{Cp_H}$  across the leeward wall of the model following Castro and Robins (1977). In flow past bluff bodies, base pressure is observed to be relatively uniform on surfaces unaffected by separated flow behaviour. The base pressure coefficient ought to be consistent across model scales if flow conditions and upstream turbulence behaviour are similar. If upstream turbulence is similar, vortex

generation and subsequently wake behaviour downstream ought to be similar across model scales, leading to a similar base pressure (Lander, Letchford, Amitay, & Kopp, 2016).

Using this normalizing approach, it was shown that the  $\overline{Cp_H}$  distributions on the roof and leeward wall collapse onto a single curve as shown in Figure 3-3. Subsequently, for comparison of results across model scales,  $\overline{Cp_D}$  will be used as a nominal value for determining  $w_{Cp_H}$  as well as to compare  $Cp_H$  results across different model scales.

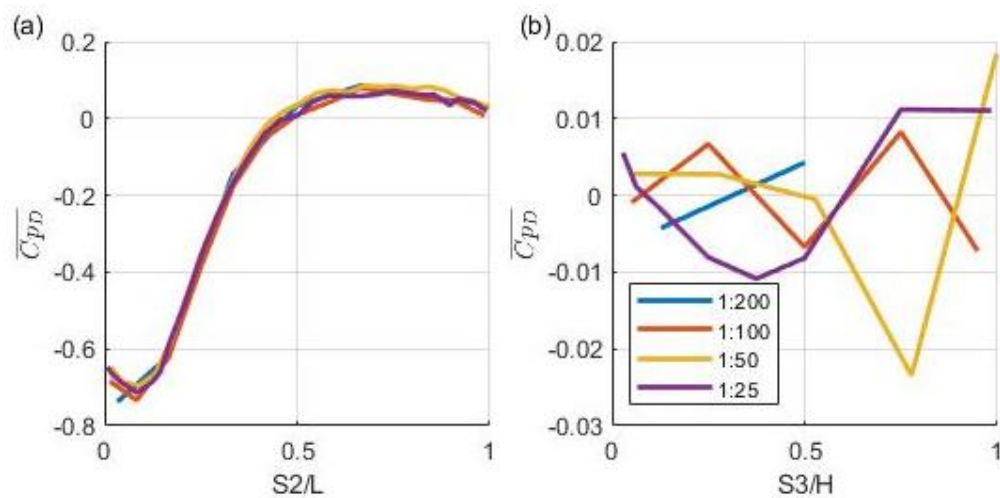


**Figure 3-3  $\overline{Cp_D}$  at  $R/H = 0.3\%$  plotted along the M1 midline on (a) S2 roof and (b) S3 leeward wall.**

As pressure varies spatially on a model surface, the maximum  $\overline{Cp_D}$  measured on the roof along the midline M1 at a  $0^\circ$  azimuth for the sharpest ( $R/H = 0.3\%$ ) model taken as the nominal value of  $Cp_H$  two reasons.

1. It is a relatively high value and would provide a reasonably large estimation of  $w_{Cp_H}$
2. This nominal value of  $Cp_D$  is relatively consistent across most model configurations (all model scales,  $0.3\% \leq R/H < 5\%$ ),

Further expanding on the second point, for a given model scale, the average of the nominal  $\overline{Cp_D}$  across varying  $R/H$  are presented in Table 3-3 along with the coefficients of variance. As shown below, these values are similar across model scales and edge radii.

**Table 3-3 Nominal  $Cp_D$  used for determination of  $w_{Cp_H}$**

SCALE	$\overline{Cp_D}$	CoV
1:200	-1.153	0.022
1:100	-1.091	0.019
1:50	-0.937	0.031
1:25	-0.947	0.062

### 3.3 Results

Three different approaches were used to determine  $w_{Cp_H}$ , each with a different application.

**Method A** –  $w_{Cp_H}$  estimated assuming pressures scanners and Cobra probes are accurate and that the only source of uncertainty is random error. In other words, equation 3-9 becomes

$$\frac{w_{Cp_H}}{Cp_H} = \frac{w_{Cp_{ref}}}{Cp_{ref}} \text{ and } w_{Cp_{ref}} = tS_{Cp_{ref}} \quad (3-15)$$

Uncertainty determined in this manner is useful for comparing results from experiments that are repeated using the exact same experimental setup.

**Method B** –  $w_{Cp_H}$  estimated assuming that cobra probes are accurate and that pressure scanners are the only source of uncertainty or

$$\frac{w_{Cp_H}}{Cp_H} = \frac{w_{Cp_{ref}}}{Cp_{ref}} \text{ and } w_{Cp_{ref}} = \left[ B_{Cp_{ref}}^2 + (tS_{Cp_{ref}})^2 \right]^{\frac{1}{2}} \quad (3-16)$$

This method assumes that when comparing  $Cp_H$  from models of the same scale, since  $U_{ref}$  and  $U_H$  come from the same set of Cobra probe measurements, uncertainty from the velocity measurements are already accounted for.

**Method C** – All sources of uncertainty are included. The  $w_{Cp_H}$  estimated with this method is an absolute uncertainty i.e., how far off measured results can potentially be from the “true” values. Uncertainties from this method could be used to compare values with studies from other wind tunnel laboratories. By including all sources of errors, all elemental errors used in Table 3-1 are included and all terms in equation 3-9 are used, i.e.,

$$\frac{w_{Cp_H}}{Cp_H} = \left[ \left( \frac{w_{Cp_{ref}}}{Cp_{ref}} \right)^2 + \left( 2 \frac{w_{\bar{U}_{ref}}}{\bar{U}_{ref}} \right)^2 + \left( -2 \frac{w_{\bar{U}_H}}{\bar{U}_H} \right)^2 \right]^{\frac{1}{2}} \quad (3-17)$$

Results from these three methods are presented below in Table 3-4. As more elemental errors are considered from A to C, it is clear that uncertainty bounds increase. Also, there is observed to be an increase in  $w_{Cp_H}$  with the model-scale which is further discussed in the following section.

**Table 3-4  $w_{C_{pH}}$  determined using various methods**

	Scale	$w_{C_{ref}}$	$w_{\bar{u}}$	$w_{\overline{C_{pH}}}$	$w_{\widetilde{C_{pH}}}$
<b>A</b>	200	0.0322	N/A	0.110	0.109
	100	0.0322	N/A	0.091	0.091
	50	0.0322	N/A	0.059	0.059
	25	0.0322	N/A	0.050	0.050
<b>B</b>	200	0.0756	N/A	0.256	0.256
	100	0.0756	N/A	0.213	0.213
	50	0.0756	N/A	0.139	0.138
	25	0.0756	N/A	0.118	0.118
<b>C</b>	200	0.0815	0.5	0.277	0.277
	100	0.0815	0.5	0.230	0.230
	50	0.0815	0.5	0.150	0.150
	25	0.0815	0.5	0.127	0.127

Application of the estimated  $w_{C_{pH}}$  to  $\overline{C_{pH}}$  and  $\widetilde{C_{pH}}$  measured in the sharpest configuration  $R/H=0.3\%$  along the M1 roof (S2) is shown in Figure 3-4 and Figure 3-5, respectively. Differences in  $\overline{C_{pH}}$  amongst different models scales is larger than in  $\widetilde{C_{pH}}$ . Also, scalar offsets in  $\overline{C_{pH}}$  is within  $w_{\overline{C_{pH}}}$  determined via methods B and C. This would suggest that the scalar offset attributed to measurement of uncertainty rather than significant differences in aerodynamic behaviour.

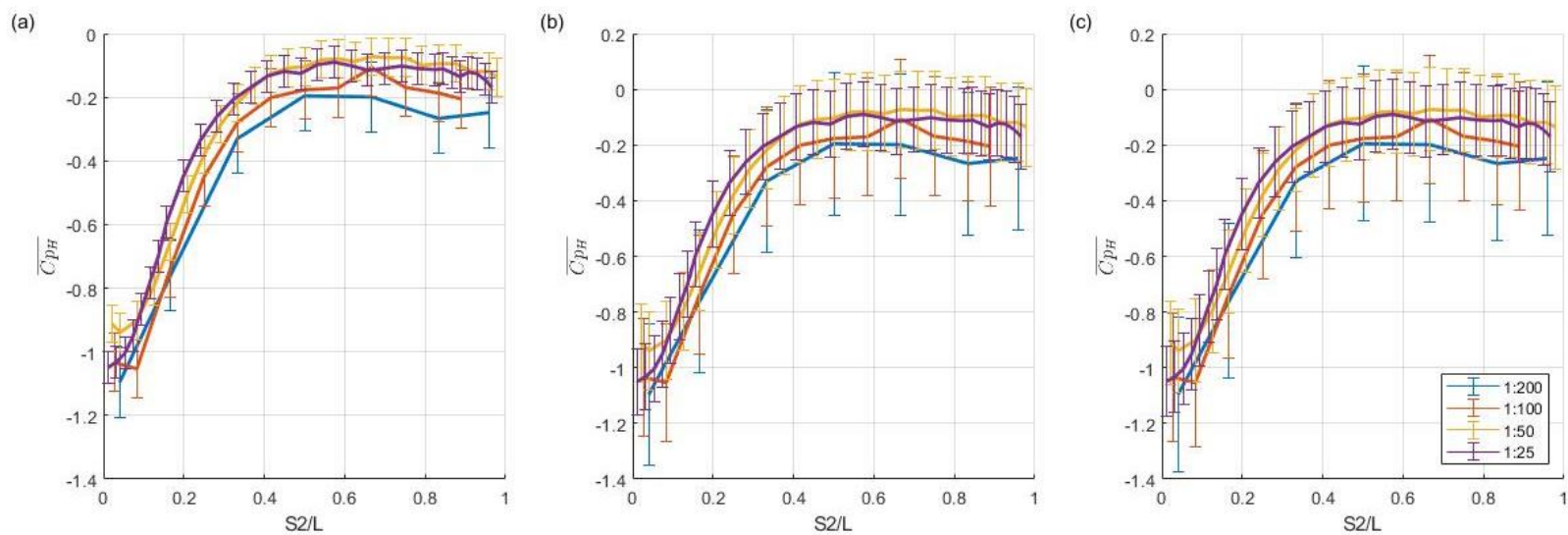


Figure 3-4  $\overline{C_{pH}}$  on M1 roof at  $R/H = 0.3\%$  with  $w_{\overline{C_{pH}}}$  determined from (a) Method A (b) Method B (c) Method C.

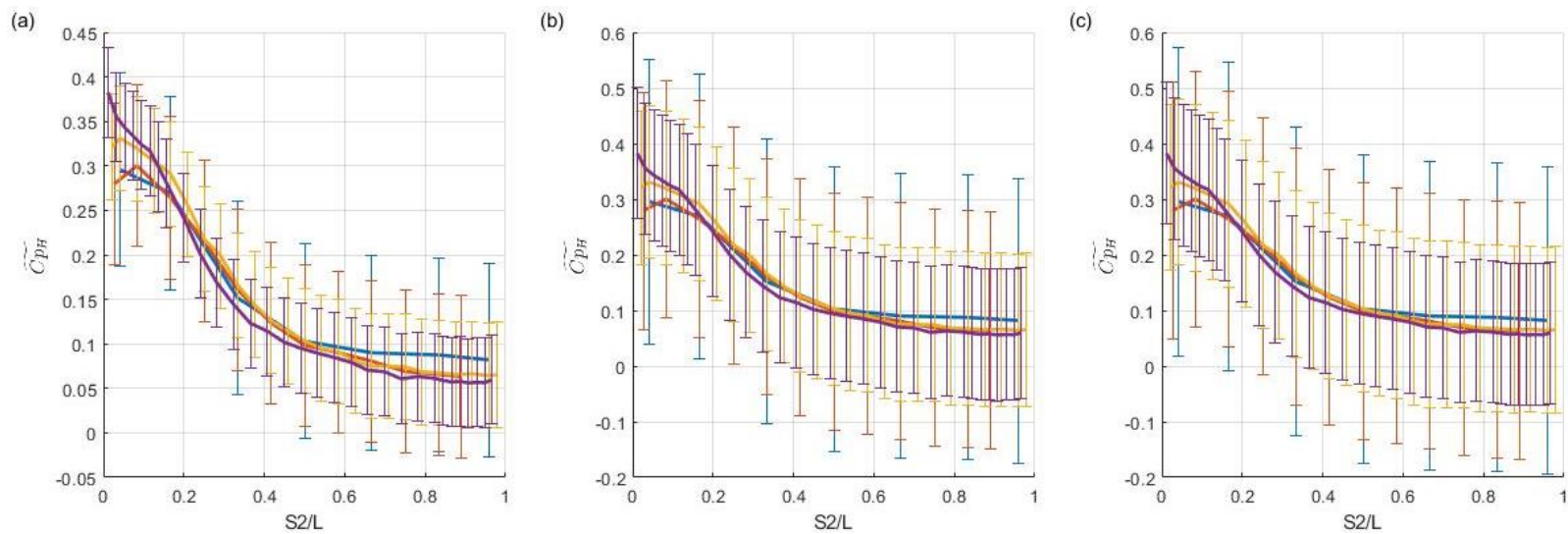


Figure 3-5  $\widetilde{C_{pH}}$  on M1 roof at  $R/H = 0.3\%$  with  $w_{\widetilde{C_{pH}}}$  determined from (a) Method A (b) Method B (c) Method C.



### 3.4 Discussion of uncertainty estimates

As previously noted, Table 3-4 shows that  $w_{\overline{Cp_H}}$  and  $w_{\overline{Cp_H}}$  decrease as the model scale increases. This trend would seem peculiar, as uncertainty estimates may be interpreted as absolute values, independent of the model-scale and instead, wholly dependent on the equipment used. Following this line of thought, since the same equipment is used for each test, the uncertainty estimate shouldn't change. However, the trend is explained by examining the uncertainty estimation process, and it will be shown to be caused by the differences in  $\overline{U_H}$ .

Focusing on Method A, the first step in determining  $w_{Cp_H}$  is to determine the sources of uncertainty (as summarized in Table 3-1). Elemental errors associated with  $Cp_{ref}$  came from scanner manufacturing specifications and are expressed as percentages of the full measurement range. In the case of the pressure scanners, the full measurement range is 5V and random uncertainty, such as the zero thermal shift, is as small as 0.2% of the full range or 0.01V. These elemental errors are constant since they only depend on the scanners themselves, which are reused from test to test.

The sources and magnitudes of the elemental errors do not change between scales since equipment is reused; however, what changes is the magnitude of pressures measured by the scanner. Though the scanners have a full-range of 5V, only a very small portion of this range is used during testing. According to Quiroga Diaz (2006), a value of  $Cp_{ref} = 1$  or free stream dynamic pressure measured in the center of the wind tunnel test section, relates only to a voltage of 0.328V on the scanners. Out of all the tests conducted, the largest instantaneous  $Cp_{ref}$  measured was 1.62, implying that the largest voltage experienced by scanners amongst all tests were, at most, 0.53V, merely 10% of the full-range. As a result, uncertainties whose voltages are small compared to the full measurement range (5V) become much more significant considering the actual range of voltage being used.

In the current approach, the largest  $\overline{Cp_D}$  from a roof midline, summarized in Table 3-3, are used to estimate  $w_{\overline{Cp_H}}$  and  $w_{\overline{Cp_H}}$  since they represent a reasonably large magnitude of

$Cp_H$  measured in testing. The actual pressures measured and their associated voltages at these points ( $Cp_{ref}$ ), are very small and decrease with scale as shown below in Table 3-5. Consequently, as the scale decreases, the actual pressure decreases, as does the voltage output. Thus, sources of uncertainty, which are fixed, become larger relative to the actual scanner voltage output, leading to the higher  $w_{Cp_H}$  estimates.

**Table 3-5: Nominal values of variables used in uncertainty estimation**

NOMINAL VALUES					
Scale	$\overline{Cp_D}$	$\overline{U}_H$ [m/s]	$\overline{U}_{ref}$ [m/s]	$\overline{Cp_{ref}}$	$w_{\overline{Cp_H}}$ (Method A)
200	-1.15	8.05	14.82	-0.34	0.110
100	-1.09	8.83	14.82	-0.39	0.091
50	-0.94	10.87	14.71	-0.51	0.059
25	-0.95	11.79	14.71	-0.61	0.050

For instance, the nominal  $\overline{Cp_D}$  in Table 3-5 at 1:25 and 1:200 scales would produce 0.21V and 0.11V, respectively. Considering just the thermal-zero offset of 0.01V, the uncertainty increases from 4.7% to 9.1% relative to the scanner output voltage in the 1:200 and 1:25 scale tests, respectively. From this example, it is clear that as scale increases, the relative significance of elemental errors decreasing, reducing  $w_{Cp_H}$ . This is further illustrated by examining equation 3-15. In Method A, since it is assumed that there is no variation in  $U_{ref}$  and  $U_H$  and so,

$$\frac{w_{Cp_H}}{Cp_H} = \frac{w_{Cp_{ref}}}{Cp_{ref}} \quad (3-18)$$

However, as illustrated by Table 3-5, the nominal  $\overline{Cp_D}$  is nearly constant between scales, and, as shown by Table 3-4,  $w_{Cp_{ref}}$  is unchanged as it is dependent on the equipment which does not change. Consequently, since  $Cp_H$  and  $w_{Cp_{ref}}$  are essentially fixed values it could be said that  $w_{Cp_H} \propto \frac{1}{Cp_{ref}}$ .

This reasoning could also be applied to Method C which includes the bias errors associated with  $Cp_{ref}$  and the influence of the velocity terms, with results summarized in Table 3-6. In this method, equation equation 3-17 can rearranged to observe the relative influence of each variable,

$$\frac{w_{Cp_H}}{Cp_H} = \left[ \left( \frac{w_{Cp_{ref}}}{Cp_{ref}} \right)^2 + \left( 2 \frac{w_{U_{ref}}}{U_{ref}} \right)^2 + \left( -2 \frac{w_{U_H}}{U_H} \right)^2 \right]^{\frac{1}{2}} \Rightarrow \frac{w_{Cp_H}}{Cp_H} = [a + b + c]^{\frac{1}{2}} \quad (3-19)$$

where,  $a$ ,  $b$  and  $c$  represent the relative importance of uncertainty associated with  $Cp_{ref}$ ,  $U_{ref}$  and  $U_H$ , respectively.

**Table 3-6: Influence of various terms in Method C**

SCALE	$w_{Cp_{ref}}$	$w_U$	$a$	$b$	$c$	$w_{\overline{Cp_H}}$	$w_{\overline{Cp_H}}$
<b>1:200</b>	0.081	0.5	0.239	0.005	0.015	0.277	0.277
<b>1:100</b>	0.081	0.5	0.211	0.005	0.013	0.230	0.230
<b>1:50</b>	0.081	0.5	0.159	0.005	0.008	0.150	0.150
<b>1:25</b>	0.081	0.5	0.134	0.005	0.007	0.127	0.127

From Table 3-6, it is clear that  $p_{ref}$ , or the ‘ $a$ ’ term in equation 3-19, has the greatest influence on the estimation of  $w_{Cp_H}$ . However, the magnitude of surface pressures is dependent on the velocity of the flow which decreases with model scale for the way in which these experiments were conducted. Thus, it can be said that the true driver of varying estimations of  $w_{Cp_H}$  is the velocity in the wind tunnel. In other words, the higher the velocity, the higher the surface pressures, and, thus, the lower the relative significance of elemental error sources.

Since uncertainty in  $Cp_H$  is dependent on velocity, it would suggest that studies using pressure scanners ought to be performed at the highest velocity possible. By increasing wind tunnel velocity, the pressure and subsequently voltage range experienced by the scanner would increase. A larger range of measurement reduces the relative significance of measurement uncertainties in scanner uncertainties, thereby producing results that are more accurate. However, running the tunnel at its maximum speed could present additional challenges.

From experience of the BWLTL staff, testing at speeds beyond the standard 15 m/s at the reference height can destroy proximity models used to replicate the effects of surrounding structures on local wind flow. This would especially be a challenge for studies on buildings in urban areas, since models of surrounding buildings are constructed with light

weight foam. If tests were to be conducted at higher wind speeds, these models may require additional reinforcement from guy-wires, which may alter the local flow.

In the present study, no surrounding buildings were considered. In hindsight, it may have been possible to run tests at higher speeds to minimize uncertainty in results, though vibrations on the cobra probe mast may become an issue at these speeds.

Another concern with increased velocities is whether sampling rates of pressure scanners are fast enough to capture peak pressures.

Sampling rates are typically scaled with the non dimensional parameter

$$\frac{f_s L}{\bar{U}} \quad (3-20)$$

where  $f_s$ ,  $L$  and  $\bar{U}$  are sampling rate, length scale (typically building height) and mean wind speed, respectively.

On a low-rise building at full-scale, peaks are observed to rise and fall within about 0.2 seconds (Surry, et al., 2007). In order to capture these peaks, a sampling rate at least twice as fast as the occurrence of peaks is needed, i.e.  $2 \times 1/0.2$  seconds. Therefore, to adequately capture these peaks at full-scale, the required full-scale sampling rate,  $n_p$ , would be at least 10 Hz.

Using the present generic building ( $H_p = 4m$ ) and assuming a full-scale  $\bar{U}_H$  of 38 m/s to represent strong wind conditions (Stathopoulos & Surry, 1983), the resultant non-dimensional sampling rate is 1.053. Assuming a typical model scale of 1:50 and assuming the tunnel can run such that  $U_H$  for the model is 30 m/s, matching non-dimensional sampling rate would require a model scale sampling rate  $n_m$  of 394 Hz. Considering the pressure scanners at the BLWTL can reach sampling rates of up to 800 Hz, being able to sample at an adequate rate does not seem to be a concern.

### 3.5 Summary of findings

In conclusion, the uncertainty  $w_{Cp_H}$  was estimated by examining the pressure measurement system and following analysis procedures outlined in Quiroga (2006) and Wheeler and Ganji (2009). The determined uncertainty  $w_{Cp_H}$  from Method B can be used to compare datasets with from configurations with the same model scale. However,  $w_{Cp_H}$  determined from Method C is more appropriate to compare datasets from different wind laboratories.

It was also observed that  $w_{Cp_H}$  increased as velocity at the model height,  $\overline{U}_H$  decreased. Uncertainties in pressure scanners are fixed values and are relatively small compared to the entire measurement range of the device. However, since measurements in the present experiments only use a small portion of the full range, the uncertainties were large relative to measurements. Due to the way experiments were conducted, at smaller scales,  $\overline{U}_H$  reduces and subsequent pressures experienced on model surfaces decreased, diminishing the measurement range. Consequently, as  $\overline{U}_H$  reduces, measurement uncertainty from pressure scanners became more significant, leading to larger uncertainty estimates for  $w_{Cp_H}$ . Based on this, it is recommended that future studies of low-rise buildings be run at higher wind speeds.

## Chapter 4: Spatial pressure coefficient distributions

### 4.1 Introduction

Spatial pressure coefficient distributions across the building surfaces differ depending on flow directions. For low-rise buildings, flow directions can be categorized as:

1. Normal flow directions; where the wind direction is normal to a building wall. As flow approaches a windward wall, it separates at the windward roof edge, producing high suction on the windward portion of the roof.
2. Oblique flow directions; where wind direction is angled relative to the building surfaces. As flow approaches the roof, a pair a pair of conical vortices form at the windward corner and extend downstream. These vortices produce high suction on surfaces underneath their core.

As previously discussed in Chapter 1, edge radius can significantly alter the magnitude and spatial distribution of  $Cp_H$ . The focus of this chapter is to examine the effect of edge radius on roof pressure distributions at both normal and oblique wind directions. Changes to distributions can then be used to define a practical limit on model edge radius.

### 4.2 Normal flow directions

For normal flow directions, pressure distributions and flow behaviour can be characterized using pressure coefficients measured along a line of taps at the middle of body surfaces. An example is shown below in Figure 4-1. In the study by Castro and Robins (1977), mean pressure coefficients were determined along the middle a sharp-edge, surface mounted cube. The results in Figure 4-1 is representative of typical pressures that would be observed around a sharp-edged bluff body in turbulent boundary layer flow.

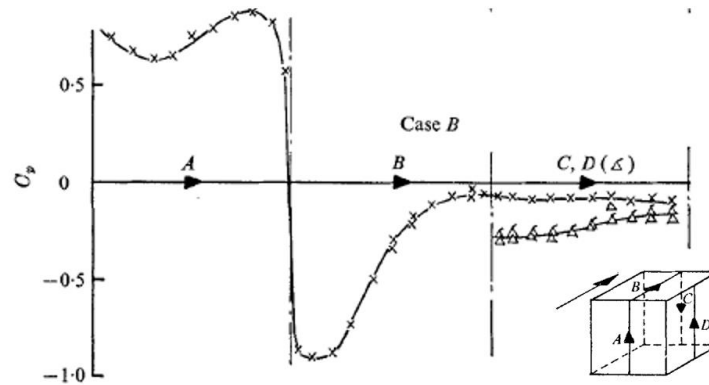


**Figure 4-1 Mean  $C_p$  on a surface mounted cube in turbulent flow (from Castro and Robins, 1977).**

Up the windward wall (A in Figure 4-1), pressure rises to a maximum at the stagnation point. The location of the stagnation point is at  $0.65H$  from the base of the wall and is invariant with upstream turbulence intensity (Akon & Kopp, 2016). Additionally, literature has shown that the magnitude of the mean pressure coefficient at the stagnation point is usually between 0.7 to 0.85 (Hong, 2017).

On the roof (B in Figure 4-1), mean pressure coefficients reach a maximum value of about -1 near the leading edge due to separated flow and the production of vortices. Downstream, flow reattaches, reducing the pressure coefficient to a base magnitude. Pressure coefficients beyond this point remain, uniform as shown on the leeward wall (C in Figure 4-1).

It is expected that  $R/H$  would have greatest influence on the pressures along the top surface where flow separates. As  $R/H$  increases, the vortices produced at the windward roof edge weaken and shrink in size (Mahmood, 2011). Weaker vortices would subsequently produce smaller magnitudes of mean and fluctuating  $C_{pH}$ . Additionally, increased  $R/H$  has been found to promote earlier flow reattachment (Robertson, 1991) so it is expected that  $\overline{C_{pH}}$  would recover further upstream, thereby reducing the size of the area near the windward roof edge, affected by high suction.

### 4.2.1 M1 and M2 Midline Results

Mean, RMS and peak  $Cp_H$  along the M1 midlines on 1:25 models are plotted in Figure 4-2, as per sign conventions in Figure 2-7. Results from other model scales can be found in Appendix E.

Mean and fluctuating  $Cp_H$  along the windward wall, Figure 4-2 (a), (d) and (g), showed similar behaviour across all model scales and edge radii. Similar to the findings in Figure 4-1,  $\overline{Cp_H}$  rises to a maximum at the stagnation point. The average magnitude of  $\overline{Cp_H}$  and location of the stagnation point across all model configurations were shown to be fairly consistent and similar to findings in literature, as summarized below in Table 4-1. At larger  $R/H$ , however, the stagnation point seems to occur further down the wall as the size of the curvature begins to significantly alter the geometry of the windward wall.

**Table 4-1 Comparison of stagnation points**

<b>Study</b>	<b>Geometry</b>	$\overline{Cp_H}$	<b>Location (H)</b>
<b>Mean Value M1 (CoV)</b>	Low-rise building	0.70 (0.04)	0.7 (0.17)
<b>Mean Value M2 (CoV)</b>	Low-rise building	0.63 (0.06)	0.68 (0.17)
<b>Castro and Robins (1977)</b>	Cube	0.8	0.7 - 0.8
<b>Richards et al. (2001)</b>	Cube	0.67 - 0.92	0.8
<b>Hong (2017)</b>	Various	0.7- 0.85	~0.8



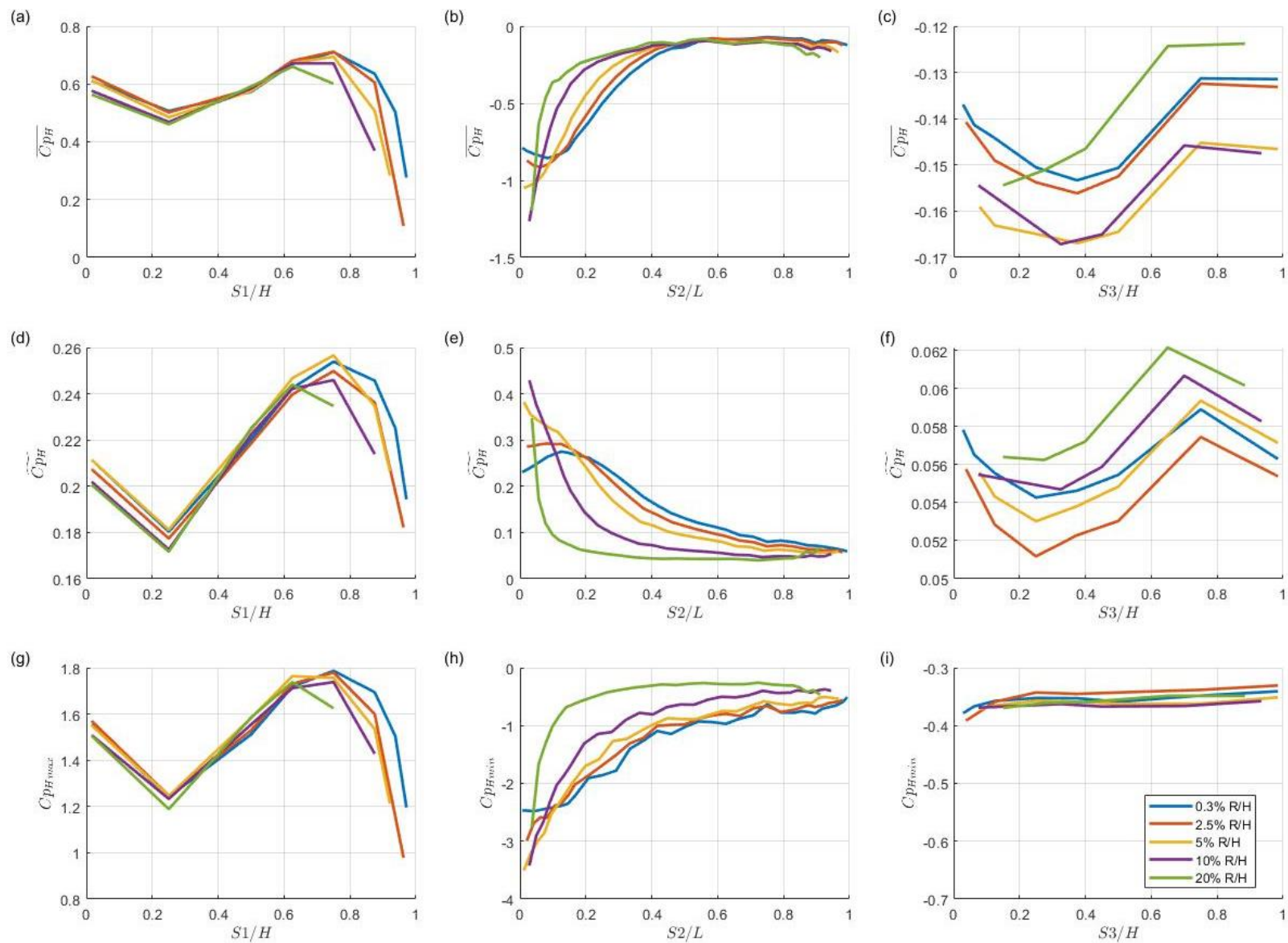


Figure 4-2 Results for 1:25 models along M1 for (a) to (c) mean, (d) to (f) RMS, and (g) to (i) peak  $C_{pH}$ .

Pressure coefficients along the roof (Figure 4-2 (b), (e) and (h)) is where the influence of the edge radius is most apparent. Similar to Castro and Robins (1977), an immediate jump in mean and fluctuating  $Cp_H$  occurs on the windward portion of the roof near the separation point. Downstream, mean and fluctuating  $Cp_H$  decrease towards a constant value.

As  $R/H$  increases, three notable trends in the  $Cp_H$  distributions are observed on the roof.

1. The magnitude of the maximum observed  $Cp_H$  increases.
2. The location of the maximum  $Cp_H$  moves upstream, and for  $R/H > 5\%$ , the highest magnitudes are observed on the roof edge itself.
3.  $Cp_H$  recovers to uniform base values further upstream.

The three trends are likely associated with earlier flow reattachment on the roof as  $R/H$  increases. Should the flow reattach further upstream, it would be expected that the absence of separated flow would cause both mean and fluctuating  $Cp_H$  to decrease towards base values further upstream.

Furthermore, a drastic change in  $Cp_H$  distributions on the roof occur at  $R/H \geq 10\%$ . At these larger radii, magnitudes on the windward portion of the roof are significantly reduced and the largest magnitudes of  $Cp_H$  were observed on the edge itself. Robertson (1991) reports similar findings for a roof where eave radii were increased to  $R/H = 12.5\%$ . In his study, it was suggested that this behaviour is associated with the flow remaining attached around windward eave. Subsequently, in the present experiments, the flow around the roof edge may also remain attached at  $R/H \geq 10\%$ . Also, at these larger radii, the increased suction at the edge may be caused by the acceleration of the attached flow around the edge.

Pressure coefficients along the leeward wall, Figure 4-2 (c), (f) and (i), are unaffected by the varying edge radius. Differences in  $\overline{Cp_H}$  and  $\widetilde{Cp_H}$  across the leeward wall are within the measurement uncertainty, suggesting that there is no discernable change in pressure coefficients along these surfaces. The unchanged pressure distribution along the leeward

wall would imply that within the range of  $R/H$  examined, the behaviour of the the leeward separated shear layer and fluid recirculation behind the model is unaffected, (Taylor, Palombi, Gurka, & Kopp, 2010).

#### 4.2.2 M3 Midlines

The pressure coefficient distributions across the walls are characterized by the M3 midlines. M3 results for the 1:25 models are shown in Figure 4-3, and are plotted according to the sign convention in Figure 2-8. Plots for models at other scales are found in Appendix E.

Results of the M3 midlines are in good agreement with observations along the M1 and M2 midlines. On the windward wall (Figure 4-3(a), (e) and (i)),  $Cp_H$  does not change along the breadth of the wall and is unaffected by a change in  $R/H$ . The only difference is at the edges of the wall ( $S1/H \approx \pm 0.5$ ) where suctions increase on the edge as the radius of edge curvature increases.

Along the sidewalls (Figure 4-3 (b), (d), (f) and (h)), where the flow separates, the mean and RMS  $Cp_H$  distributions show the same trends with  $R/H$  that were observed on the roof of M1 and M2. Near the separation point at the wall edge, mean and RMS  $Cp_H$  increase to a maximum and then recover to a base value downstream as flow reattaches. Just like the  $Cp_H$  behaviour along the roof, as  $R/H$  increases, the magnitude of mean and fluctuating  $Cp_H$  along the side walls increases and the pressure recovers further upstream. Thus, from the identical behaviour, the same flow mechanism is likely occurring on the wall and roof edges.

Along the leeward wall (Figure 4-3 (c), (g) and (k)),  $R/H Cp_H$  across the breadth of the wall is unchanged with  $R/H$ . The lack of variation would further support the hypothesis that the radii examined have no effect on flow recirculation behind the model, as long as the flow on the building has reattached on the roof and side walls.

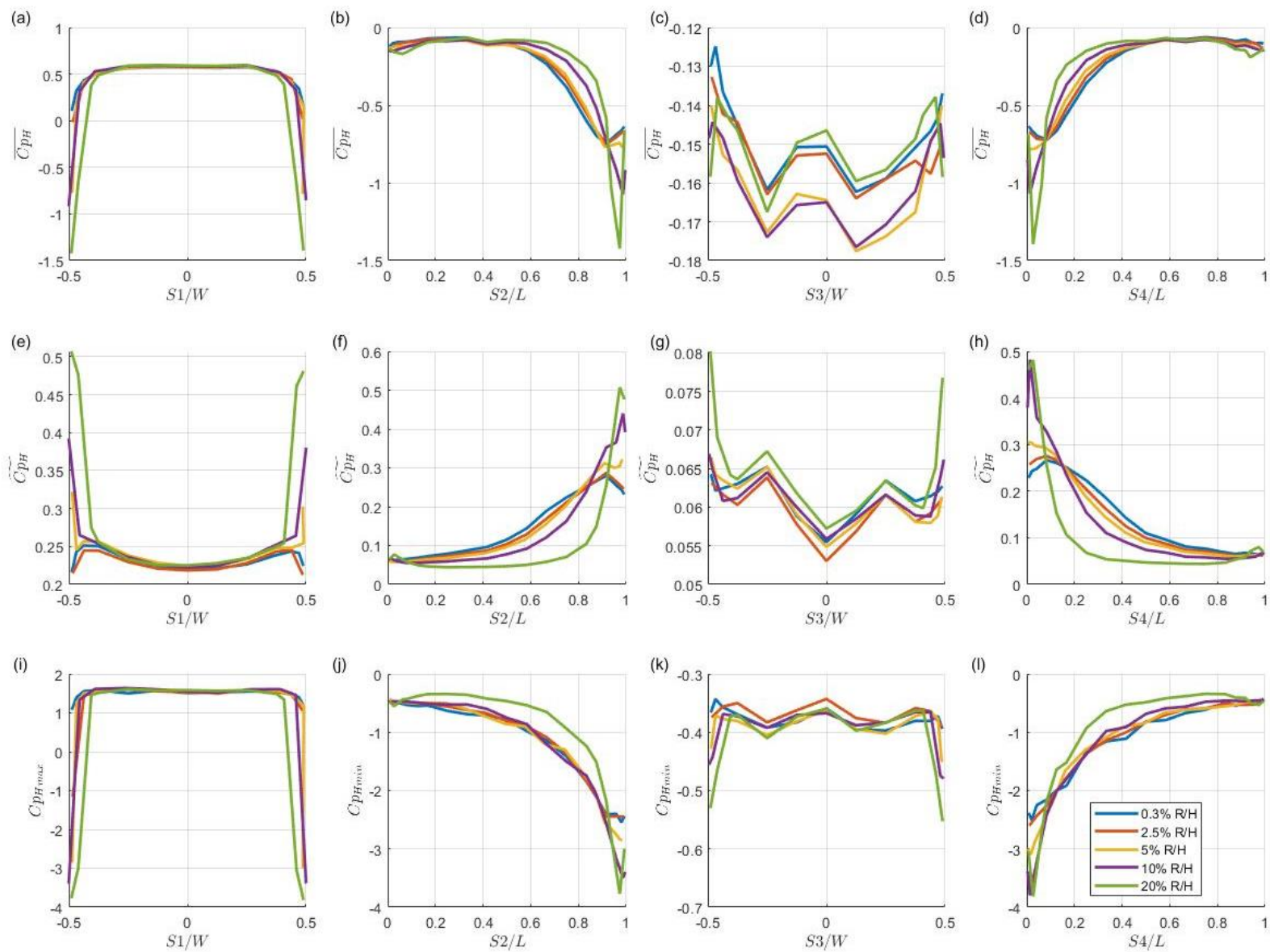


Figure 4-3 Results for 1:25 models along M3 for, (a) to (d) mean, (e) to (h) RMS, and (i) to (l) peak  $C_{pH}$ .

## 4.2.3 Discussion

### 4.2.3.1 Changes in roof $\overline{Cp_H}$ distributions

A limit on  $R/H$  may be defined as an edge radius that produces changes in pressure distributions beyond uncertainty. In other words, should a given  $R/H$  produce differences in the magnitude of  $\overline{Cp_H}$  beyond  $w_{\overline{Cp_H}}$ , it could be confidently said that a change in aerodynamics has occurred.

It is clear from the results that for normal wind directions, edge curvature primarily affects the separating and reattaching flow behaviour responsible for high suction near building edges. As shown in the previous section, spatial pressure distributions varied the greatest with  $R/H$  along the roof of M1 and M2. Two observations are clear, for larger  $R/H$  values:

1. The maximum observed magnitude of  $\overline{Cp_H}$  observed along the midline increases.
2. Pressure recovers to base magnitudes further upstream.

To quantify these two trends, two parameters,  $\overline{Cp_{D_{max}}}$ , and  $l_s$ , were used, as defined in Figure 4-4.  $\overline{Cp_{D_{max}}}$  is defined as the maximum  $\overline{Cp_D}$  observed across the midline and characterizes the change in maximum observed magnitudes of  $\overline{Cp_H}$  distributions.

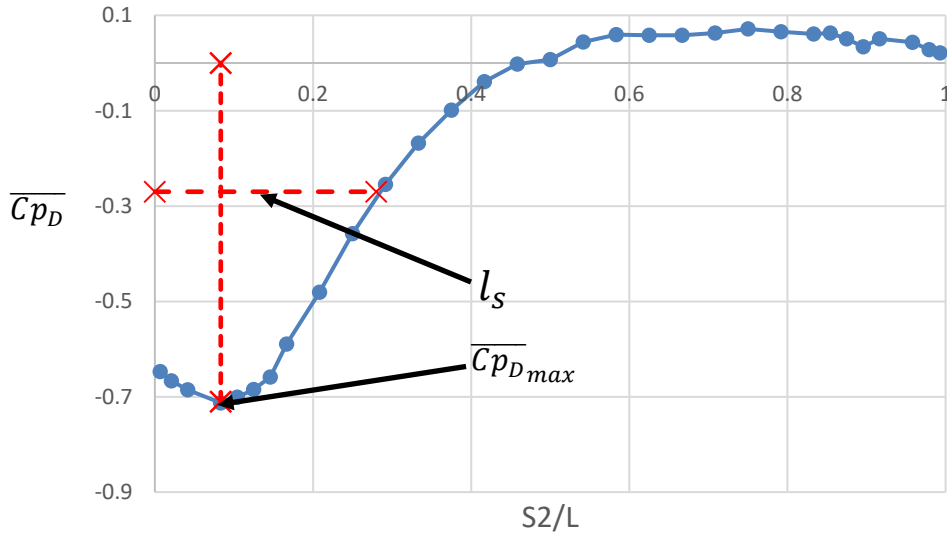


**Figure 4-4 Definitions of  $\overline{Cp_{D,max}}$  and  $l_s$ .**

The reattachment length of the separated flow is characterized by the distance from the leading edge,  $l_s$ , where the pressure distribution reduces to base values, i.e.,  $\overline{Cp_H} = Cp_b$ . In terms of the  $\overline{Cp_D}$  distributions,  $l_s$  is the location  $S2/L$  at which  $\overline{Cp_D} = 0$  since

$$\overline{Cp_D} = \overline{Cp_H} - Cp_b \quad (4-1)$$

However, due to measurement uncertainty, the actual location where  $\overline{Cp_D} = 0$  may be ambiguous, since this point can be anywhere the pressure measurement is within

$$\overline{Cp_D} = 0 \pm w_{\overline{Cp_H}} \quad (4-2)$$

Thus, to eliminate this ambiguity,  $l_s$  is defined as the point at which the pressure has crossed the uncertainty bounds of the base pressure magnitude or

$$(\overline{Cp_D})_{l_s} = 0 + w_{\overline{Cp_H}} \quad (4-3)$$

This definition of  $l_s$  is shown above in Figure 4-4.

Though uncertainty varies with  $U_H$ , the uncertainty of the 1:200 scale case of method C ( $w_{\overline{Cp_H}} = 0.277$ ) was used, since it has the largest bounds and hence encompasses the uncertainty related to results of models of all scales that were considered.

Values for  $Cp_{Dmax}$  and  $l_s$  for M1 and M2 midlines are in Figure 4-5 and Figure 4-6, respectively.

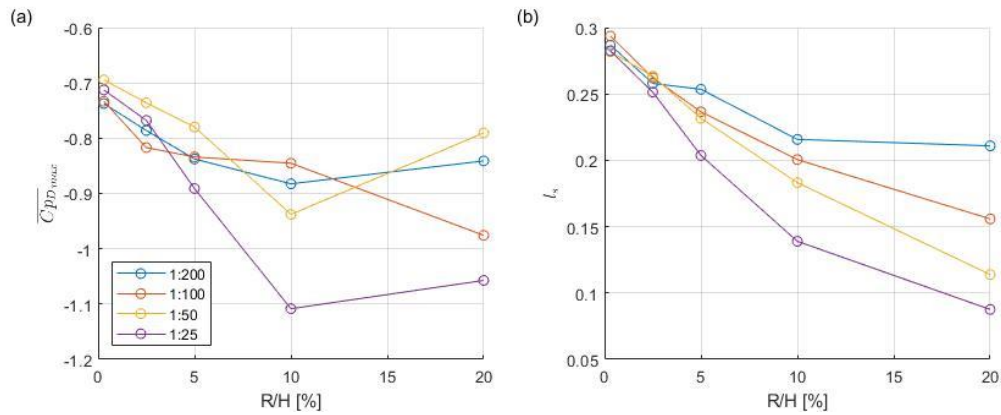


**Figure 4-5 (a) M1  $\overline{Cp_{Dmax}}$  and (b) M1  $l_s$**

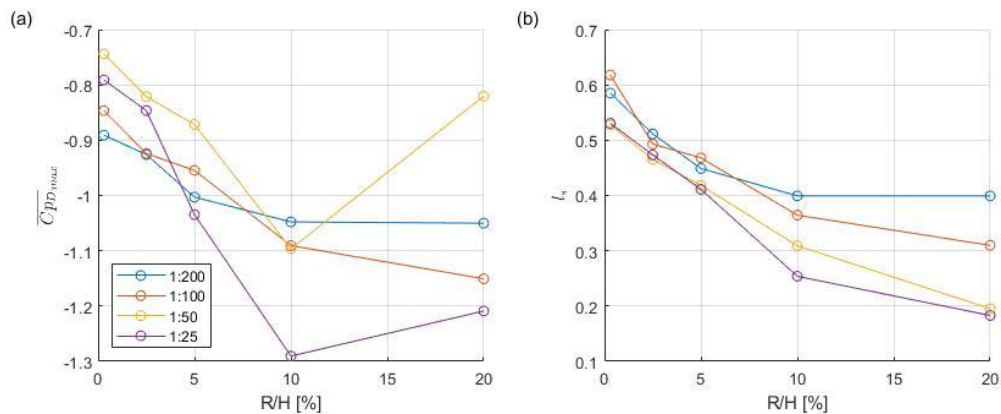


**Figure 4-6 (a) M2  $\overline{Cp_{Dmax}}$  and (b) M2  $l_s$**

From the figures above, as  $R/H$  increases,  $\overline{Cp_{Dmax}}$  increases, and the reattachment length characterized by  $l_s$  reduces. The observations would suggest that as edge radii increases, the separated shear layer reattaches earlier, but produces stronger suction on

the windward portion of the roof. Trends in  $l_s$  with  $R/H$  are continuous within the range of edge radii considered.

To determine the edge radii at which  $\overline{Cp}_H$  distributions are altered, the  $\overline{Cp}_{D_{max}}$  observed on the sharpest models were compared to those observed on models at  $R/H > 0.3\%$ .

Should the difference in  $\overline{Cp}_{D_{max}}$  be greater than measurement uncertainty, it can be said that a change in the pressure coefficient distribution and subsequent aerodynamic behaviour had occurred. In other words for a given model scale, should,

$$[\overline{Cp}_{D_{max}}]_{0.3\%} - [\overline{Cp}_{D_{max}}]_{\frac{R}{H}} > w_{Cp_H} \quad (4-4)$$

a clear change in flow behaviour has occurred, and it can be said that the given  $R/H$  should not exceeded. A summary of findings for M1 and M2, are shown below in Table 4-2 and Table 4-3, respectively. Differences which were beyond measurement uncertainty are highlighted in red.

**Table 4-2 Differences in  $\overline{Cp}_{D_{max}}$  in M1 (values exceeding uncertainty in red)**

		$[\overline{Cp}_{D_{max}}]_{0.3\%} - [\overline{Cp}_{D_{max}}]_{\frac{R}{H}}$			
Scale		1:200	1:100	1:50	1:25
R/H [%]	2.5	-0.05	-0.08	-0.04	-0.06
	5	-0.10	-0.10	-0.09	-0.18
	10	-0.15	-0.11	-0.24	-0.40
	20	-0.10	-0.24	-0.10	-0.34

**Table 4-3 Differences in  $\overline{Cp}_{D_{max}}$  in M2 (differences exceeding uncertainty in red)**

		$[\overline{Cp}_{D_{max}}]_{0.3\%} - [\overline{Cp}_{D_{max}}]_{\frac{R}{H}}$			
Scale		1:200	1:100	1:50	1:25
R/H [%]	2.5	-0.04	-0.08	-0.08	-0.06
	5	-0.11	-0.11	-0.13	-0.24
	10	-0.16	-0.24	-0.35	-0.50
	20	-0.16	-0.30	-0.08	-0.42



From these results, differences beyond  $w_{\overline{Cp_H}}$  are observed at  $R/H = 5\%$  for models in both 1:50 and 1:25 scale. As a result, it is clear that flow behaviour at normal wind directions is altered when edge curvature is increased to  $R/H$  is increased to 5%.

Another notable observation is the spread of  $\overline{Cp_{D_{max}}}$  and  $l_s$  as  $R/H$  increases amongst the different model scales. As  $Re$  was not kept constant amongst model scales, there is a variation in  $Re$  by up to an order of magnitude. The subsequent spread of results would suggest that  $Re$  effects become more prominent as the edge radii increases.

The increased  $Re$  sensitivity with larger radii could be explained by considering the flow around a cylinder. On a cylinder, the separation point and the transition point in the shear layer is highly dependent on  $Re$ . Changes in the locations of these two points can have significant effects on the aerodynamics and subsequent surface pressures (Schewe, 2001). It is possible, that around a rounded edge, flow is analogous to that around a cylinder in that the separation point located on the edge may vary significantly with  $Re$ , thereby altering the pressure distribution. The shift in the separation point may scale with the size of the edge radii itself. For instance, at sharper edges, changes in the separation point is small relative to the dimensions of the model, producing minimal changes in the pressure distributions and so the pressure distribution is perceived as  $Re$  insensitive. However, as the radii increases, the shift in the separation point could be significantly larger relative to the size of the model, leading to more pronounced differences surface pressure distributions.

However, differences in  $\overline{Cp_{D_{max}}}$  at  $R/H=0.3\%$  are within uncertainty amongst the various model scale, suggesting that at  $R/H = 0.3\%$ , pressures are independent of  $Re$  over this range. Since  $Re$  independence is a key feature of sharp-edged bluff behaviour, within the limitations of current measurement equipment,  $R/H = 0.3\%$  may be considered “sufficiently sharp” and representative of that on a sharp-edged building.

#### 4.2.4 Fluctuating pressure coefficient spectra

To further examine the effect of  $R/H$  on fluctuating pressures, the power spectral densities of the fluctuating pressure coefficients are examined along the M1 midline. The normalized pressure spectra,  $fSp(f)/\widetilde{Cp}_H^2$ , was determined near the leading edge at  $S2/L = 0.16$ , and further downstream at  $S2/L = 0.5$  as shown in Figure 4-7. Additionally, the non-dimensional power spectral density of the fluctuating velocity at roof height from Figure 2-14 are included for comparison. Spectra from other model scales are in Appendix F.

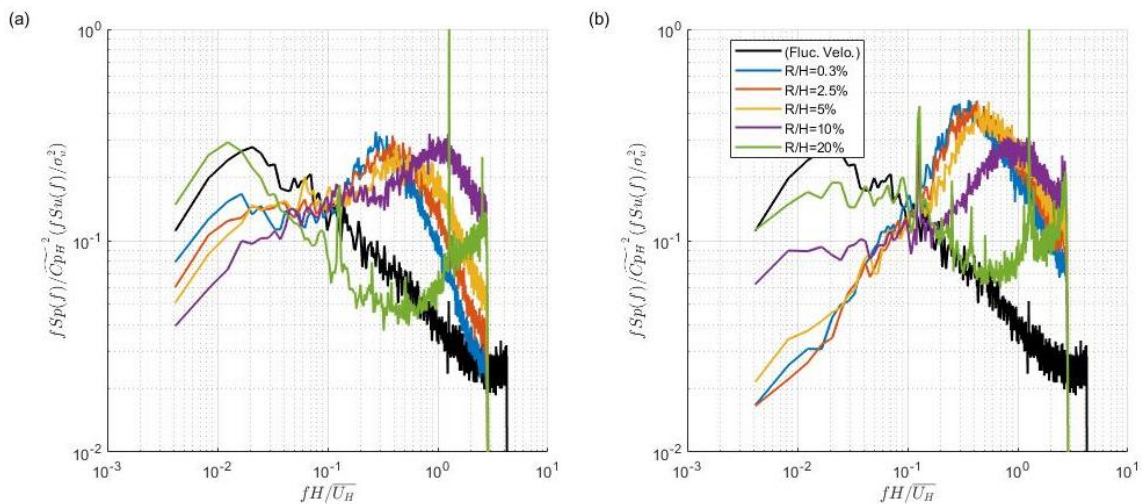


**Figure 4-7 Normalized fluctuating pressure coefficient and velocity spectra on M1 of 1:25 models at (a)  $S2/L = 0.16$  and (b)  $S2/L = 0.5$ .**

It is clear from Figure 4-7 that across the roof span, the edge radii produces a continuous change in the fluctuating pressure spectra. There are two notable trends that appear, which may shed light on the influence of edge radii on the behavior of the separated shear layer. As  $R/H$  increases:

- 1) The high-frequency peak in the fluctuating pressure spectra, observed at  $fH/\overline{U}_H \approx 0.3$  at  $R/H = 0.3\%$ , shifts towards the small-scale range.
- 2) The large-scale, low frequency content increases, while small-scale, high-frequency content reduces. When  $R/H$  is significantly increased, a second peak

appears at the low-frequency range at around the same wave number of the peak in the fluctuating velocity spectra.

First, the peak at  $fH/\overline{U}_H \approx 0.3$  for the sharpest model shifts towards the small-scale region as  $R/H$  increases. At  $R/H = 20\%$ , based on the trends of the pressure spectra, it is quite possible that the peak continues to shift beyond  $fH/\overline{U}_H = 3$ . However, the actual location of the peak is not observable in the above plots due to the 200 Hz low-pass filter applied to pressure signals.

The peak in the high-frequency range of the pressure spectra is associated with the predominant vortical structure in separated shear layer. In similar studies, this peak is widely reported at  $fX_r/\overline{U} \approx 0.5$ , where  $X_r$  is the reattachment length of the separated flow (Cherry et al. 1984; Lee and Sung 2001; Hudy et al. 2003). As this peak moves towards the small-scale range, it is inferred that the vortical structures in the shear layer shrink in size. Subsequently, it is possible that as the edge radius increases, the vortical structures responsible for severe suction shrink and weaken, thereby reducing surface pressures near the leading edge, as observed in section 4.2.1.

The second notable observation is the increase in low-frequency content and decrease in high-frequency content in the pressure spectra as  $R/H$  increases. The high-frequency content of the pressure spectra caused by the turbulent structures produced by the separated flow at the roof edge. As radii increases, the high-frequency content reduces, implying that the influence of the separated shear layer weakens or disappears.

Most notably, at  $R/H = 20\%$ , the high frequency content of the pressure spectra has significantly diminished and the shape of the pressure spectra at the low-frequency range resembles that of the fluctuating velocity spectra. It is therefore suggested that at  $R/H = 20\%$ , the fluctuations in the surface pressures are predominantly due to fluctuations in the upstream flow, rather than the influence of vortices in the separated shear layer. Dalley (1996) proposes that this behavior in the fluctuating pressure spectra can imply that rather than separating at the leading edge, the flow has remained attached and has accelerated around the edge.

### 4.2.5 Possible flow mechanisms

It is clear from present findings and literature that as  $R/H$  is sufficiently increased, the flow will remain attached, leading to a drastic change in spatial pressure coefficient distributions. However, at smaller  $R/H$ , before complete flow reattachment occurs, the flow behaviour is not fully explained.

One hypothesis is that as  $R/H$  increases, the separated shear layer is forced to curve increasingly in the streamwise direction (Ota et al., 1981). In doing so, the separated shear layer is closer to the surface downstream of the separation point. Subsequently, the vortices produced by the shear layer may be much closer to the roof and the proximity of the shear layer to the surface may encourage the flow to reattach further upstream. Additionally, these vortices may be smaller as suggested by the fluctuating pressure spectra discussed in the previous section.

The proposed flow mechanism may be able to explain the trends in  $RMS$  and peak  $Cp_H$  on the roof in Figure 4-2 (e) and (h). Typically speaking, vortices that have greater vorticity and are closer to the surface, produce larger fluctuating surface suctions (Saathoff & Melbourne, 1997). From Figure 4-2 (e) and (h), it is clear that the maximum magnitudes  $RMS$  and peak  $Cp_H$  increases with  $R/H$  and these maximums occur closer to the separation point. It could be inferred that as  $R/H$  increases, the separated shear layer is forced closer to the roof, and the vortices that are shed remain close to the roof near the edge as well, producing the large fluctuating suctions that are observed.

## 4.3 Oblique flow directions

At oblique flow directions, conical vortices are formed at the windward roof corner and are responsible for severe suctions near the roof edges. To examine the effect of edge radii on conical vortices, contours of mean and fluctuating pressures on the roof were examined. Additionally, pressure coefficients were examined along three line of taps along the longest edge of the models as shown previously in Figure 2-9. Similar to analysis at normal wind direction, differences pressure coefficients with  $R/H$  beyond measurement uncertainty can also be used to define a practical limit on edge radii.

### 4.3.1 Roof contours

Roof contours of mean, RMS and peak  $Cp_H$  are plotted for 1:25 scale models in Figure 4-8. The white area on the edges of the contours represent the area occupied by the edge curvature, which are not considered in the contour.

Near the edges of the roof are petal-shaped regions of severe mean and fluctuating suction produced by conical vortices. As the radius of roof edges increase, both the magnitude of the suction and size of the regions diminish. Subsequently, it can be inferred that the size and strength of the conical vortices diminish as  $R/H$  increases. Flow visualization by Mahmood (2011) confirms this behaviour. For a  $45^\circ$  azimuth, vortices on the roof corner were observed to shrink when  $R/H$  at 12.5% and disappear at  $R/H = 25\%$  (Mahmood, 2011). Additionally, Mahmood (2011) reports significant reductions in mean pressure coefficients along the roof edge at these radii. Similarly, contours of  $\overline{Cp_H}$  on the roof of low-rise models by Dong et al. (2019) report that areas behind roof edges at oblique angles shrink significantly as curvature is increased to  $R/H = 12.5\%$ .

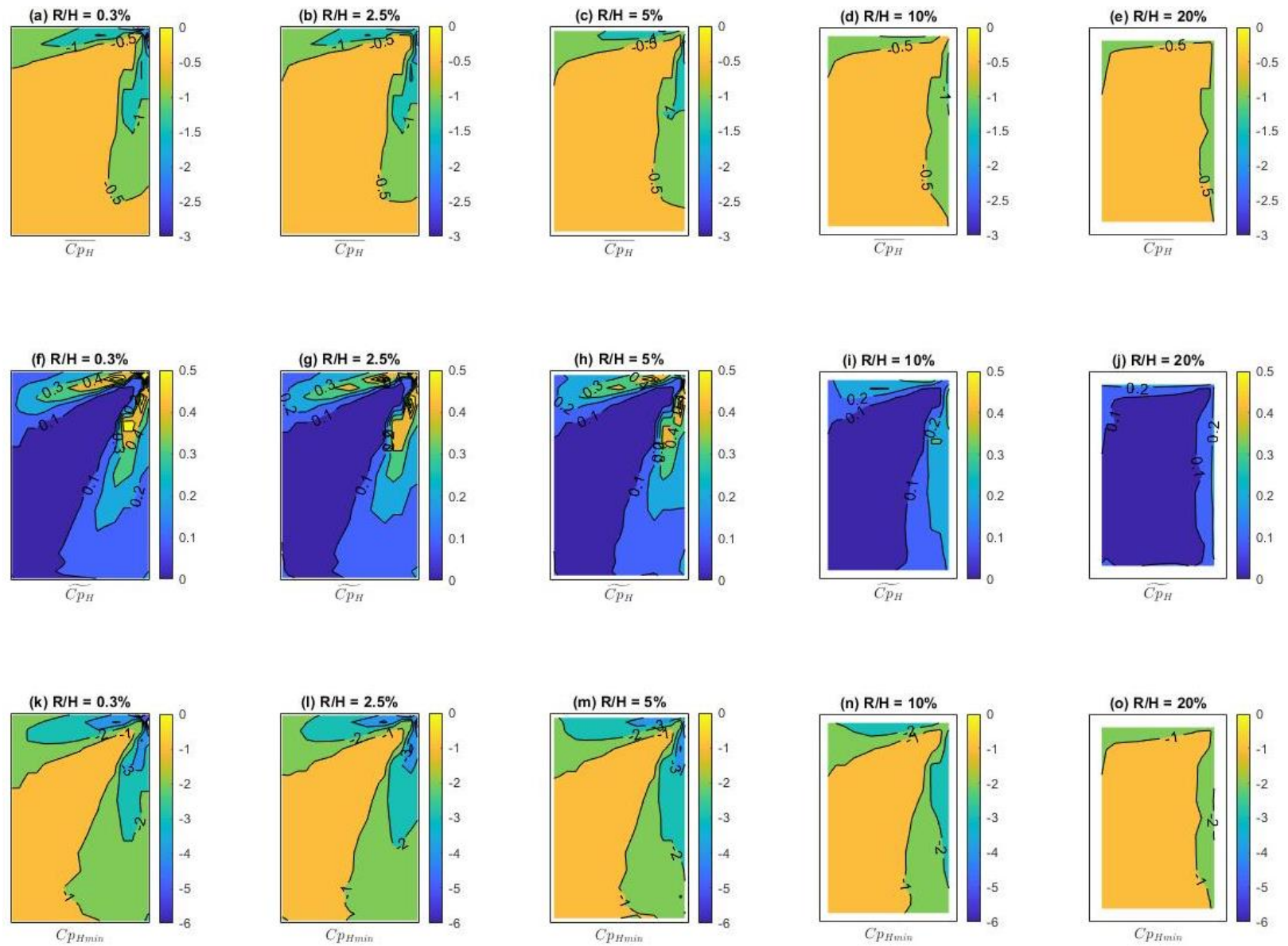


Figure 4-8 Contours of 1:25 models at  $\theta = 45^\circ$  with various  $R/H$  for, (a) to (e) mean, (f) to (j) RMS and, (k) to (o) peak  $C_{pH}$ .

### 4.3.2 Pressures along the roof edges

To quantify the changes in spatial distributions,  $Cp_H$  along the longest roof edge were examined along lines of taps defined in Figure 2-9. Results for the 1:25 models are shown in Figure 4-9 to Figure 4-11. Findings from other model scales are presented in Appendix G.

Spatial pressure distributions change significantly near the roof edges. As shown in Figure 4-9 the magnitudes of both mean and fluctuating  $Cp_H$  are the highest at the roof edge, at  $x/L = 0.01$ , where the entire tap line is the closest to the separation point at the roof edge. The most severe suction along this line were at the roof corner, at  $y/L \approx 0$ , appear to be very sensitive to changes in edge radii. As  $R/H$  increases, the magnitudes of  $Cp_H$  seem to reduce drastically, suggesting a weakening of the conical vortices.

Further from the roof edge, in Figure 4-10 and Figure 4-11, the magnitudes of  $Cp_H$  are not as high. High suction are observed near the shorter roof edge, at  $y/L \approx 0$ , and are attributed to the conical vortex produced at that shorter edge. However, a second local maximum in mean and fluctuating  $Cp_H$  magnitudes occurs further downstream and are produced by the conical vortex formed on the longer roof edge. The location of the maximum mean and peak pressures along this region is strongly associated with the mean location of the vortex core (Banks et al., 2000) and is used in later analysis to estimate the effect of edge radii on the vortex location.

Pressure coefficients within this local maximum are shown to vary continuously with  $R/H$ . As edge radii increases, suction are reduced. When  $R/H$  is increased to 20%, it could be inferred from the uniform  $Cp_H$  distribution that conical vortices may have been suppressed altogether. Mahmood (2011) observed a similar uniform pressure distribution along the roof edge at  $R/H = 25\%$ , and reported a disappearance in conical vortices near the windward corner.

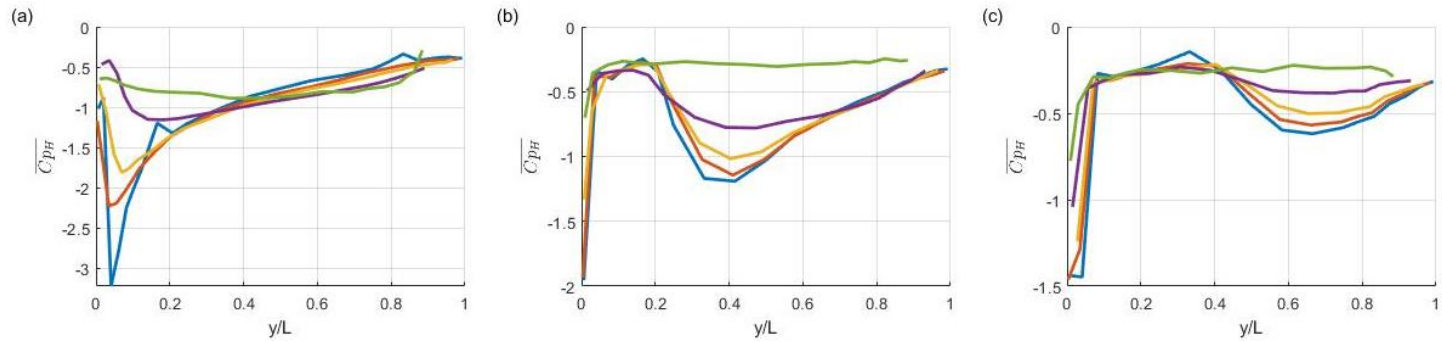


Figure 4-9 Mean  $Cp_H$  along longest roof edge at  $\theta = 45^\circ$  at (a)  $x/L = 0.01$ , (b)  $x/L = 0.10$  and (c)  $x/L = 0.23$ .

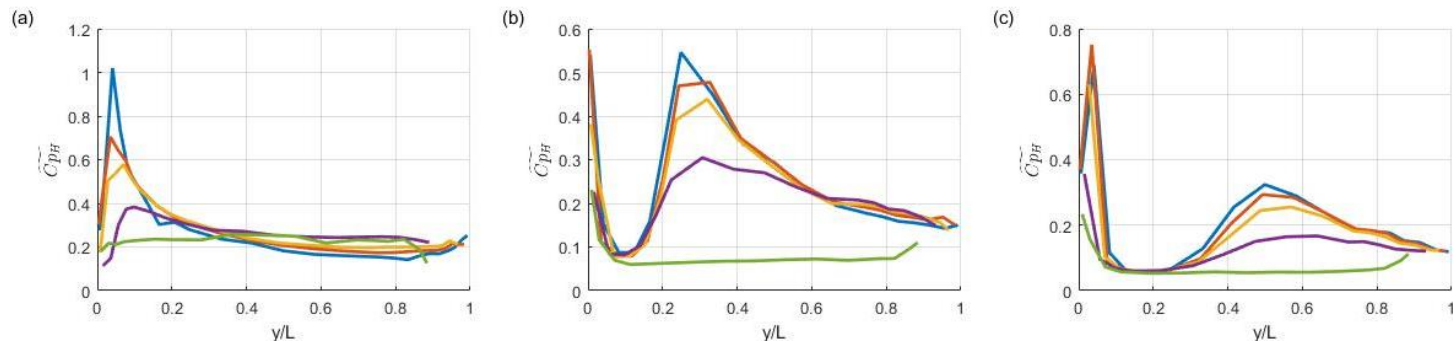


Figure 4-10 RMS  $Cp_H$  along longest roof edge at  $\theta = 45^\circ$  at (a)  $x/L = 0.01$ , (b)  $x/L = 0.10$  and (c)  $x/L = 0.23$ .

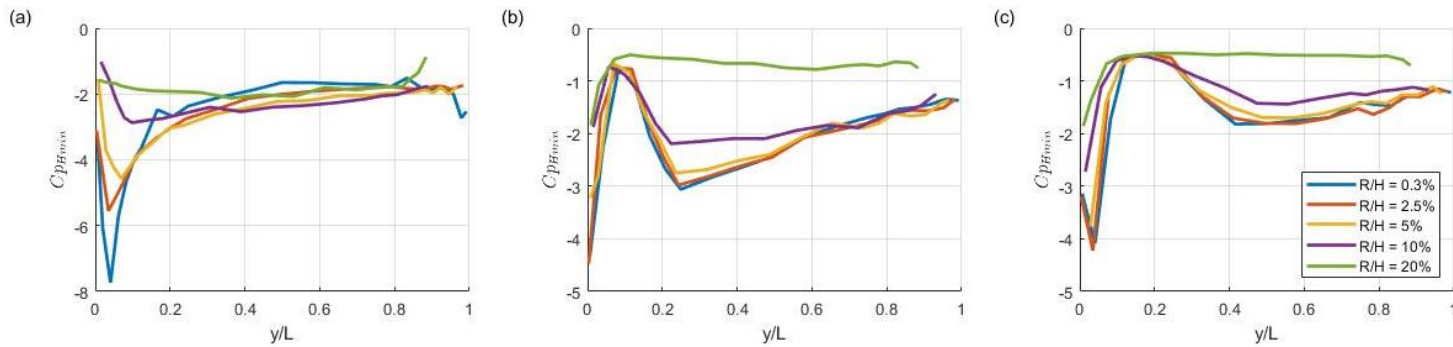


Figure 4-11 Peak  $Cp_H$  along longest roof edge at  $\theta = 45^\circ$  at (a)  $x/L = 0.01$ , (b)  $x/L = 0.10$  and (c)  $x/L = 0.23$ .



### 4.3.3 Discussion

#### 4.3.3.1 Changes in $\overline{Cp_H}$ distributions

From Figure 4-9 to Figure 4-11, it is clear that increased edge radii weaken the conical vortices, and thereby reduce the magnitudes of the severe mean and fluctuating pressure coefficients. In order to compare the data from various model scales, the normalized mean pressure coefficient  $\overline{Cp_D}$ , defined in equation 3-14, was used to account for a scalar offset observed in data from varying model scales. An example of this scalar offset is shown below in Figure 4-12.

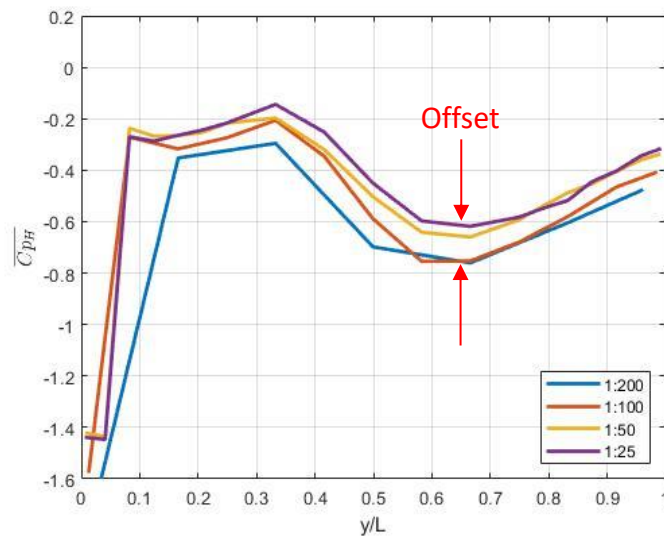


**Figure 4-12 Mean  $Cp_H$  along roof edge at oblique angles at  $x/L=0.23$  and  $R/H=0.3\%$ .**

However, unlike the analysis of midline pressures, the base pressure coefficient,  $Cp_b$ , was taken to be  $\overline{Cp_H}$  at the tap at the center of the roof, rather than the mean pressure along a leeward surface. The reason for the change in definition is because at a  $45^\circ$  azimuth, the center of the roof is observed to be outside of the influence of conical vortices, as shown by the contours in Figure 4-8, and the tap location is identical on all model configurations. Using this alternate definition for base pressure,  $\overline{Cp_H}$  appears to collapse well as shown in Figure 4-13.

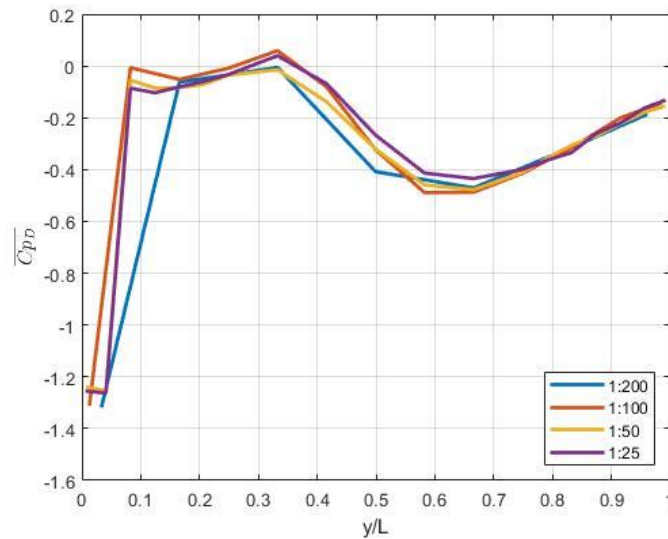


**Figure 4-13 Mean  $Cp_D$  along roof edge at oblique angles at  $x/L=0.23$  and  $R/H=0.3\%$ .**

Similar to the analysis in the normal flow directions, changes in the pressure distributions were quantified using the largest observed  $\overline{Cp_D}$  magnitude along the line of taps. Depending on the proximity of the tap line to the roof edge, different pressure distribution patterns were observed. As a result different definitions of the local maximum are used, depending on the proximity of the tap line to the roof edge. For the tap line closest to the roof edge ( $x/W = 0.01$ ), the parameter,  $Cp_{cmax1}$ , is used, defined in Figure 4-14 as the maximum  $\overline{Cp_D}$  observed near the roof corner.

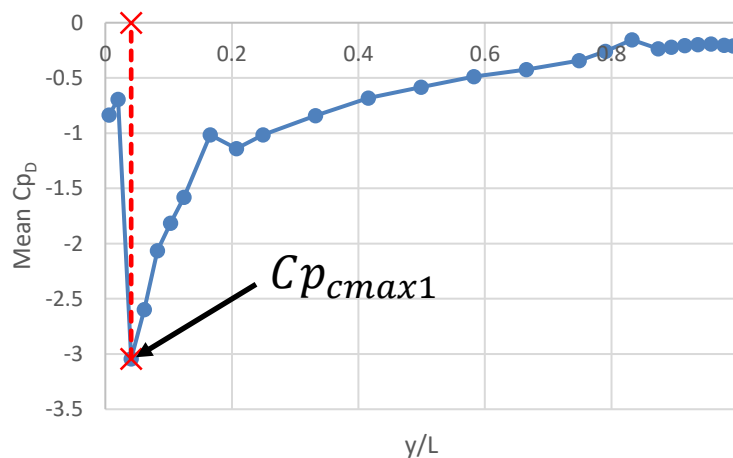


**Figure 4-14 Definition of  $Cp_{cmax1}$  along  $x/W = 0.01$ .**

For tap lines further away from the roof edge ( $x/W = 0.01$  and  $0.23$ ), a second maximum is observed away from the corner that is associated with the conical vortex formed along the long roof edge. This second maximum is defined as  $Cp_{cmax2}$  as shown in Figure 4-15. Also, since the location of maximum suction is associated with the location of the vortex core, the parameter  $l_c$  was used, defined as the location of the  $Cp_{cmax2}$  relative to the short roof edge.  $l_c$  could subsequently be used to estimate the angle of the vortex  $\phi_c$ , as shown in Figure 2-10 and examine any potential changes in vortex location with  $R/H$ .

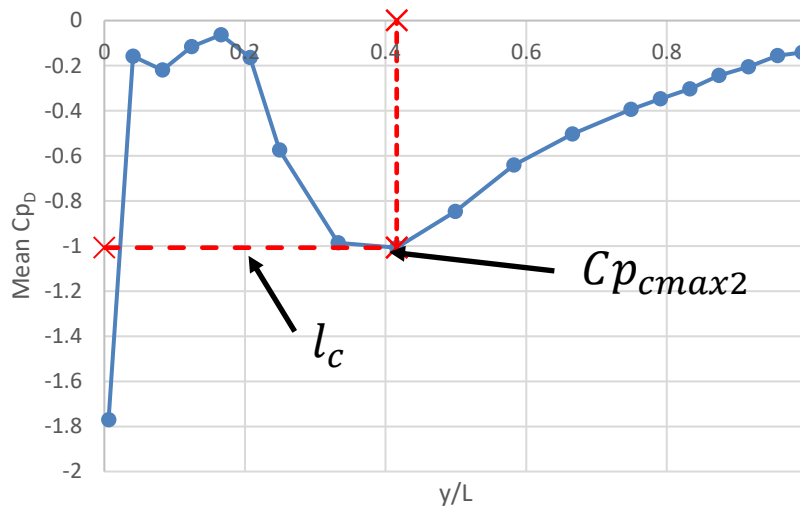


**Figure 4-15 Definition of  $Cp_{cmax2}$  and  $l_c$  along  $x/W = 0.1$ .**

Results for  $Cp_{cmax1}$  are plotted against  $R/H$  in Figure 4-16 and it is clear that suctions are reduced as edge radii increases. At 1:25 scale, a slight increase of  $R/H$  to 2.5% produces a difference well beyond uncertainty ( $w_{\overline{Cp_H}} = 0.118$ ). The behaviour of the 1:25 model shows that  $R/H$  should not exceed 2.5% as pressure coefficients near the windward corner are especially sensitive to changes in edge radii.

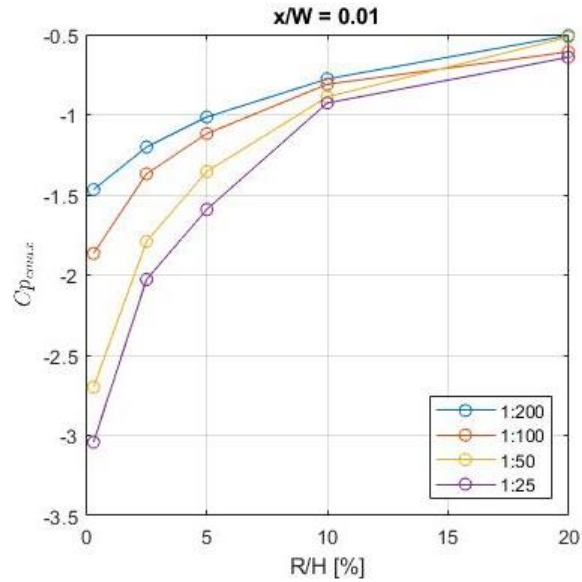


**Figure 4-16  $Cp_{cmax1}$  at  $x/W = 0.01$  at  $45^\circ$  azimuth.**

However, the difference observed between  $R/H = 0.3\%$  and  $2.5\%$  is well beyond the uncertainty bounds, and so it is possible, that a change beyond the measurement uncertainty may occur at radii smaller than  $2.5\%$ . In other words, a practical limit on edge radii may be smaller than  $2.5\%$ . Since the behavior of  $Cp_{cmax1}$  appears to be a continuous function of  $R/H$ , a linear interpolation of the points from the 1:25 curve shows that a difference in  $Cp_{cmax1}$  of  $w_{\overline{Cp_H}} = 0.118$  would occur at  $R/H = 1.3\%$ . This interpolated edge radii would present a more suitable limit on edge curvature.

Another notable observation in Figure 4-16 is the significant spread in findings at the sharpest edge curvature. Since there is a significant spatial variation in pressure coefficients at the corner, the discrepancy in data may have been due to varying tap density. At larger scales, the larger model surfaces allowed for higher tap density. As a result, taps at the edge of larger models may have been able to better capture severe suction on roof corner. This is best illustrated by the  $\overline{Cp_D}$  near the corner of the  $x/L = 0.01$  tap line in Figure 4-17.

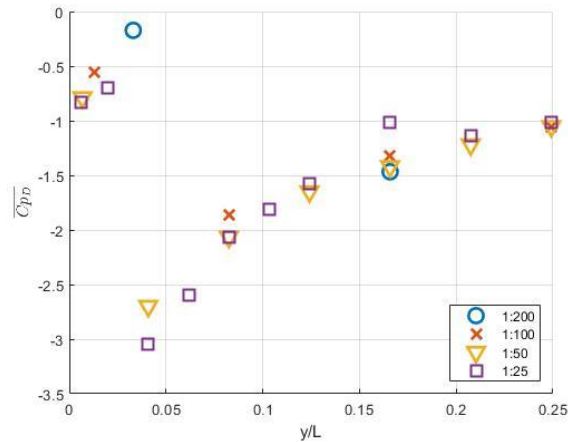


**Figure 4-17  $\overline{Cp_D}$  at  $x/W = 0.01$  near the roof corner for  $R/H = 0.3\%$ .**

As shown above, the largest mean suction is observed within a small region between  $0 < \frac{y}{L} < 0.1$  where there is significant spatial variation. The higher tap density of the 1:25 and 1:50 was able to capture the maximum suction at  $y/L = 0.04$ . However, it is clear that the tap density of the 1:100 and 1:200 models could not capture this maximum, leading to smaller estimations of  $Cp_{cmax1}$  in Figure 4-16.

However,  $Re$  dependency of the flow behaviour at the windward corner still seems possible. In Figure 4-17, the 1:25 and 1:50 have similar tap density but still observe a reduction in the suction at  $y/L = 0.04$ . Other literature have similarly found that pressure coefficients influenced by conical vortices are prone to  $Re$  effects. At a  $45^\circ$  flow direction, Lim et al. (2007) report an increase of -0.5 beneath conical vortices when  $Re$  was increased by an order of magnitude. Despite the perceived  $Re$  effects, it is still clear that as  $R/H$  increases, the maximum suction observed at the corner reduces significantly at the corner.

Further away from the roof edge the maximum observed mean suction shows better collapse. Compared to  $Cp_{cmax1}$ , it is shown in Figure 4-18, magnitudes of  $Cp_{cmax2}$  are smaller in magnitude, but still reduce as  $R/H$  increases, suggesting the continual reduction in vortex strength. It should be noted that no tap line was present at  $x/W = 0.1$  in 1:200 models.

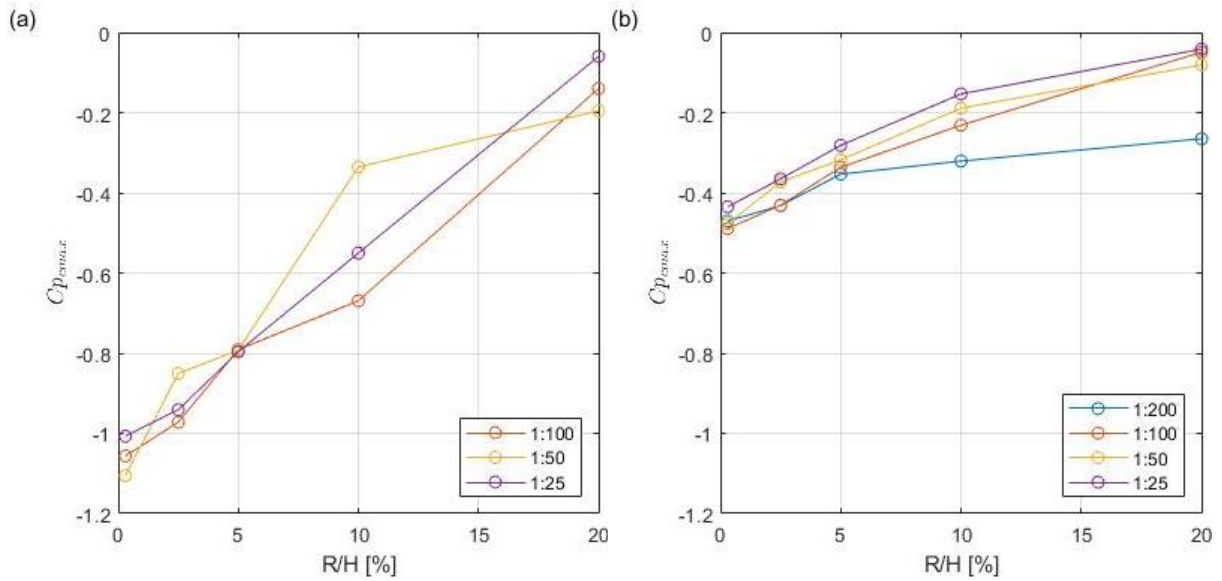


**Figure 4-18  $Cp_{max2}$  at (a)  $x/W = 0.1$  and (b)  $x/W = 0.23$ .**

Differences in  $Cp_{max2}$  from the sharpest case are summarized below in Table 4-4 and Figure 4-6 where difference beyond measurement uncertainty are highlighted in red. It is clear that pressure coefficients at oblique wind directions are significantly more sensitive to changes in  $Re$ . As  $R/H$  increases to 2.5%, changes in pressure magnitudes are beyond measurement uncertainty, though the differences are not as dramatic compared to at the windward roof corner.

**Table 4-4 Comparison of  $Cp_{max2}$  at  $x/W = 0.1$**

Scale		$[Cp_{max2}]_{0.3\%} - [Cp_{max2}]_R$		
		1:100	1:50	1:25
R/H [%]	2.5	-0.08	-0.25	-0.07
	5	-0.27	-0.31	-0.21
	10	-0.39	-0.77	-0.46
	20	-0.92	-0.91	-0.95

**Table 4-5 Comparison of  $Cp_{max2}$  at  $x/W = 0.23$**

Scale		$[Cp_{max2}]_{0.3\%} - [Cp_{max2}]_R$			
		1:200	1:100	1:50	1:25
R/H [%]	2.5	-0.04	-0.06	-0.10	-0.07
	5	-0.12	-0.15	-0.16	-0.20
	10	-0.15	-0.26	-0.29	-0.32
	20	-0.21	-0.44	-0.40	-0.44

Estimates of the vortex position  $l_c$  are shown in Figure 4-19 but do not show a clear trend in vortex position. However, the estimate of  $\phi_c$  in Figure 4-20 shows that as  $R/H$  increases,  $\phi_c$  reduces, indicating that the axis of rotation of the conical vortices are angled increasingly closer to the roof edge.

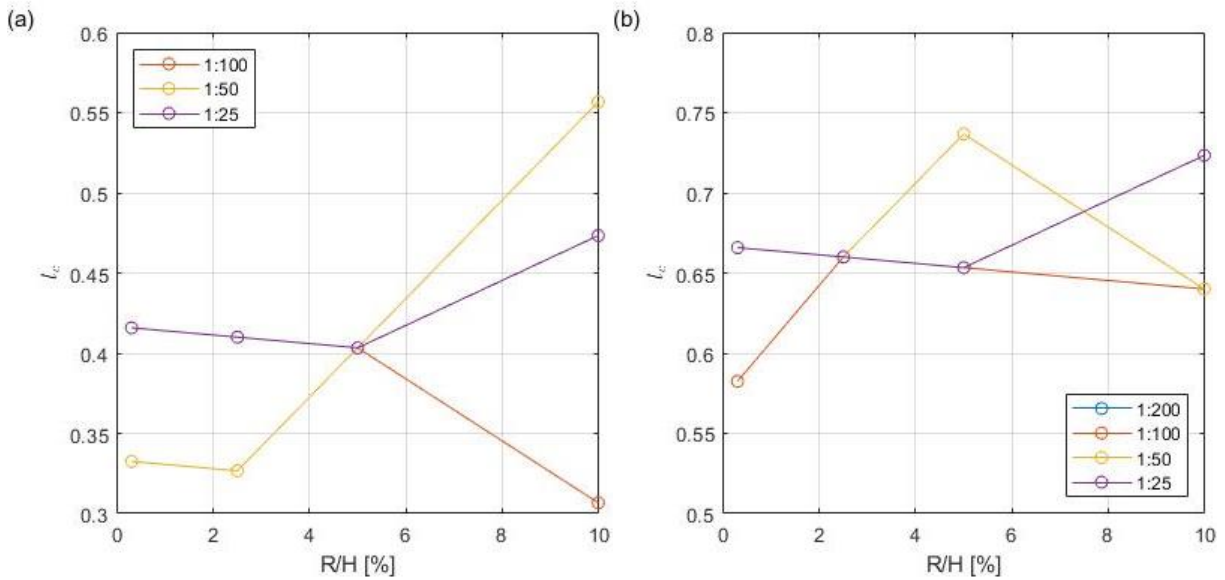


**Figure 4-19  $l_c$  at (a)  $x/W = 0.1$  and (b)  $x/W = 0.23$ .**

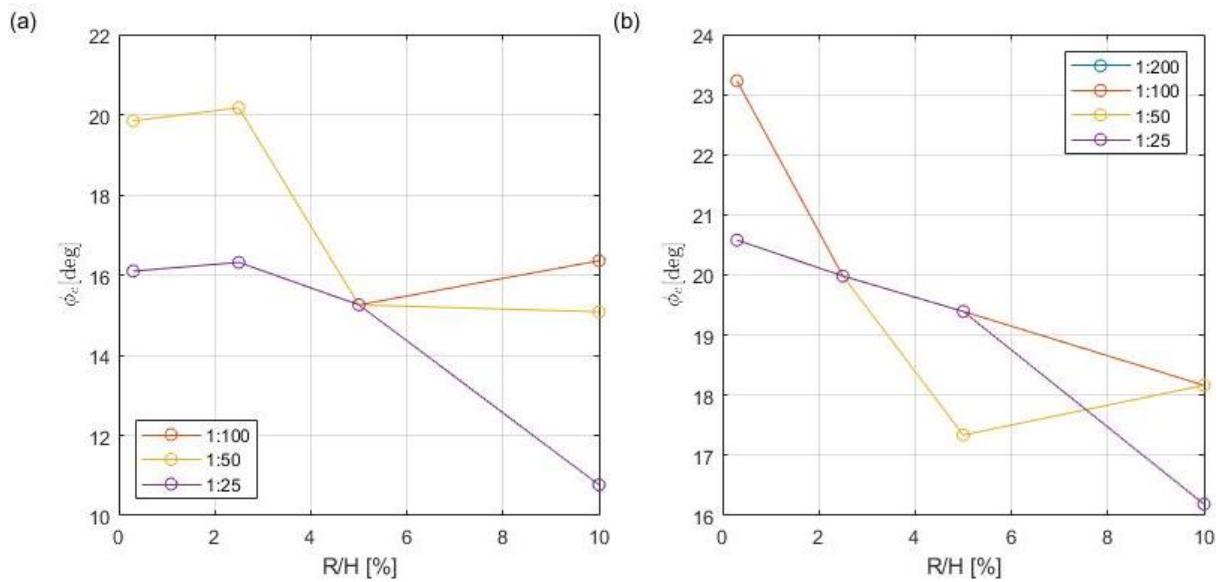


**Figure 4-20  $\phi_c$  at (a)  $x/W = 0.1$  and (b)  $x/W = 0.23$ .**

### 4.3.3.2 Possible flow mechanisms

In the analysis of the normal flow directions, it was hypothesized that the increased edge curvature caused the separated shear layer to form closer to the roof surface, and allowing the separated flow to reattach closer to the separation point. The hypothesis may extend to the shear layer behaviour in oblique wind direction. If the increased edge radii caused the flow to reattach closer to the roof edge at oblique angles, the subsequent conical vortex would potentially form closer to the roof edge, resulting in the reduction in  $\phi_c$  observed in Figure 4-20. Additionally, since flow at the roof edges may reattach closer to the separation point, it may be possible that the maturation of the conical vortices is impeded, resulting in weaker vortices, producing the observed reduction in suctions at the roof edge.

The hypothesis that increased  $R/H$  values force the separated shear layer to form closer to the roof may be supported by turbulence intensity measurements by Mahmood (2011). At oblique wind directions, the turbulence intensity profiles were measured above the windward roof corner with varying edge radii, as shown in Figure 4-21.

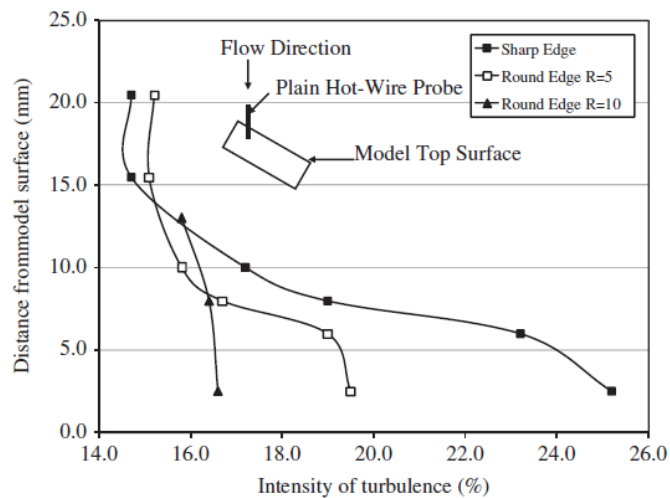


**Figure 4-21** Turbulence intensity above roof corner with varying radii at  $\theta = 45^\circ$  where  $R$  is in mm and  $H= 40\text{mm}$  (from Mahmood, 2011).

As shown above, turbulence intensity at the top of the profile is remains relatively invariant with height and is close to the turbulence intensity in the upstream flow (about 17% at roof height). Approaching the roof, the turbulence intensity exceeds the ambient values which would be



indicative of the region occupied by conical vortex. On the sharpest case, ( $R=0$ ), increased turbulence intensity was observed up to a height of 10mm or  $0.25H$  above the model roof. However, when the edge curvature was increased to  $R = 10$  mm (or  $R/H=25\%$ ), turbulence intensities close to roof do not exceed ambient values, suggesting that the separated shear layer, or conical vortex is very close to the roof surface. As a result, it can be said that as edge curvature is increased, the height of the conical vortex itself is smaller, or the core is perhaps closer to roof.

#### 4.4 Summary of findings

For normal flow directions, the maximum observed  $\overline{Cp_H}$  near the roof edge increases with edge radius, and the flow reattaches closer to the roof edge. When increased to  $R/H=10\%$ , suction near the windward roof were significantly reduced, and the lack of local maxima suggested that flow had remained attached. However, differences in  $\overline{Cp_H}$  distributions beyond measurement uncertainty were found when  $R/H$  was increased to 5%.

For oblique flow directions, high magnitudes of  $Cp_H$  attributed to conical vortices reduced for larger  $R/H$  values. Based on flow visualization and flow measurements by Mahmood (2011) the reduction in suction may be attributed to the weakening and shrinking of conical vortices as edge curvature increases.  $Cp_H$  were highest at the windward corner, and the maximum observed  $\overline{Cp_H}$  near the corner where differences beyond uncertainty were observed at  $R/H=2.5\%$ .

However, since pressures at the windward corner were extremely sensitive to changes in edge radius, it is possible that differences will continue to appear at edge radii smaller than 2.5%. Since the changes in the pressure profiles appear to be a continuous function of  $R/H$ , by interpolating the current data set, it was estimated that changes to the mean pressure profile would continue up to  $R/H = 1.3\%$ , below which, differences would not be discernable due to measurement uncertainty.

As a result, it is recommended that edge radii on low-rise building models do not exceed  $R/H = 1.3\%$  to avoid significant changes aerodynamic behaviour and subsequent surface pressures. However, since these differences vary continuously with  $R/H$ , it may be more prudent to ensure models edges are simply as sharp as possible.

## Chapter 5: Area-Averaged Pressure Coefficients and Uplift

### 5.1 Introduction

Pressure coefficients from a number of measurement points on a building surface are averaged so that an overall wind load can be determined on the building component (Holmes, 2015). In the previous chapter, an increase to curvature was shown to alter the spatial distribution of pressures on a surfaces, namely that it reduces the sizes of areas the experiencing high suction.

Consequently, edge curvature may lead to underestimations of area-averaged pressure coefficients and subsequently wind loads. The purpose of this chapter is to investigate this issue.

Three areas on the building models are examined to observe curvature effects on area-averaged pressure coefficients: the roof corner, the middle of the roof edge and the wall edge. These three locations are selected since pressure coefficients are significantly influenced by  $R/H$  in these regions. Additionally, the overall uplift coefficients were examined using pressure coefficients on the model roofs to investigate the effect of edge curvature on uplift.

### 5.2 Calculation method

For a region on the model with a surface area of  $A_{tot}$  and  $n$  taps in the region, the time history of the area-averaged pressure coefficient  $Cp_{avg}(t)$ , is

$$Cp_{avg}(t) = \sum_{i=1}^n \frac{Cp_{H_i}(t)A_i}{A_{tot}} \quad (5-1)$$

where  $Cp_{H_i}(t)$  and  $A_i$  are the pressure coefficient time history and tributary area of the  $i^{th}$  tap, respectively. From  $Cp_{avg}(t)$ , mean, RMS and peak values can be determined for comparison.

The overall uplift acting on the roof can also be determined by applying equation 5-1 to the entire roof area to determine overall uplift coefficient

$$C_{FZ}(t) = \sum_{i=1}^n \frac{Cp_{H_i}(t)A_i}{A_{roof}} \quad (5-2)$$

where  $A_{roof}$  is the total surface area of the roof.

For a given tap, the tributary area is defined as a rectangular region surrounding the tap, whose boundaries are equidistant between the tap of interest and its neighboring taps. An example of a tributary area for a tap on the roof corner is shown in Figure 5-1.

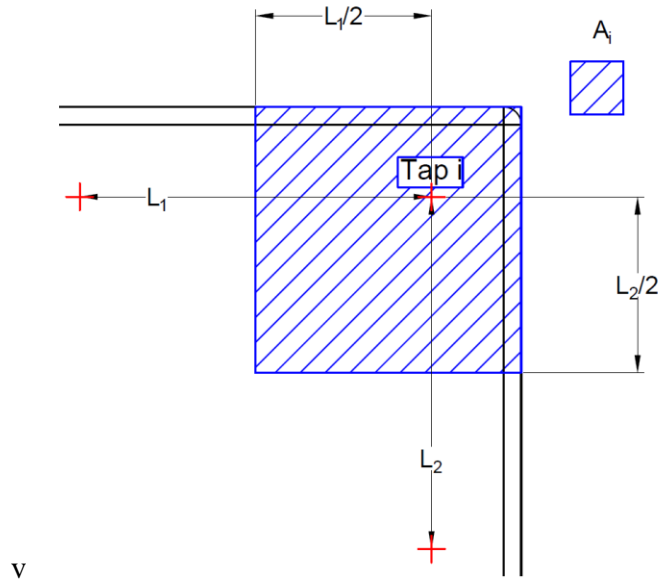


**Figure 5-1 Tributary area example for a tap at a roof corner.**

To note in Figure 5-1, is that tributary areas extend over the projected area occupied by curvature. The rationale to this approach is that typical wind tunnel studies neglect edge radii on models, as these curved area would not exist on the full-scale building.

For  $Cp_{avg}$  to be comparable amongst the different model configurations, identical tap locations and tributary areas need to be used. Tap layouts on the models are designed such that tap locations on the smallest (1:200) models are present in tap layouts of all model configurations. Consequently,  $Cp_{avg}$  determined with tap locations and tributary areas using the 1:200 layouts would produce results that are comparable amongst all models. However, the concern with the 1:200 tap layouts is that the sparsity of taps may not adequately capture the dramatic spatial variation of surface pressure near the edges. To address this issue,  $Cp_{avg}$  is also determined using tap layouts from larger model scales where taps are more closely spaced. As a result, for each surface of interest,  $Cp_{avg}$  was determined using three tap configurations, A, B and C, which refer to the use of tap locations from 1:200, 1:100 and 1:50 models, respectively. The

average tap spacing for each regions and tap configuration is summarized below in where tributary area is normalized by  $H^2$ .

**Table 5-1 Average tributary area,  $A_i/H^2$ , per tap configurations and model regions**

		Tap Configuration		
		A	B	C
Region	Roof Corner	0.27	0.08	0.02
	Middle of Roof Edge	0.27	0.08	0.03
	Wall Edge	0.26	0.13	0.05
	Entire Roof	0.27	0.08	n/a

Since tap density is sparser on smaller model scales, tap configurations from larger model scales may not be applicable to smaller models. The applicability of the tap configurations to each model scale is summarized in Table 5-2.

**Table 5-2 Tap and tributary area configurations and their applicability to model scales, denoted with ×**

		Tap Configuration		
		A	B	C
Scale	1:200	×		
	1:100	×	×	
	1:50	×	×	×
	1:25	×	×	×

The tributary areas of these three tap configurations at the windward roof corner, are shown in Figure 5-2.  $Cp_{avg}$  at the roof corner is determined for a  $\theta = 45^\circ$  flow direction. The smallest tributary area considered in each of the three configurations consist of a single tap at the corner. For larger areas, neighbouring taps and their tributary areas are included, with the area growing towards the center of the roof. As shown by Figure 5-2, tap resolution increases and tributary areas shrink from configurations A to C, which would presumably better capture high suction and the effects of  $R/H$ .

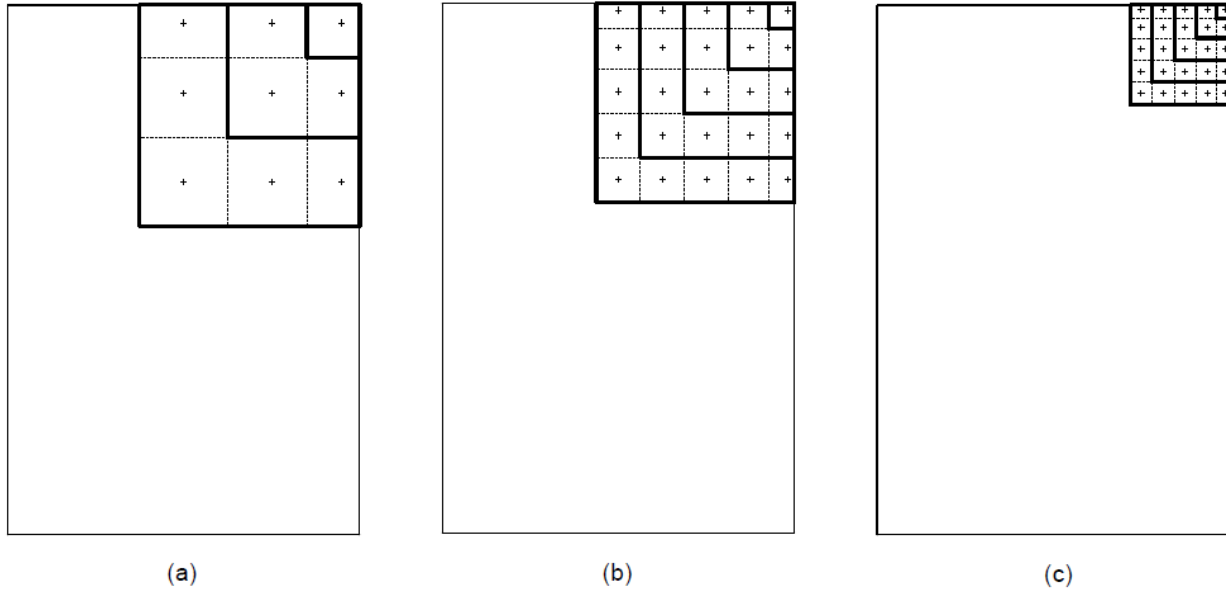


**Figure 5-2 Tap locations and tributary areas on roof corner using (a) "A" Configuration, (b) "B" Configuration and (c) "C" Configuration. Tap locations are denoted with + and boundaries of  $A_{tot}$  considered are shown in bold lines.**

The tap locations and tributary areas for  $Cp_{avg}$  determined by the middle of the roof edge are illustrated in Figure 5-3. Similar to the roof corner, the smallest area considered consists of a single tap at the middle of the roof edge.  $Cp_{avg}$  in this region were determined for a  $\theta = 0^\circ$  flow direction. For larger areas,  $Cp_{avg}$  is determined by including surrounding taps with the total area growing towards the center of the roof.

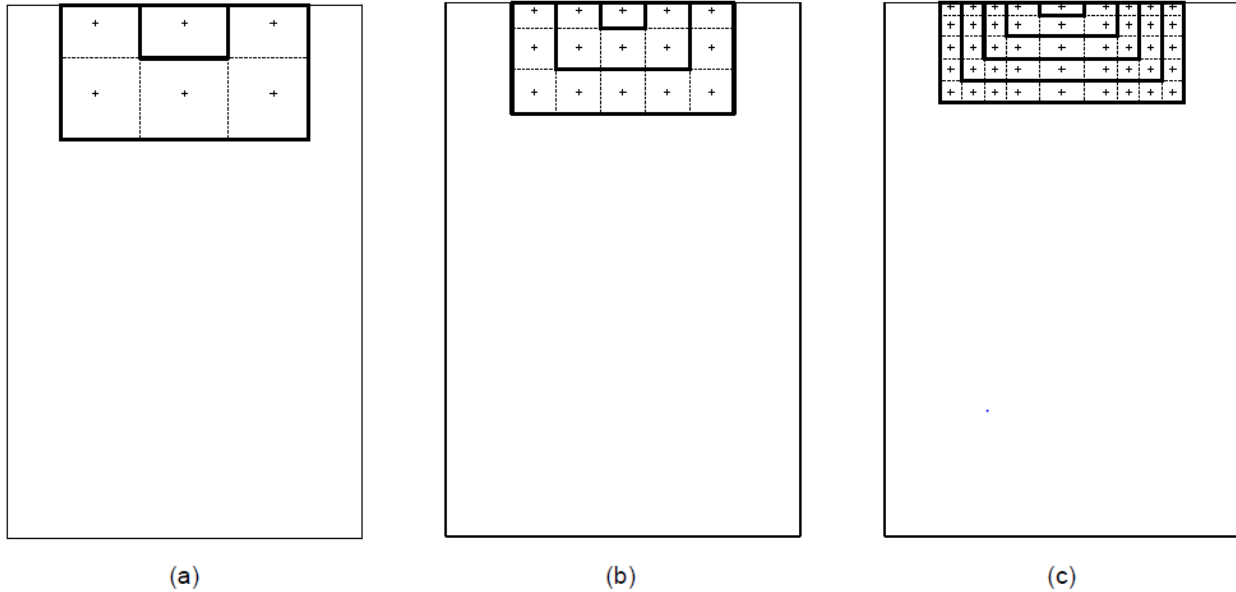


**Figure 5-3 Tap locations and tributary areas on the middle of roof edge using (a) “A” Configuration, (b) “B” Configuration and (c) “C” Configuration. Tap locations are denoted with + and boundaries of  $A_{tot}$  considered are shown in bold lines.**

Area-averages on the wall were determined by the windward wall edge on the eastern elevation for a  $\theta = 0^\circ$  flow direction. The smallest area considered taps along the entire height of the wall, as it is expected that surface pressure varies spatially with breadth more than height. The tributary areas used to determine  $Cp_{avg}$  at the walls are illustrated below in Figure 5-4.

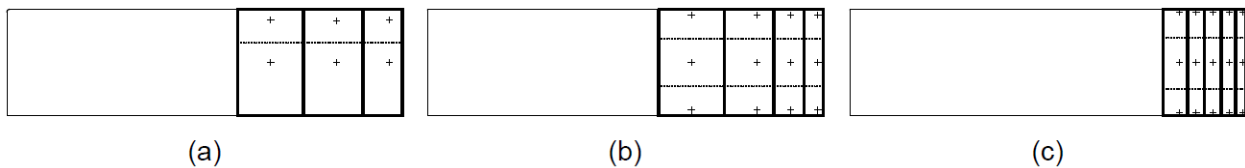


**Figure 5-4 Tap locations and tributary areas on wall using (a) “A” Configuration, (b) “B” Configuration and (c) “C” Configuration. Tap locations are denoted with + and boundaries of  $A_{tot}$  considered are shown in bold lines.**

Total uplift on roof the were considered using a grid of taps as shown in Figure 5-5. Only configurations A and B were considered since, as will be shown in later analysis, the effect of tap resolution on area-averaged pressure coefficients lessens as the size of the total area increases.

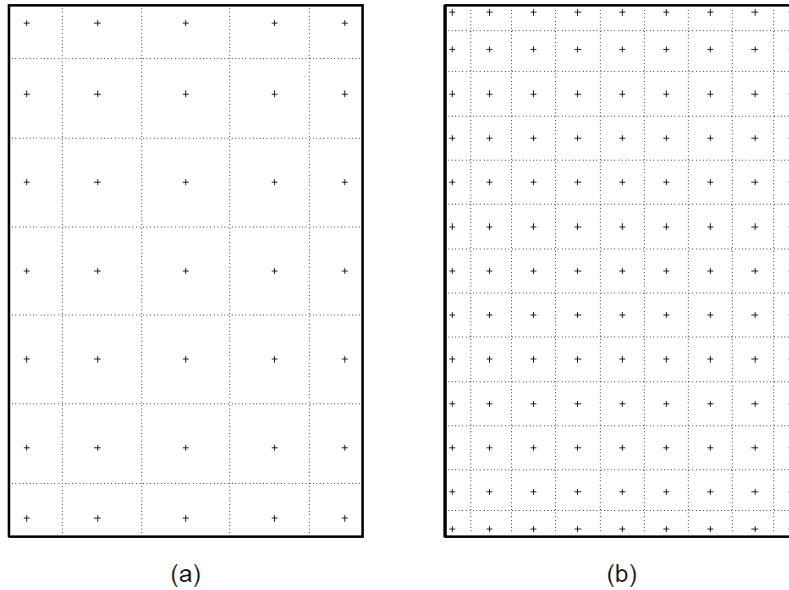


**Figure 5-5 Tap location and tributary areas for determination of uplift using (a) "A" Configuration and (b) "B" Configuration.**

## 5.3 Results

### 5.3.1 Area-averaged pressure coefficients

Mean, RMS and peak area-averaged pressure coefficients using the "A" tributary areas are plotted as a function of surface areas in full-scale dimensions in Figure 5-6 for the 1:25 models. Results from other model scales can be found in Appendix I.

In general, differences are most notable for smaller area near the edges where flow separates. As the total area increases,  $Cp_{avg}$  curves tends to collapse towards a singular value since areas away from edges are not as influenced by separated flow behaviour and, thereby, invariant with  $R/H$ .

$Cp_{avg}$  in all regions within  $0.3\% \leq R/H \leq 5\%$  show close agreement, particularly on the roof corner ((a) to (c)) and the wall edge ((g) to (i)). However, it is likely that the similarity of results were due to the lack of tap resolution, which could not capture the rapid changes in spatial pressure distributions near the model edges. This is immediately clear when compared to results determined from "C" tributary areas in Figure 5-7.

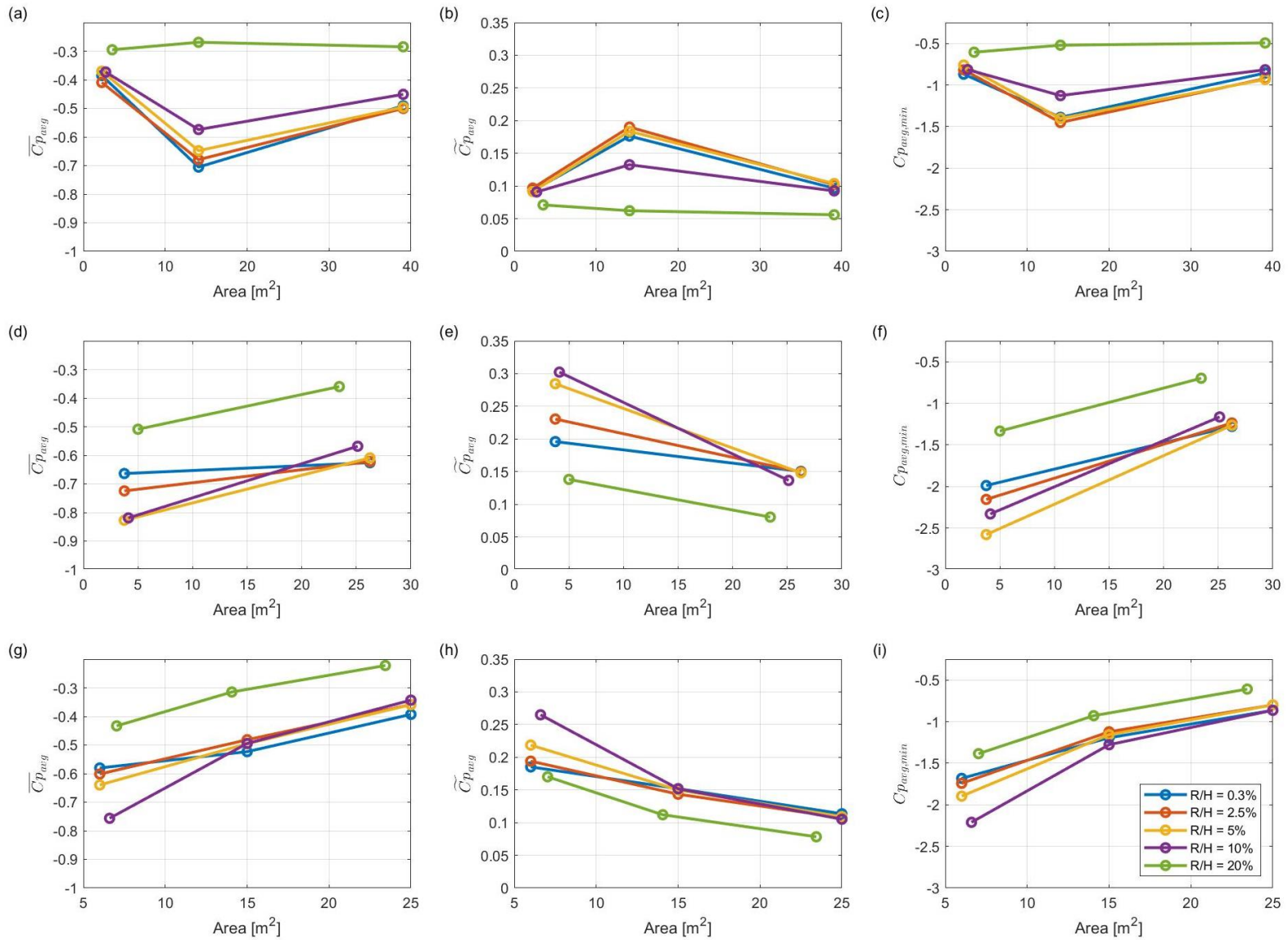


Figure 5-6 1:25  $C_{p_{avg}}$  using configuration A of (a) to (c) roof corner , (d) to(f) middle of roof edge and, (g) to (i) wall.



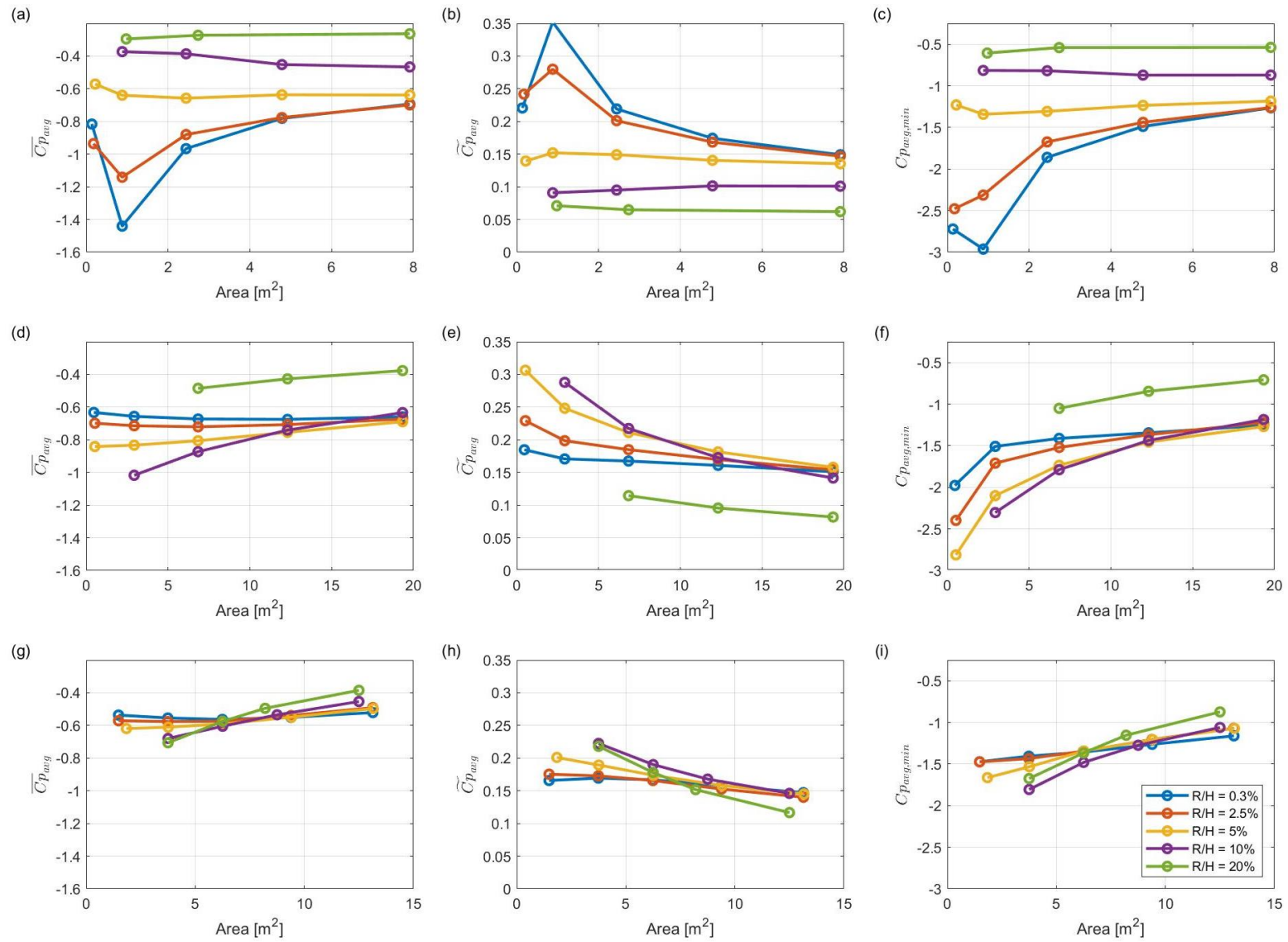


Figure 5-7 1:25  $C_{p,avg}$  using configuration C of, (a) to (c) roof corner , (d) to(f) middle of roof edge and, (g) to (i) wall.

The behaviour of area-averaged pressure coefficients is better captured by the denser tap layout. The susceptibility of smaller areas near edges to changes in  $R/H$  is clearly illustrated in Figure 5-7, the most significant of which are on roof corner, in (a) to (c). The observations reflect findings from section 4.3, where at oblique flow directions, the magnitude of both mean and fluctuating  $Cp_H$  at the roof corner are sensitive to small changes in  $R/H$ . The trends observed in 1:25 Scale models are reflected in other models scales. For the present discussion of trends, the results of the 1:25 models using “C” Configuration will be used since they better capture the effects of  $R/H$  in smaller areas.

### 5.3.1.1 Roof corner

At the roof corner, Figure 5-7(a) to (c), the magnitude of  $Cp_{avg}$  steadily reduces as  $R/H$  increases. The effects of edge radius are most prominent in smaller areas ( $A_{tot} < 8 \text{ m}^2$ ) which suggests that the effects may be limited to regions close to building edges. From previous findings in Chapter 4, the reduction in  $Cp_{avg}$  in this region is likely related to the weakening of conical vortices as the edge radii increase. Differences in  $Cp_{avg}$  between the sharpest configuration and  $R/H=2.5\%$  are shown to be significant up to an area of  $2.25 \text{ m}^2$ . However, as the area continues to increase, the effects of  $R/H$  become negligible.

### 5.3.1.2 Middle of roof edge and wall

$Cp_{avg}$  on the middle of the roof edge, Figure 5-7 (d) to (f), and the wall, Figure 5-7 (g) to (i) show similar behaviour. As  $R/H$  increases, the magnitude  $Cp_{avg}$  increases, reflecting the increase in local  $Cp_H$  magnitudes as  $R/H$  increases in normal flow directions, as discussed in section 4.2. The observation seems to be contrary to the initial hypothesis that at increased  $R/H$ , the earlier flow reattachment produces smaller regions of high suction, thereby reducing  $Cp_{avg}$  estimates. It can then be said that for normal flow directions, the change of  $Cp_H$  magnitude with  $R/H$  plays a greater role than changes in spatial distribution in producing discrepancies in  $Cp_{avg}$ . It is also shown that the influence of  $R/H$  lessens in these regions as the area increases, which again highlights the susceptibility of smaller areas near edges to the effects of varying  $R/H$ .

### 5.3.2 Uplift coefficient

Uplift coefficients determined using “A” and “B” tap configurations are shown below in Figure 5-8 and Figure 5-9, respectively. Findings from other model scales are found in Appendix J.

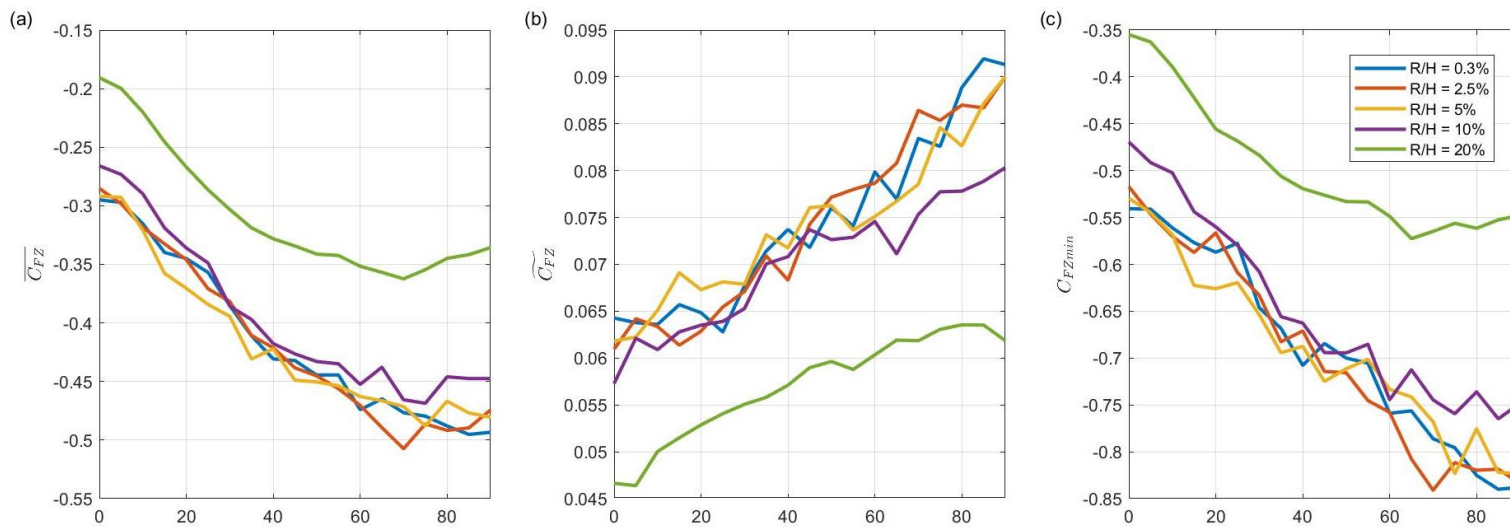


**Figure 5-8 (a) Mean, (b) RMS and (c) Peak  $C_{FZ}$  from 1:25 model using configuration "A".**

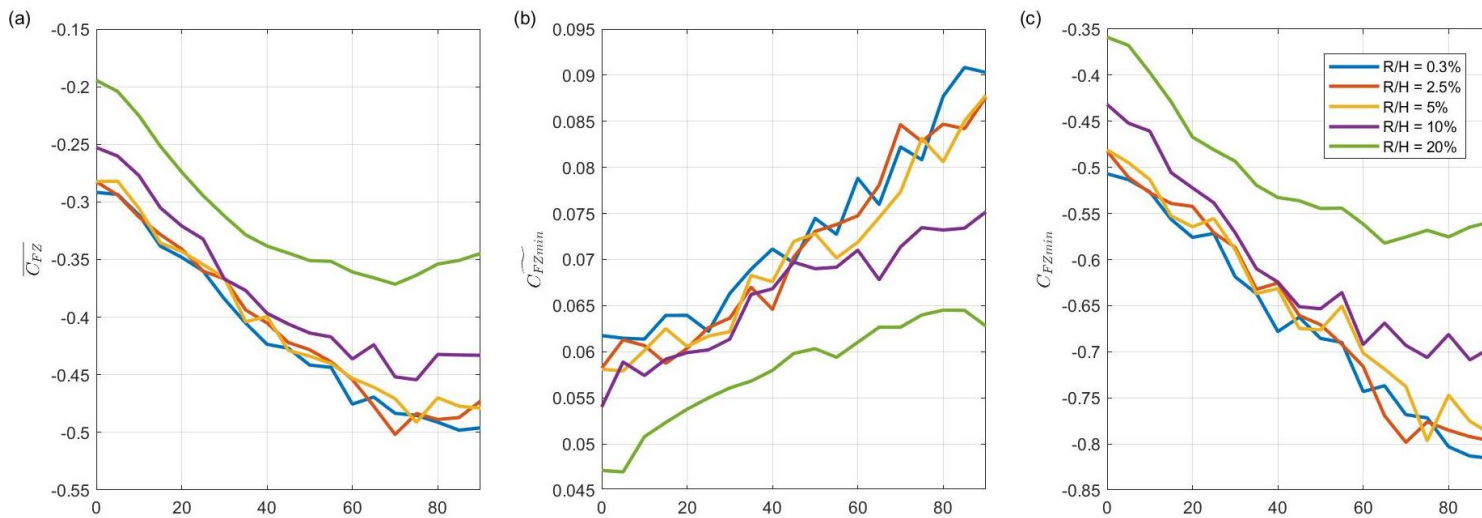


**Figure 5-9 (a) Mean, (b) RMS and (c) peak  $C_{FZ}$  of 1:25 Model using configuration "B".**

Comparing Figure 5-8 and Figure 5-9, tap resolution does not seem to produce significant differences in  $C_{FZ}$ . The similarity of  $C_{FZ}$  between both figures demonstrates that the effect of tap resolution on area-averaged pressure coefficient is not as significant as the area considered increases. Also, as  $C_{FZ}$  where  $R/H \leq 5\%$  seem to overlap, the effect of  $R/H$  is shown to not be as pronounced at larger areas. The effect of increased edge radii are not apparent until  $R/H$  was increased to 10% where a significant reduction in the uplift coefficient was observed. As noted in Chapter 4, as  $R/H$  increases, separated flow tends to reattach further upstream as  $R/H$ . Subsequently, with less of the roof exposed to separated flow, a smaller portion of the roof area experiences high suction when  $R/H$  increases, leading to lower uplift coefficients.

Another notable observation is that the  $C_{FZ}$  increases steadily with azimuth. As azimuth increases, the flow direction becomes increasingly perpendicular to the longest roof edge. With a larger edge upstream, flow separates over a greater portion of the roof, and the area on the roof subjected to high suctions increases, thereby increasing the up lift.

## 5.4 Discussion

### 5.4.1 Influence of edge curvature

From the results, it is clear that the change in  $Cp_{avg}$  is continuous with  $R/H$  and that the behaviour may be explained by the changes to pressure profiles examined in Chapter 4. To quantify the effect of edge radius, a ratio comparing the  $\overline{Cp}_{avg}$  to the sharpest case was used

$$\bar{r} = \frac{[\overline{Cp}_{avg}(A_{tot})]_R}{[\overline{Cp}_{avg}(A_{tot})]_{0.3\%}} \quad (5-3)$$

where  $\bar{r} = 1$  would indicate a perfect match with the  $\overline{Cp}_{avg}$  determined from the sharpest model.

The ratio  $\bar{r}$  from 1:25 models are shown below in Figure 5-10. It is clear that the effects of edge radius is continual as the curves approach  $\bar{r} = 1$  as  $R/H$  reduces. Additionally, smaller areas, i.e.  $< 10 m^2$ , are especially prone to  $R/H$  effects, the most sensitive area being the roof corner in Figure 5-10 (a) where an increase to  $R/H = 5\%$  resulted in a reduction in  $\overline{Cp}_{avg}$  of over 50%.

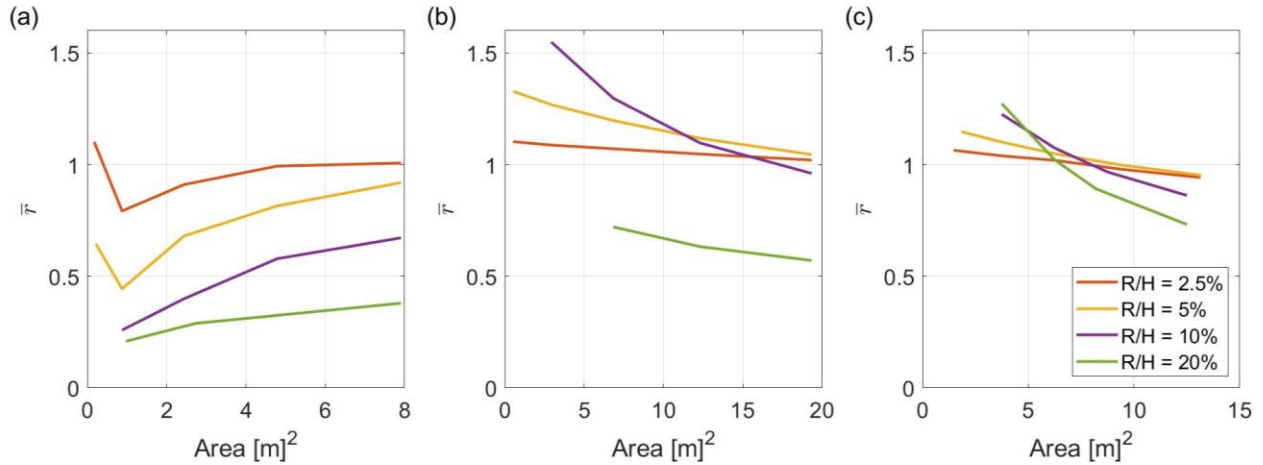


**Figure 5-10  $\bar{r}$  of 1:25 using “C” tributary areas at(a) roof corner, (b) middle of roof edge and (c) wall.**

The peaks were also examined using a similar a ratio as defined below and show similar behaviour in Figure 5-11.

$$r_{min} = \frac{[Cp_{avgmin}(A_{tot})]_R}{[Cp_{avgmin}(A_{tot})]_{0.3\%}} \quad (5-4)$$

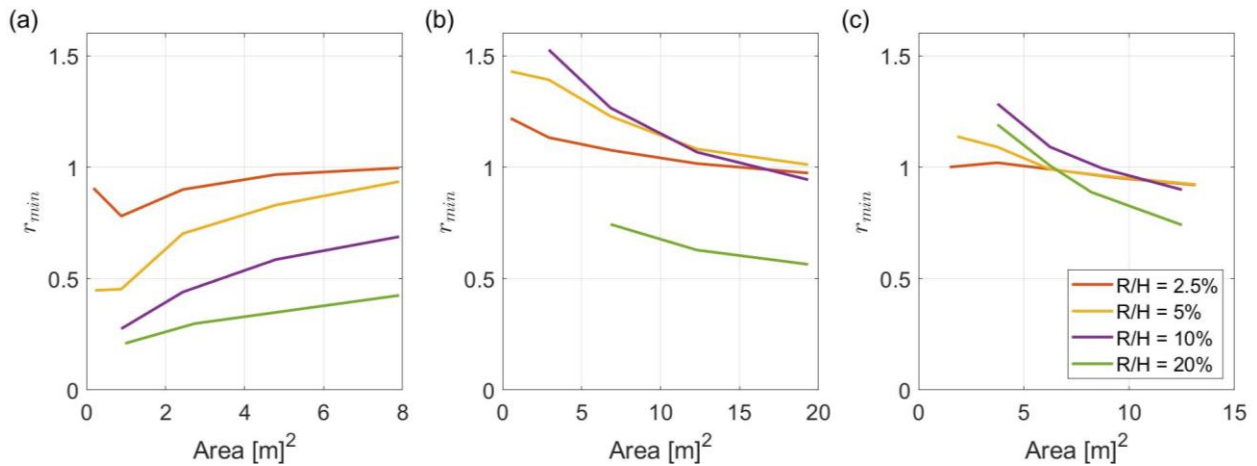


**Figure 5-11  $r_{min}$  of 1:25 using “C” tributary areas at(a) roof corner, (b) middle of roof edge and (c) wall.**

Amongst the radii considered,  $R/H = 2.5\%$  most closely replicates the mean and peak  $Cp_{avg}$  of the sharpest model, and effects of edge curvature reduce as the area increases. However, for

areas smaller than  $2m^2$ , peak and mean  $Cp_{avg}$  experience reductions as high as 30% at  $R/H = 2.5\%$  at the roof corner.

When applying  $\bar{r}$  and  $r_{min}$  to uplift coefficients, the effects of  $R/H$  are not as significant. As shown in, Figure 5-12, reductions in both mean and peak uplift are not apparent until  $R/H$  was increased to 10%. However, at  $R/H = 2.5\%$ , discrepancies within 7% are observed in the mean and peak uplift coefficient.

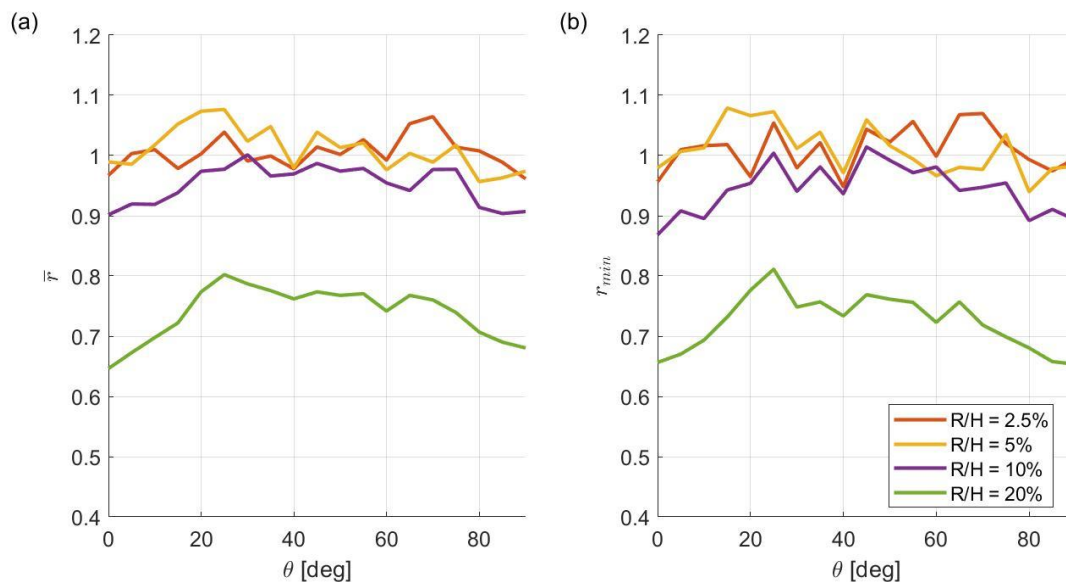
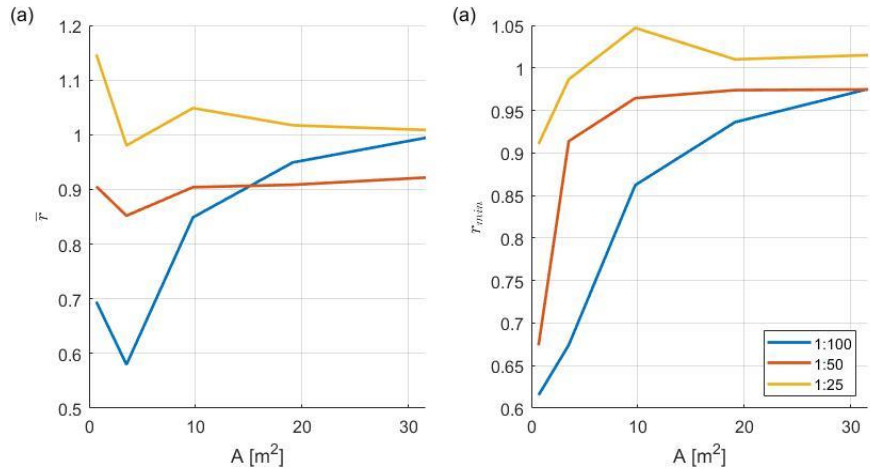


Figure 5-12 (a)  $\bar{r}$  and (b)  $r_{min}$  of  $C_{FZ}$  from 1:25 models using "A" tributary areas.

#### 5.4.2 Influence of model scale

Results at the other model scales illustrate the behaviour presented so far with  $R/H$  and  $A_{tot}$ . However, the magnitude to which these differences are observed tend to differ, which would suggest some kind of **Re** effect. Scaling effects are best illustrated by comparing  $\bar{r}$  and  $r_{min}$  determined from various models at the roof corner where  $R/H = 2.5\%$  in Figure 5-13.



**Figure 5-13 Comparison of (a)  $\bar{r}$  and (b)  $r_{min}$  at the roof corner with  $R/H=2.5\%$  and "B" tributary areas.**

From the three model scales, it is clear that at smaller areas, mean and peak  $Cp_{avg}$  experience a greater reduction at smaller model scales. The trend illustrates that that  $Re$  effects may be significant in pressures affected by conical vortices which is in agreement with literature (Lim, Castro, & Hoxey, 2007). For uplift coefficients, scaling effects are not clear at  $R/H = 2.5\%$ , however, at  $R/H = 20\%$ , it is clear that a greater reduction in  $C_{FZ}$  is experienced at larger model scales, as shown below.

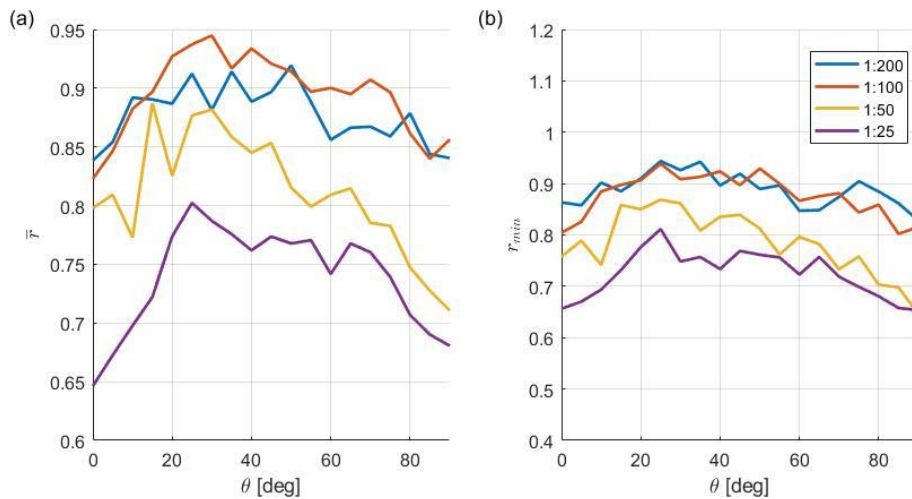


**Figure 5-14 Comparison of (a)  $\bar{r}$  and (b)  $r_{min}$  of  $C_{FZ}$  with  $R/H = 20\%$  at various model scales.**



### 5.4.3 Influence of tap resolution and tributary area

The comparison of  $Cp_{avg}$  in Figure 5-6 and Figure 5-7 clearly show that higher tap resolution can better estimate  $Cp_{avg}$  and capture the effects of  $R/H$  near the edges. Higher tap density near edges would better capture high suctions, leading to higher estimations of  $Cp_{avg}$  for small areas near edges. An example of this observation would be comparing the  $\overline{Cp}_{avg}$  on the roof corners on Figure 5-6(a) and Figure 5-7(a). In Figure 5-6(a) where the sparser “A” taps were used, at  $A_{tot} = 2.25 m^2$ , the magnitude of  $\overline{Cp}_{avg}$  is -0.4 and appears to be invariant with  $R/H$ . Conversely, in Figure 5-7(a), “C” tributary areas report  $\overline{Cp}_{avg}$  as high as -1.1, and was able to capture the reduction of  $\overline{Cp}_{avg}$  with  $R/H$ .

The concern then, is that the predicted effect of  $R/H$  may be more dramatic as the tap resolution increases. To investigate this effect, a portion of the windward roof corner was examined on the 1:25 models where there was enough space for added accent taps. The area considered is illustrated below Figure 5-15 and is equivalent to a full-scale area of  $2.45 m^2$

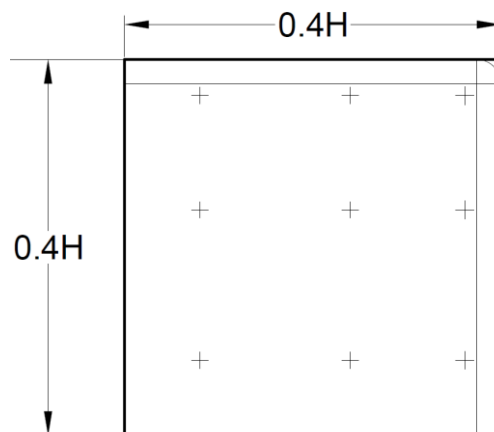


**Figure 5-15**  $2.45m^2$  area on windward roof corner of 1:25 models considered.

Using the grid of taps in the area,  $\overline{Cp}_H$  contours were plotted along with tap locations used in “A” and “B” in Figure 5-16. These contours were determined by interpolating  $\overline{Cp}_H$  of all taps in Figure 5-15. It can be seen that taps from “A”, were not close enough to the edge to capture the highest suctions, nor were able to capture the changes in spatial distribution with  $R/H$ .

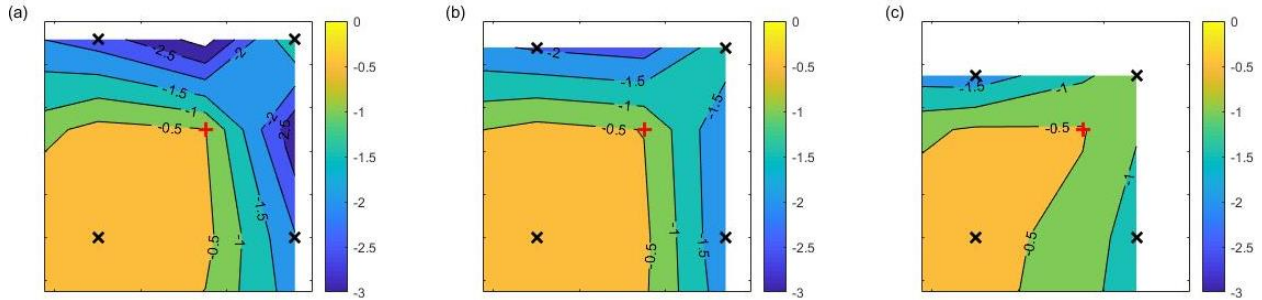


**Figure 5-16  $\overline{Cp}_H$  contours ° roof corner of 1:25 models at  $\theta = 45^\circ$  and “A” taps (+) and “B” taps (x) with (a)  $R/H = 0.3\%$ , (b)  $R/H = 2.5\%$  and (c)  $R/H = 5\%$ .**

As tap density increases, the magnitude of  $Cp_{avg}$  may increase and the perceived effect of  $R/H$  may be more dramatic. From the area illustrated in Figure 5-15,  $Cp_{avg}$  were determined using all three tap configurations and plotted below in Figure 5-17. It is clear that the “A” tap layout underestimates  $Cp_{avg}$  and does not capture the effect of increasing edge radii. When tap density was increased in layout “B” the reduction in  $Cp_{avg}$  as  $R/H$  increases is now observable, but the magnitude is overestimated

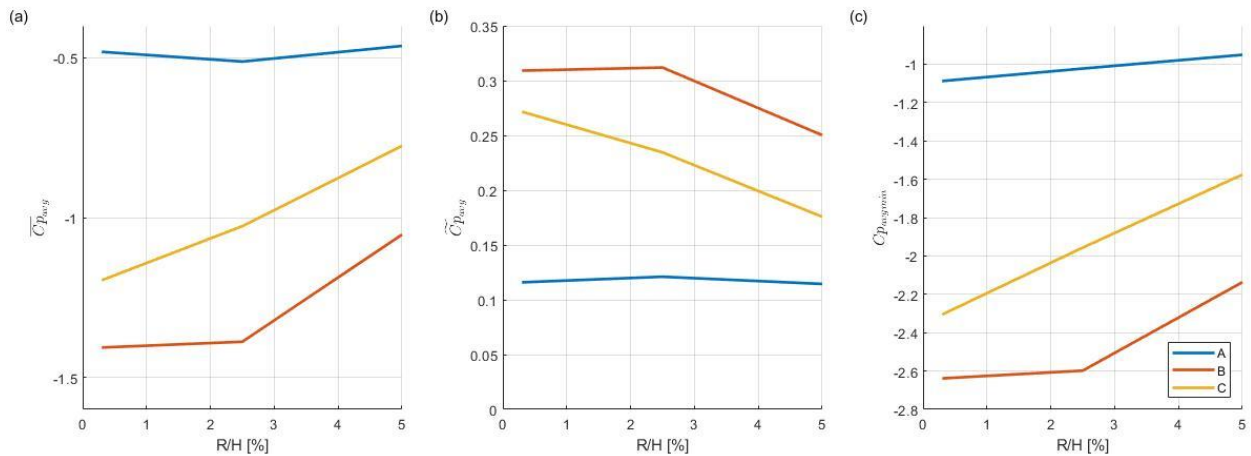


**Figure 5-17 (a) Mean, (b) RMS and (c) peak  $Cp_{avg}$  determined on  $2.45m^2$  roof corner at  $\theta = 45^\circ$  on a 1:25 model.**

However, the effect of tap resolution disappears as the area grows larger. Repeating the comparison of  $Cp_{avg}$  with tap resolution a larger region at the roof corner in Figure 5-18,  $Cp_{avg}$  shows closer agreement amongst tap resolutions as plotted in Figure 5-19. Given that the tap

resolution has less of an effect as the area increases, it may be possible to determine uplifts using “A” tributary areas without significantly underestimating results

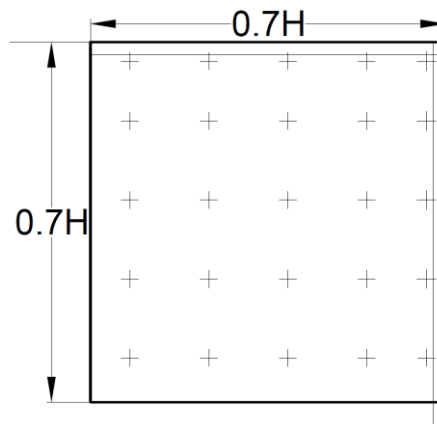


**Figure 5-18**  $7.85m^2$  area on windward roof corner of 1:25 models considered.

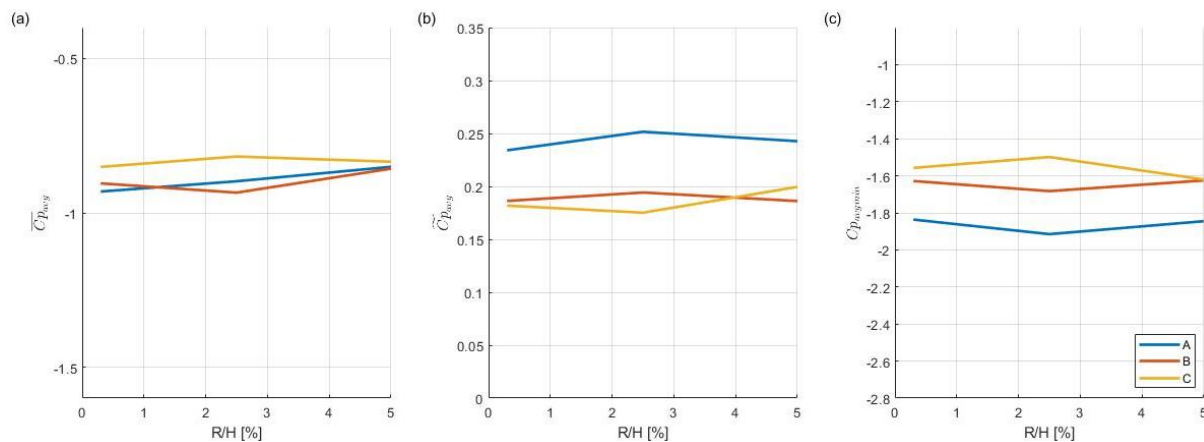


**Figure 5-19** (a) Mean, (b) RMS and (c) peak  $Cp_{avg}$  determined on  $7.85m^2$  roof corner at  $\theta = 45^\circ$  on a 1:25 model.

## 5.5 Summary of findings

Area-averaged pressure coefficients and overall uplift on the roof were examined on models with varying edge curvature. As curvature increased, trends in  $Cp_{avg}$  followed those observed in  $Cp_H$  distributions in the previous chapter. Near the roof edges in normal flow directions,  $Cp_{avg}$  increased with  $R/H$  whereas on the roof corner at oblique wind directions,  $Cp_{avg}$  steadily reduced with increased edge curvature, which is likely due to the weakening of conical vortices

on the roof. The effects of edge curvature on area-averaged pressure coefficients appeared to be the greatest for small areas near building edges. Additionally, as  $R/H$  increased,  $C_{FZ}$  reduced and is likely due to the shrinking areas of high suction on the roof produced by separated flow.

$Cp_{avg}$  in small areas at the roof corner were the most sensitive to  $R/H$  effects and also exhibit  $Re$  effects. At  $R/H=2.5\%$ , discrepancies of up to 30% in both mean and peak  $Cp_{avg}$  for areas smaller than  $2 m^2$ . Conversely, discrepancies in mean and peak uplifts remain within 10% when edge curvature is increased to 2.5%. However, with the proposed limit of 1.3% from the previous chapter, these discrepancies in area-averaged pressure coefficients may be smaller.

## Chapter 6: Conclusions

### 6.1 Summary of findings

From the series of wind tunnel tests conducted, it is clear the edge curvature of wind tunnel models can significantly affect flow behaviour and subsequent pressure distributions across model surfaces.

#### 6.1.1 Point pressure coefficients

From the point pressure measurements discussed in Chapter 4, an increase in  $R/H$  can alter the magnitude of local pressure coefficients and reduce the size of areas experiencing severe suction. The effects of edge radii are most pronounced on surfaces affected by separated and reattaching flow, i.e., areas near building edges. On these surfaces, increases in  $R/H$  can produce changes in pressure distributions that are beyond measurement uncertainty.

For flow in normal wind directions an increase in  $R/H$  to 5% increases the magnitude of mean and fluctuating pressure coefficient beyond measurement uncertainty near the roof and wall edges. Additionally, the increased edge radii causes surface pressures to recover further upstream, which would imply the larger edge radii promote flow reattachment.

Conversely, the roof corner at oblique wind directions experiences significant reductions of  $C_{pH}$  magnitudes at larger edge radii. Significant reductions in both mean and fluctuating  $C_{pH}$  at the roof corner are observed at  $R/H = 2.5\%$ . However, suction at the windward roof corner were highly sensitive to edge radii, and it is expected that differences beyond measurement uncertainty would continue to occur up to  $R/H = 1.3\%$ .

Also, for both normal and oblique flow directions, signs of  $Re$  effects in pressure coefficients become more pronounced as  $R/H$  increases, though they were not discernable for the sharpest models tested ( $R/H = 0.3\%$ ).

#### 6.1.2 Area-averaged pressure coefficients

Following the prescribed limit of  $R/H = 2.5\%$ , significant changes in area-averaged pressure coefficients were observed. In normal flow directions, areas near roof edges and wall-edges

observed increase in peak  $Cp_{avg}$  by as much as 22%, whereas on the roof corner, peak  $Cp_{avg}$  reduced by as much as 30%. These significant discrepancies in  $Cp_{avg}$  can potentially lead to inaccurate predictions of wind loads for building surfaces near edges.

The effect of edge radius is most significant for small areas ( $< 2.25 m^2$ ) near the building edges, which suggests that differences in  $R/H$  mainly affects pressures within the separation bubble. For larger areas ( $> 8m^2$ ) the effects are not as pronounced. For instance, when edge radii increased to  $R/H = 2.5\%$ , mean and fluctuating uplift coefficients produced discrepancies within 7%.

## 6.2 Definition and limit of edge radius

The present study has shown that discernable differences in pressure coefficient distributions are discernable up to  $R/H = 1.3\%$ . As such, to ensure similarity in aerodynamic behaviour, it is proposed that the edge radii of low-rise wind tunnel models should not exceed  $R/H = 1.3\%$ .

Modern 3D printing techniques should be able to reach this limit fairly easily. In the present study, models were constructed through finite deposition modeling using bead widths of 0.06 mm. Applying this radii to the 1:50 models (which is a typical scale used in low-rise building studies) would produce a model with  $R/H = 0.08\%$  which is well below the proposed limit. In addition, surface finishing on the models may be able to reduce the edge radii further.

However, since the effect of  $R/H$  on pressure distributions appeared to be continuous, the proposed edge radii is limited by the measurement uncertainty of the experimental setup. As a result, differences may continue to occur using edge radii below this limit and so it can be said that the edge radii of models ought to be as sharp as possible, or within the estimated  $R/H$  range of full scale cladding elements of 0.03% to 0.125%, as discussed in section 2.1.3.

## 6.3 Future work

Though the present work has proposed a limit on edge radii, additional work is required to refine the estimation of this limit and better understand the underlying flow mechanism. Five considerations for future work are proposed.

### 6.3.1 Repeating experiments

The effect of edge curvature on pressure distributions is shown to be continuous, so it is possible that discrepancies in  $Cp_H$  may continue to occur below  $R/H = 1.3\%$ . Subsequently, the present experiments ought to be repeated on models with  $R/H < 1.3\%$  to determine whether the changes in pressure coefficients continue to occur at smaller radii. These discrepancies may be fairly small, so in order to observe these differences, experiments ought to be designed with a focus on minimizing measurement uncertainty. This may include conducting the wind tunnel experiments at higher speeds to minimize the effect of measurement uncertainty in pressure scanners, as discussed in section 3.4. Additionally the influence of edge radii on parapets should also be investigated, as parapets are commonly used in low-rise buildings and can alter surface pressure distributions on the roof (Kopp et al., 2005).

### 6.3.2 Flow visualization

It is clear that increased edge radii alters the behaviour of the separating and reattaching flow and facilitates flow reattachment. It is hypothesized that this behaviour may be a result of the larger edge radii forcing the separated shear layer to be formed closer to the model surface. To investigate this hypothesis, a flow visualization study, such as through PIV, ought to be conducted on similar models with varying radii. By measuring the flow quantities around model edges, the effect of edge radii on the separated shear layer can be observed.

### 6.3.3 Investigating the effects of free stream turbulence

The design of the present experiments was such that small-scale turbulence and turbulence intensity matched reasonably in the upstream flow. Since upstream turbulence is known to significantly alter separating and reattaching flow behaviour, the experiments ought to be repeated in varying upstream flow conditions to determine whether similar behaviour in  $Cp_H$  with  $R/H$  occurs. Such experiments could be conducted by using the same models but varying the upstream flow conditions to simulate a variety of terrains.

### 6.3.4 Investigating potential Reynolds number effects

As presented in Chapter 4, some discrepancies in pressure profiles as well as in the pressure spectra are observed amongst the different model scales. These discrepancies become more apparent as the edge radii increases and are speculated to be due to  $Re$  effects in the separating shear layer. To investigate potential  $Re$  sensitivity of the flow around a rounded edge, the wind tunnel tests in the present study could be repeated at varying wind speeds to examine a broader range of  $Re$ .

By using multiple model scales, a broader range of  $Re$  values could be observed. However, this could present additional challenges. As noted by Lim et al. (2007) and as demonstrated by the present study, large-scale turbulence in the upstream flow is difficult to match amongst various model scales. As a result, such a study on a surface mounted bluff body in turbulent boundary layer flow may not be able to separate the influence of  $Re$  from the influence of missing large-scale turbulence.

To isolate the effect of  $Re$  and focus on only the separated shear layer at the rounded edge, a study using 2D bluff body, such as a blunt plate with rounded edges, is proposed. The body would be suspended in the middle of the tunnel, rather than be surface mounted, and would be tested in smooth flow to remove the need to scale the upstream turbulence. Additionally, the plate would need to be sufficiently elongated, such that the reattachment of the separated flow is observable and wake effects are minimized. Subsequent pressure measurements along the middle of the plate along with flow visualization may shed light on  $Re$  effects.



### 6.3.5 Application of proposed limit to high-rise buildings

The proposed limit on edge radii is presented as a radii normalized by building height since height is related to the length of the separation bubble. For high-rise buildings, plan dimensions are of greater influence on the spatial distribution of pressure coefficients (Liu et al., 2019). Thus, in order to apply the proposed limit of  $R/H=1.3\%$  to high-rise buildings, the proposed limit should be redefined using a plan dimension, rather than the building height.

A possible way to translate the proposed limit to a high-rise building model, is by using location of the stagnation point relative to the separation point,  $S$  defined in Figure 6-1, as the characteristic length. For a low-rise buildings,  $S$  is invariant with upstream turbulence, and is approximately  $0.35H$  on the windward wall (Akon & Kopp, 2016). For high-rise buildings, the stagnation point is typically in the middle of the wall breadth  $b$ , i.e.  $S = b/2$ .

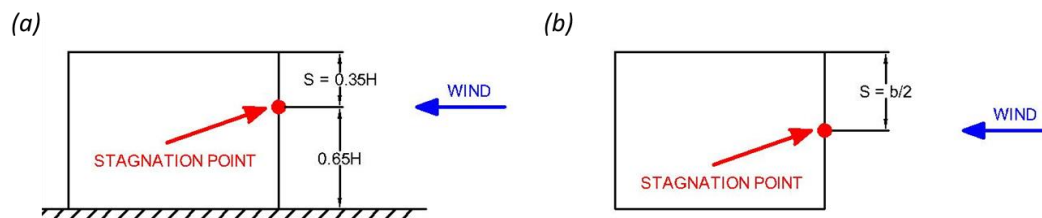


**Figure 6-1 Distance of stagnation point to separation point  $S$  on (a) a low-rise building (side view) and (b) a high-rise building (plan view).**

By redefining the limit  $R/H = 1.3\%$ , using  $S$ , the limit would become

$$\frac{R}{S} = \frac{R}{\frac{b}{2}} \rightarrow \frac{R}{b} = 1.9\% \quad (6-1)$$

However, the validity of this conversion will need to be investigated through additional wind tunnel testing of a high-rise model with varying radii.

## References

- Achenbach, E. (1968). Distribution of local pressure and skin friction around a circular cylinder in cross flow up to  $Re = 5 \times 10^6$ . *Journal of Fluid Mechanics*, 34, 625-639.
- Akon, A., & Kopp, G. (2016). Mean pressure distribution and reattachment lengths for roof-separation bubbles on low-rise buildings. *Journal of Wind Engineering and Industrial Aerodynamics*, 155, 115-125.
- American Society of Civil Engineers. (2012). *Wind Tunnel Testing for Buildings and Other Structures*. Reston: American Society of Civil Engineers.
- Arts, T., Boerrigter, H., Carbonato, M., & Charbonnier, J. (1994). *Measurement Techniques in Fluid Dynamics*. Von Karman Institute for Fluid Dynamics.
- Asghari Mooneghi, M., Irwin, P., & Chowdhury, A. G. (2016). Partial turbulence simulation method for predicting peak wind loads on small structures and building appurtenances. *Journal of Wind Engineering and Industrial Aerodynamics*, 157, 47-62.
- Banks, D., Meroney, R., Sarkar, P., Zhao, Z., & Wu, F. (2000). Flow visualization of conical vortices on flat roofs with simultaneous surface pressure measurement. *Journal of Wind Engineering and Industrial Aerodynamics*, 84, 65-84.
- Bearman, P. (1972). Some measurements of the distortion of turbulence approaching a two-dimensional bluff body. *Journal of Fluid Mechanics*, 53(3), 451-467.
- Bearman, P., & Morel, T. (1983). Effect of free stream turbulence on the flow around bluff bodies. *Progress in Aerospace Science*, 20, 97-123.
- Benedict, L., & Gould, R. (1996). Towards better uncertainty estimates for turbulence statistics. *Experiments in Fluids*, 22, 129-136.
- Cao, S. (2013). Strong Winds and Their Characteristics. In Y. Tamura, & A. Kareem, *Advanced Structural Wind Engineering* (pp. 1-26). Tokyo: Springer.

- Carassale, L., Freda, F., & Marrè-Brunenghi, M. (2014). Experimental investigation on the aerodynamic behavior of square cylinders with rounded corners. *Journal of Fluids and Structures*, *44*, 195-204.
- Castro, I., & Robins, A. (1977). The flow around a surface-mounted cube in uniform and turbulent streams. *Journal of Fluid Mechanics*, *79*, 307-335.
- Cherry, N., Hillier, R., & Latour, M. (1984). Unsteady measurements in separated and reattaching flow. *Journal of Fluid Mechanics*, *144*, 13-46.
- Coleman, H., & Steele, W. (2009). *Experimentation, Validation, and Uncertainty Analysis for Engineers*. New Jersey: John Wiley & Sons.
- Comminal, R., Serdeczny, M., Pedersen, D., & Spangenberg, J. (2019). Motion planning and numerical simulation of material deposition at corners in extrusion additive manufacturing. *Additive Manufacturing*, *29*.
- Cooper, K. (1986). The Effect of Front-Edge Rounding and Rear-Edge Shaping on the Aerodynamic Drag of Bluff Vehicles in Ground Proximity. *SAE Technical Paper*, 727-757.
- Dalley, S. (1996). Surface pressure spectra on a model of the Silsoe structures building and comparison with full-scale. *Journal of Wind Engineering and Industrial Aerodynamics*, *60*, 177-187.
- Delany, N., & Sorensen, N. (1953). *Low-speed drag of cylinders of various shapes*. Ames Aeronautical Laboratory. Moffett Field: National Advisory Committee for Aeronautics.
- Dong, X., Ding, J., & Jiao, C. (2019). Wind loads on flat roofs of a low-rise building with rounded leading edge. *Journal of the Chinese Institute of Engineers*, *42*(3), 264-277.
- Duthinh, D., Main, J., Gierson, M., & Phillips, B. (2018). Analysis of Wind Pressure Data on Components and Cladding of Low-Rise Buildings. *Journal of Structural Engineering*, *4*(1).

- Erwin, J. (1964). Experimental Techniques. In H. Hawthorne (Ed.), *Aerodynamics of Turbines and Compressors* (Vol. 10, pp. 167-269). Princeton, New Jersey: Princeton University Press.
- Flay, R. G. (2013). Bluff Body Aerodynamics. In Y. Tamura, & A. Kareem, *Advanced Structural Wind Engineering* (pp. 59-84). Tokyo, Japan: Springer.
- Fritz, W., Bienkiewicz, B., Cui, B., Flamand, O., Ho, T., Kikitsu, H., . . . Simiu, E. (2008). International Comparison of Wind Tunnel Estimates of Wind Effects on Low-Rise Buildings: Test-Related Uncertainties. *Journal of Structural Engineering*, *134*(12), 1887-1890.
- Garcey, W. (1956). *Wind-tunnel investigation of a number of total-pressure tubes at high angles of attack*. Washington: NACA.
- Gartshore, I. (1973). *The effects of free stream turbulence on the drag of rectangular two-dimensional prisms*. London: The Boundary Layer Wind Tunnel Laboratory.
- Gavanski, E., Gurley, K., & Kopp, G. (2016). Uncertainties in the estimation of local peak pressures on low-rise buildings by using the gumbel distribution fitting approach. *Journal of Structural Engineering*, *142*(11).
- Ghareghpapagh, B., Dolen, M., & Yaman, U. (2019). Investigation of variable bead widths in FFF Process. *29th International Conference on Flexible Automation and Intelligent Manufacturing (FAIM2019)*. Limerick.
- Gu, D., & Lim, H. (2012). Wind flow around rectangular obstacles and the effects of aspect ratio. *The Seventh International Colloquium on Bluff Boddy Aerodynamics and Applications*. Shanghai, China.
- Hillier, R., & Cherry, N. (1981). The effects of stream turbulence on separation bubbles. *Journal of Wind Engineering and Industrial Aerodynamics*, *8*, 49-58.
- Ho, T., Surry, D., Morrish, D., & Kopp, G. (2005). The UWO contribution to the NIST aerodynamic database for wind loads on low buildings: Part 1. Archiving format and

- basic aerodynamic data. *Journal of Wind Engineering and Industrial Aerodynamics*, 93, 1-30.
- Holmes, J. (2015). *Wind Loading of Structures*. Boca Raton: CRC Press.
- Hong, E. (2017). *Wall pressure coefficients for Low- to High-Rise Buildings*. Master's Thesis, The University of Western Ontario.
- Hoxey, R., Reynolds, A., Richardson, G., Robertson, A., & Short, J. (1998). Observations of Reynolds number sensitivity in the separated flow region on a bluff body. *Journal of Wind Engineering and Industrial Aerodynamics*, 73, 231-249.
- Hoxey, R., Robertson, A., Richardson, G., & Short, J. (1997). Correction of wind-tunnel pressure coefficients for Reynolds number effect. *Journal of Wind Engineering and industrial Aerodynamics*, 547-555.
- Hudy, L.M.; Naguib, A.M.; Humphreys, W.M.;. (2003). Wall-pressure-array measurements beneath a separating/reattaching flow region. *Physics of Fluids*, 15, 706-716.
- Irwin, P. A. (2008). Bluff body aerodynamics in wind engineering. *Journal of Wind Engineering and Industrial Aerodynamics*, 96, 701-712.
- Kim, Y., & Tamura, Y. (2014). Effects of Incident Flows on Wind Loads and Their Combinaitons on a Low-Rise Building Immersed in a Long Upstream Fetch. *Journal of Structural Engineering*, 140(5).
- Kiya, M., & Sasaki, K. (1983). Free-stream turbulence effects on a separation bubble. *Journal of Wind Engineering and Industrial Aerodynamics*, 14, 375-386.
- Kopp, G. (2013). Wind Loads on Building Components and Cladding. In Y. Tamura, & A. Kareem, *Advanced Structural ind Engineering* (pp. 177-198). Tokyo: Springer Japan.
- Kopp, G., & Morrison, M. (2018). Component and Cladding Wind Loads for Low-Slope Roofs on Low-Rise Buildings. *Journal of Structural Engineering*, 144(4).

- Kopp, G., Surry, D., & Mans, C. (2005). Wind effects of parapets on low buildings: Part 1. Basic aerodynamics and local loads. *Journal of Wind Engineering and Industrial Aerodynamics*, 93, 817-841.
- Lander, D., Letchford, C., Amitay, M., & Kopp, G. (2016). Influence of the bluff body shear layers on the wake of a square prism in a turbulent flow. *Physical Review Fluids*, 1.
- Larose, G., & D'Auteuil. (2006). On the Reynolds number sensitivity of the aerodynamics of bluff bodies with sharp edges. *Journal of Wind Engineering and Industrial Aerodynamics*, 94, 365-376.
- Lee, I., & Sung, H. (2001). Characteristics of wall pressure fluctuations in separated and reattaching flows over a backward-facing step: Part I Time-mean statistics and cross-spectral analyses. *Experiments in Fluids*, 262-272.
- Lieblein, J. (1974). *Efficient Methods of Extreme-Value Methodology*. Washington, D.C.: U.S. Department of Commerce National Bureau of Standards.
- Lim, H., Castro, I., & Hoxey, R. (2007). Bluff bodies in deep turbulent boundary layers: Reynolds-number issues. *Journal of Fluid Mechanics*, 571, 97-118.
- Liu, Y., Kopp, G., & Chen, S. (2019). Effects of plan dimensions on gust wind loads for high-rise buildings. *Journal of Wind Engineering and Industrial Aerodynamics*, 194.
- Liu, Z., Prevatt, D., Aponte-Bermudez, L., Gurley, K., Reinhold, T., & Akins, R. (2009). Field measurement and wind tunnel simulation of hurricane wind loads on a single family dwelling. *Engineering Structures*, 31, 2265-2274.
- Mahmood, M. (2011). Experiments to study turbulence and flow past a low-rise building at oblique incidence. *Journal of Wind Engineering and Industrial Aerodynamics*, 560-572.
- Mans, C., Ho, T., Surry, D., & Kopp, G. (2002). *The Factory Mutual Sensitivity Study*. Engineering Science Research Report, The University of Western Ontario, Boundary Layer Wind Tunnel Laboratory, London.

- Morrison, M., & Kopp, G. (2018). Effects of turbulence intensity and scale on surface pressure fluctuations on the roof of a low-rise building in the atmospheric boundary layer. *Journal of Wind Engineering and Industrial Aerodynamics*, 183, 140-151.
- Ota, T., Asano, Y., & Okawa, J. (1981). Reattachment length and transition of the separated flow over the blunt flat plates. *Bulletin of the Japanese Society of Mechanical Engineers*, 24, 941-947.
- Quiroga Diaz, P. (2006). *Uncertainty Analysis of Surface Pressure Measurements on Low-Rise Buildings*. London: The University of Western Ontario.
- Richardson, G. M., Roberston, A. P., Hoxey, R. P., & Surry, D. (1990). Full-scale and model investigations of pressures on an industrial/agricultural building. *Journal of Wind Engineering and Industrial Aerodynamics*, 1053-1062.
- Robertson, A. (1991). Effect of eaves detail on wind pressures over an industrial building. *Journal of Wind Engineering and Industrial Aerodynamics*, 38, 325-333.
- Saathoff, P., & Melbourne, W. (1997). Effects of free-stream turbulence on surface pressure fluctuations in separation bubble. *Journal of Fluid Mechanics*, 337, 1-24.
- Schewe, G. (2001). Reynolds-number effects in flow around more-or-less bluff bodies. *Journal of Wind Engineering and Industrial Aerodynamics*, 89, 1267-1289.
- Shao, S., Stathopoulos, T., Yang, Q., & Tian, Y. (2018). Wind Pressures on 4:12-Sloped Hip Roofs of L- and T-Shaped Low-Rise Buildings. *Journal of Structural Engineering*, 144(7).
- Shaw, R. (1960). Influence of hole dimension on static pressure measurements. *Journal of Fluid Mechanics*, 7(2), 550-564.
- Stathopoulos, T., & Surry, D. (1983). Scale effects in wind tunnel testing of low buildings. *Journal of Wind Engineering and Industrial Aerodynamics*, 13, 313-326.

- Stuart, A., & Ord, J. (1994). *Kendall's Advanced Theory of Statistics* (6th ed., Vol. 1). New York: John Wiley & Sons Inc.
- Surry, D., & Lin, J. (1995). The effect of surroundings and roof corner geometric modifications on roof pressures on low-rise buildings. *Journal of Wind Engineering and Industrial Aerodynamics*, 58, 113-138.
- Surry, D., Sinno, R. R., Nail, B., Ho, T., Farquhar, S., & Kopp, G. A. (2007). Structurally Effective Static Wind Loads for Roof Panels. *Journal of Structural Engineering*, 871-885.
- Taylor, Z., Palombi, E., Gurka, R., & Kopp, G. (2010). Features of the turbulent flow around symmetric elongated bluff bodies. *Journal of Fluids and Structures*, 27, 250-265.
- Tieleman, H. (2003). Wind tunnel simulation of wind loading on low-rise structures: a review. *Journal of Wind Engineering and Industrial Aerodynamics*, 91, 1627-1649.
- Tieleman, H., Reinhold, T., & Hajj, M. (2001). Detailed simulation of pressures in separated/reattached flows. *Journal of Wind Engineering and Industrial Aerodynamics*, 1657-1670.
- Tieleman, H., Surry, D., & Lin, J. (1994). Characteristics of mean and fluctuating pressure coefficients under corner (delta wing) vortices. *Journal of Wind Engineering and Industrial Aerodynamics*, 263-275.
- Turbulent Flow Instrumentation. (n.d.). *Cobra Probe Catalogue*. Retrieved July 20, 2019, from Turbulent Flow Instrumentation Web site:  
[https://www.turbulentflow.com.au/Downloads/Cat\\_CobraProbe.pdf](https://www.turbulentflow.com.au/Downloads/Cat_CobraProbe.pdf)
- van Hinsberg, N., Schewe, G., & Jacobs, M. (2017). Experiments on the aerodynamic behaviour of square cylinders with rounded corners at Reynolds numbers up to 12 million. *Journal of Fluids and Structures*, 74, 214-233.

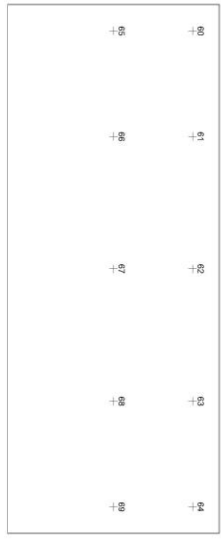
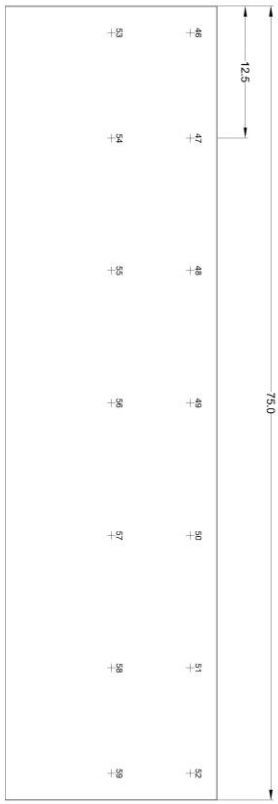
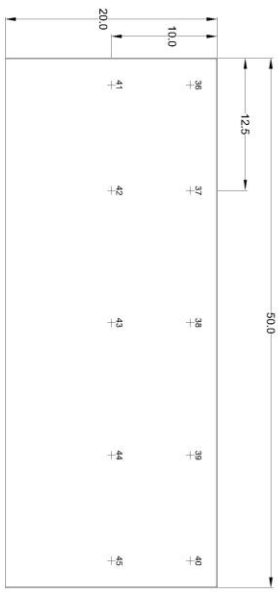


- Wang, X., & Gu, M. (2015). Experimental investigation of Reynolds number effects on 2D rectangular prisms with various side ratios and rounded corners. *Wind and Structures*, 21(2), 183-202.
- Wheeler, A., & Ganji, A.R. (1996). *Introduction to Engineering Experimentation*. New Jersey: Prentice-Hall.
- White, F. (2009). *Fluid Mechanics* (7th ed.). New York: McGraw -Hill.
- Wu, C., & Kopp, G. (2018). A quasi-steady model to account for the effects of upstream turbulence characteristics on pressure fluctuation on a low-rise building. *Journal of Wind Engineering and Industrial Aerodynamics*, 338-357.
- Wu, F., & Sakar, P. (2006). Bivariate Quasi-Steady Model for Prediction of Roof Corner Pressures. *Journal of Aerospace Engineering*, 19(1), 29-37.
- Wu, F., Sarkar, P., Mehta, K., & Zhao, Z. (2001). Influence of incident wind turbulence on pressure fluctuations near flat-roof corners. *Journal of Wind Engineering and Industrial Aerodynamics*, 89, 403-420.

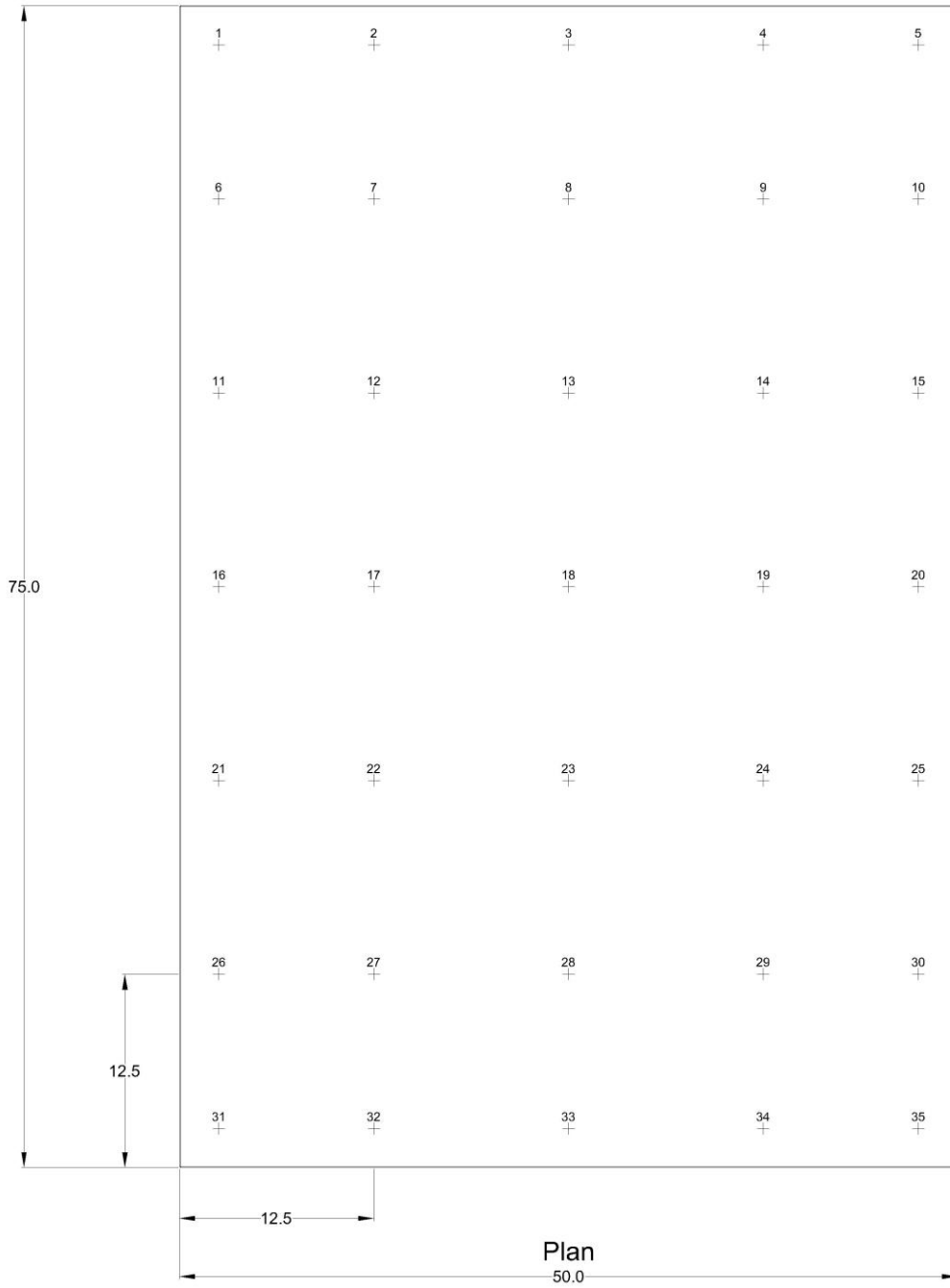
# Appendices

## Appendix A: Tap Layouts

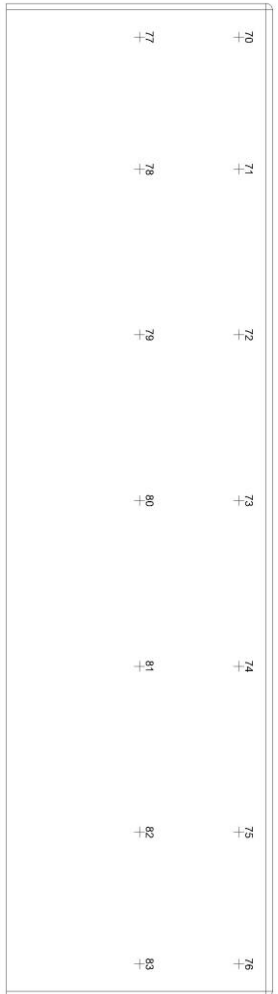
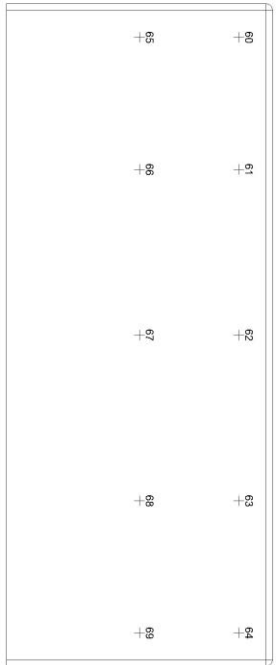
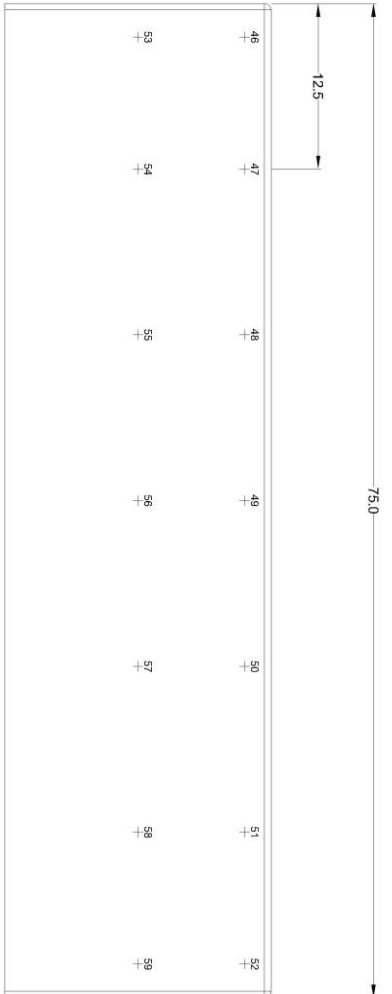
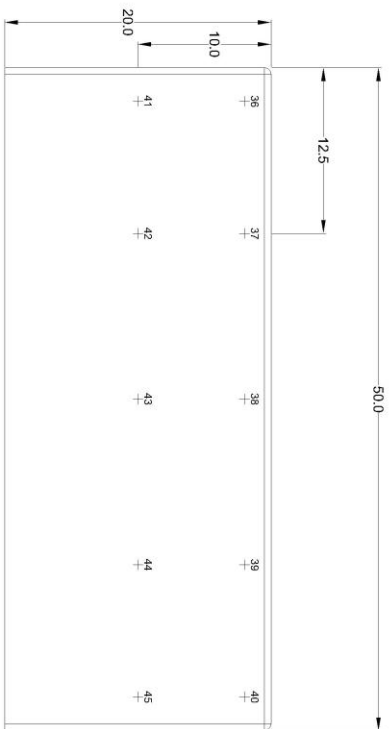
1:200 Model	0.3% Radius (R=0.0635mm)
All Dimensions in mm	



1:200 Model	0.3% Radius (R=0.0635mm)
	All Dimmensions in mm



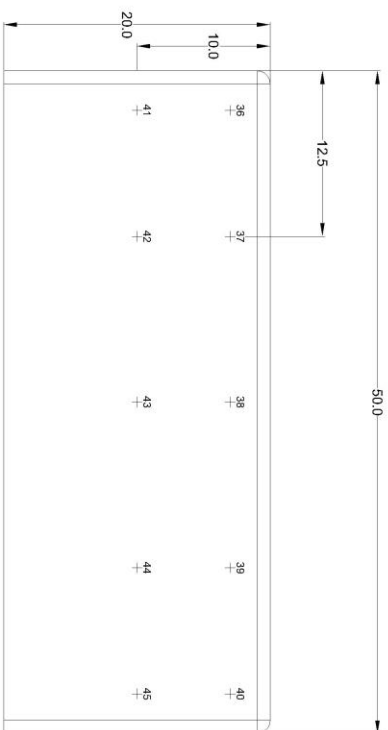
<b>1:200 Model</b>	<b>2.5% Radius (R=0.5mm)</b>
All Dimensions in mm	



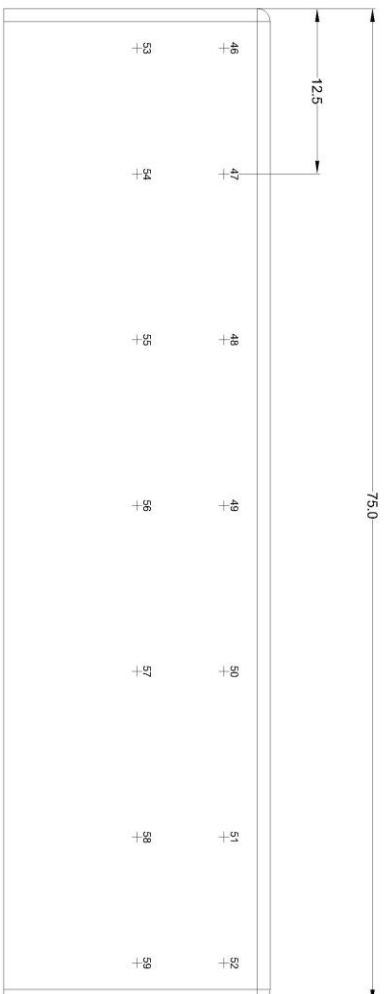
1:200 Model	2.5% Radius (R=0.5mm)
	All Dimmensions in mm



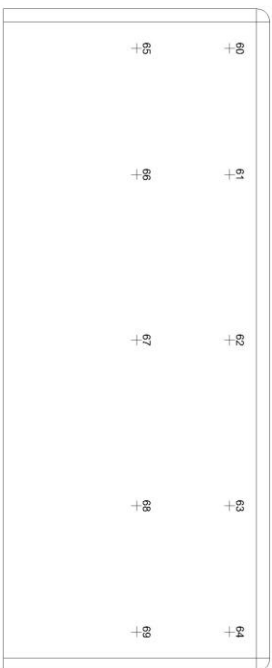
<b>1:200 Model</b>	<b>5% Radius (R=1mm)</b>
<b>All Dimensions in mm</b>	



North Elevation



East Elevation

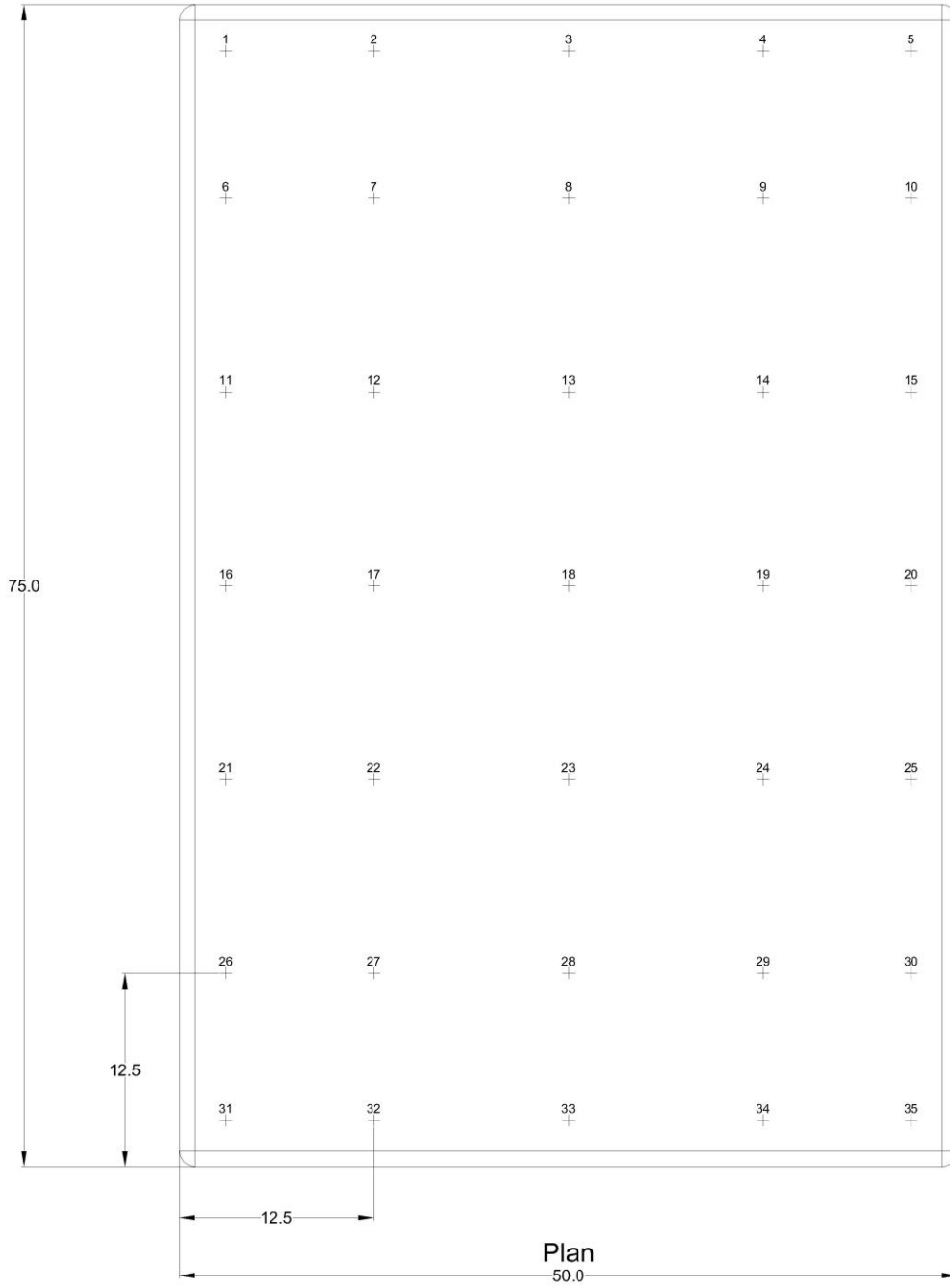


South Elevation

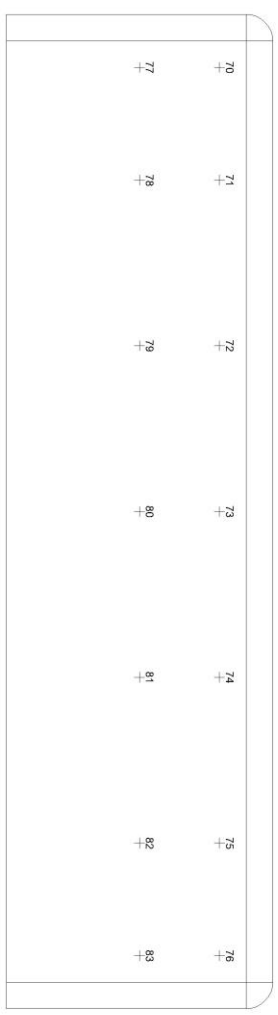
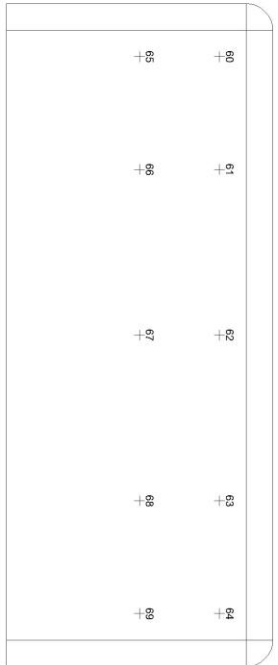
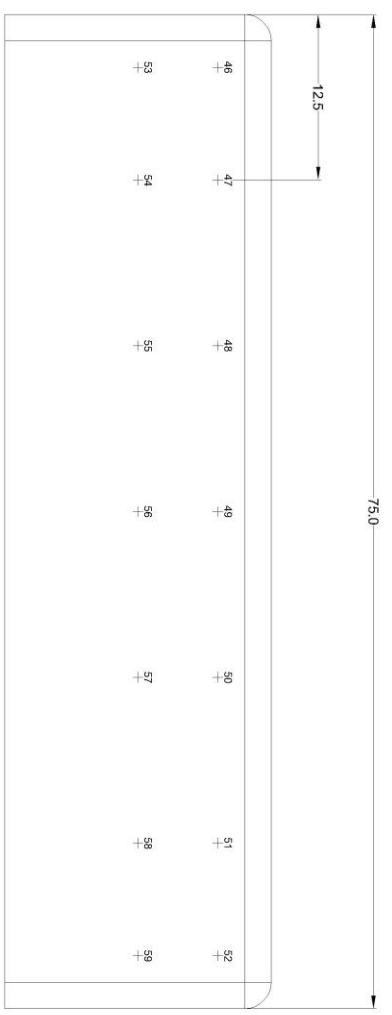
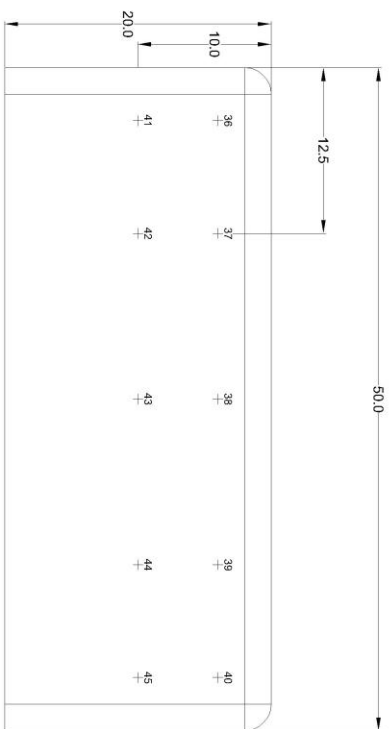


West Elevation

1:200 Model	5% Radius (R=1mm)
	All Dimmensions in mm

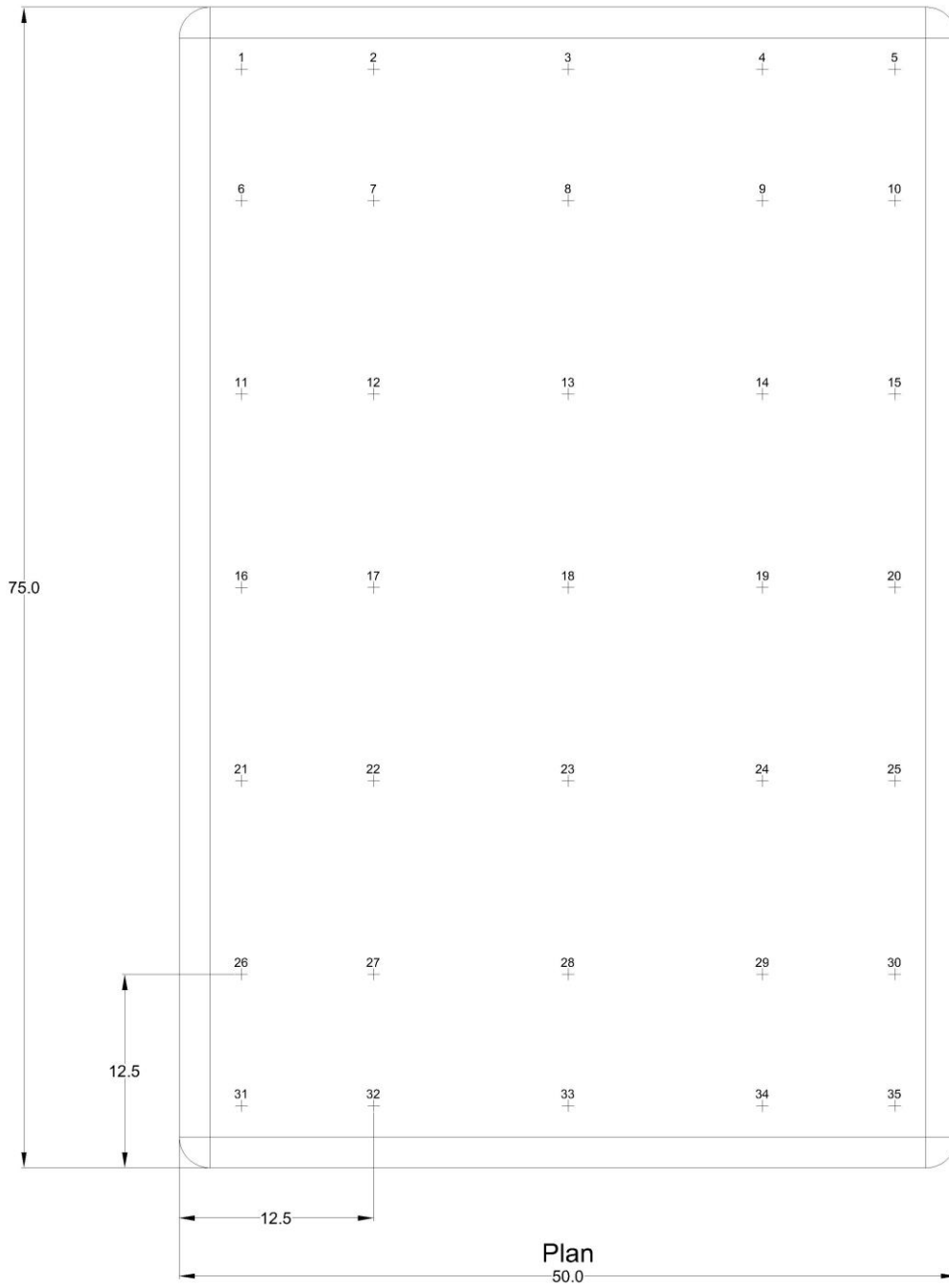


<b>1:200 Model</b>	<b>10% Radius (R=2mm)</b>
All Dimensions in mm	

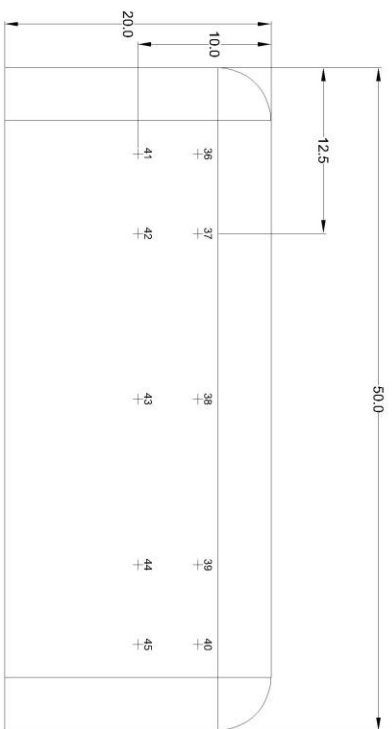




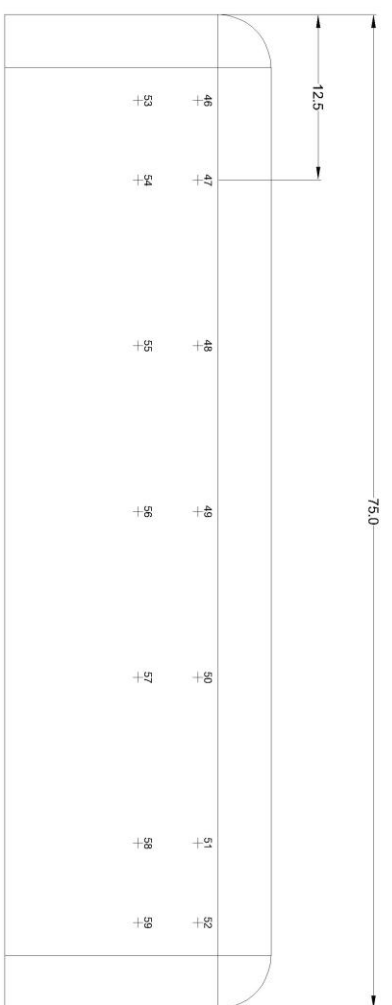
1:200 Model	10% Radius (R=2mm)
	All Dimmensions in mm



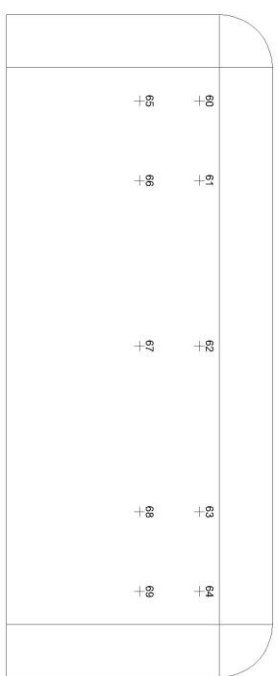
<b>1:200 Model</b>	20% Radius (R=4mm)
All Dimensions in mm	



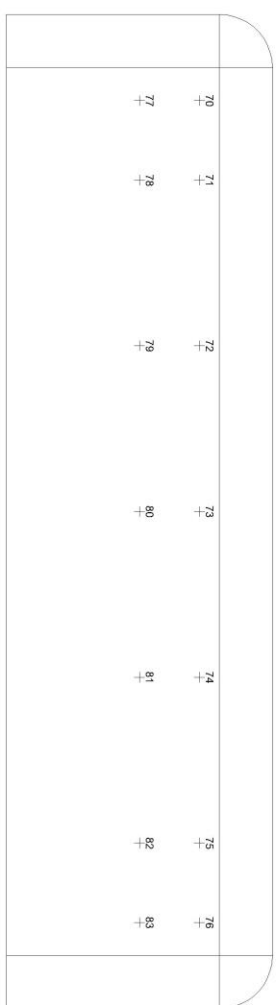
North Elevation



East Elevation

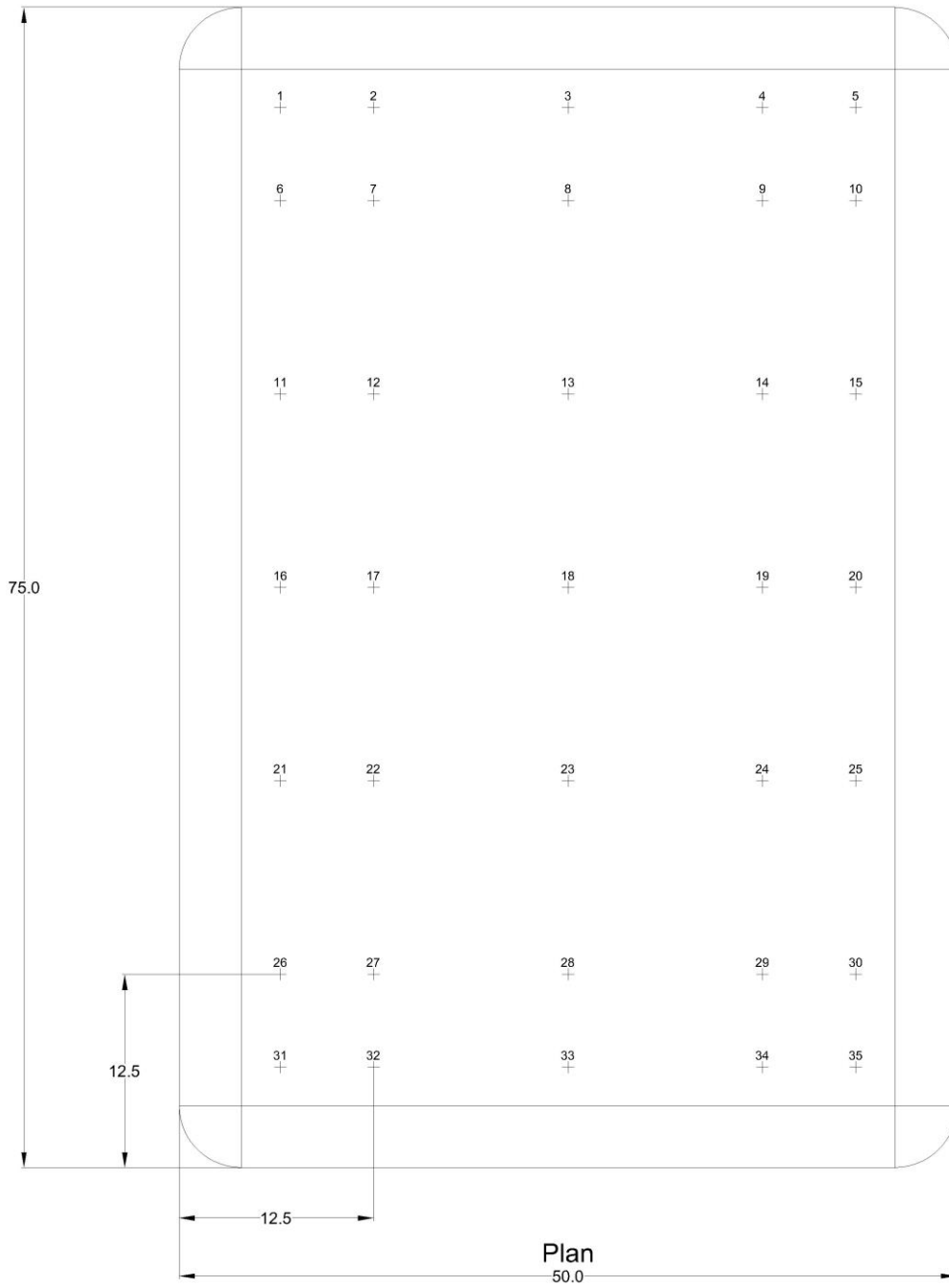


South Elevation

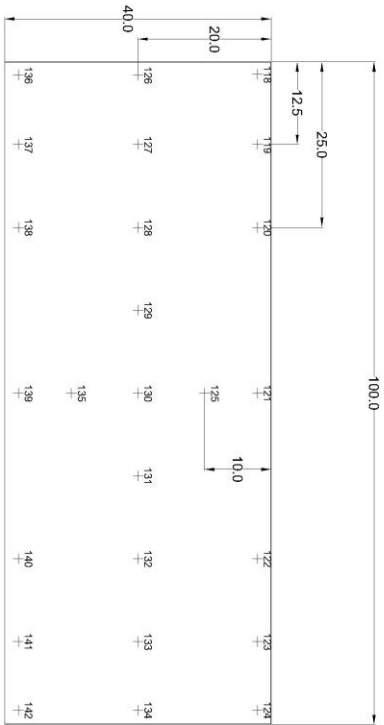


West Elevation

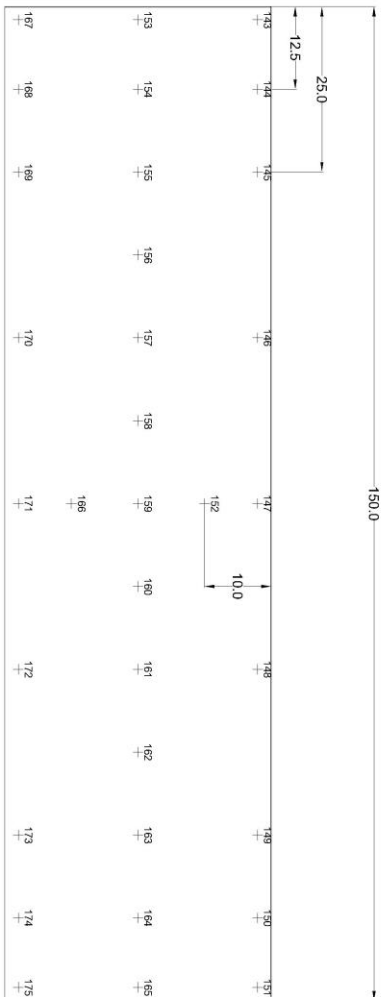
1:200 Model	20% Radius (R=4mm)
	All Dimmensions in mm



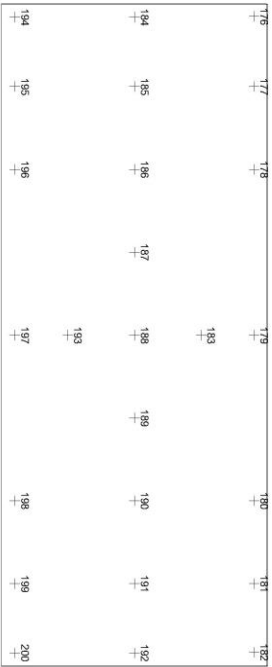
<b>1:100 Model</b>	<b>0.3% Radius (R=0.127mm)</b>
<b>All Dimensions in mm</b>	



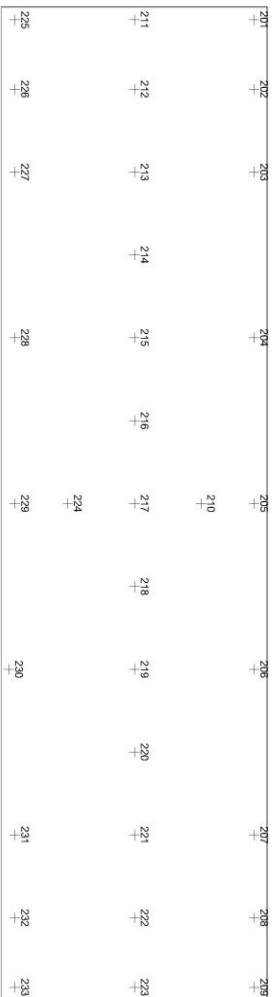
North Elevation



East Elevation

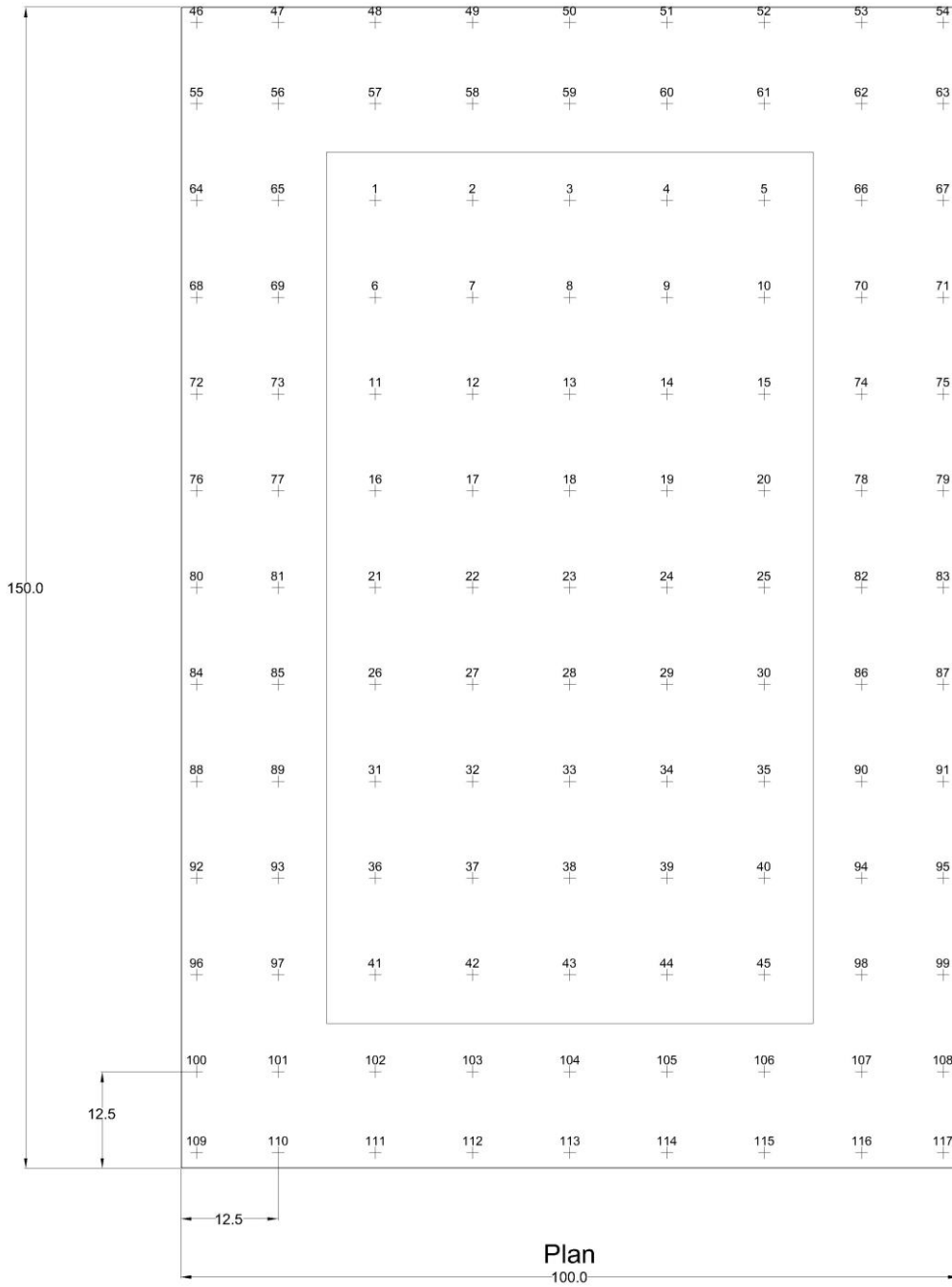


South Elevation

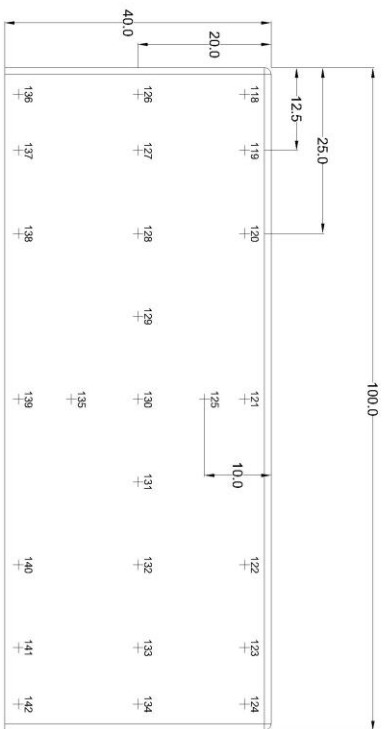


West Elevation

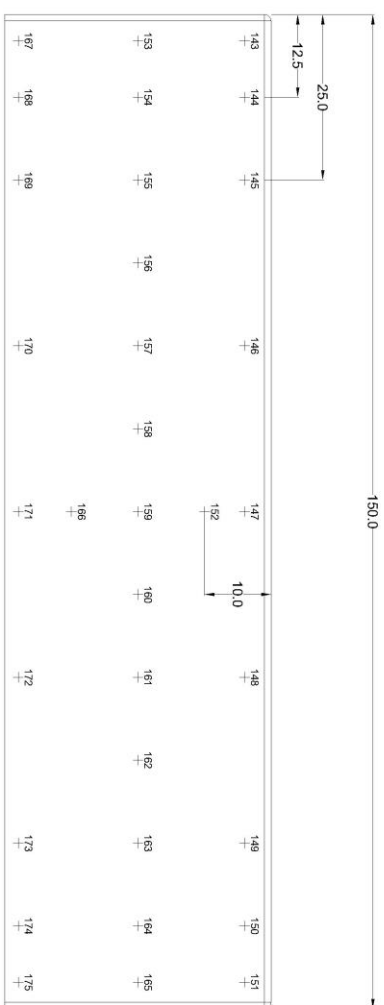
1:100 Model	0.3% Radius (R=0.127mm)
	All Dimmensions in mm



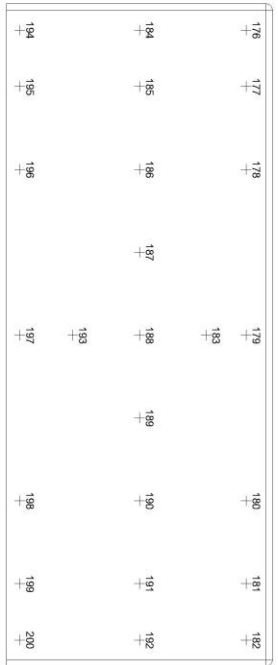
**1:100 Model**  
 2.5% Radius (R=1mm)  
 All Dimensions in mm



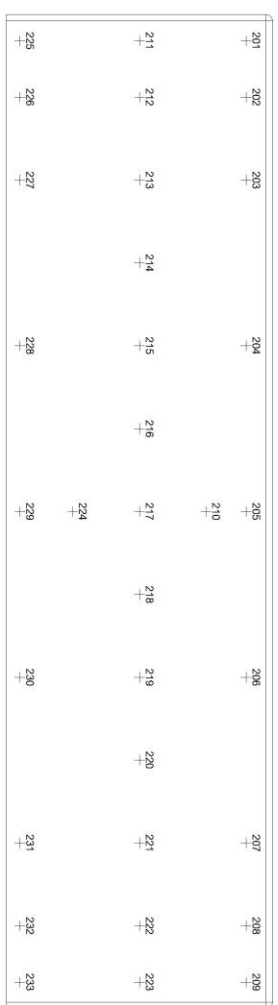
North Elevation



East Elevation

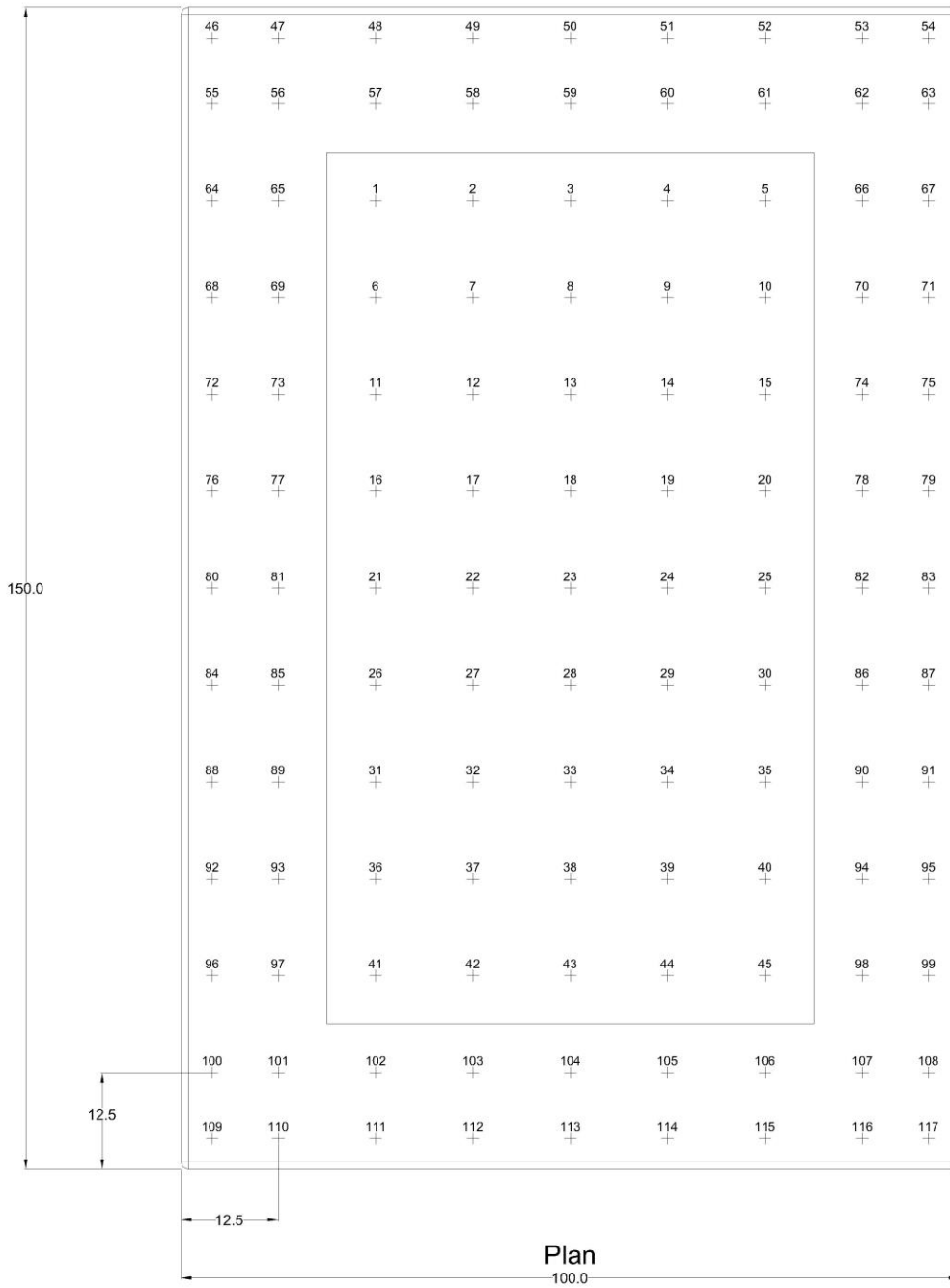


South Elevation

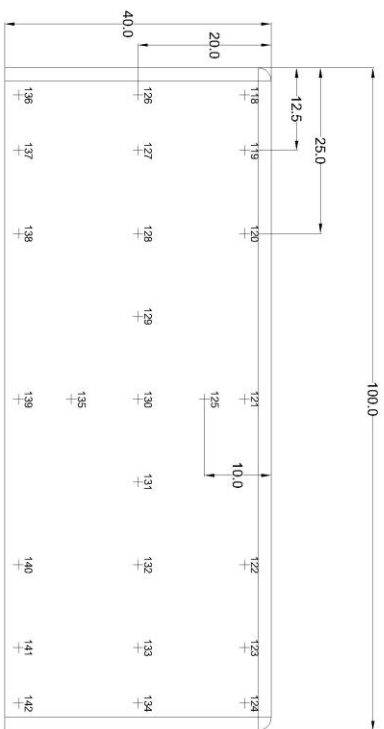


West Elevation

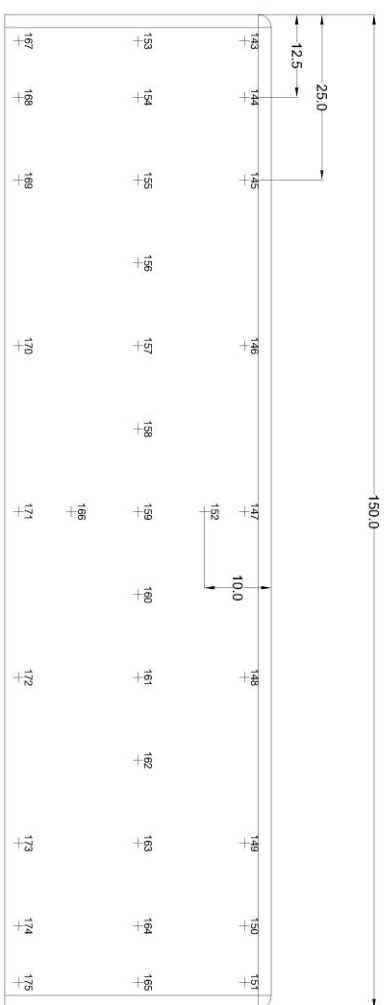
1:100 Model	2.5% Radius (R=1mm)
	All Dimmensions in mm



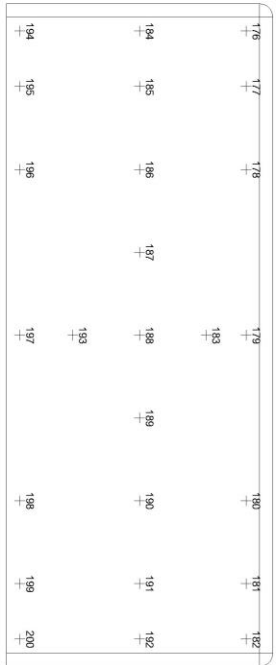
<b>1:100 Model</b>	<b>5% Radius (R=2mm)</b>
All Dimensions in mm	



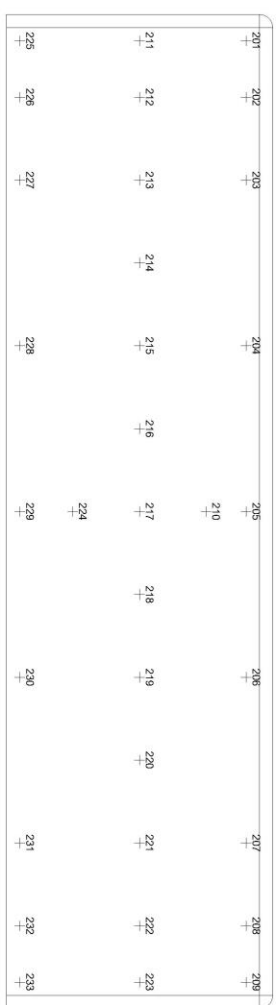
North Elevation



East Elevation



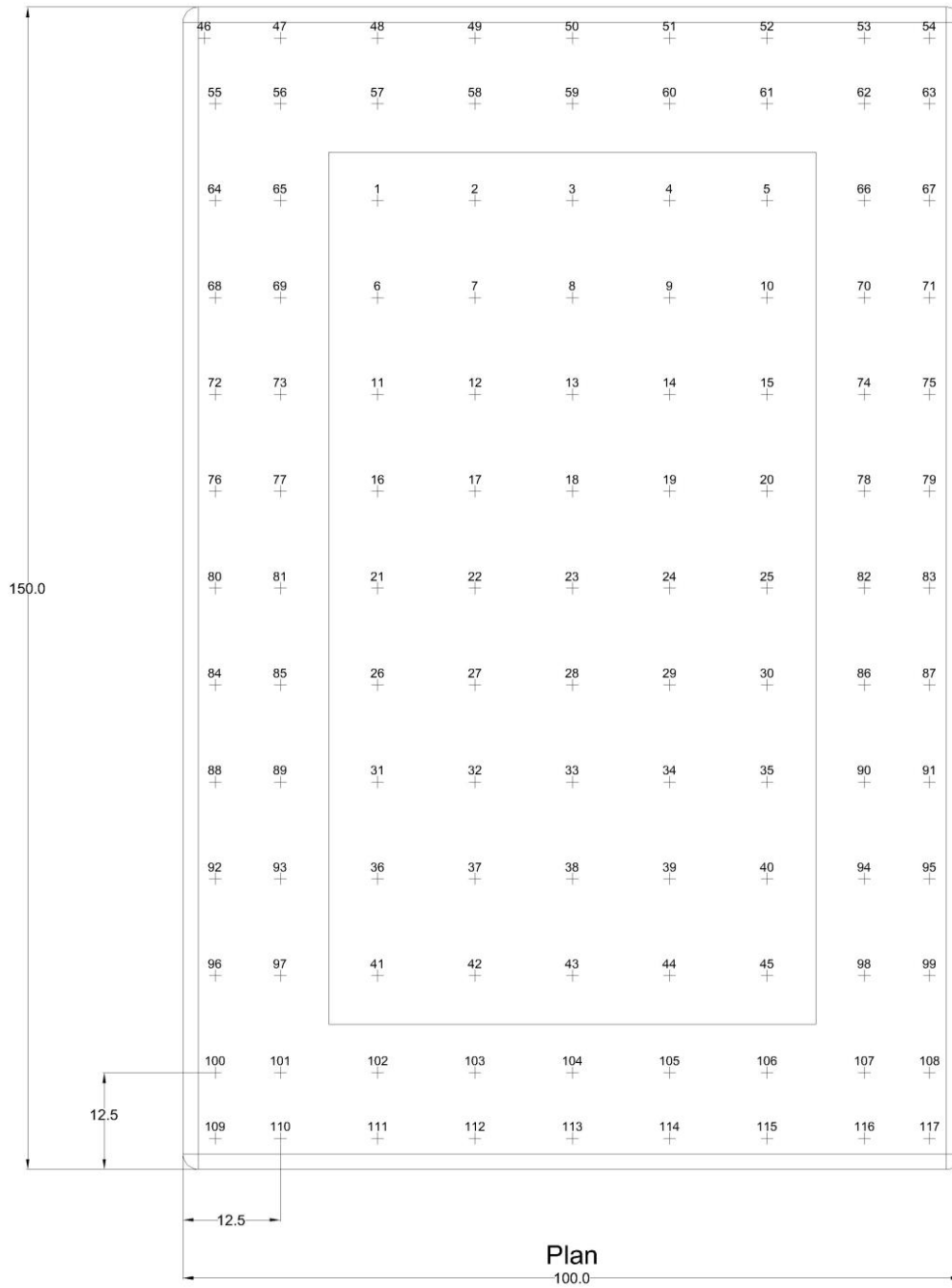
South Elevation



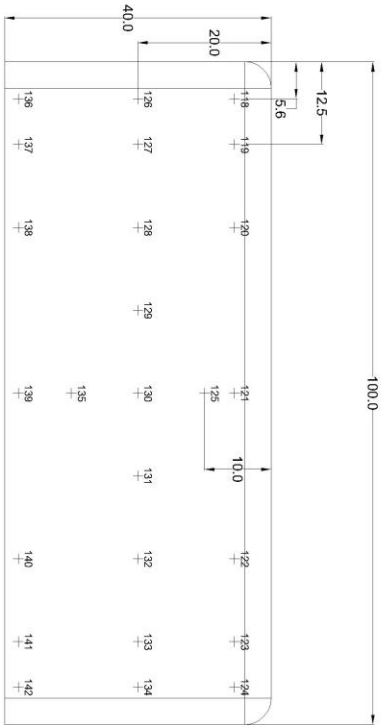
West Elevation



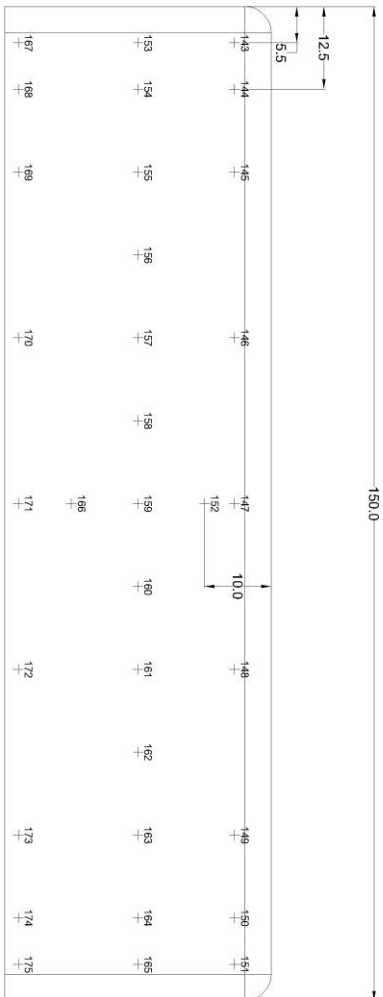
1:100 Model	5% Radius (R=2mm)
	All Dimmensions in mm



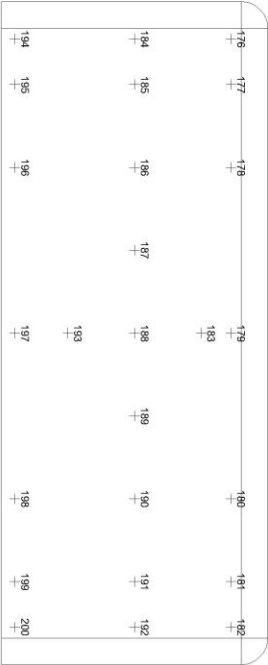
**1:100 Model**  
 10% Radius (R=4mm)  
 All Dimensions in mm



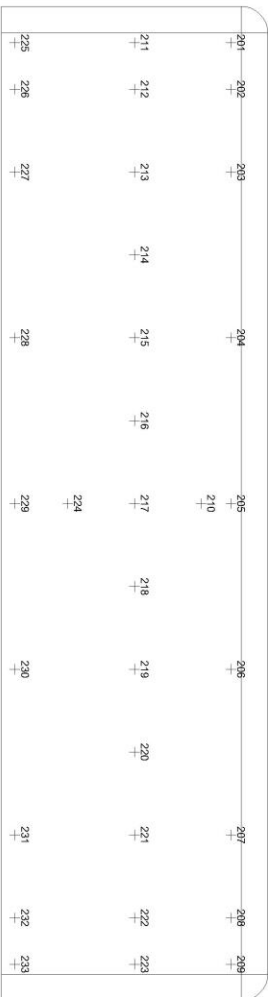
North Elevation



East Elevation

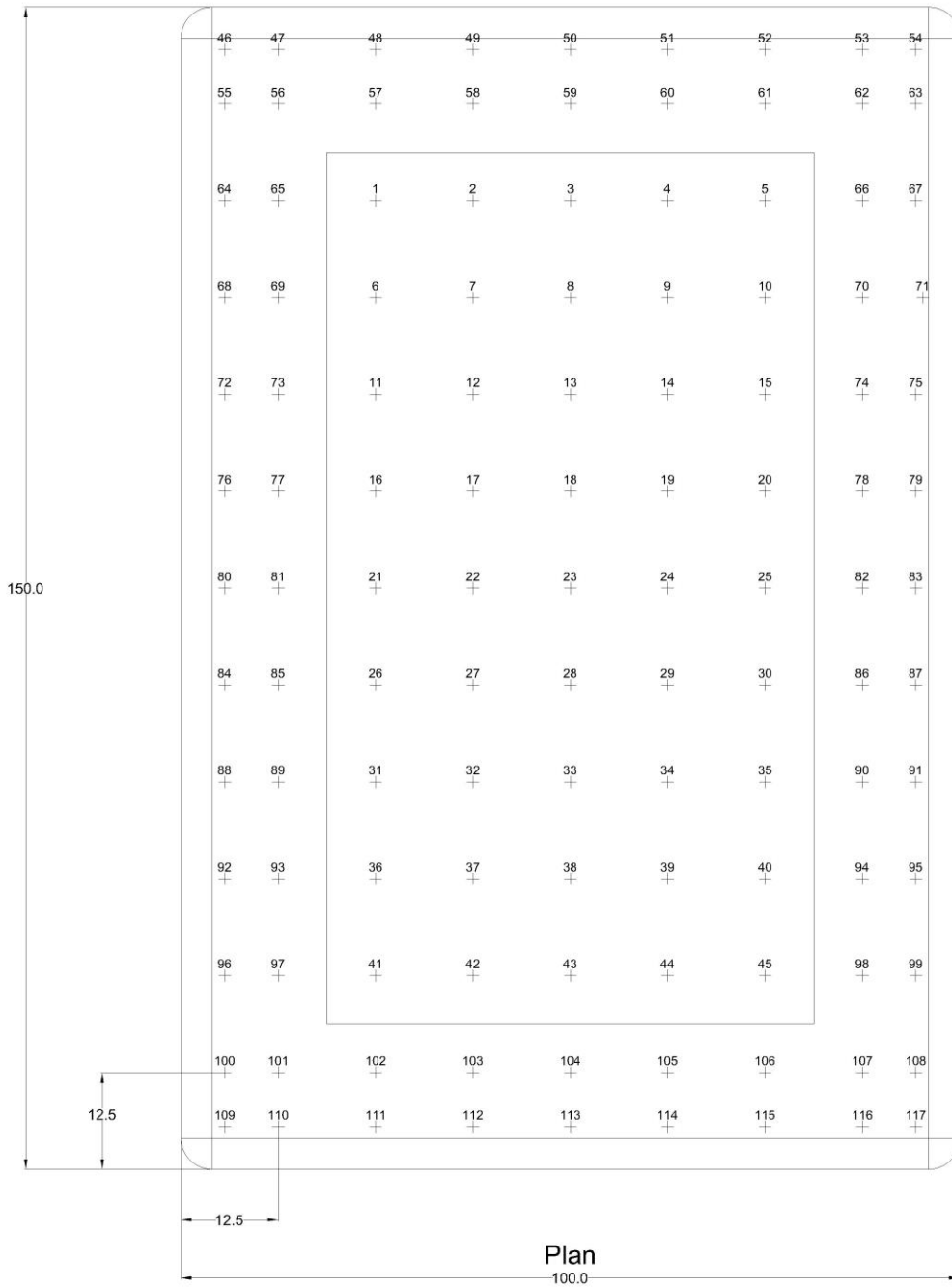


South Elevation

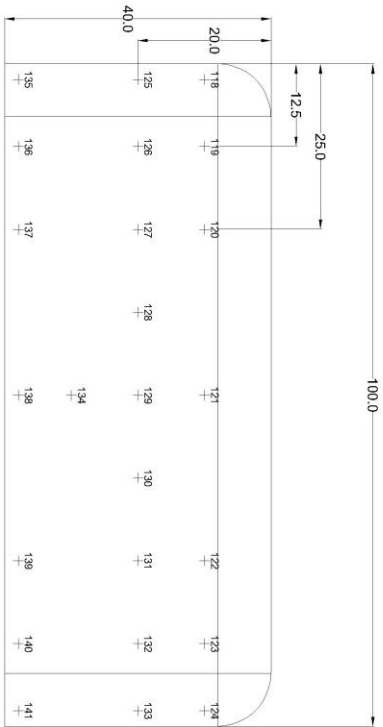


West Elevation

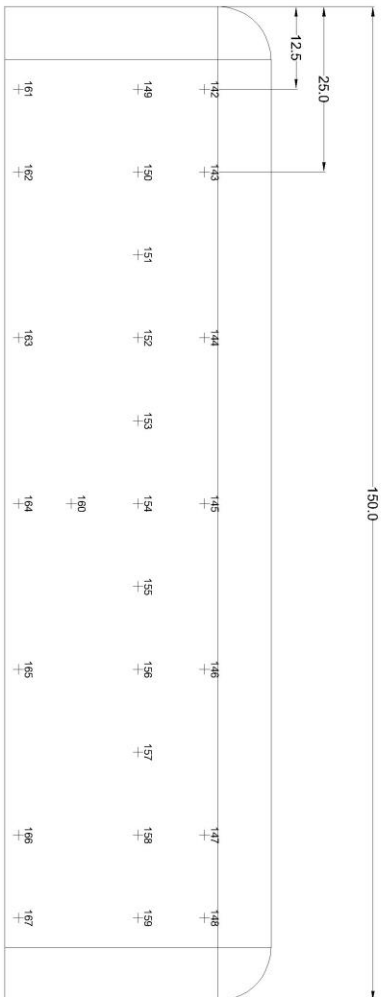
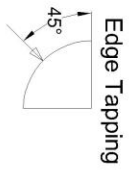
1:100 Model	10% Radius (R=4mm)
	All Dimmensions in mm



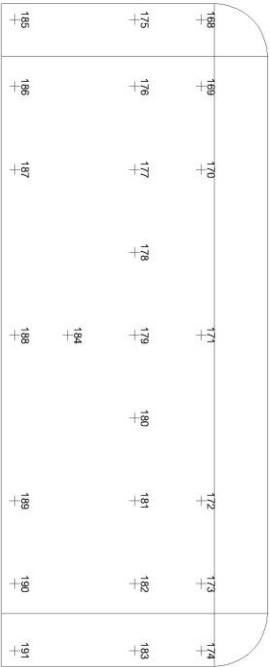
<b>1:100 Model</b>	20% Radius (R=6mm)
	All Dimensions in mm



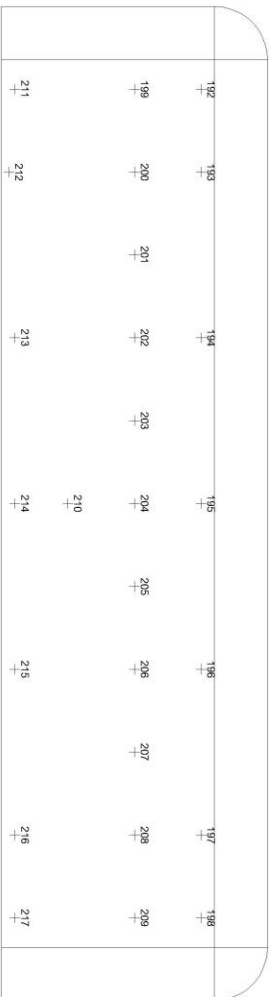
North Elevation



East Elevation



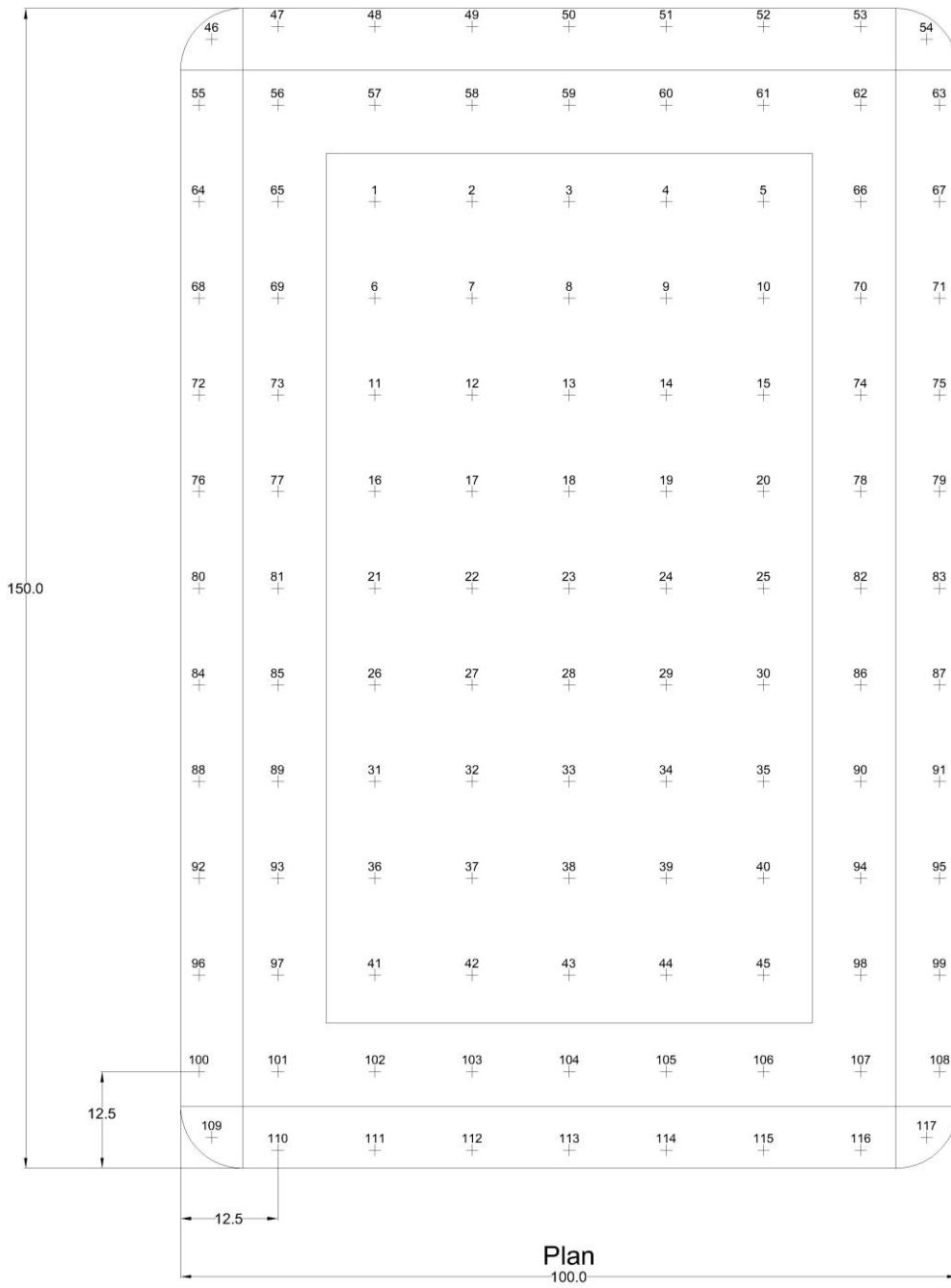
South Elevation



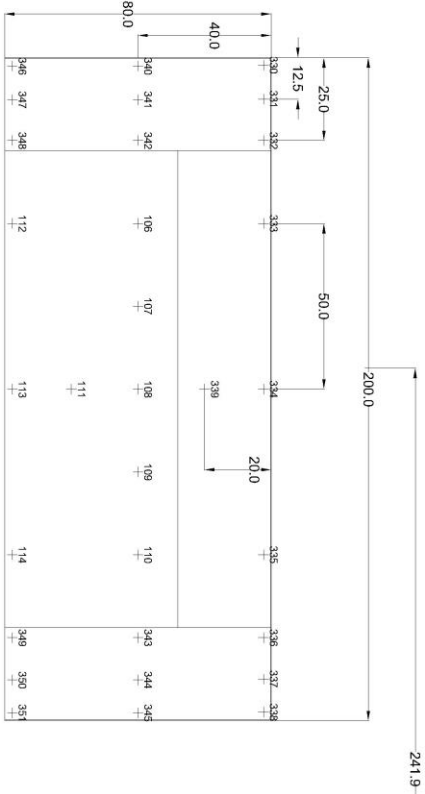
West Elevation

1:100 Model	20% Radius (R=8mm)
	All Dimmensions in mm

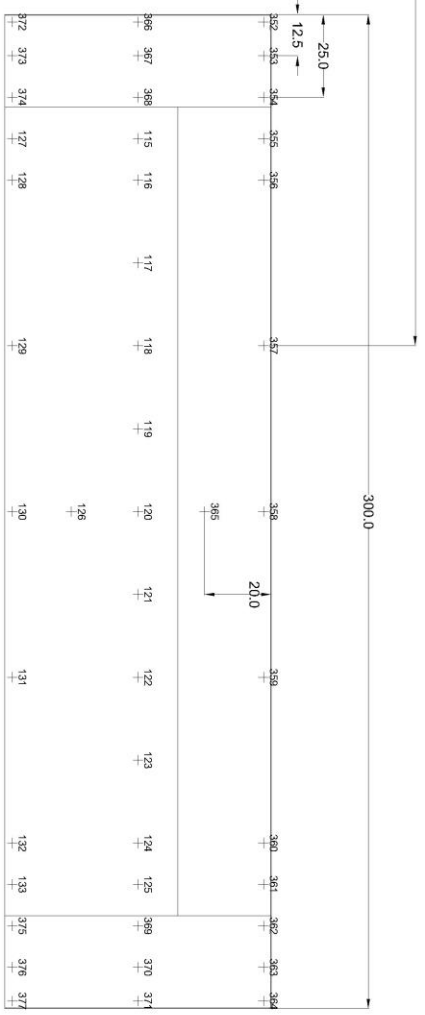
Edge Tapping



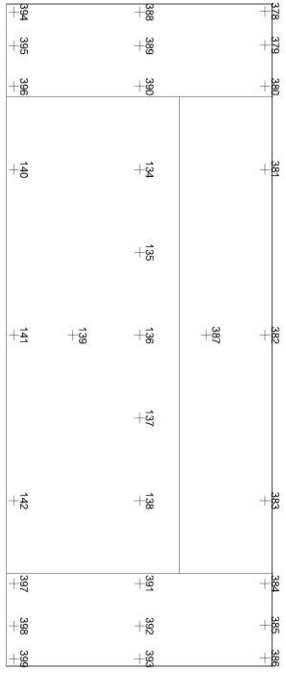
<b>1:50 Model</b>	<b>0.3% Radius (R=0.254mm)</b>
All Dimensions in mm	



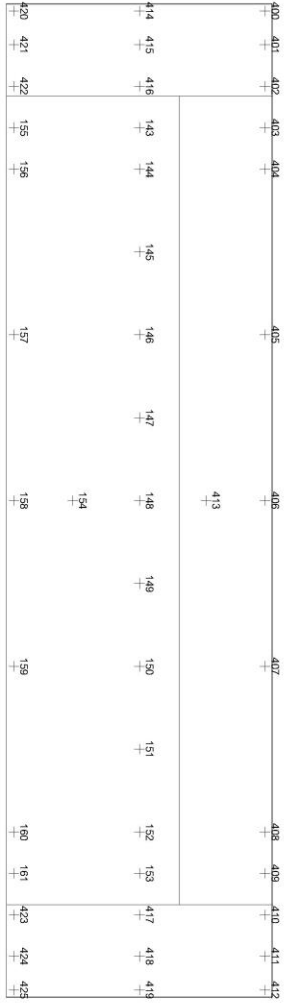
North Elevation



East Elevation

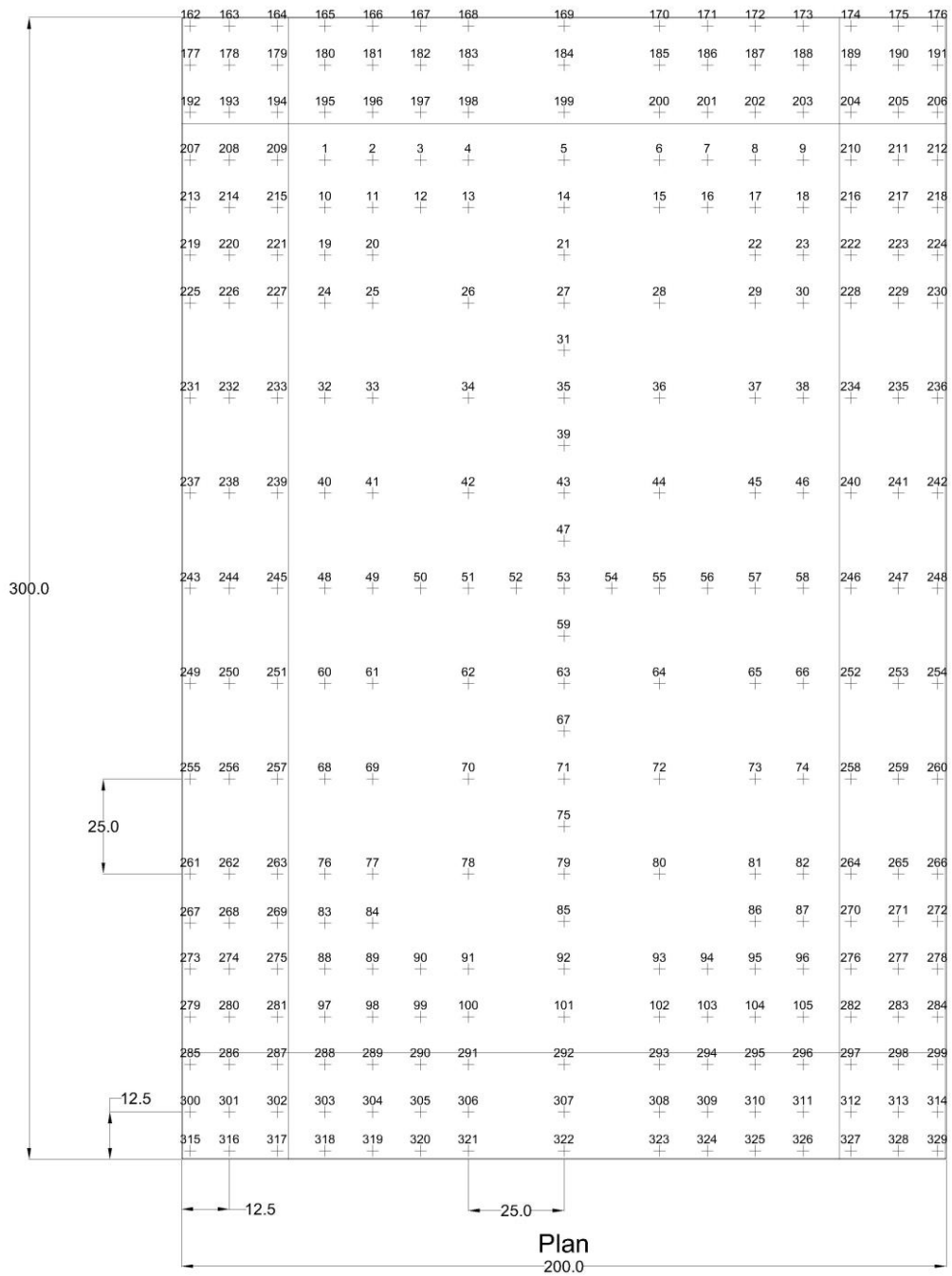


South Elevation

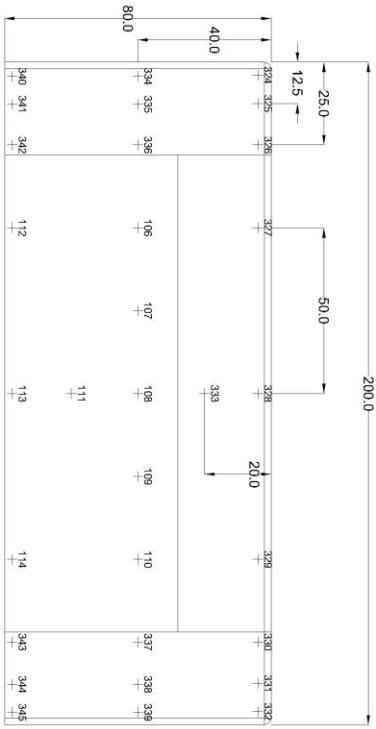


West Elevation

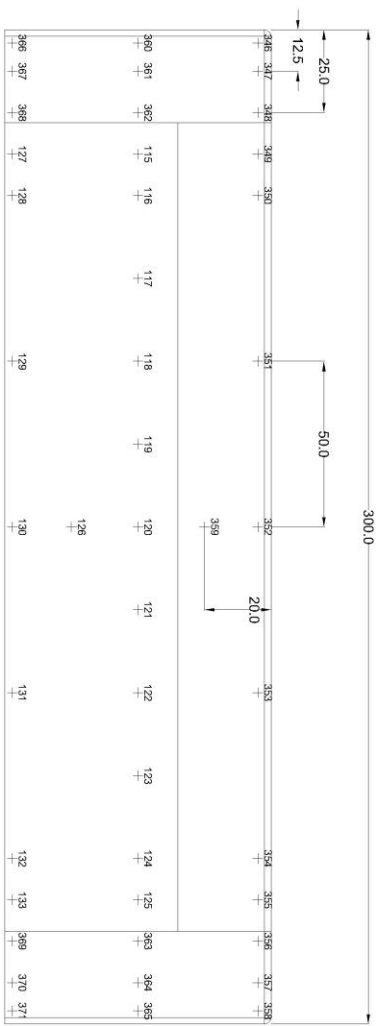
1:50 Model	0.3% Radius (R=0.254mm)
	All Dimmensions in mm



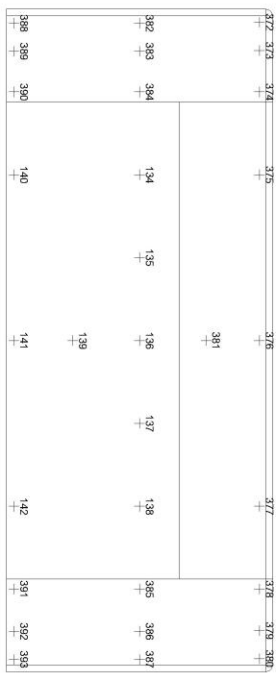
**1:50 Model**  
 2.5% Radius (R=2mm)  
 All Dimensions in mm



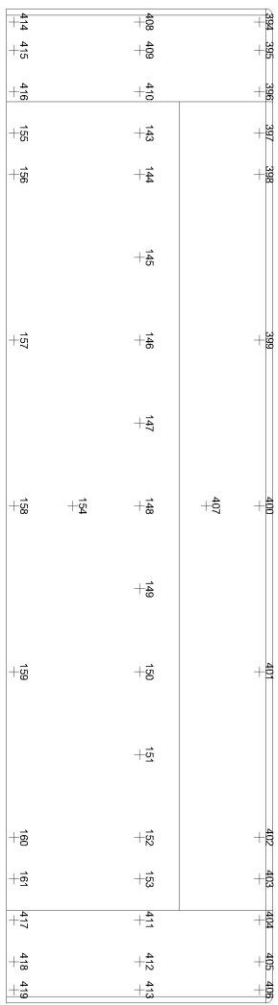
North Elevation



East Elevation



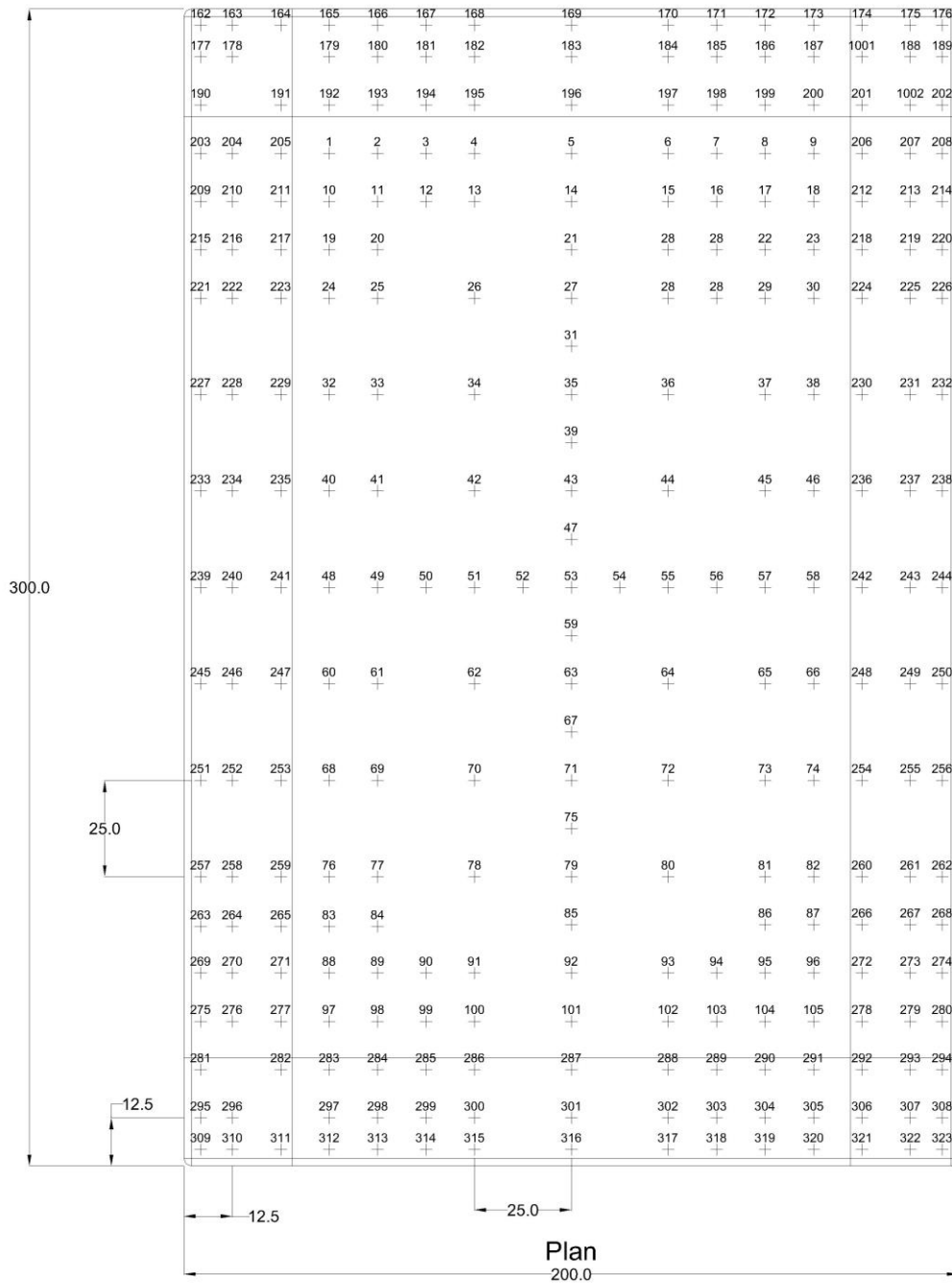
South Elevation



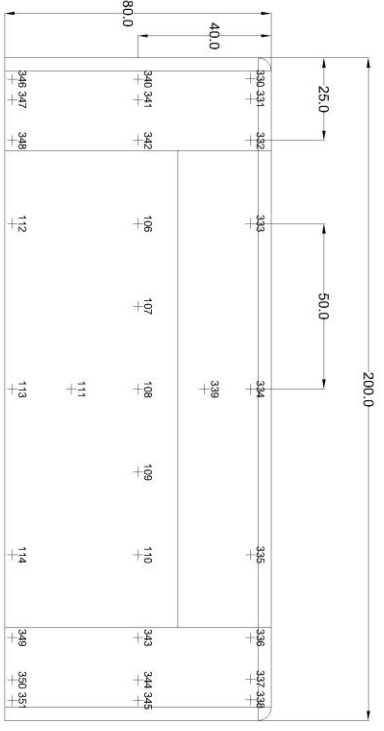
West Elevation



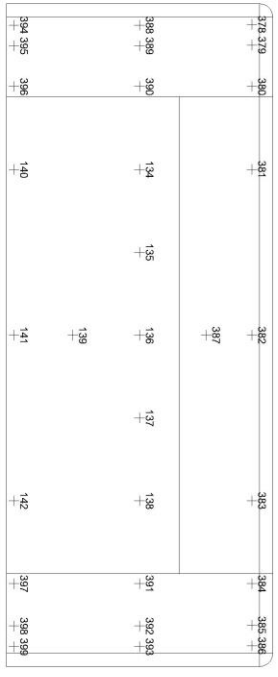
1:50 Model	2.5% Radius (R=2mm)
	All Dimmensions in mm



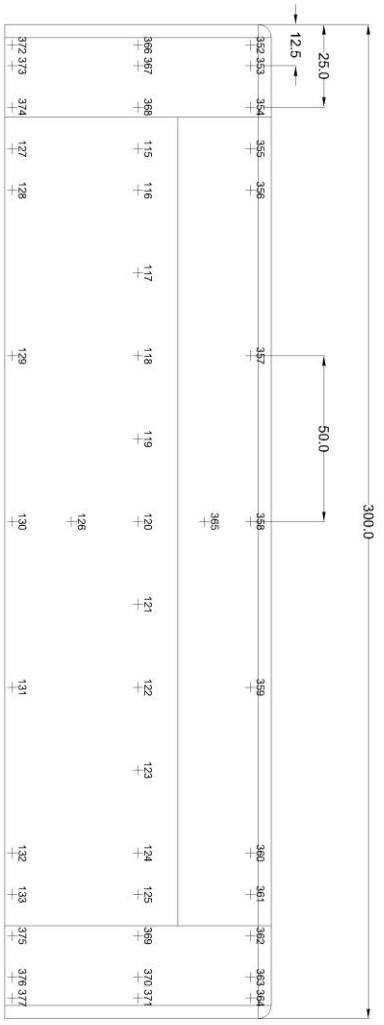
<b>1:50 Model</b>	<b>5% Radius (R=4mm)</b>
<b>All Dimmensions in mm</b>	



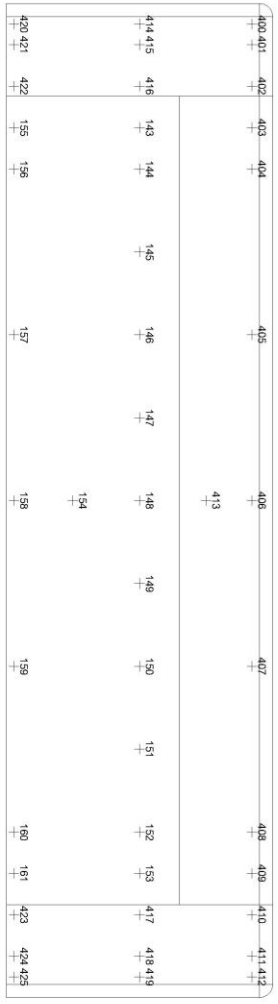
North Elevation



South Elevation

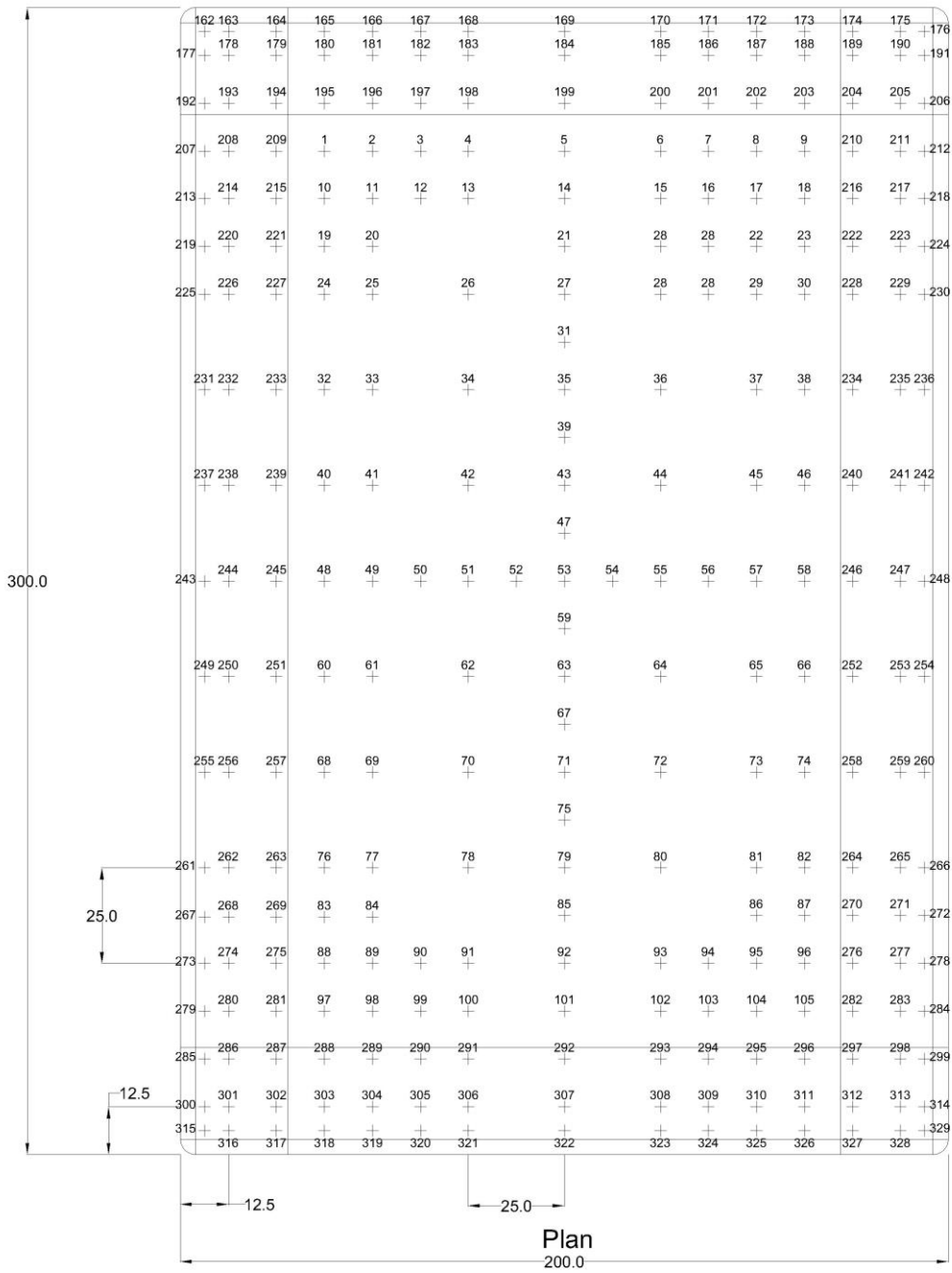


East Elevation

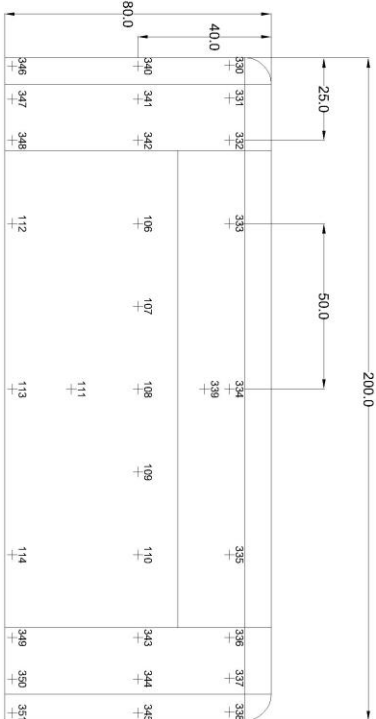


West Elevation

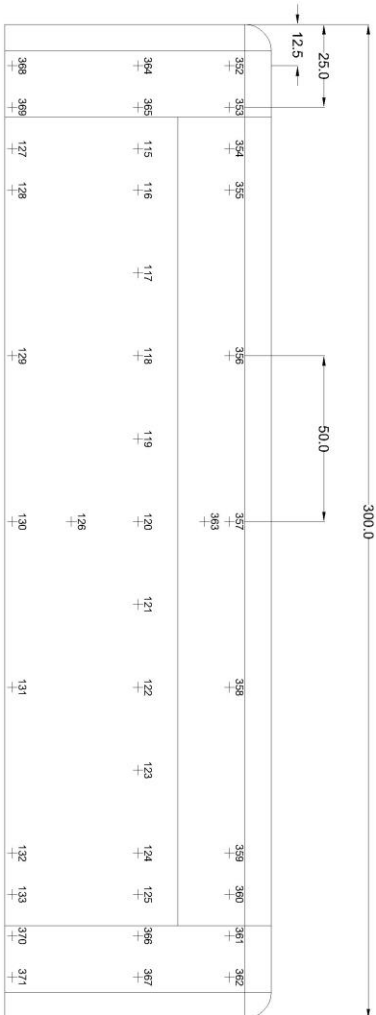
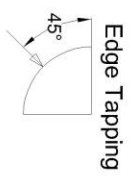
1:50 Model	5% Radius (R=4mm)
	All Dimmensions in mm



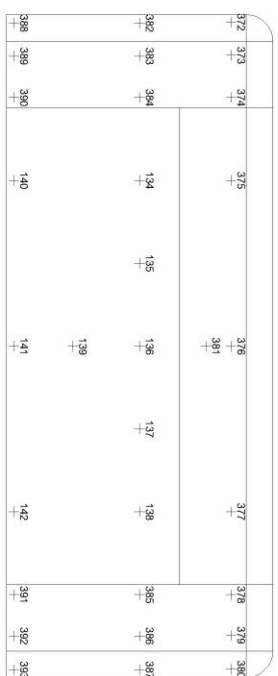
**1:50 Model**  
 10% Radius (R=8mm)  
 All Dimensions in mm



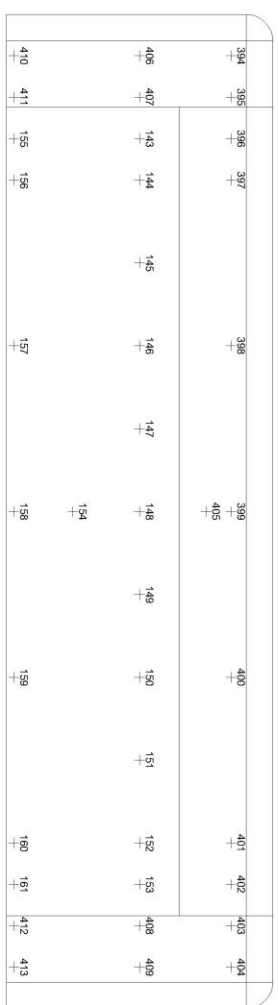
North Elevation



East Elevation



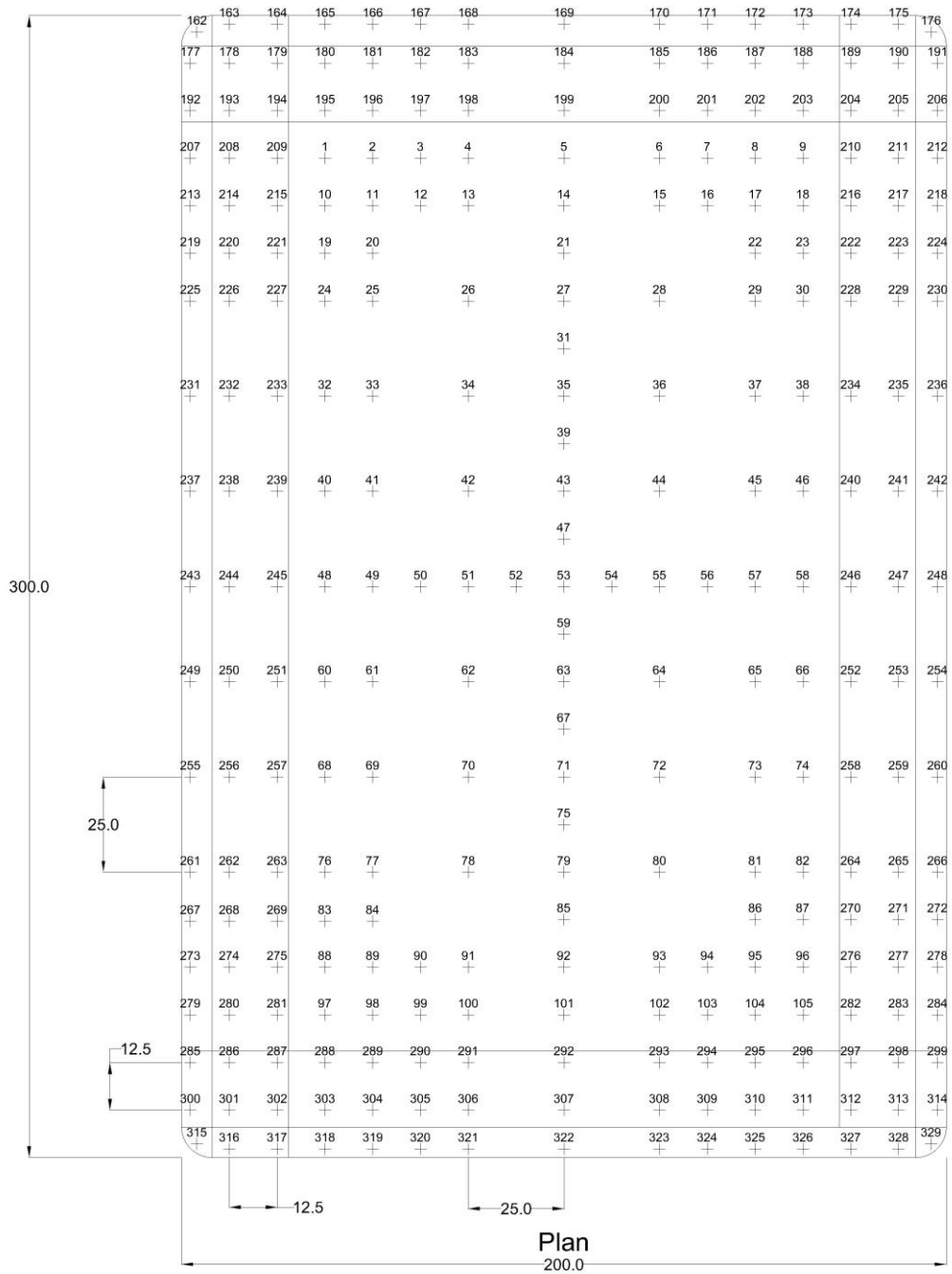
South Elevation



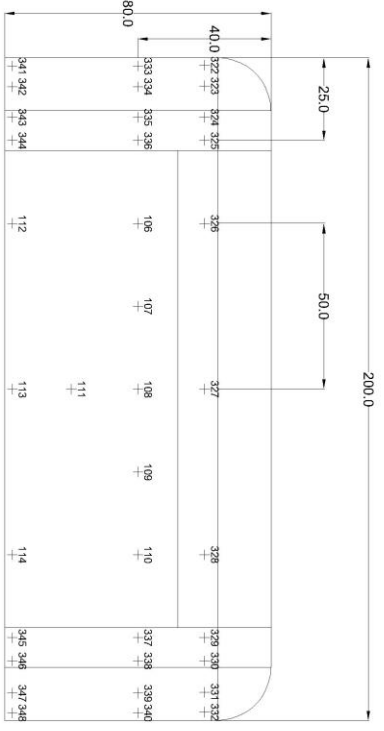
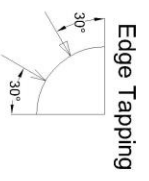
West Elevation

1:50 Model	10% Radius (R=8mm)
	All Dimmensions in mm

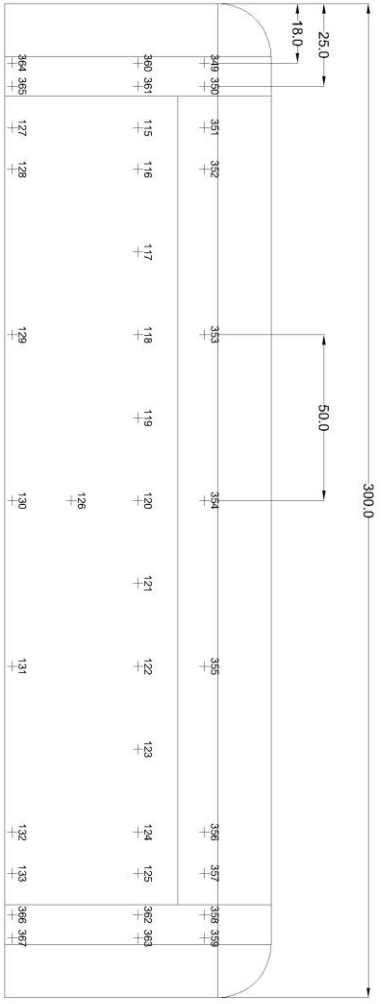
Edge Tapping



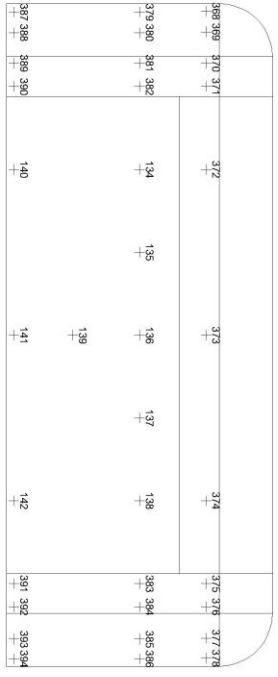
**1:50 Model**  
 20% Radius (R=16mm)  
 All Dimmensions in mm



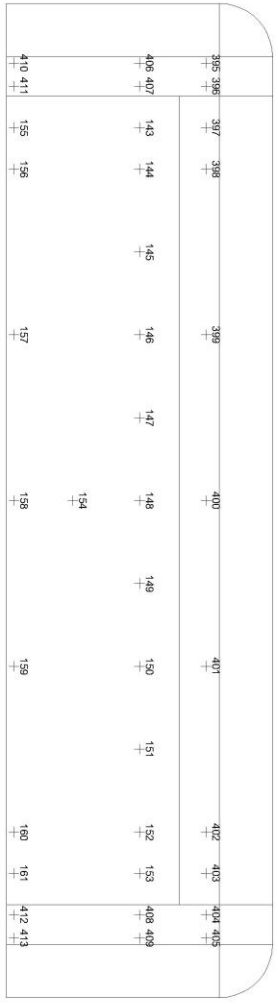
**North Elevation**



**East Elevation**



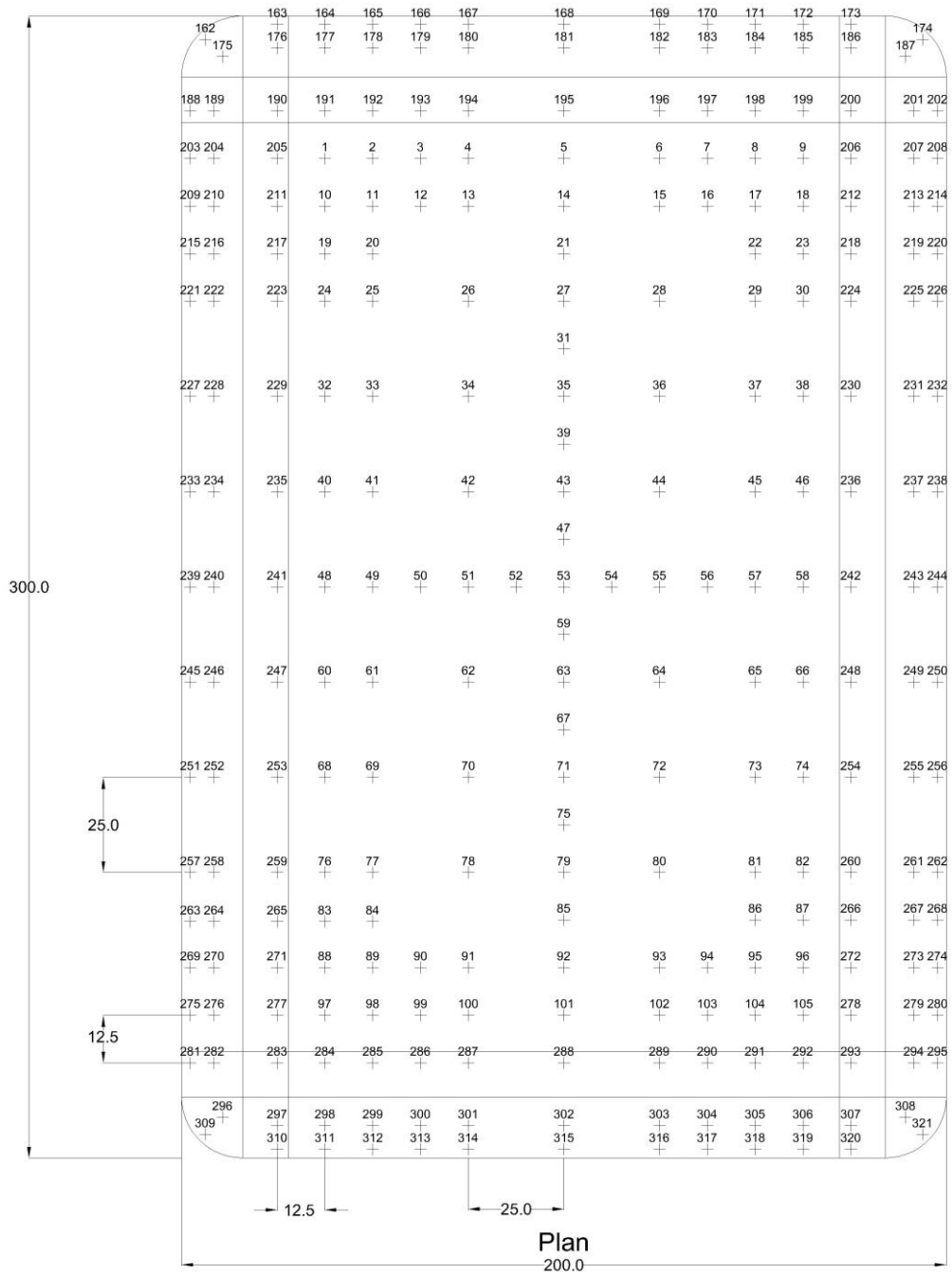
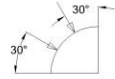
**South Elevation**



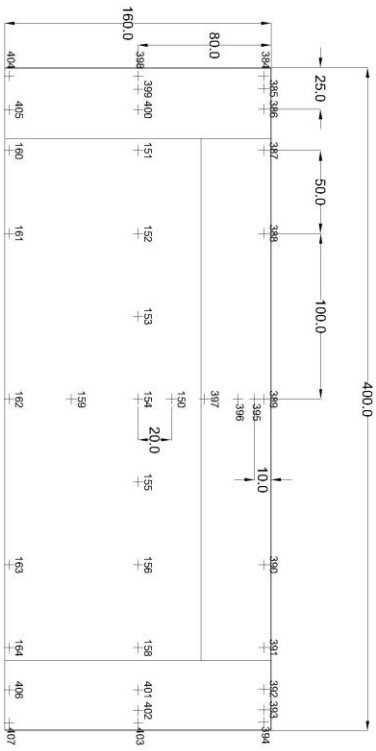
**West Elevation**

1:50 Model	20% Radius (R=16mm)
	All Dimmensions in mm

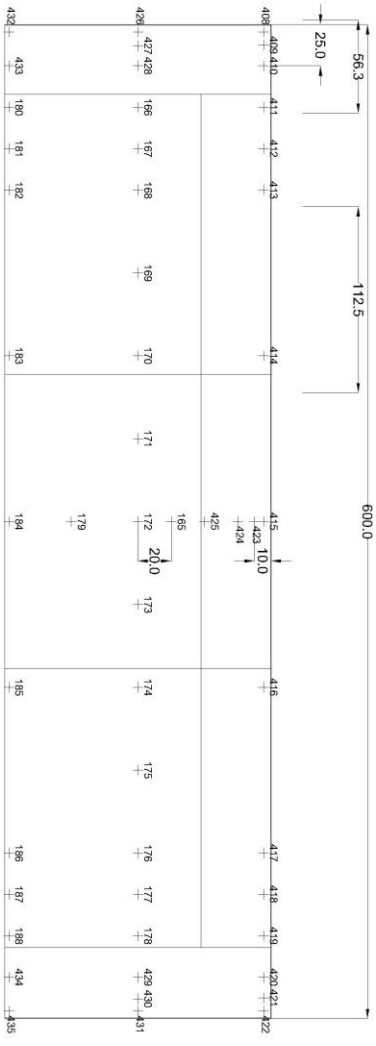
Edge Tapping



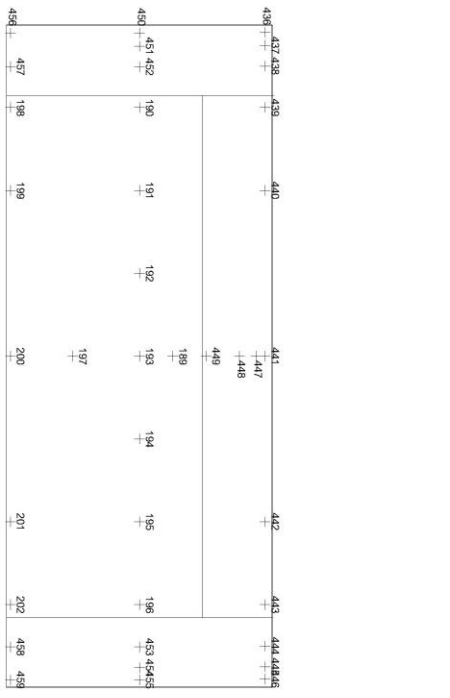
<b>1:25 Model</b>	<b>0.3% Radius (R=0.508mm)</b>
All Dimensions in mm	



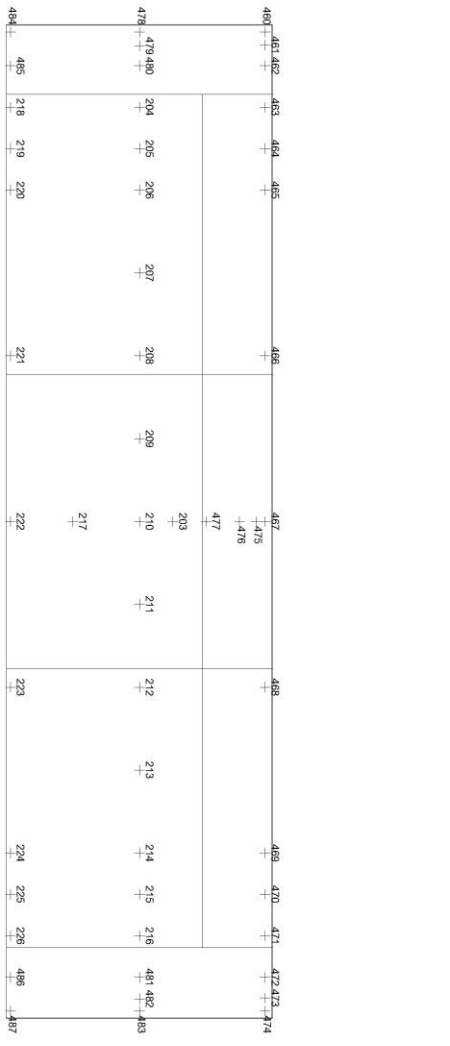
North Elevation



East Elevation



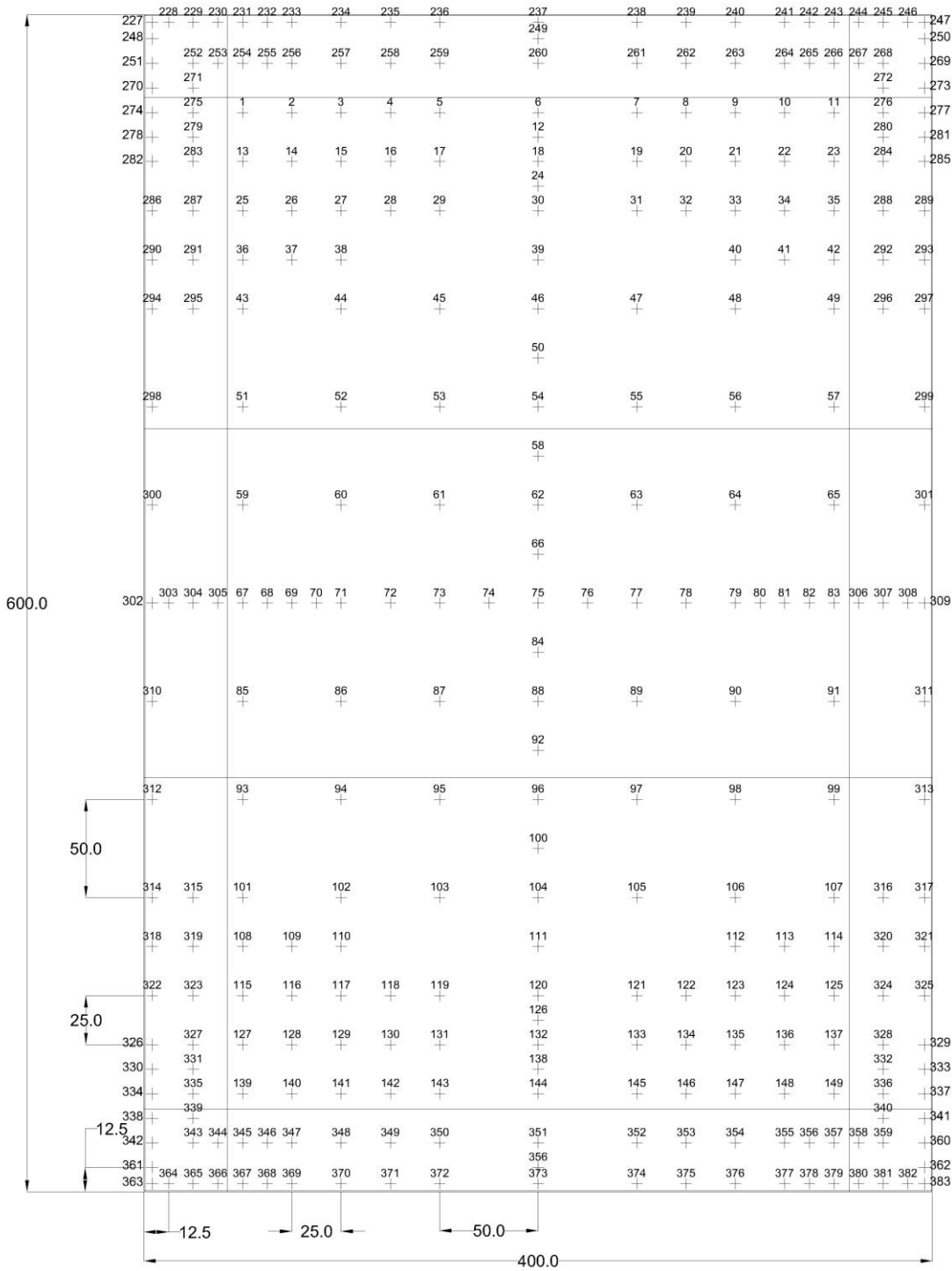
South Elevation



West Elevation

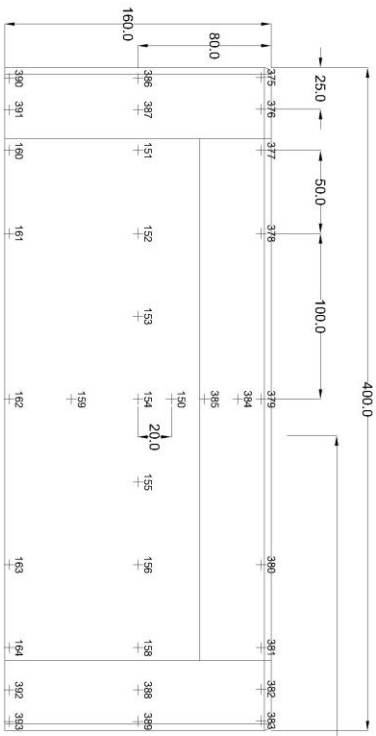


<b>1:25 Model</b>	0.3% Radius (R=0.508mm)
	All Dimmensions in mm

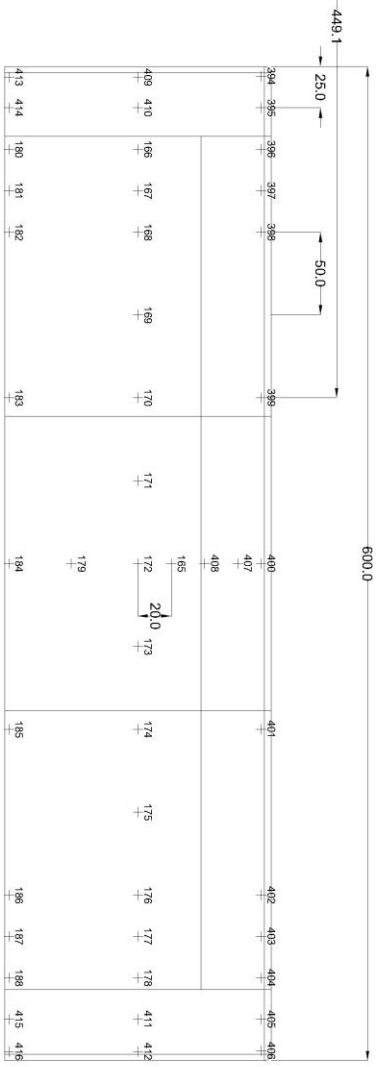


Plan

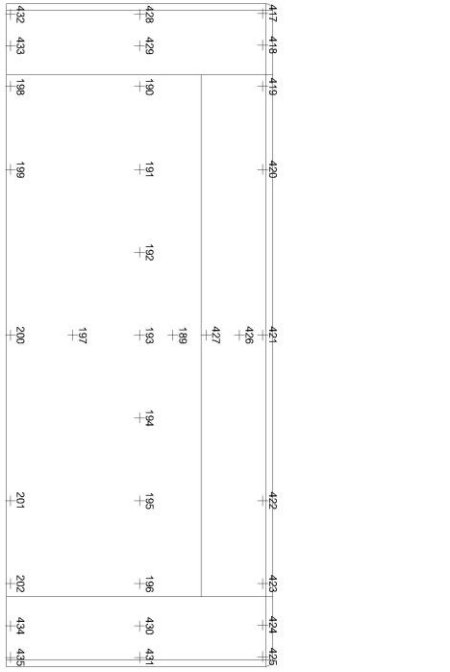
1:25 Model  
 2.5% Radius (R=4mm)  
 All Dimensions in mm



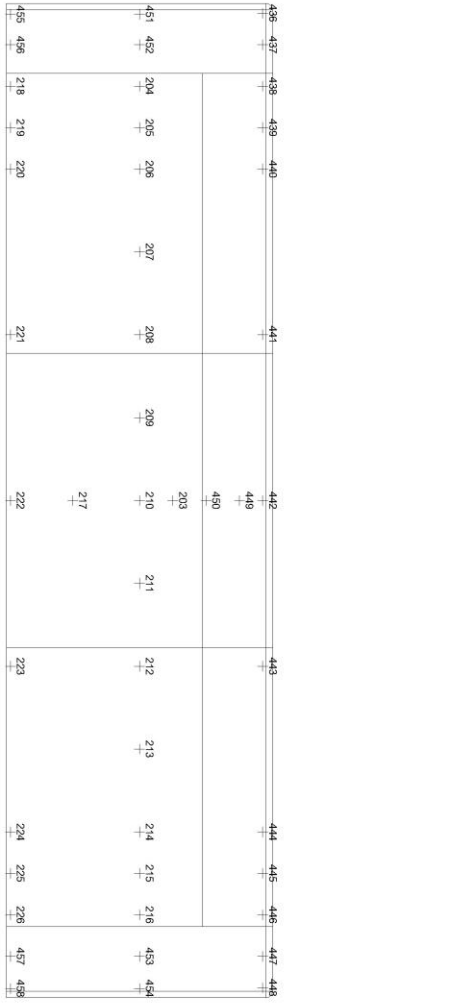
North Elevation



East Elevation

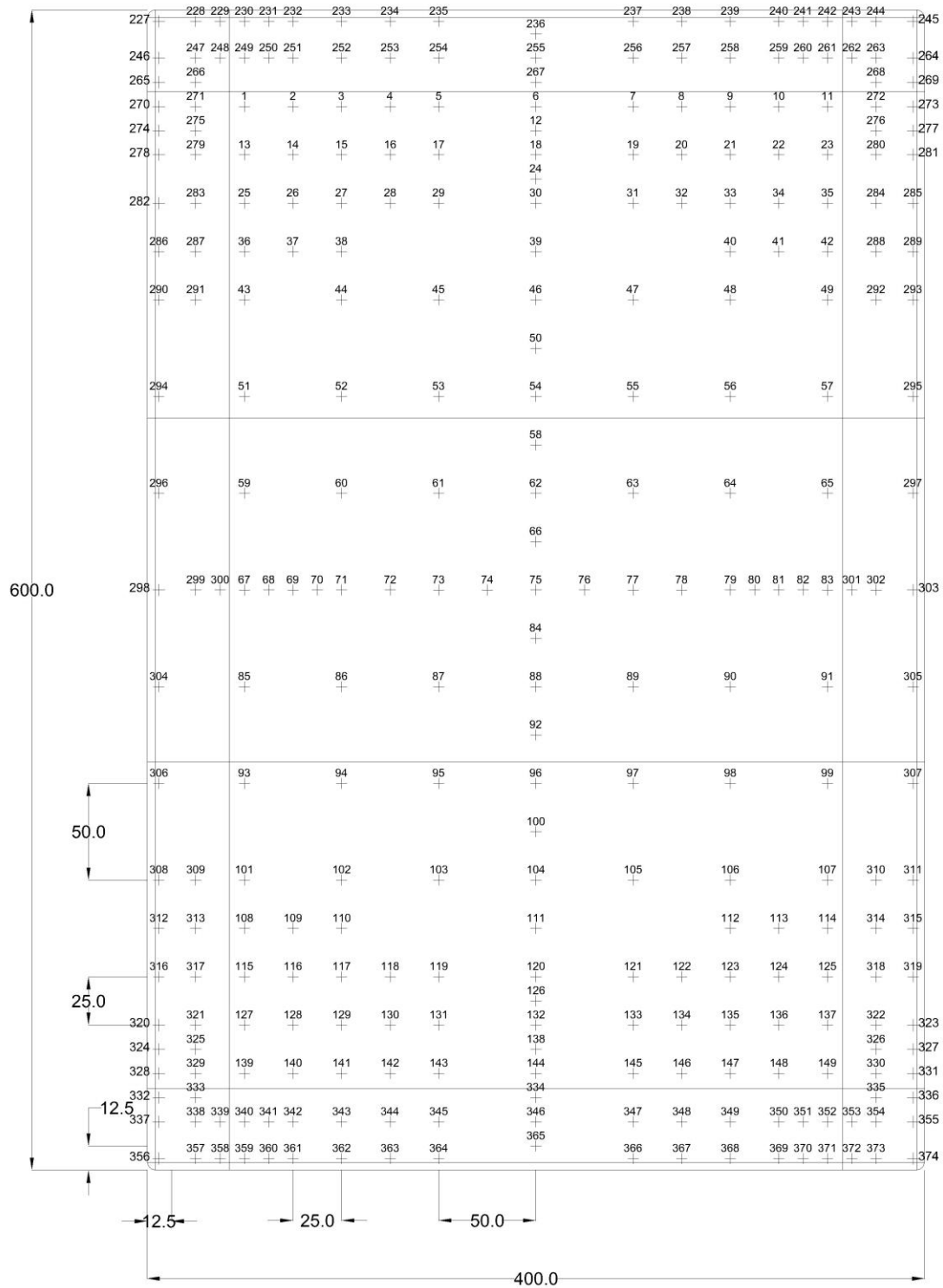


South Elevation



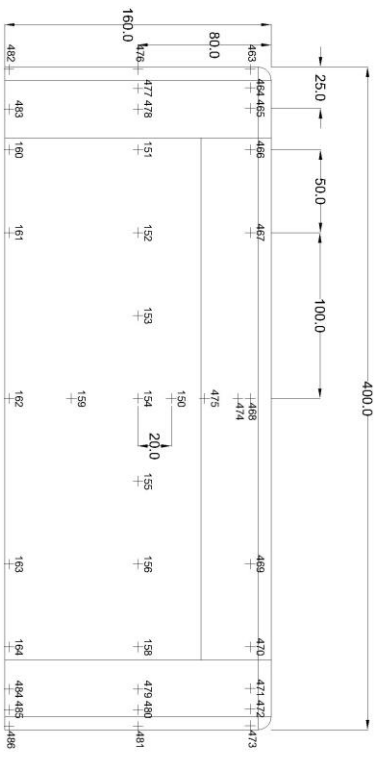
West Elevation

<b>1:25 Model</b>	2.5% Radius (R=4mm)
	All Dimmensions in mm

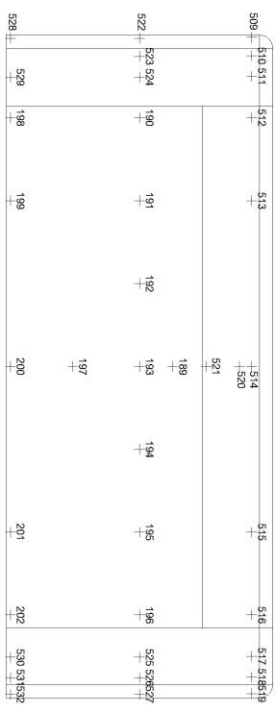


Plan

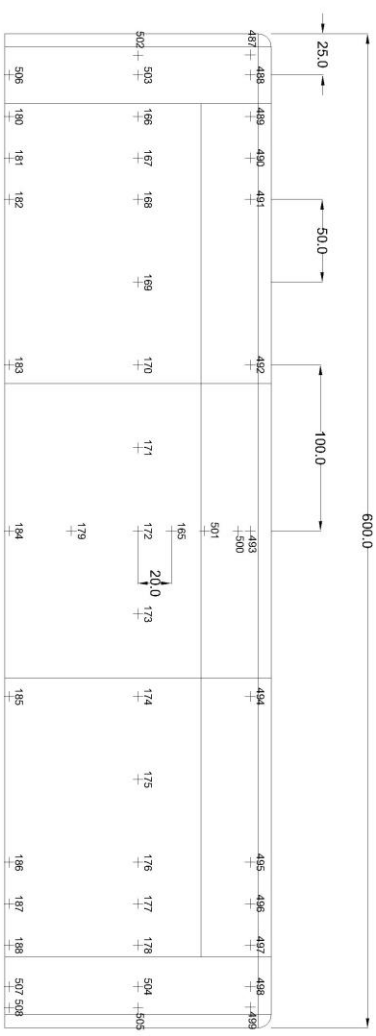
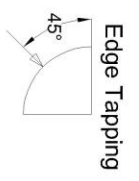
**1:25 Model**  
 5% Radius (R=8mm)  
 All Dimensions in mm



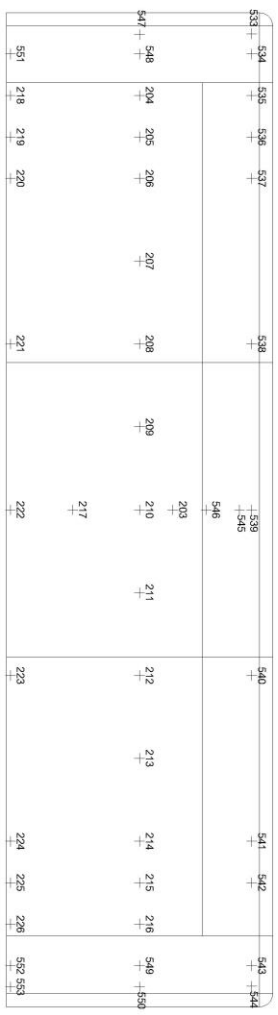
North Elevation



South Elevation

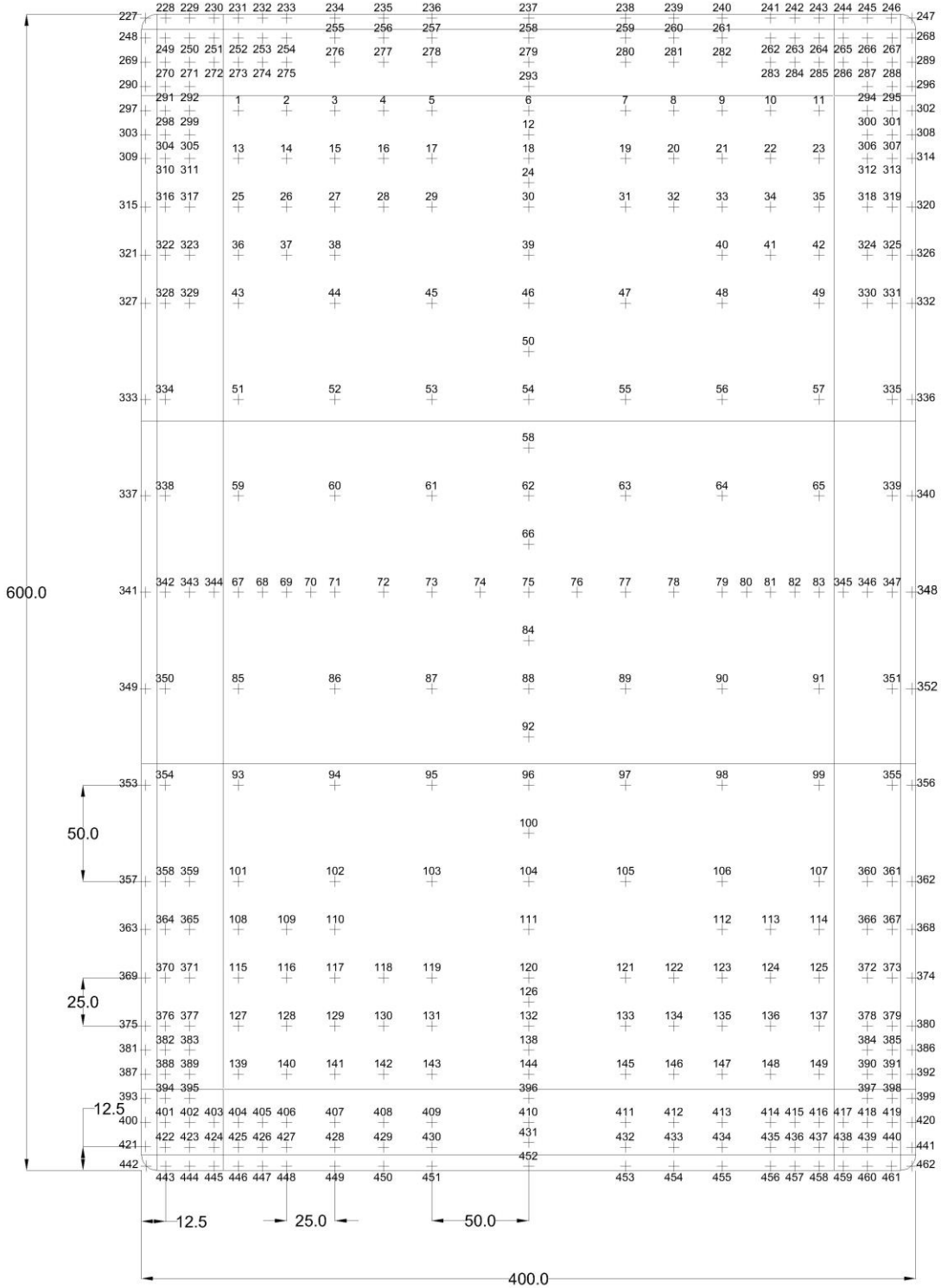


East Elevation



West Elevation

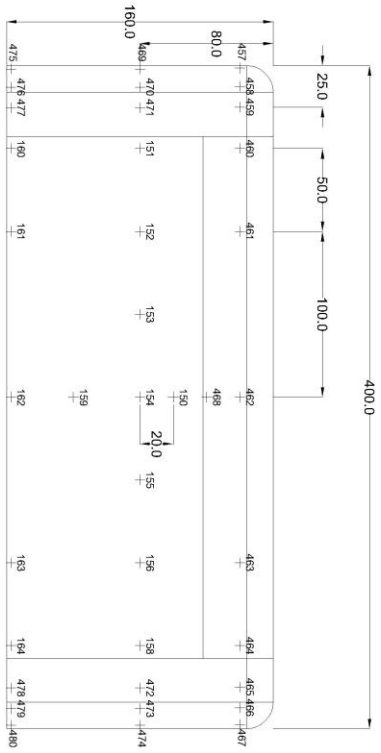
1:25 Model  
5% Radius (R=8mm)  
All Dimmensions in mm



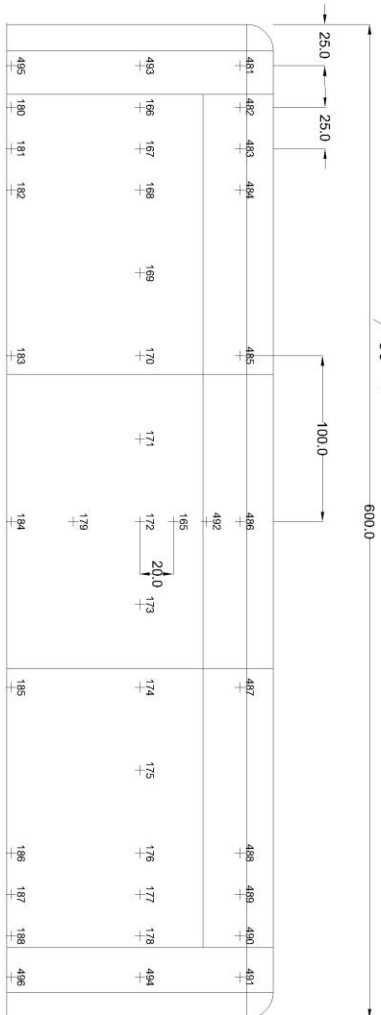
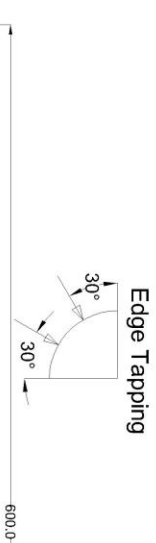
Plan

1:25 Model

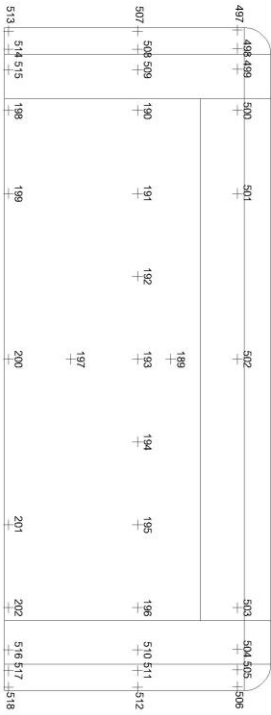
10% Radius (R=16mm)  
All Dimensions in mm



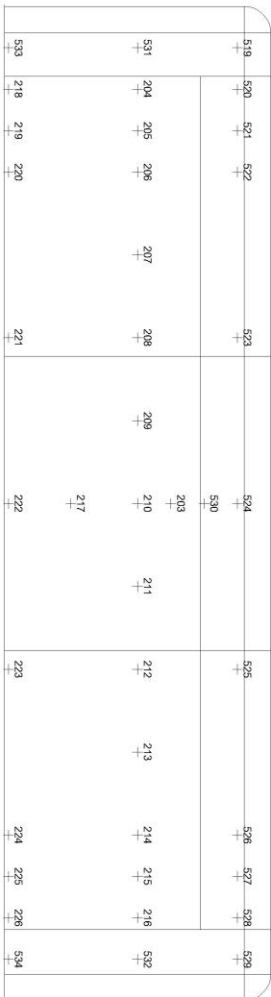
North Elevation



East Elevation

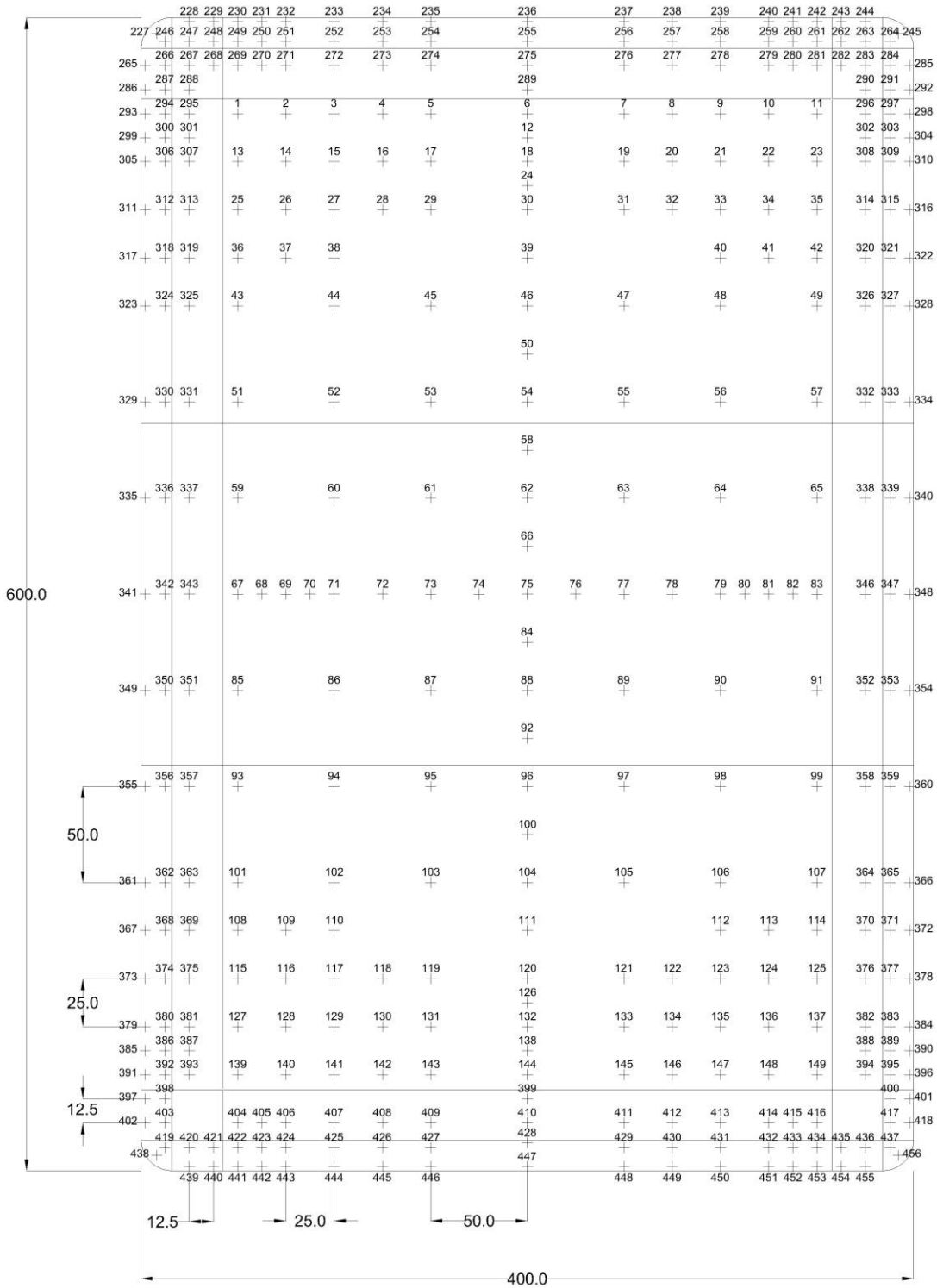
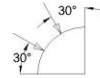


South Elevation



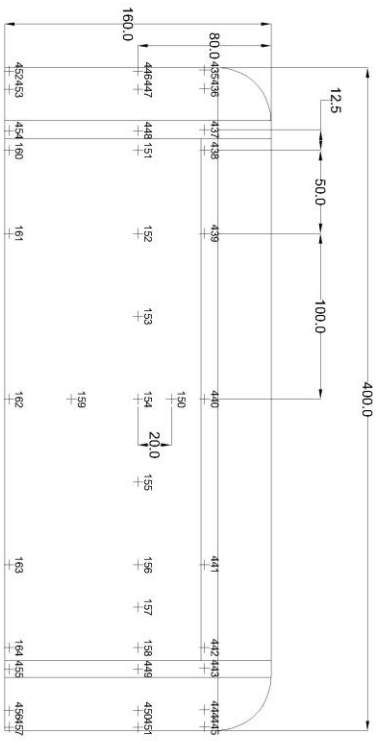
West Elevation

<b>1:25 Model</b>	10% Radius (R=16mm)
	All Dimmensions in mm

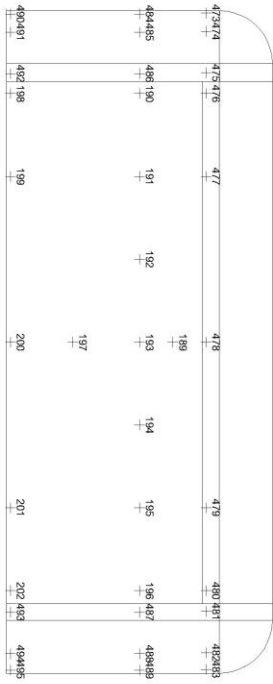


Plan

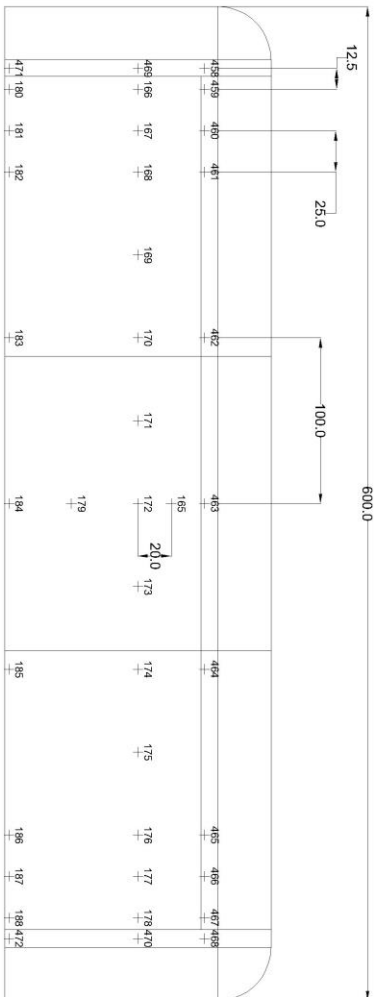
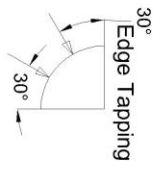
<b>1:25 Model</b>	<b>20% Radius (R=32mm)</b>
All Dimmensions in mm	



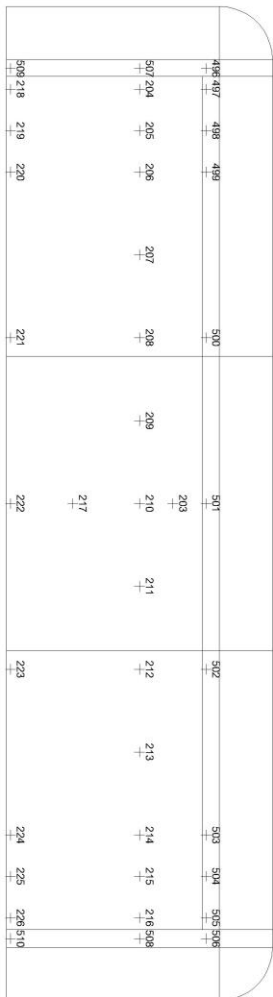
North Elevation



South Elevation



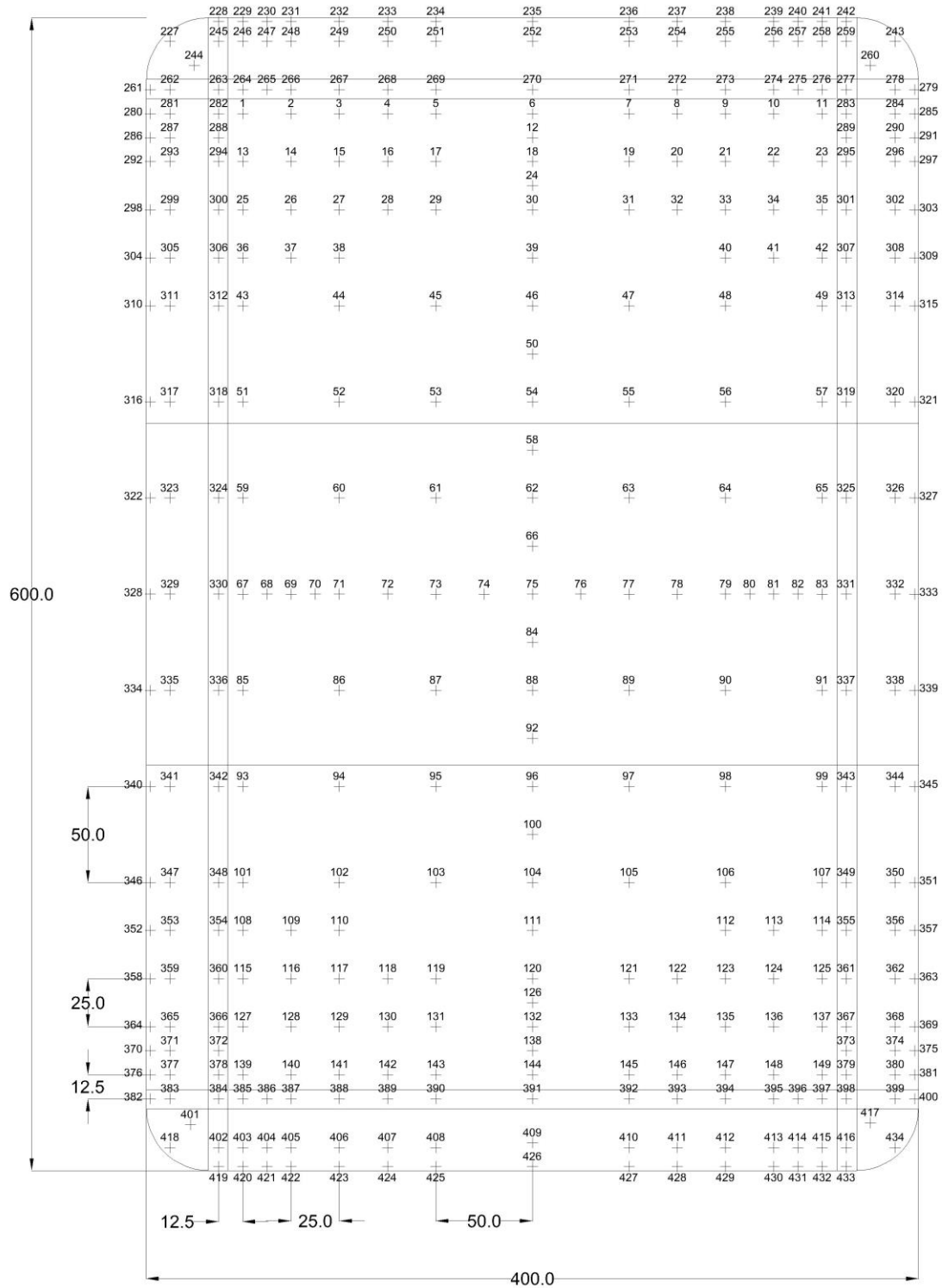
East Elevation



West Elevation

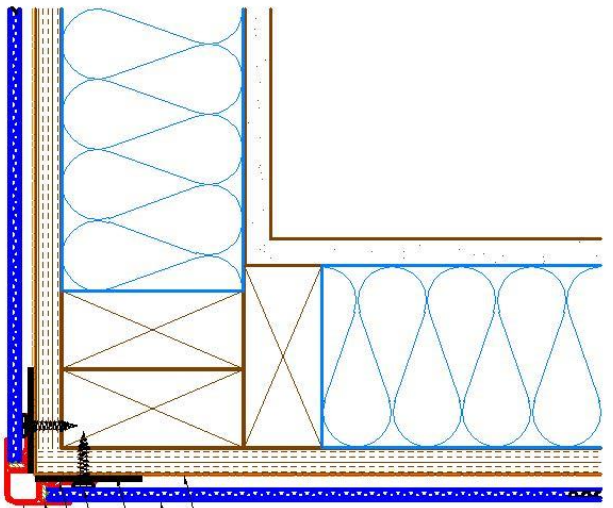


1:25 Model  
20% Radius (R=32mm)  
All Dimmensions in mm

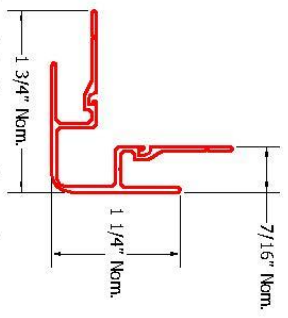


Plan

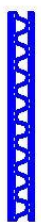




Substrate  
 SterraCore Panel  
 Water and Air Resistive Barrier  
 Appropriate Fastener  
 Foam Tape  
 Appropriate Sealant  
 Outside Corner Extrusion



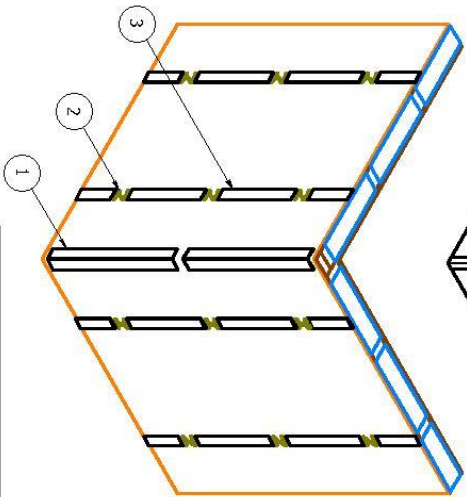
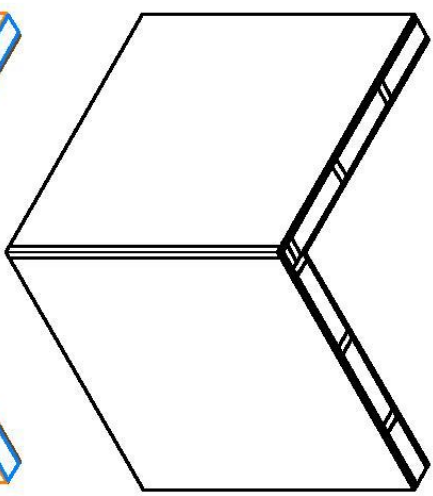
Outside Corner Extrusion



SterraCore Panel

**Note:** Spacing between Panels and Water and Air Resistive Barrier are shown for Clarity.


- (1) Outside Corner Extrusion installed on Foam Tape. 2" min. gap at 24" O.C. and at transition to vertical moldings.
- (2) Panel Adhesive applied 24" O.C. Horizontally and 15" O.C. Vertically.
- (3) Foam Tape Installed Vertically in between Panel Adhesive.

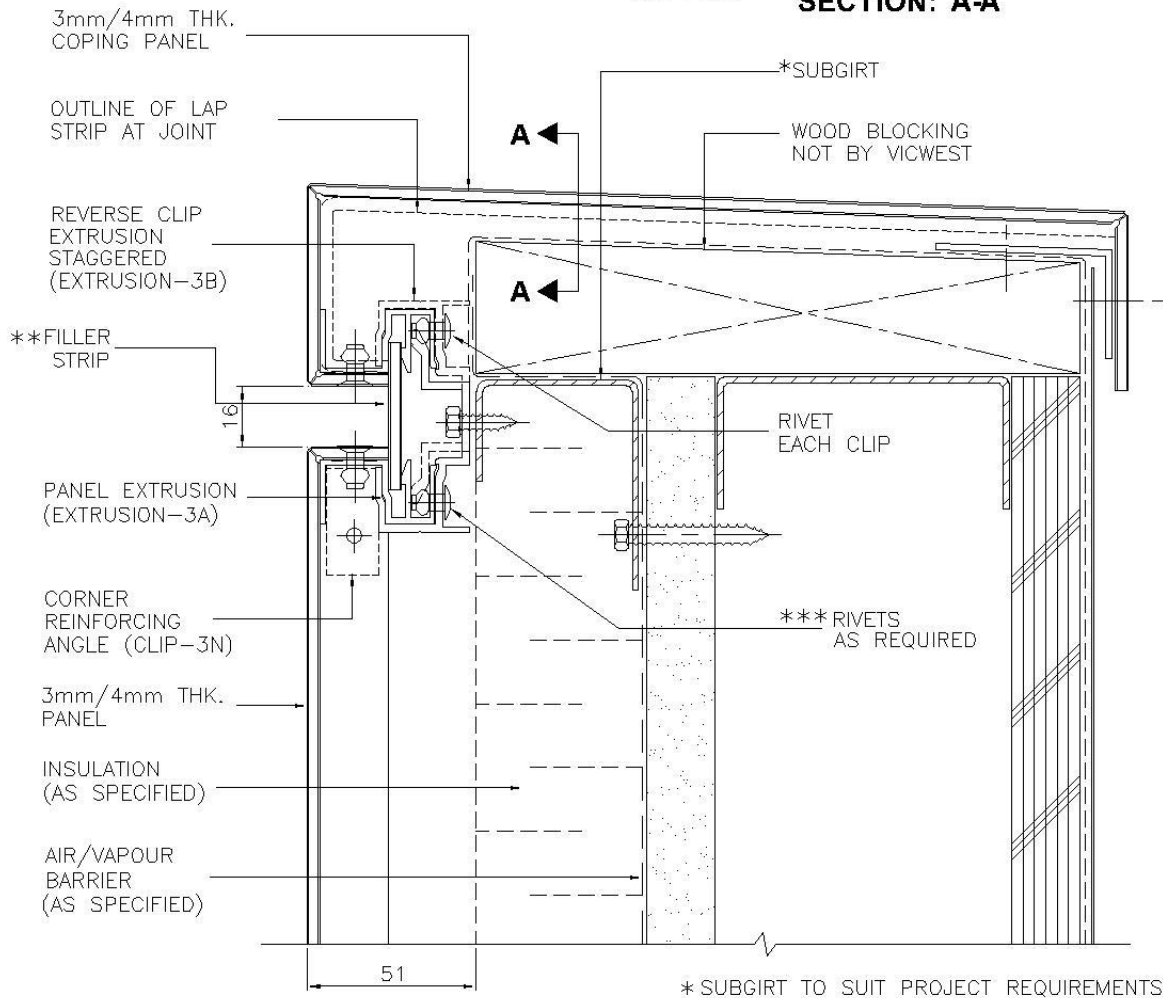
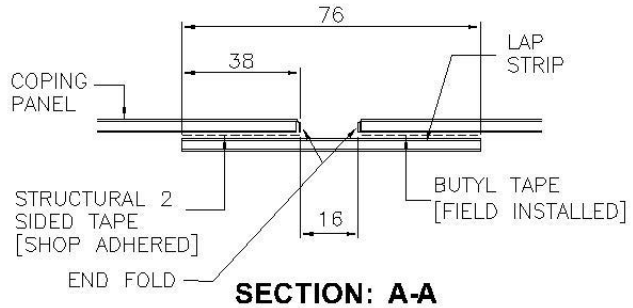


REV	DATE	DESCRIPTION OF REVISION	BY	APP

ATAS INTERNATIONAL, INC. Allentown, PA 610 395 5445 Mesa AZ 480 555 7210	Project No: _____ Title: <b>SterraCore Outside Corner Detail - 1 Piece</b> Date: 5/26/2015 Scale: <b>B</b> Plot: <b>X X</b>

	CADD BY:	TITLE:	JOB No:
	DATE: DEC. 17, 2002	<b>COMPOSITE PANEL SYSTEM 3</b>	SHEET No: 3C
	APPD. BY:		CAD FILE: CPS3R-DETAILS
	REV. No: REV. $\Delta$ MAY 31, 2004		
ENGINEERING DEPT.			



**3C PARAPET DETAIL (ALTERNATE DETAIL)**

\* SUBGIRT TO SUIT PROJECT REQUIREMENTS  
 \*\* 40mm FOR 4mm PANEL  
 \*\*\* RIVET ONE CLIP TO EXTRUSION FOR EVERY 1500mm OF PANEL LENGTH. INSTALL RIVETED CLIPS IN MIDDLE 1200mm OF PANEL

Details must be reviewed and modified as required to suit individual project conditions

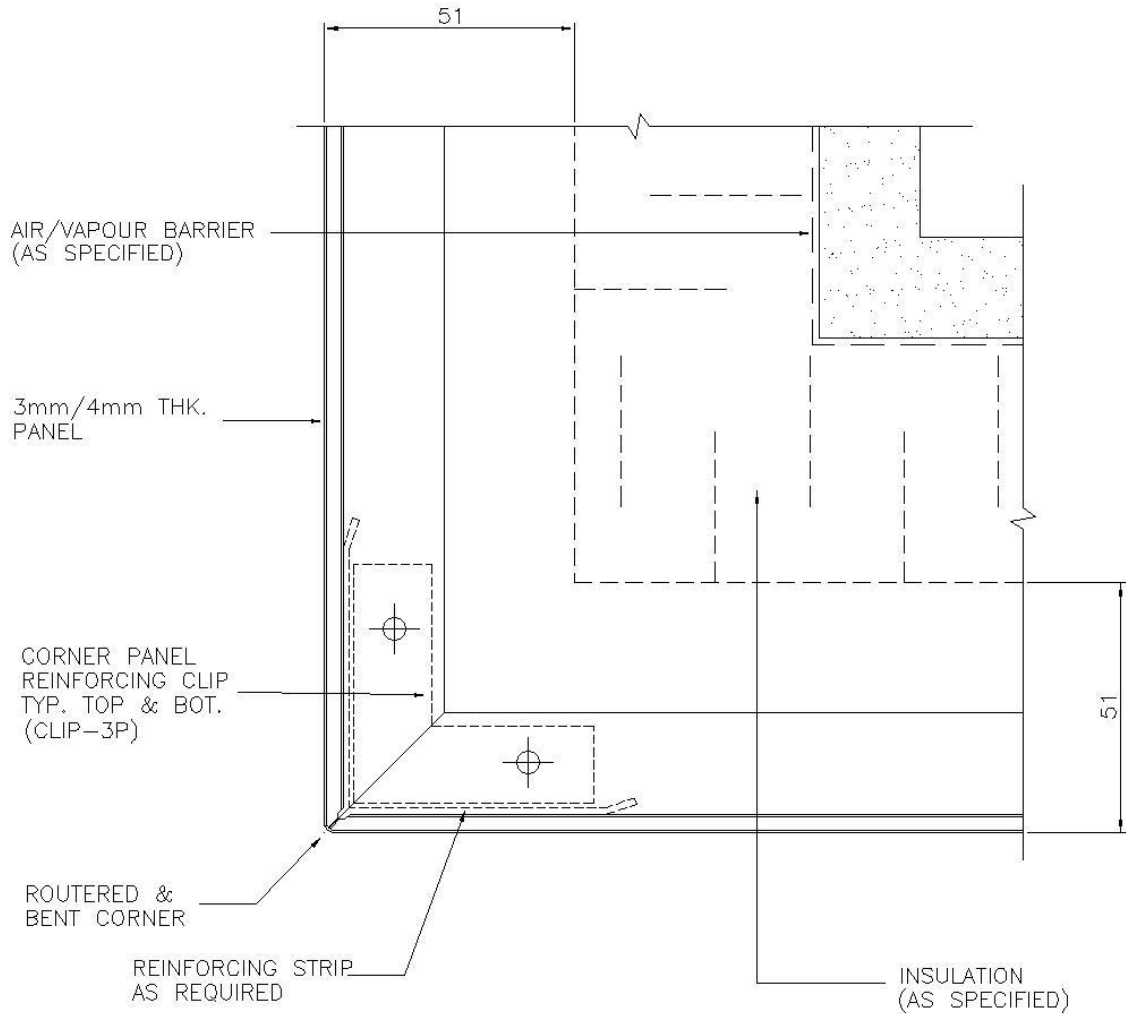


CADD BY:  
 DATE: DEC. 17, 2002  
 APPD. BY:  
 REV. No:

TITLE:  
**COMPOSITE PANEL SYSTEM 3**

JOB No:  
 SHEET No:  
 5  
 CAD FILE:  
 CPS3-DETAILS

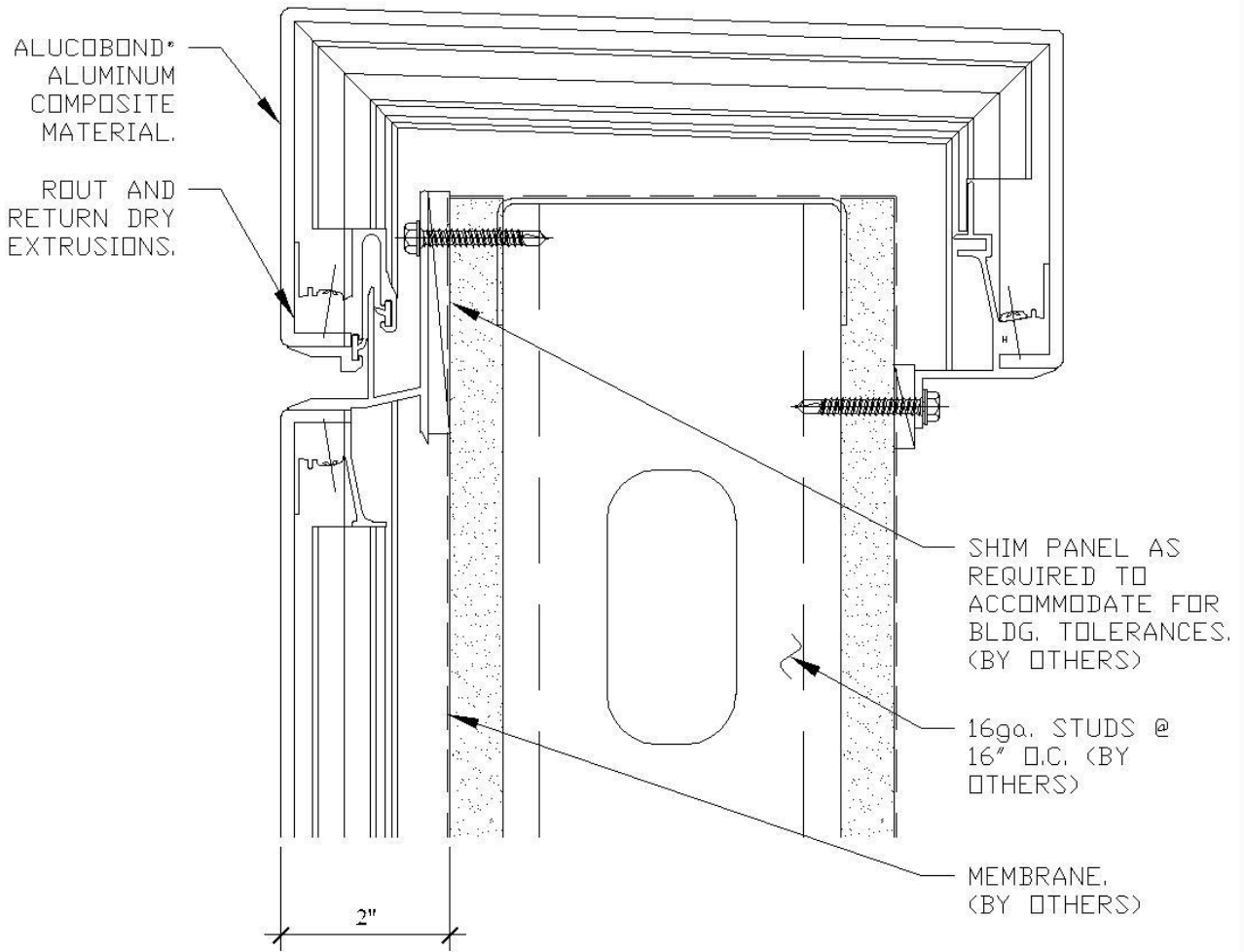
ENGINEERING DEPT.



**5** CORNER DETAIL

Details must be reviewed and modified as required to suit individual project conditions

DISCLAIMER NOTE: THIS ALUCOBOND DETAIL IS PROVIDED FOR CONCEPTUAL PURPOSES ONLY. THE ACTUAL DESIGN, PANEL SYSTEM, FABRICATION, AND INSTALLATION ARE PROVIDED BY A NETWORK OF QUALIFIED FABRICATORS AND INSTALLERS. 3A COMPOSITES USA, INC. DOES NOT MAKE ANY WARRANTIES, EXPRESS OR IMPLIED INCLUDING MERCHANTABILITY AND FITNESS FOR PURPOSE.



1

PARAPET CONDITION

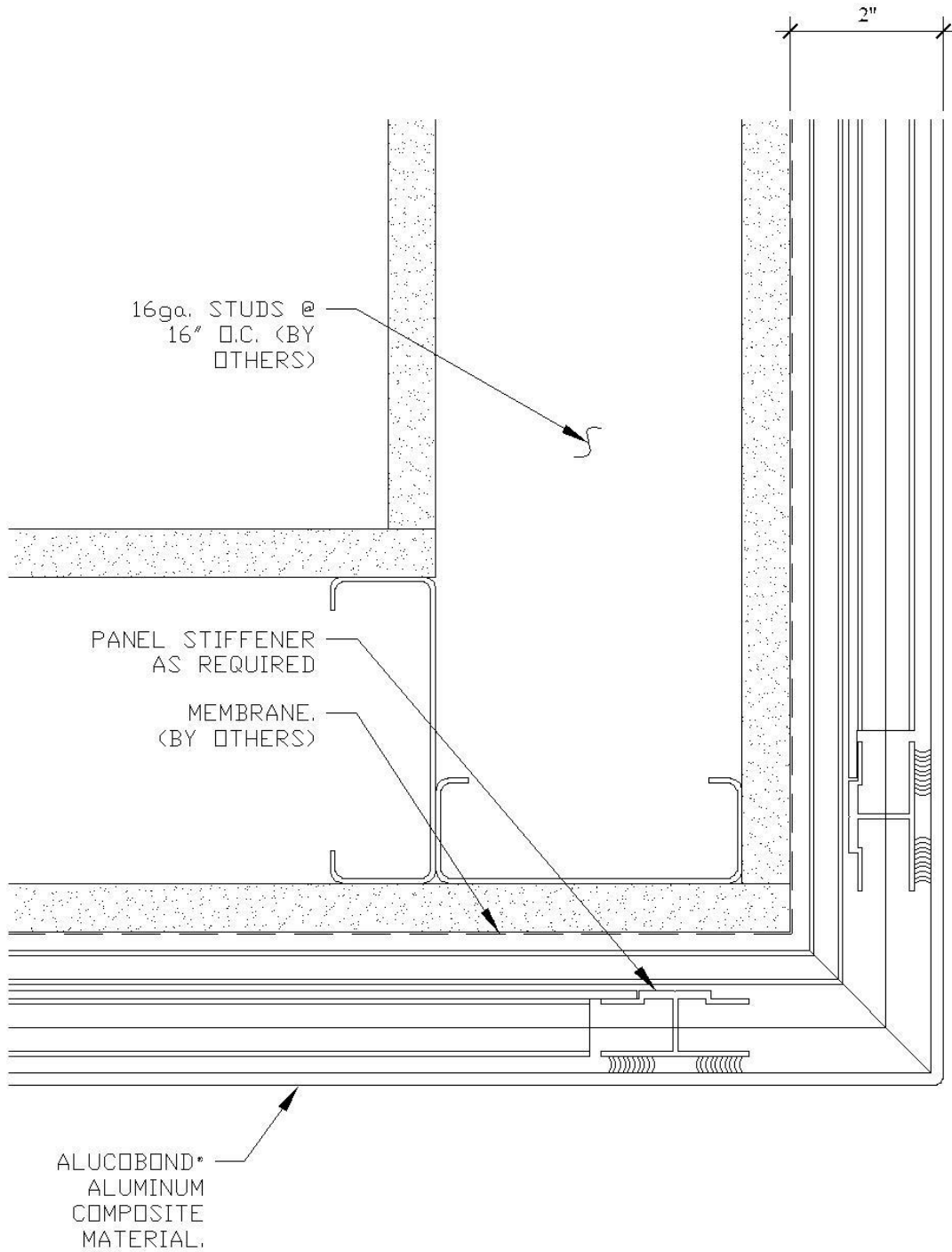
NOT TO SCALE

ROUT AND  
RETURN  
DRY-SEAL

THE NAME SAYS IT ALL  
**ALUCOBOND**®



DISCLAIMER NOTE: THIS ALUCOBOND DETAIL IS PROVIDED FOR CONCEPTUAL PURPOSES ONLY. THE ACTUAL DESIGN, PANEL SYSTEM, FABRICATION, AND INSTALLATION ARE PROVIDED BY A NETWORK OF QUALIFIED FABRICATORS AND INSTALLERS. 3A COMPOSITES USA, INC. DOES NOT MAKE ANY WARRANTIES, EXPRESS OR IMPLIED INCLUDING MERCHANTABILITY AND FITNESS FOR PURPOSE.



OUTSIDE CORNER

NOT TO SCALE

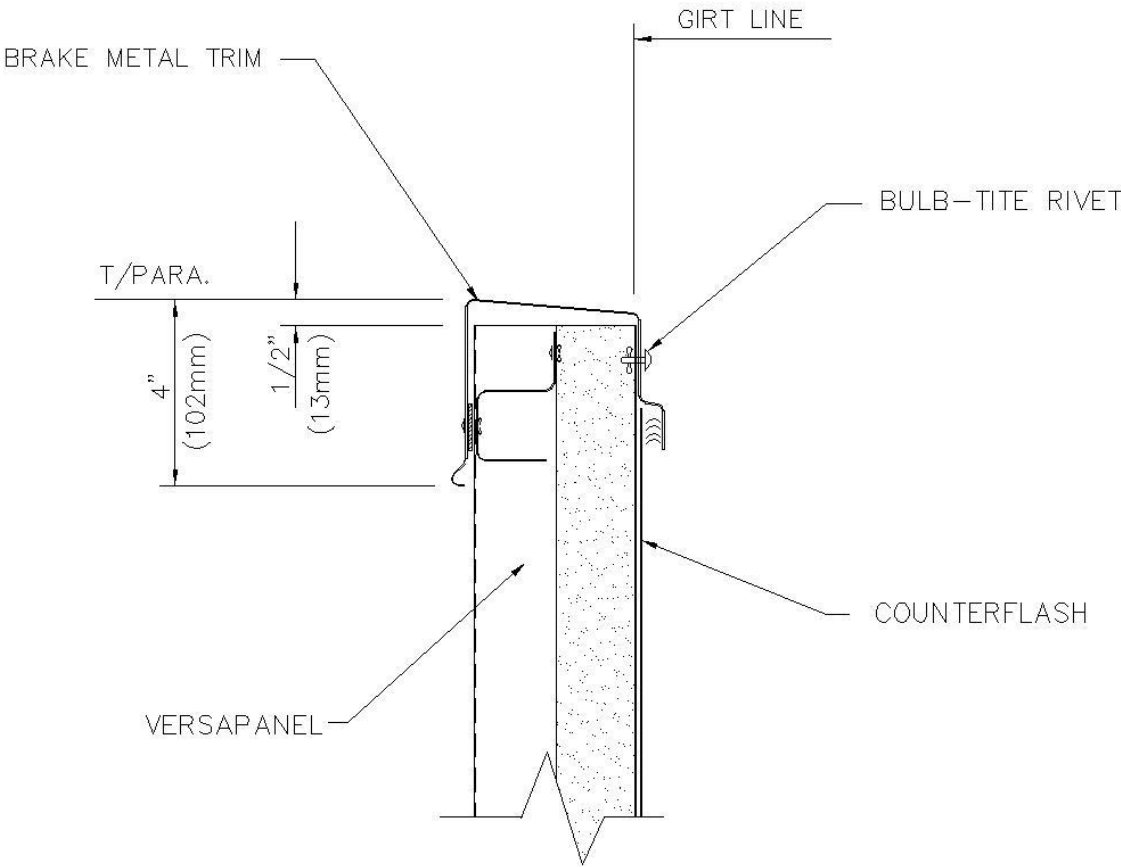
ROUT AND  
RETURN  
DRY-SEAL

THE NAME SAYS IT ALL  
**ALUCOBOND**<sup>®</sup>



# VERSAPANEL

PROMOTIONAL  
DETAIL # 007



NOTE:  
LINER SEAL IS PROPERLY LOCATED @ INTERSECTION  
WITH ROOF VAPOR BARRIER.



**CENTRIA**  
CENTRIA Architectural Systems

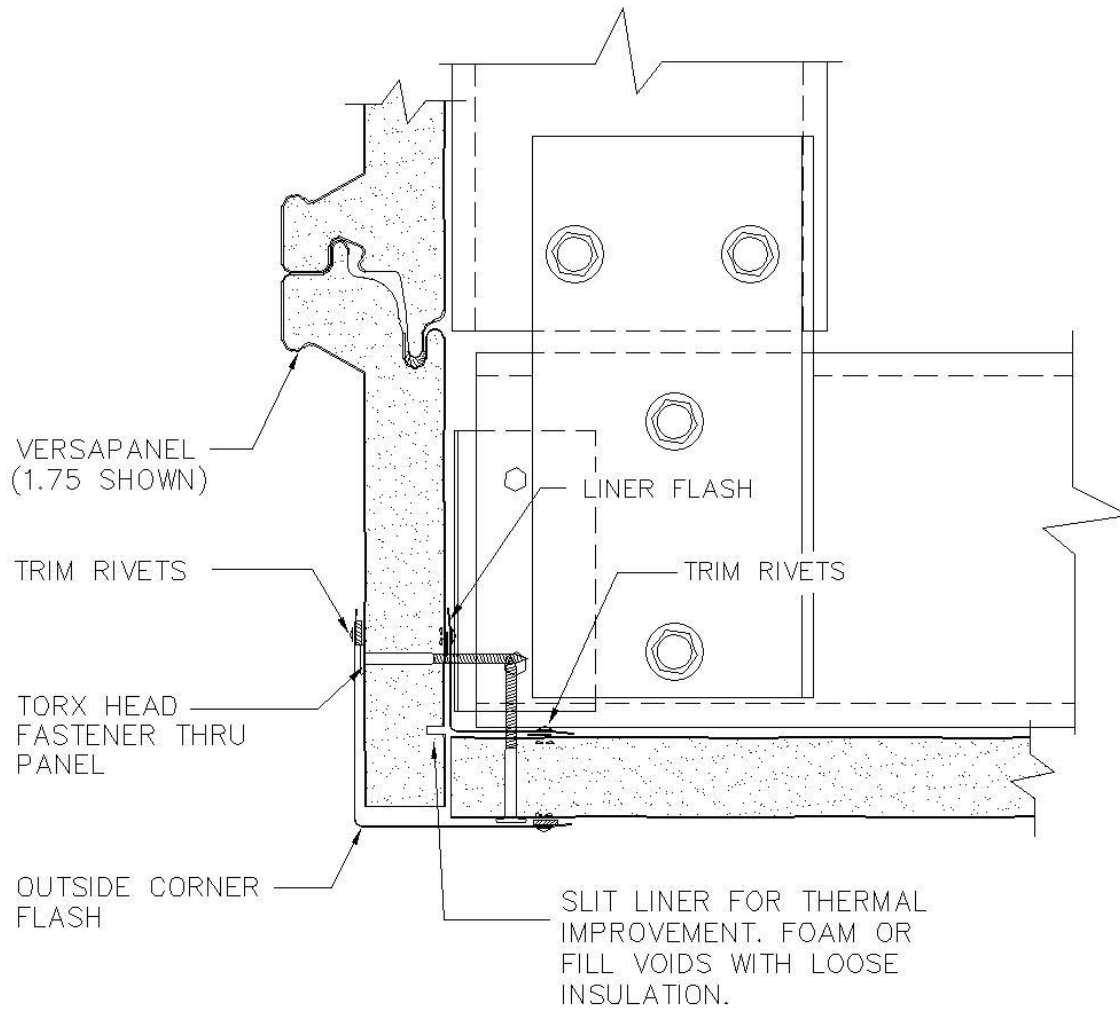
PARAPET

Jan 18



# VERSAPANEL

PROMOTIONAL  
DETAIL # 009



NOTE:  
SET ALL FLASHING  
IN SEALANT



**CENTRIA**  
CENTRIA Architectural Systems

OUTSIDE CORNER

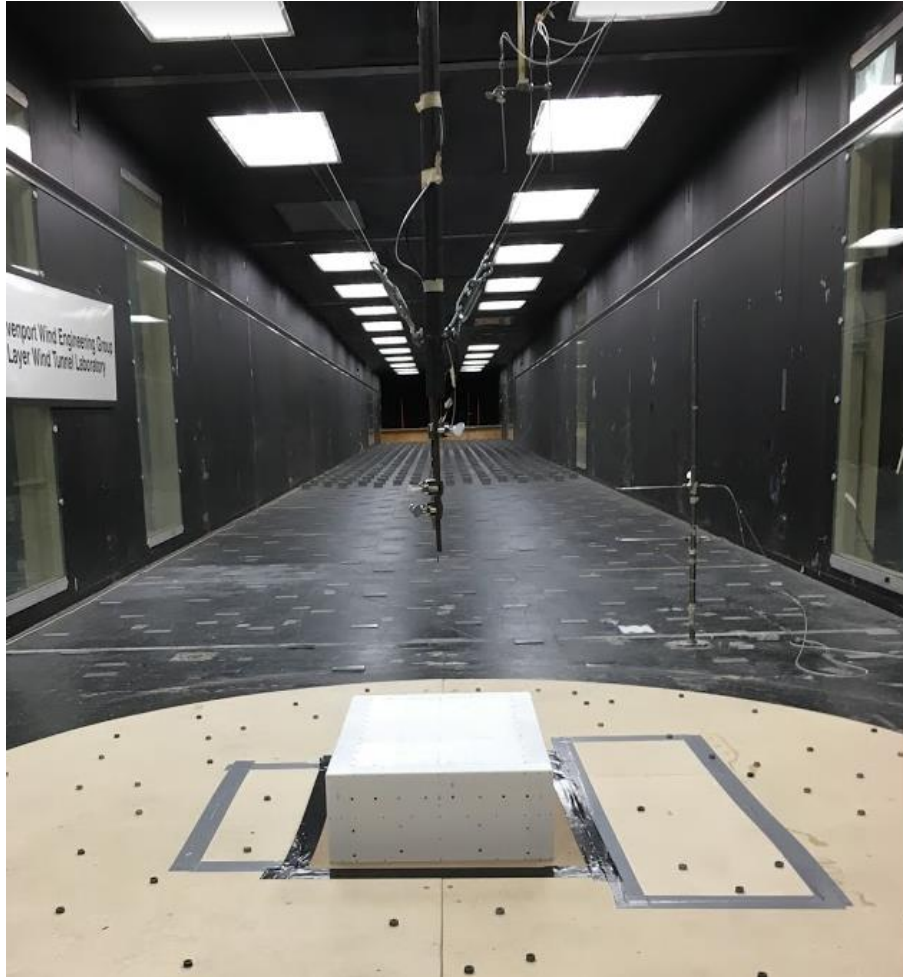


Based on the exposures used, which in the present work are banks are raised to various heights. Roughness block heights for “Flat 0” and “Open 15” are summarized below along with the use of other devices in the tunnel.

<b>Bank #</b>	<b>Block Height [inch]</b>	
	<b>Flat 0</b>	<b>Open 15</b>
<b>1</b>	0	2.7
<b>2</b>	0	2.7
<b>3</b>	0	2.7
<b>4</b>	0	2.7
<b>5</b>	0	2.7
<b>6</b>	0	2.7
<b>7</b>	0	0.3
<b>8</b>	0	0.3
<b>9</b>	0	0.3
<b>10</b>	0	0.3
<b>11</b>	0	0
<b>Machine Nuts</b>	No	Yes
<b>Red Spires</b>	Yes	Yes
<b>15" Barrier</b>	No	Yes

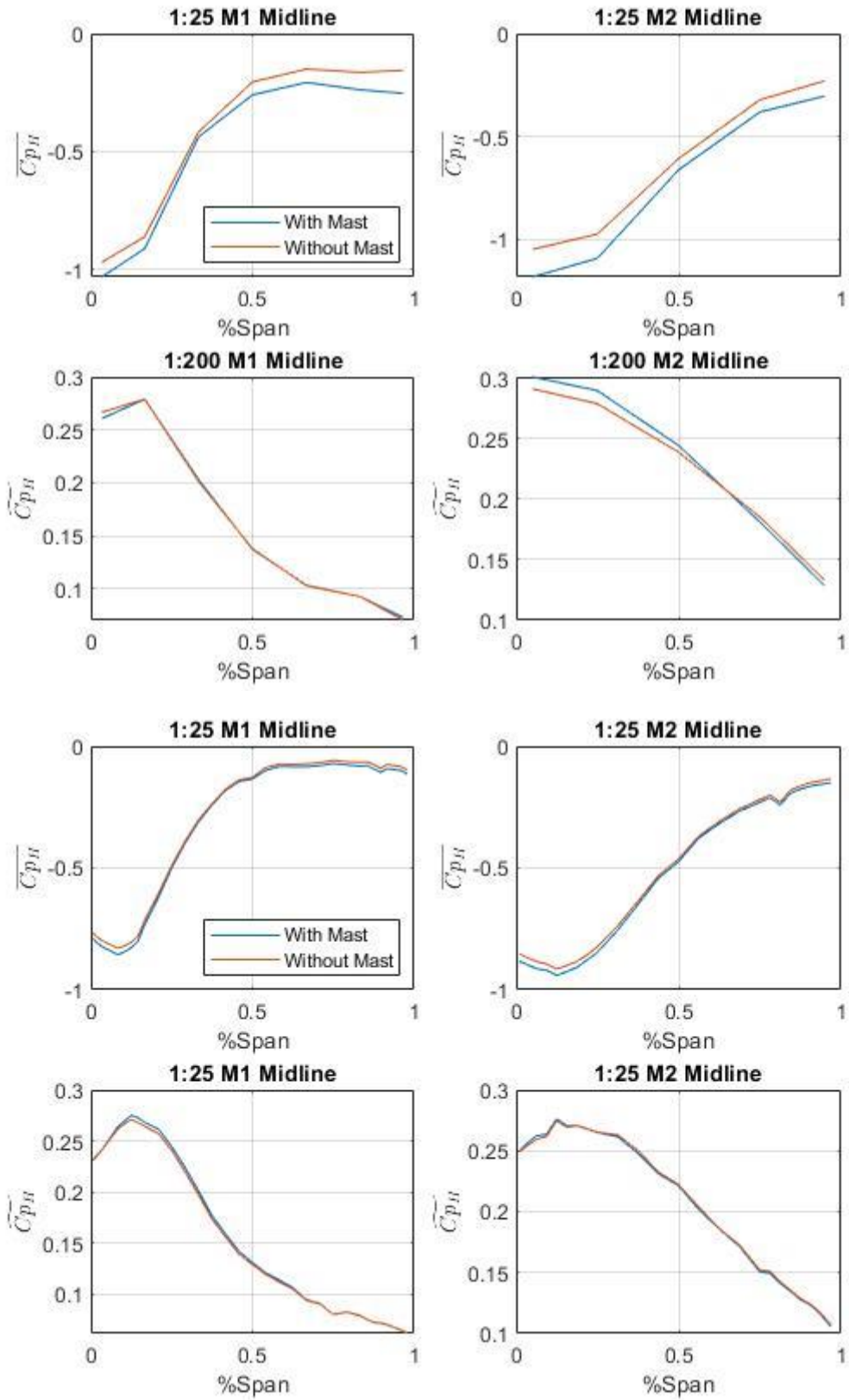
### Appendix D: Comparison of data with mast

During testing, a mast was placed above building model to simultaneously measure velocity above the model during testing as shown below. For  $R/H = 0.3\%$ , the 1:25 and 1:200 scale models were tested with and without the mast to check for blockage effects.

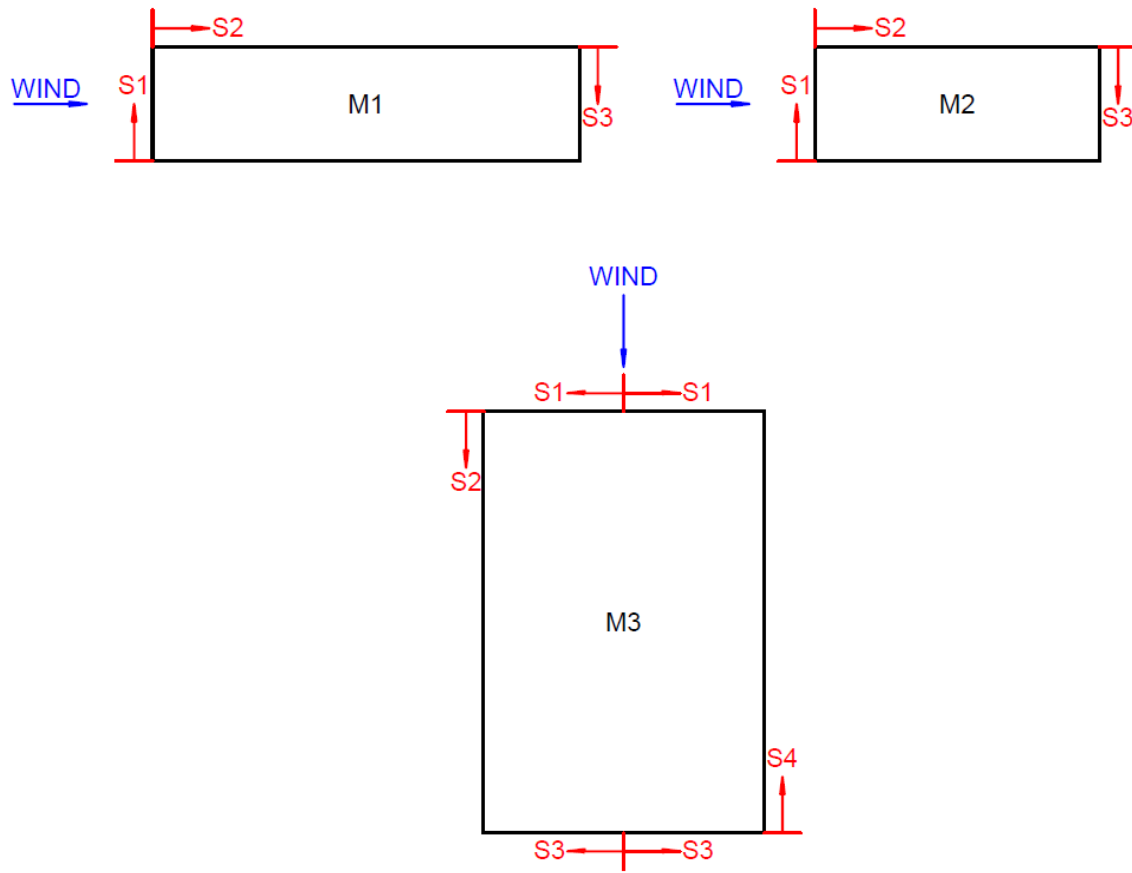


**1:25  $R/H = 0.3\%$  model with mast**

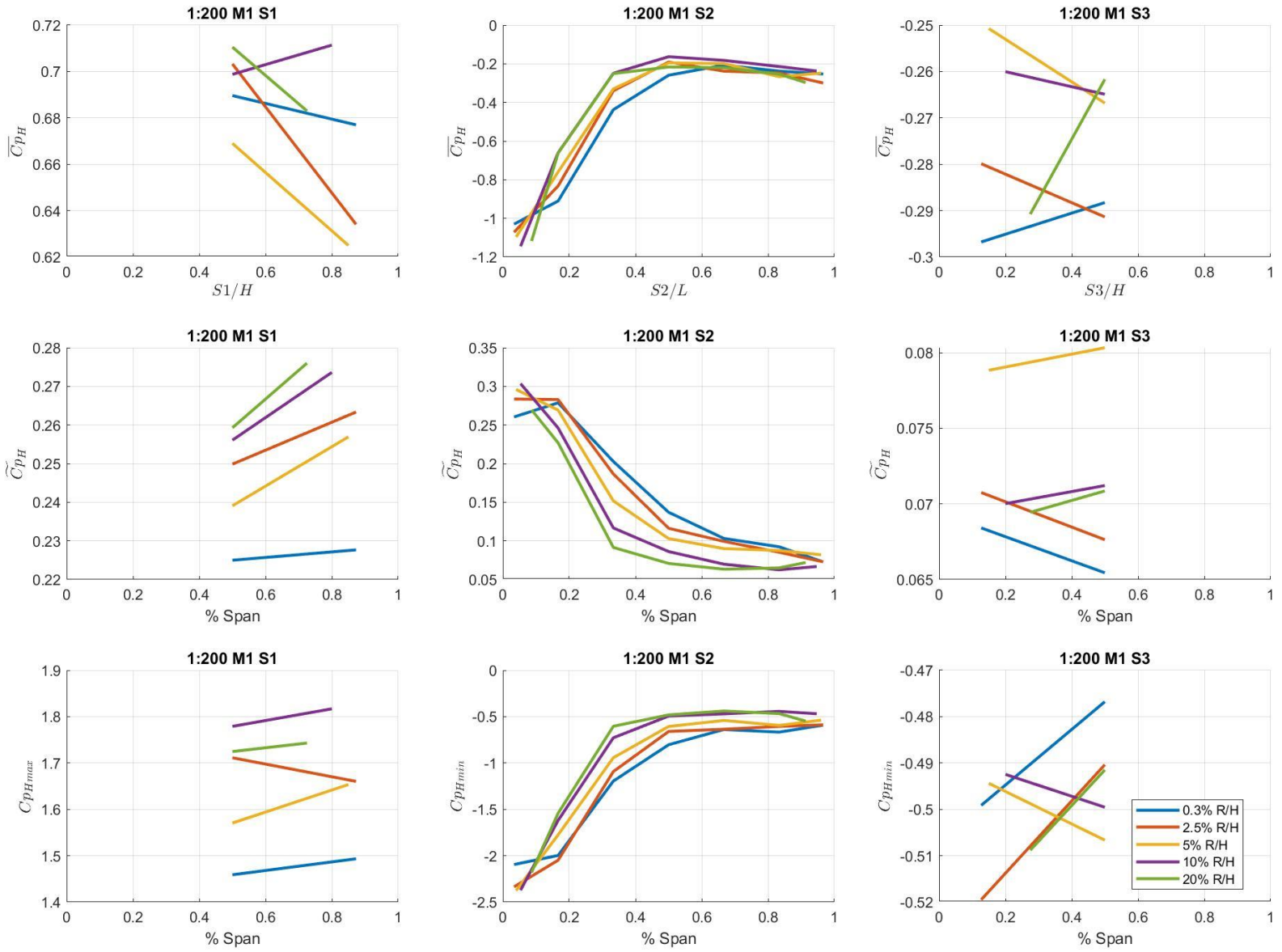
Plotted below are mean and RMS pressure coefficients for the two midlines on the model roofs as defined in chapter 4. No discernable difference is observed for 1:25 scale results, though a slight scalar offset is observed in  $\overline{Cp_H}$  for the 1:200 scale results. However, differences were within uncertainty bounds, and thus it was assumed that the mast posed no blockage issues

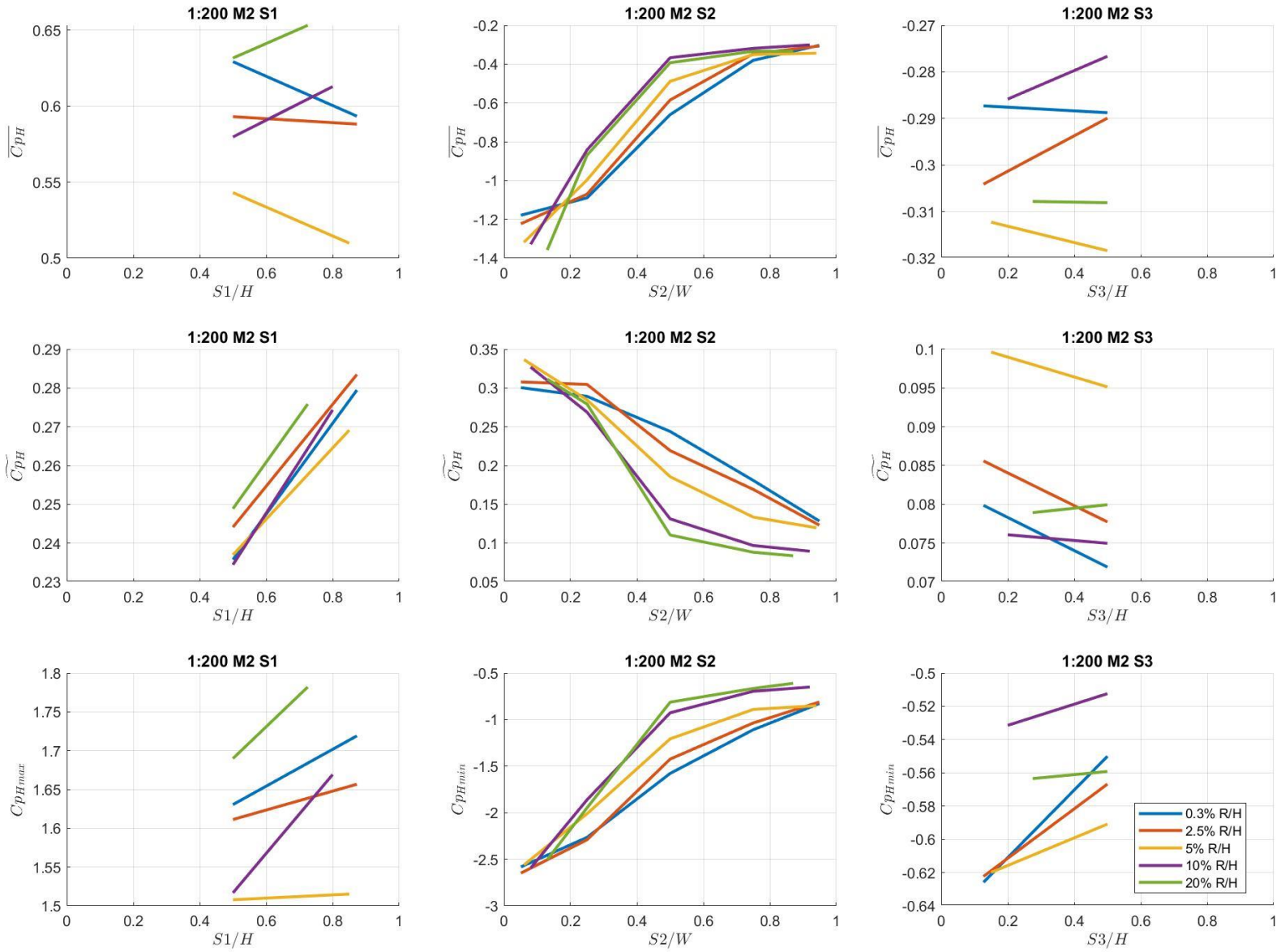


### Appendix E: Midline plots

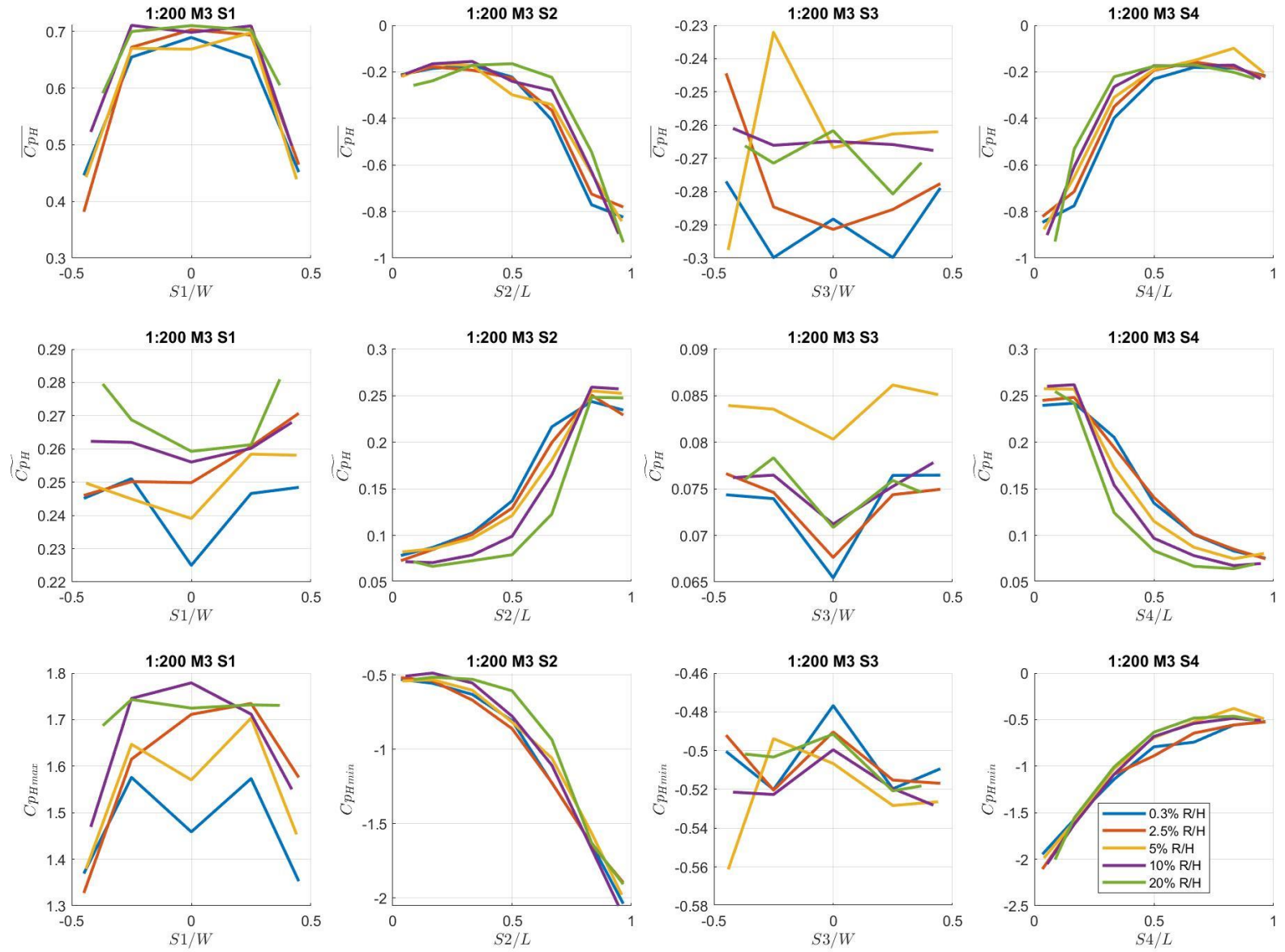


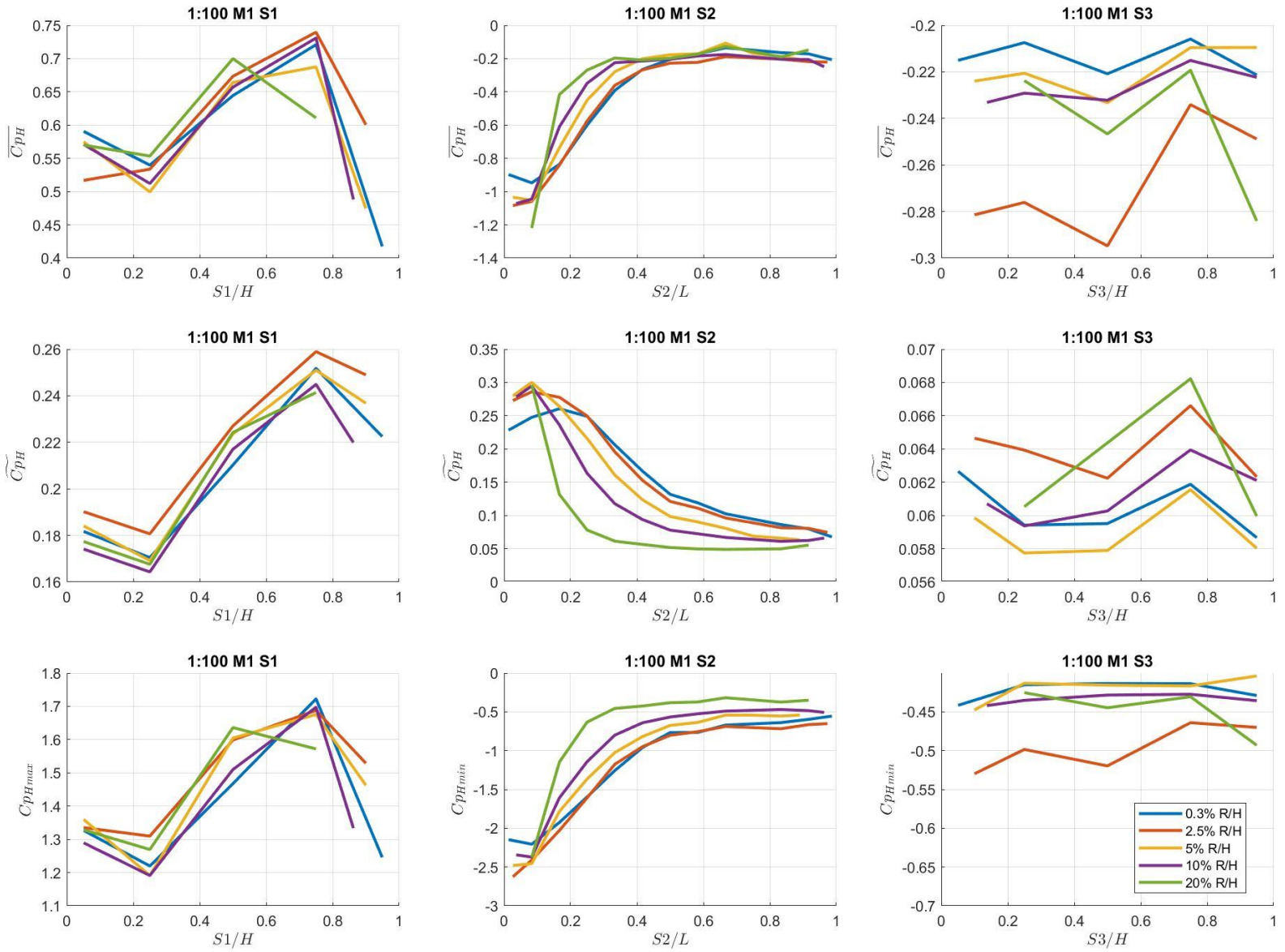
### Midline Sign Conventions

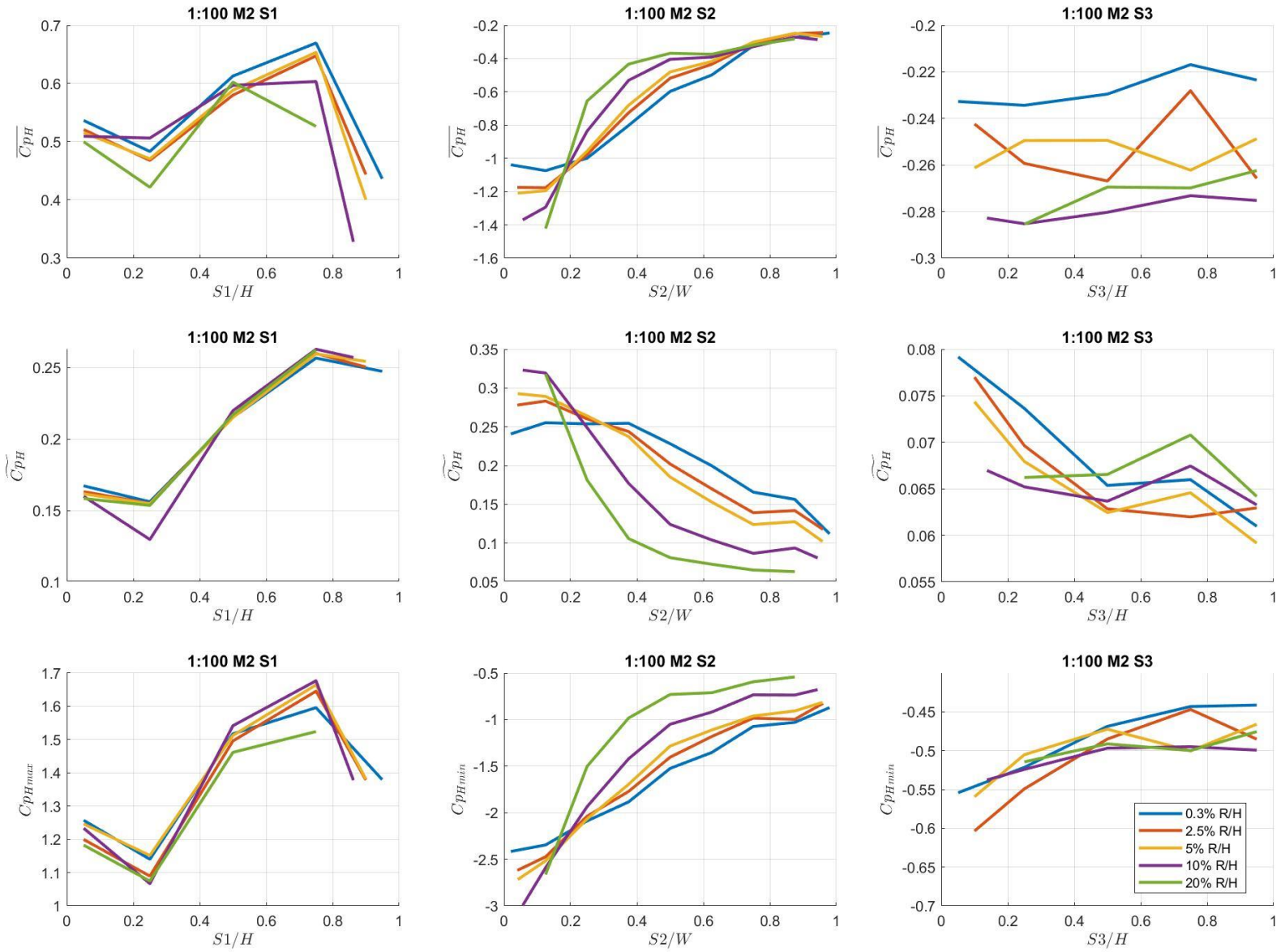


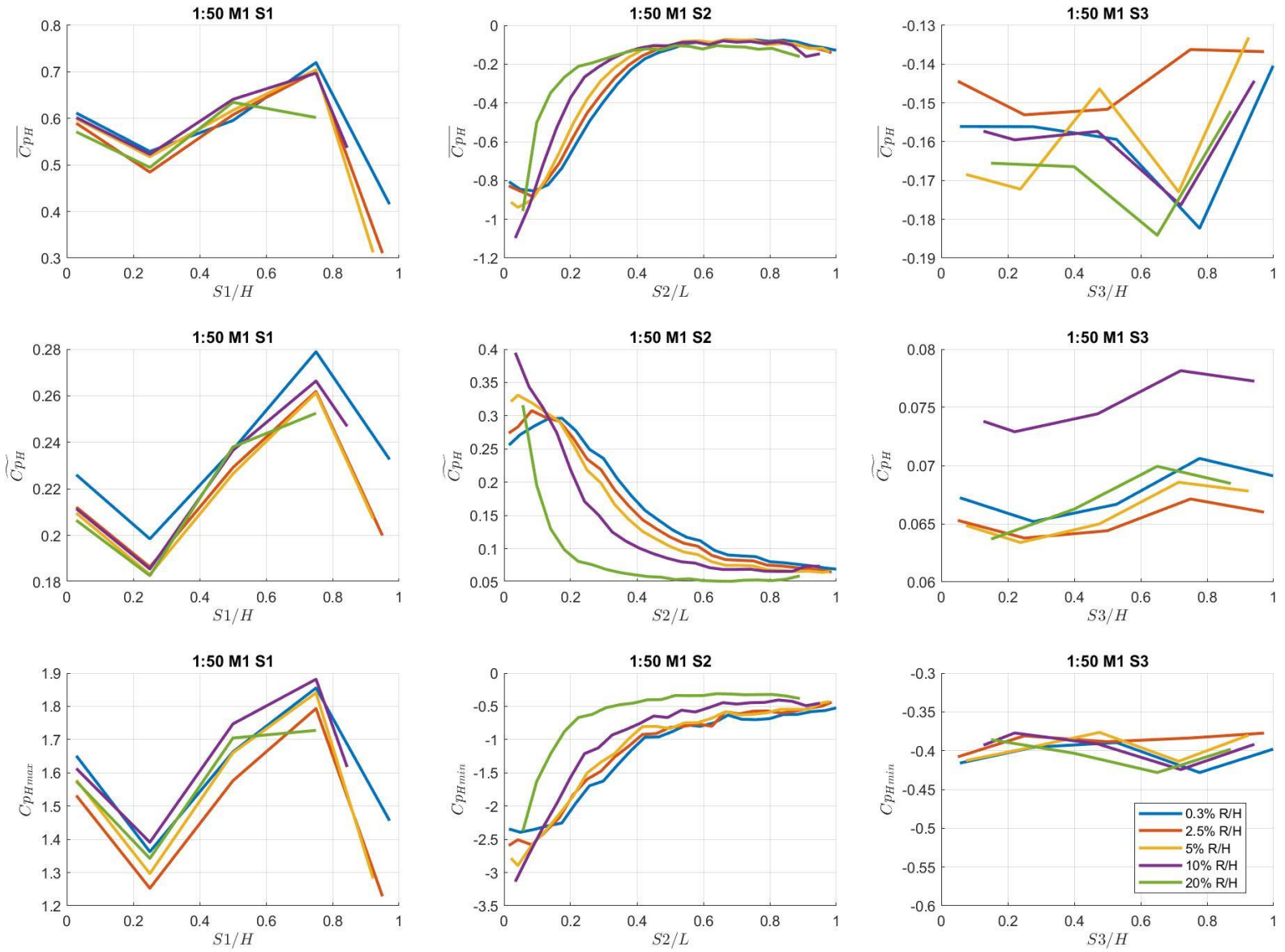




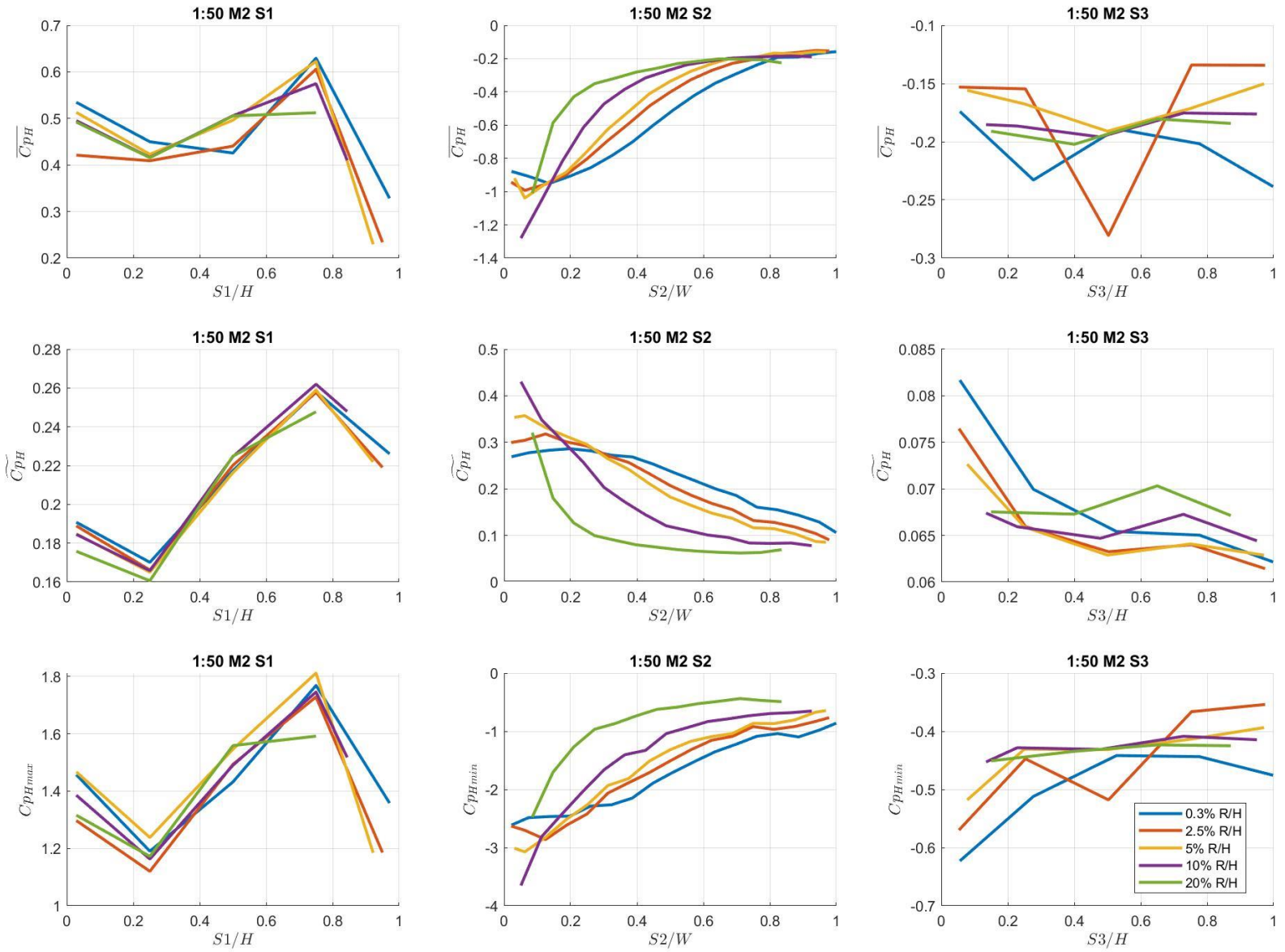


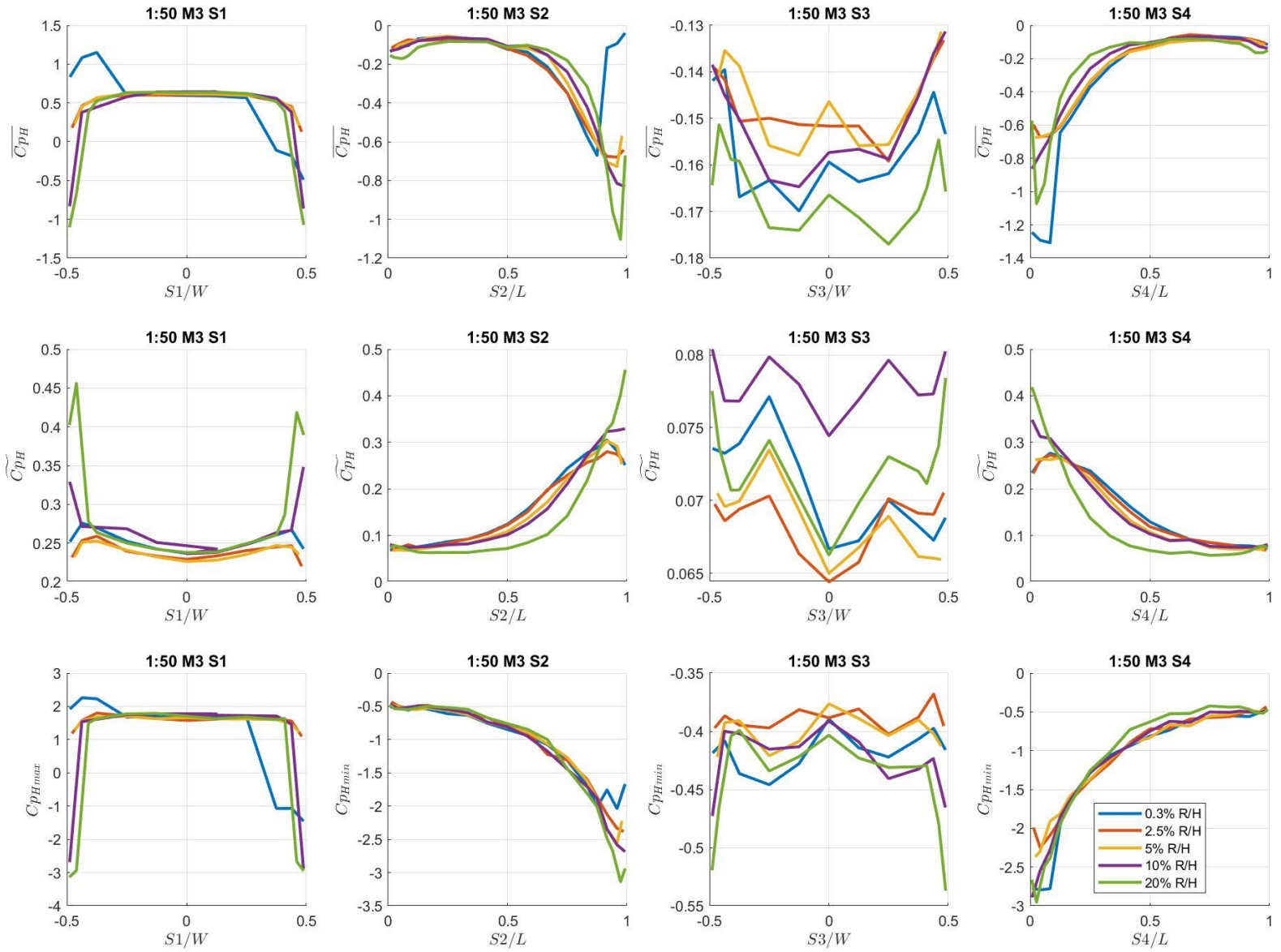


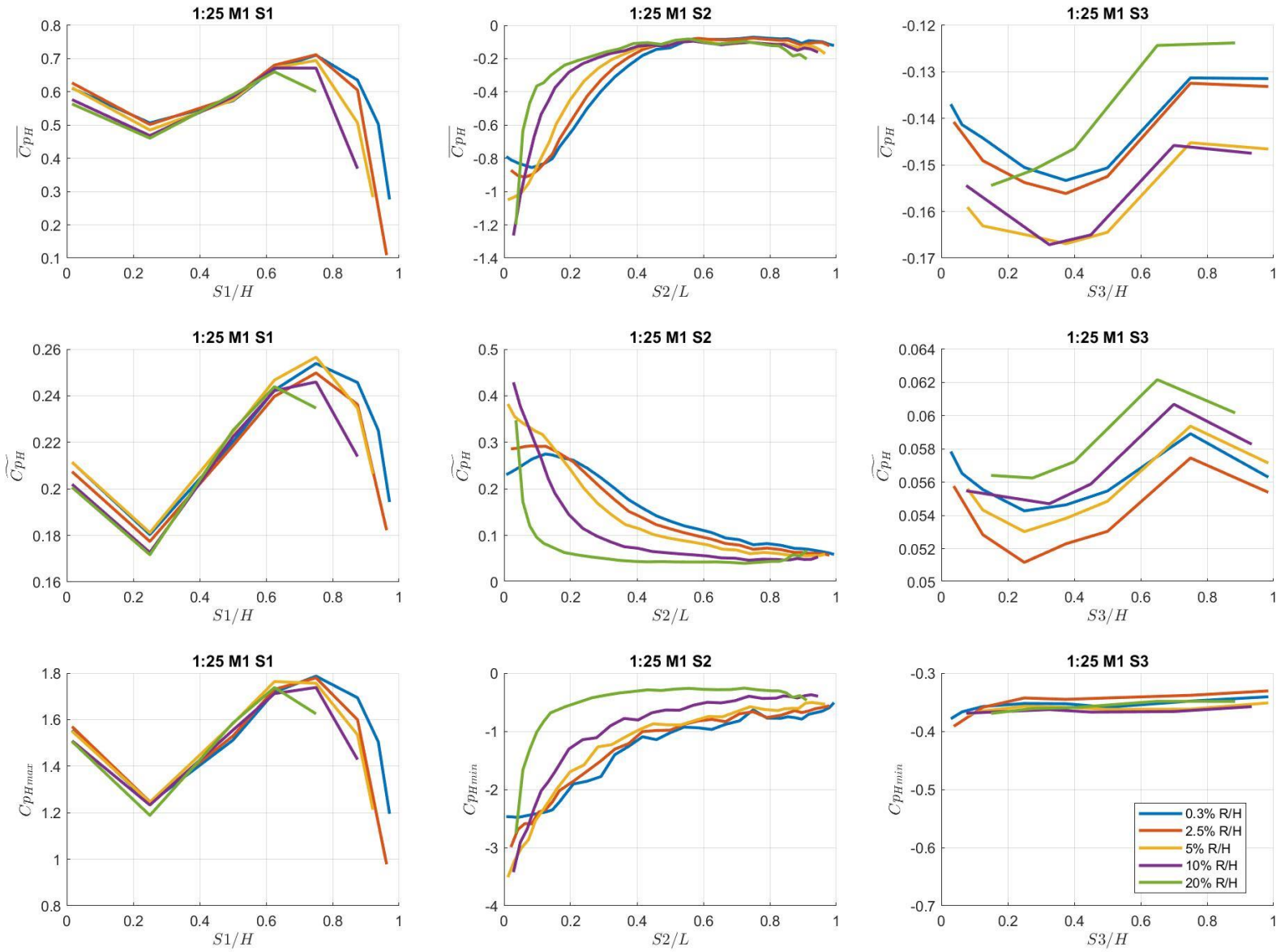


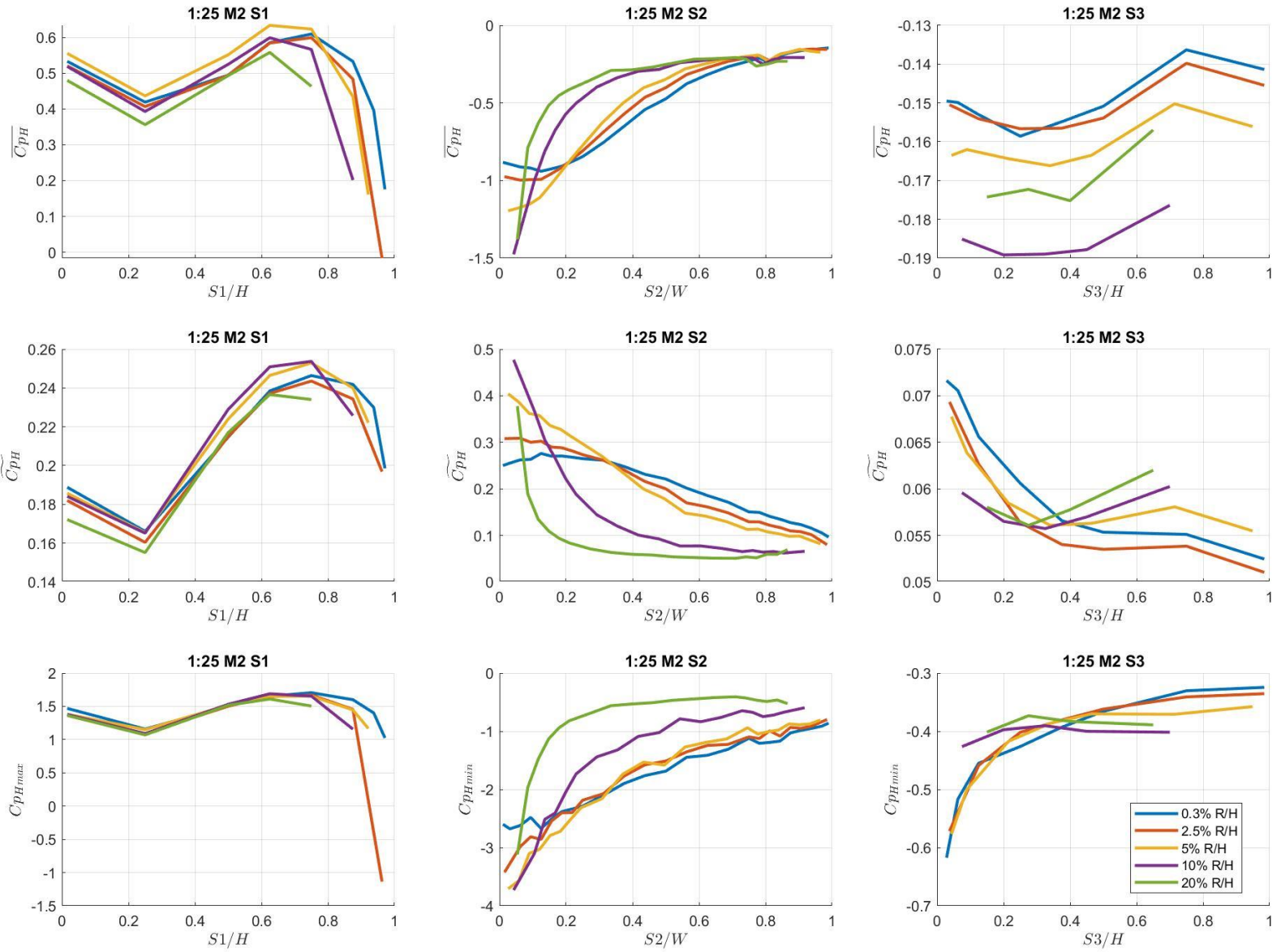






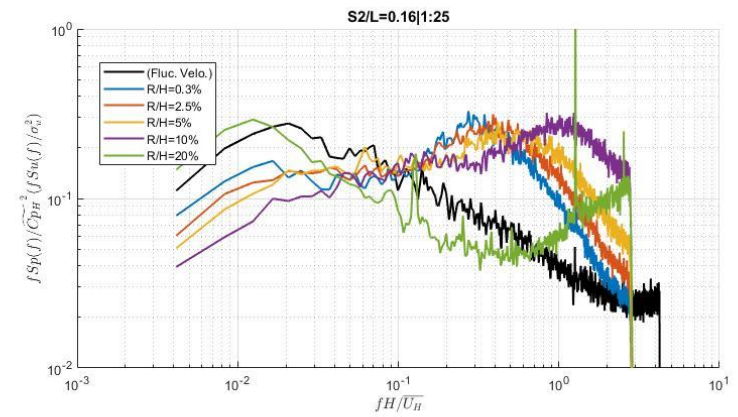
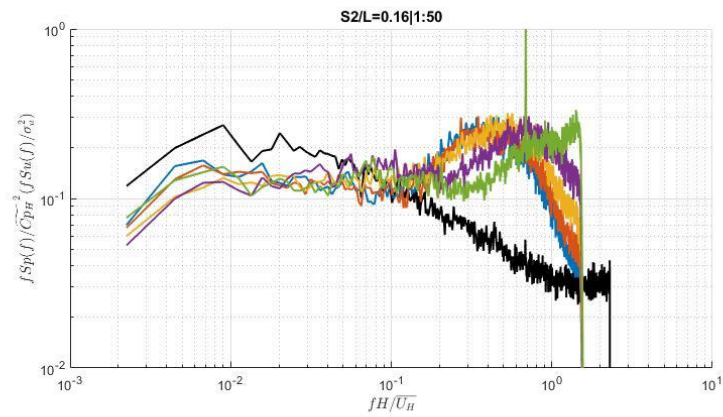
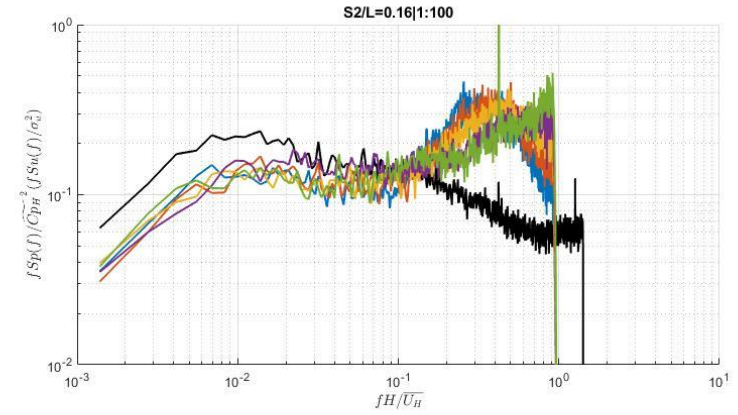
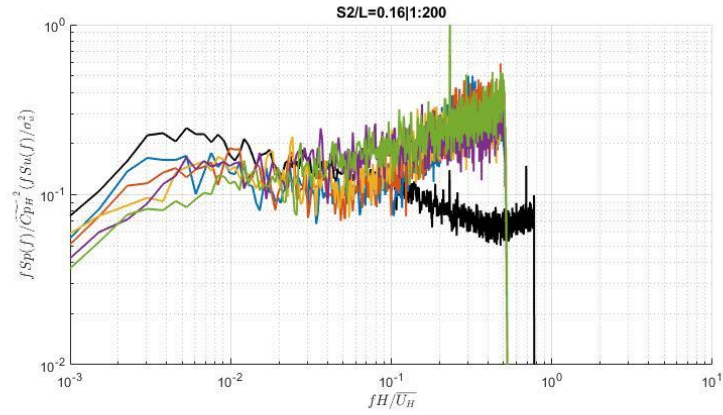


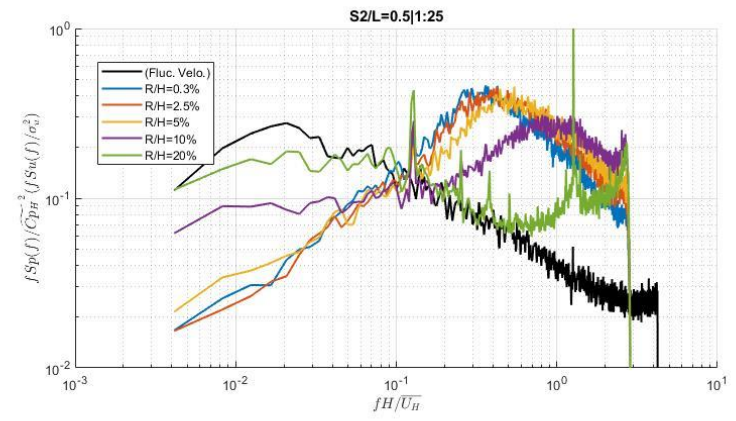
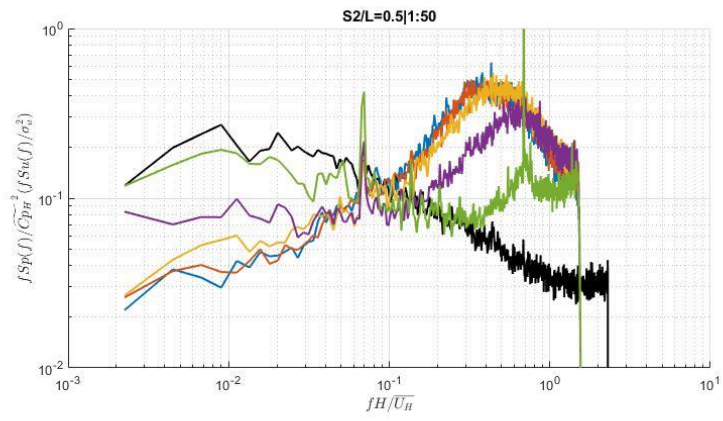
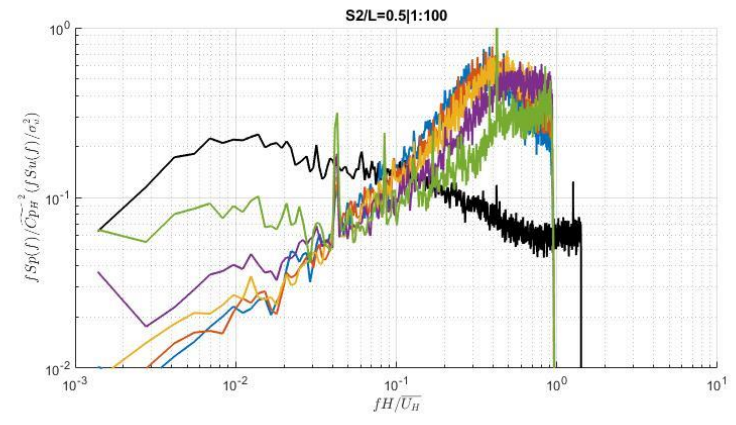
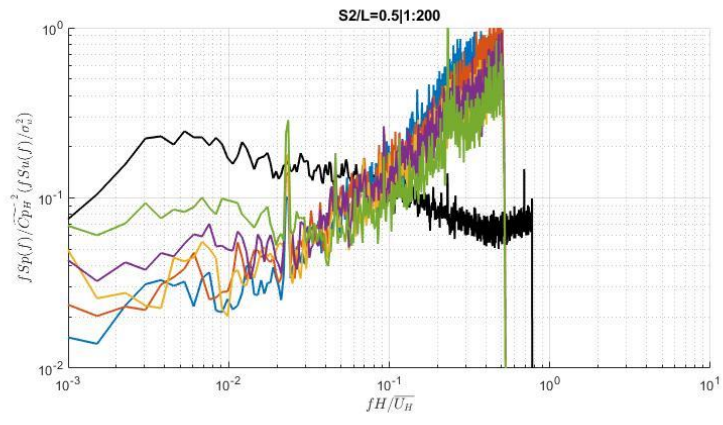


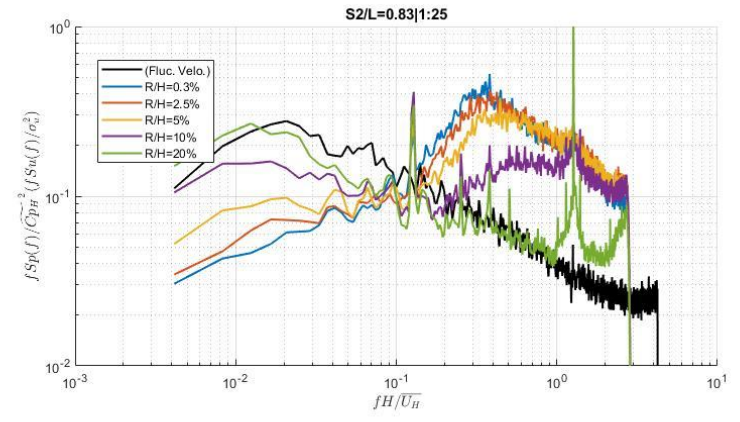
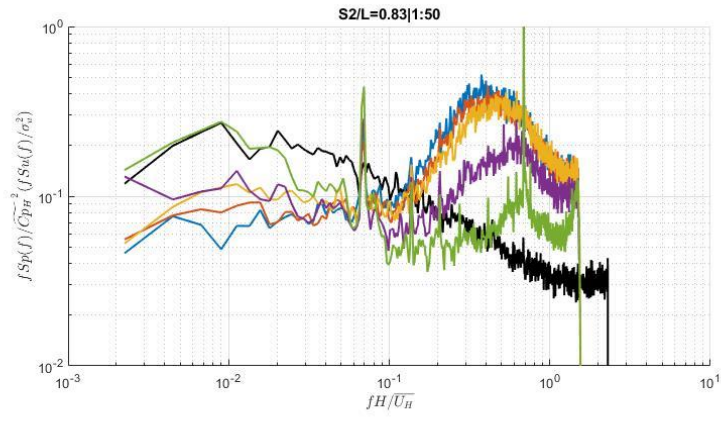
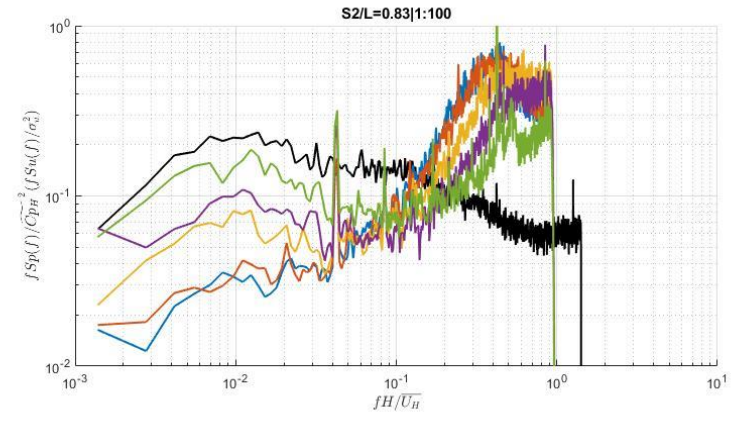
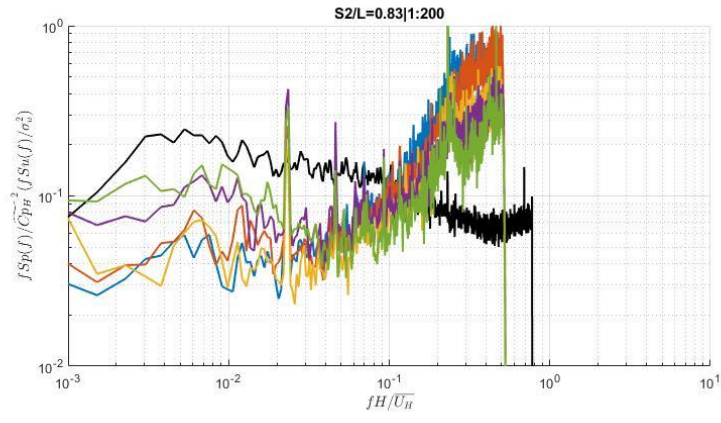




## Appendix F: Fluctuating pressure coefficient spectra along M1

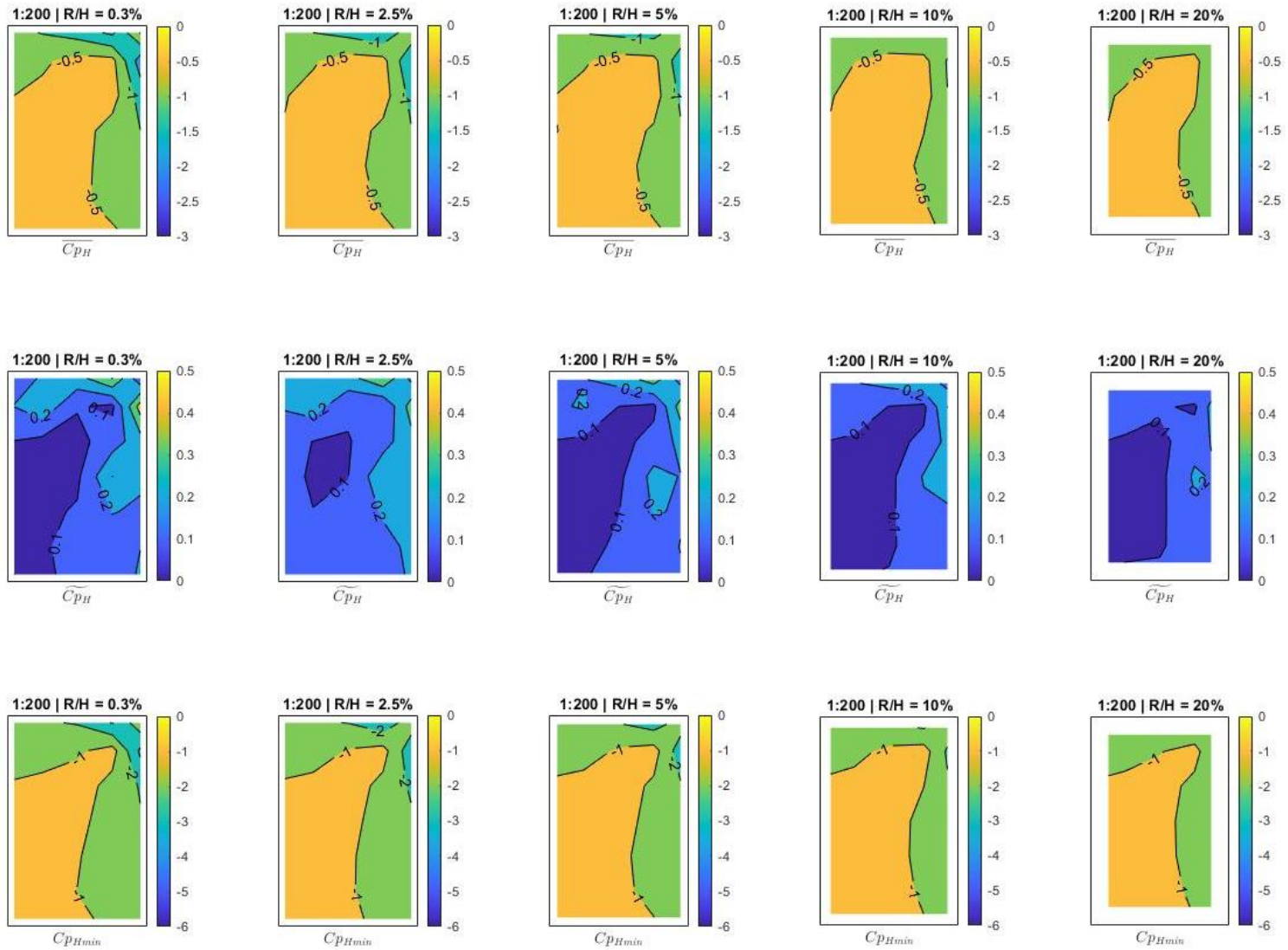


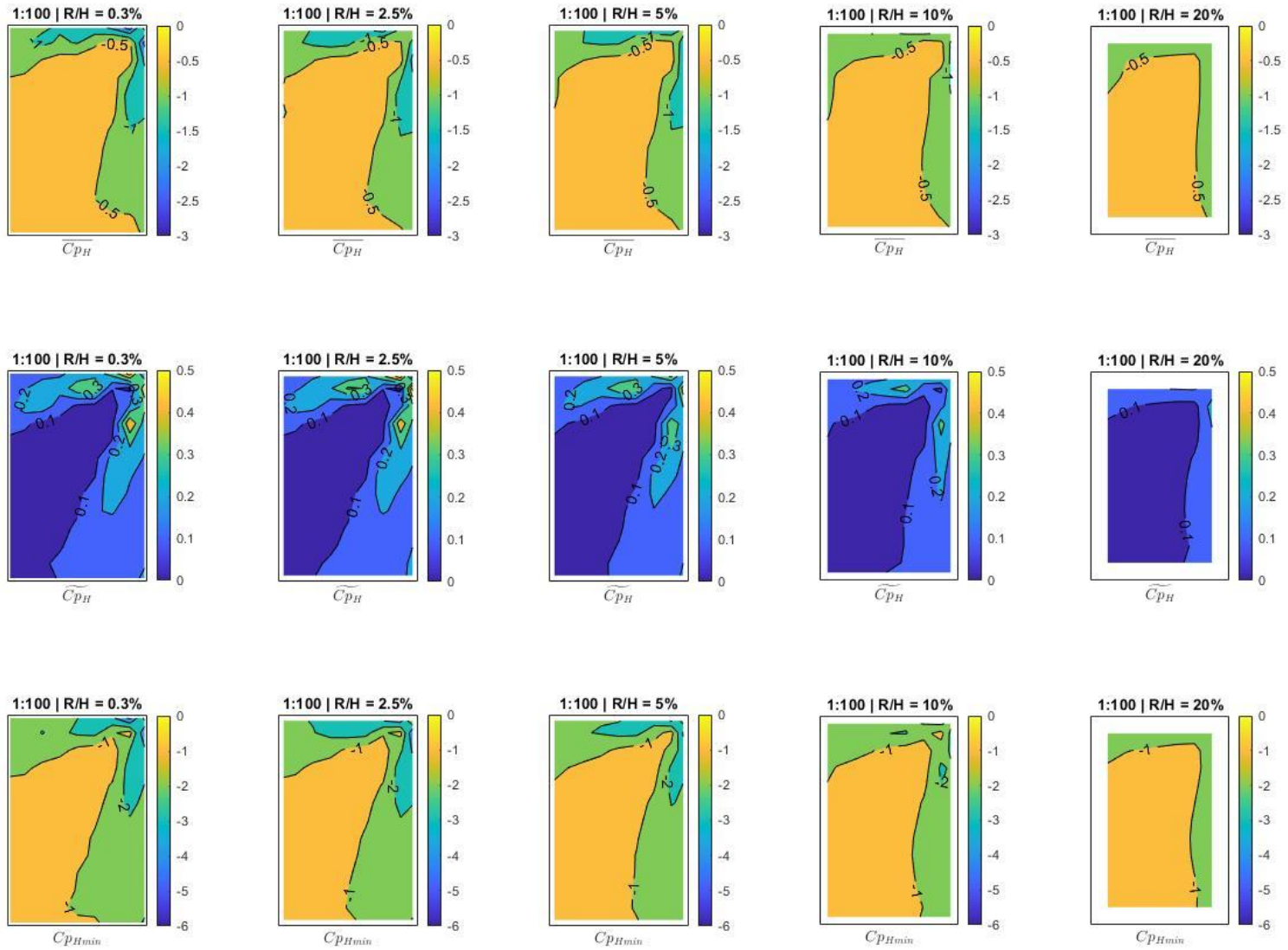


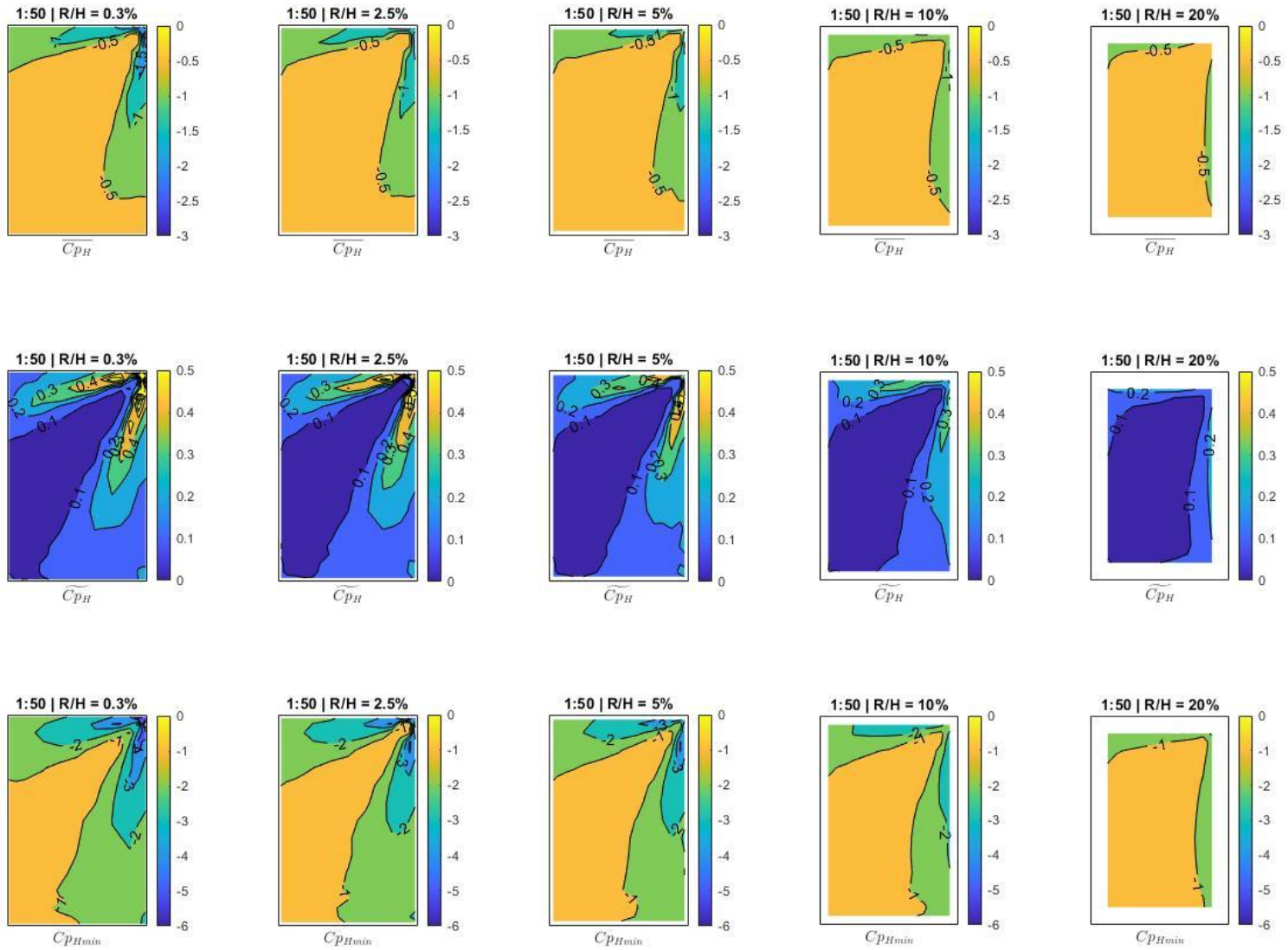




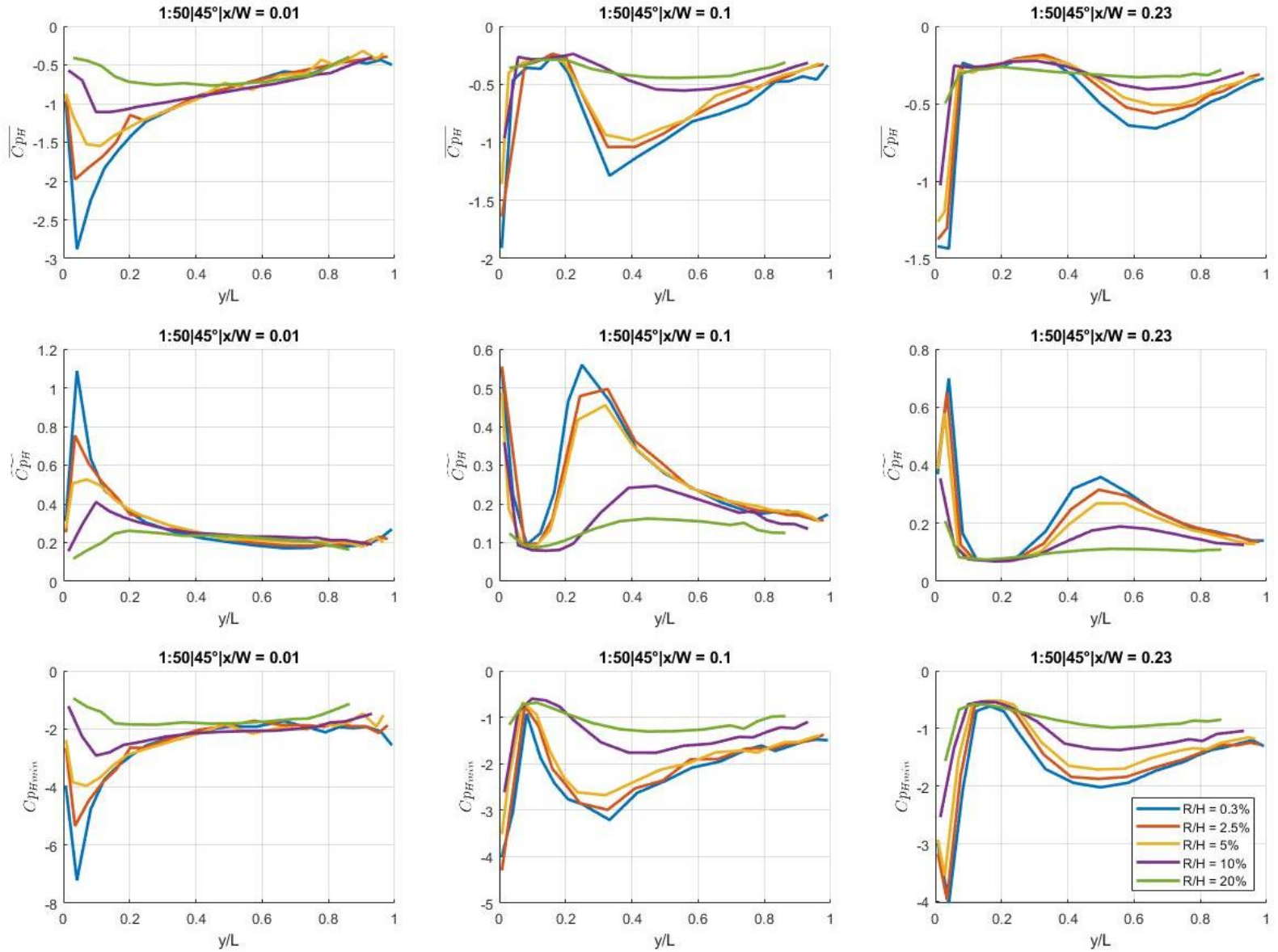
### Appendix G: Roof pressure contours at $\theta = 45^\circ$



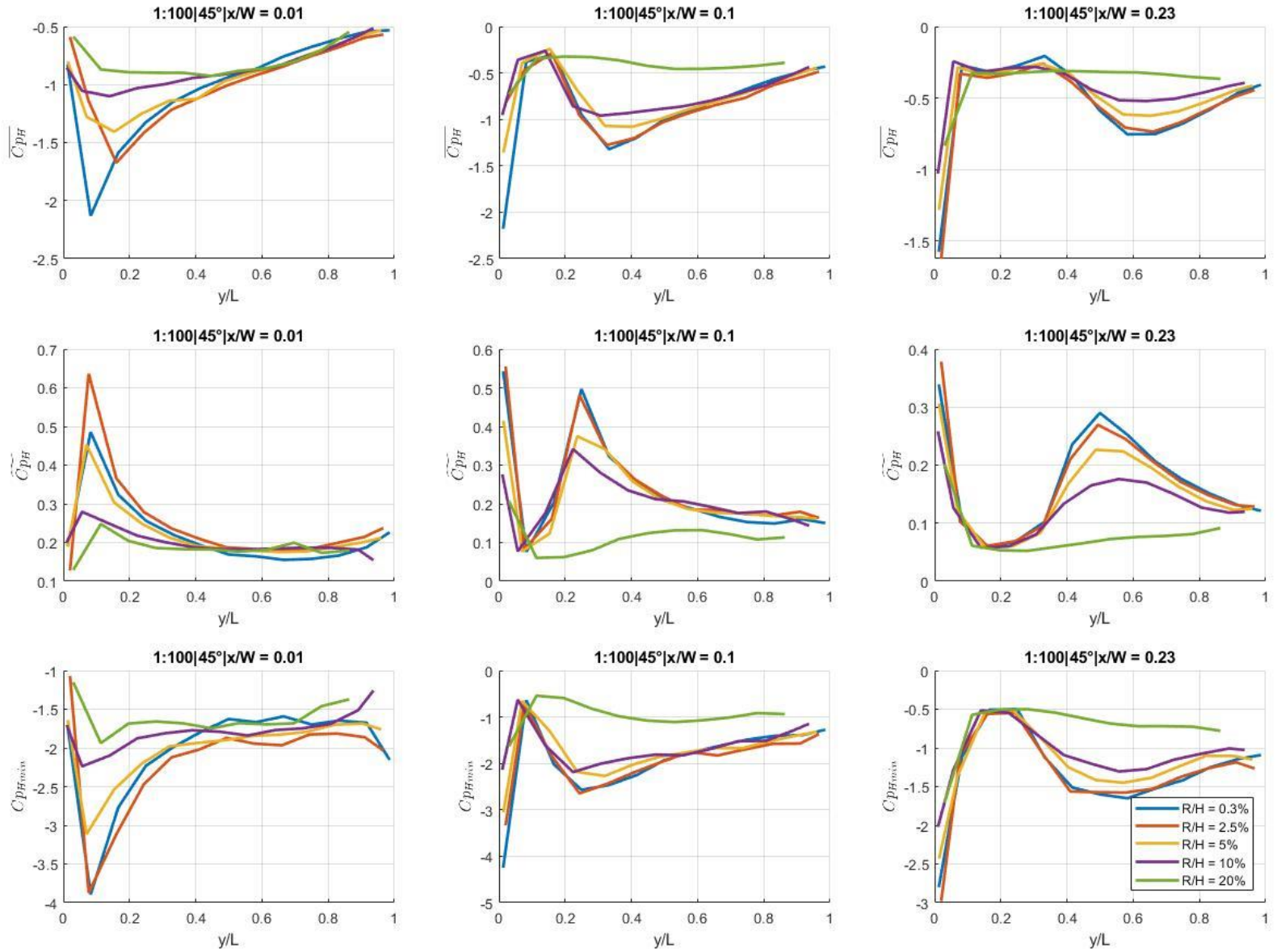




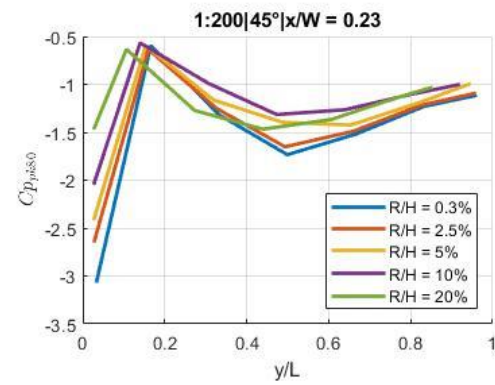
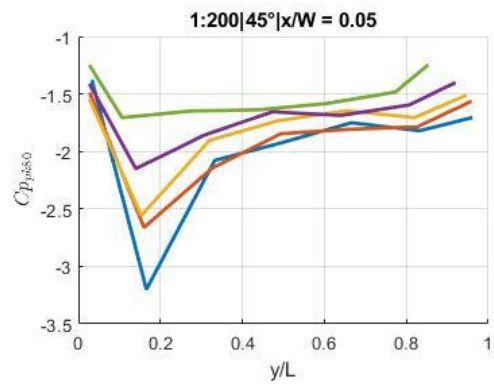
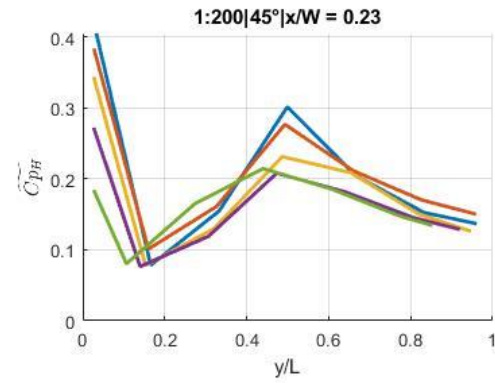
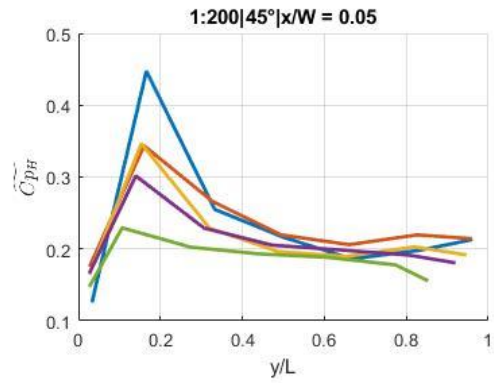
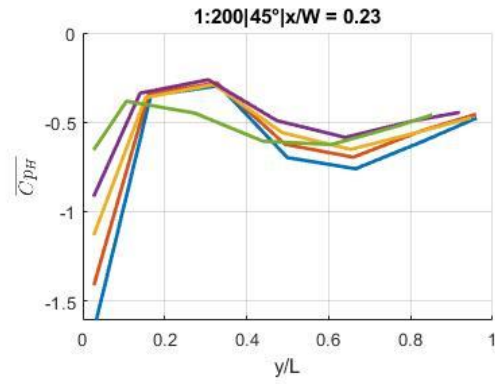
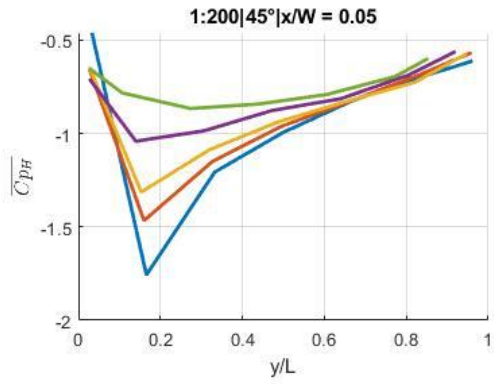
## Appendix H: Corner line $C_{pH}$ plots



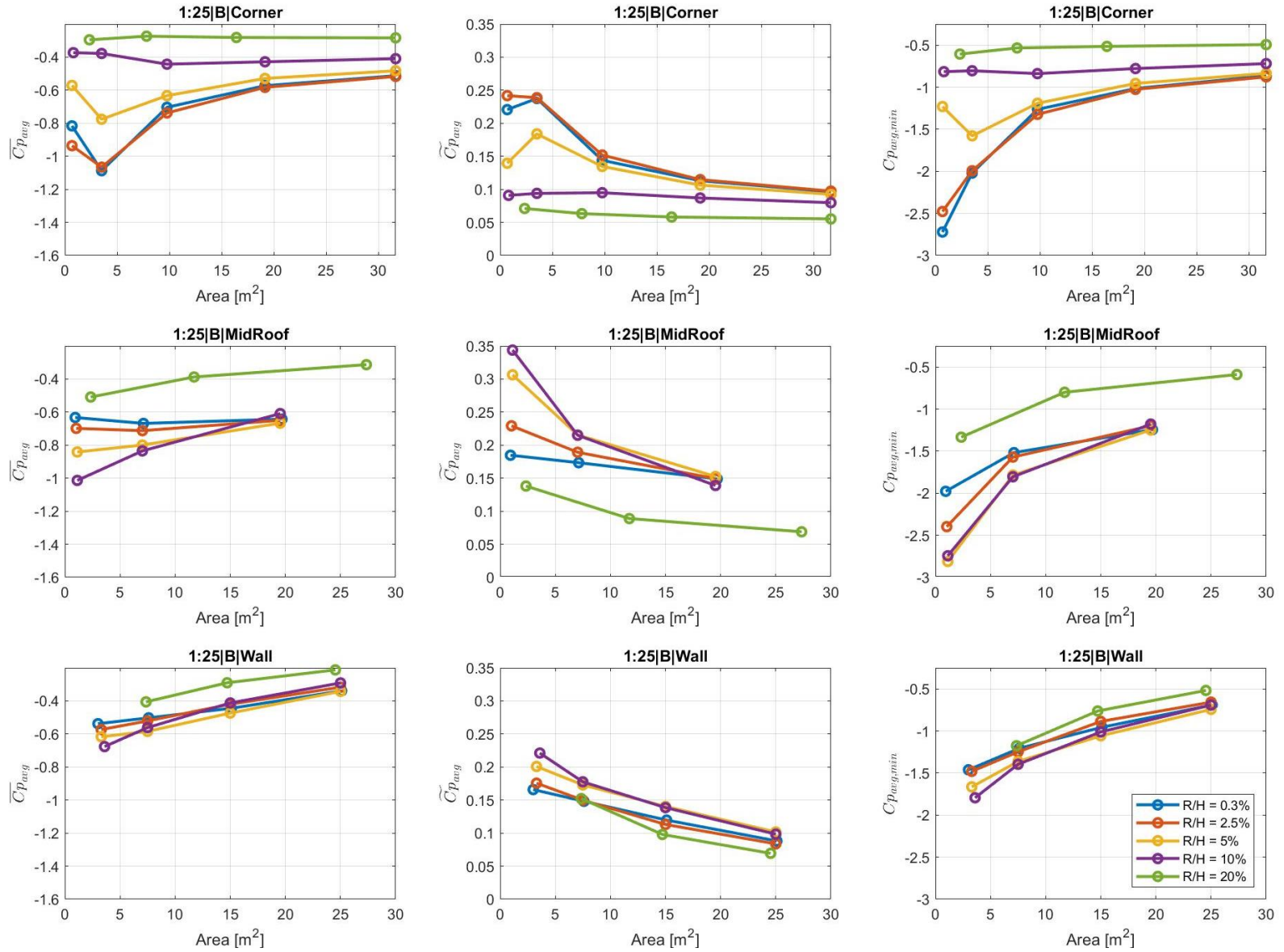


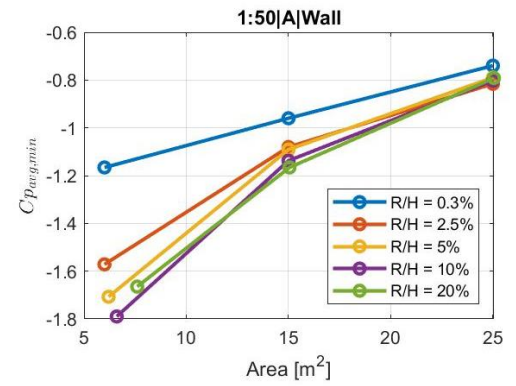
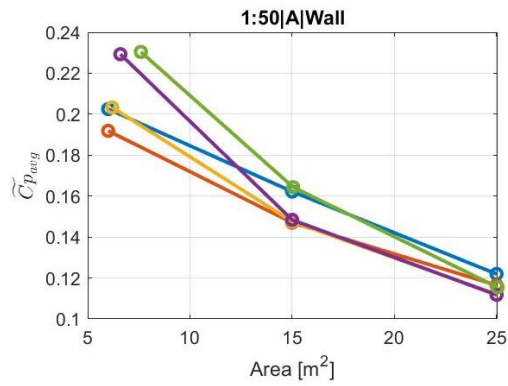
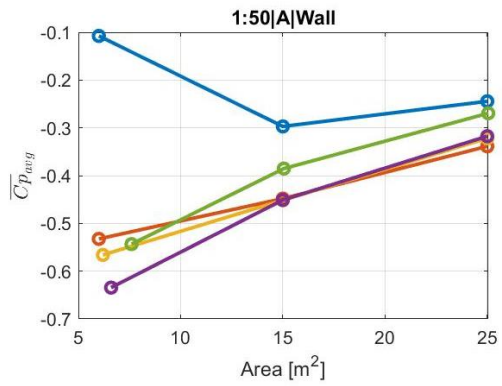
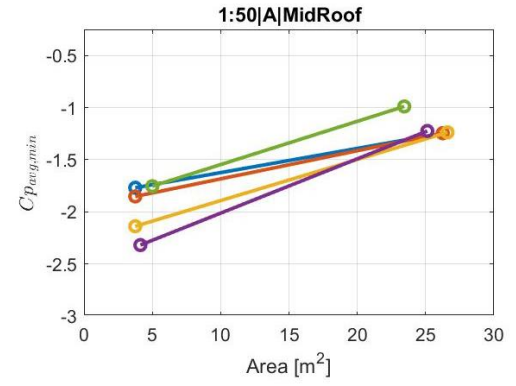
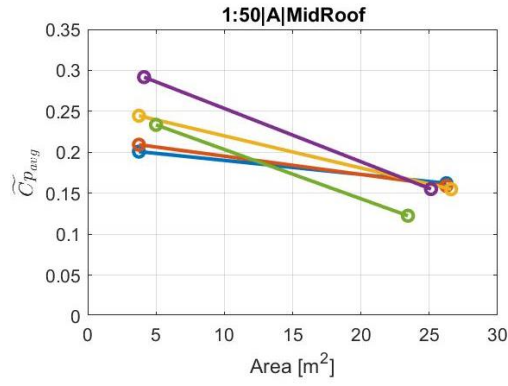
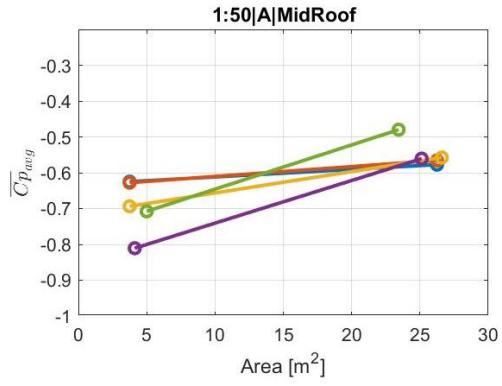
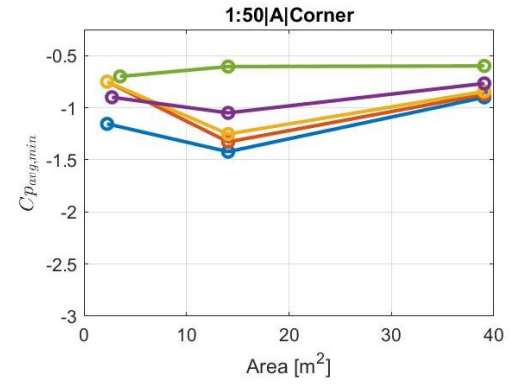
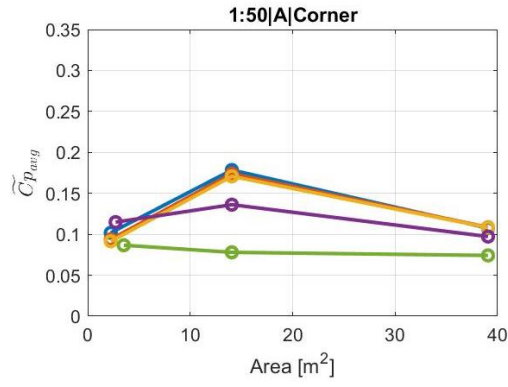
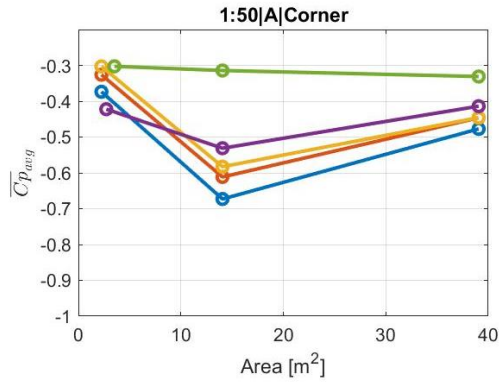


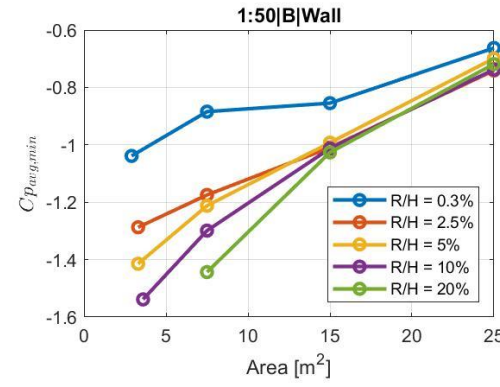
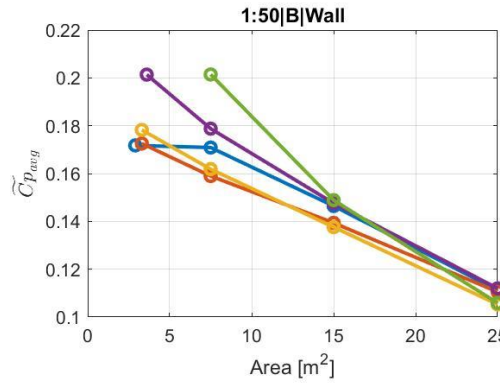
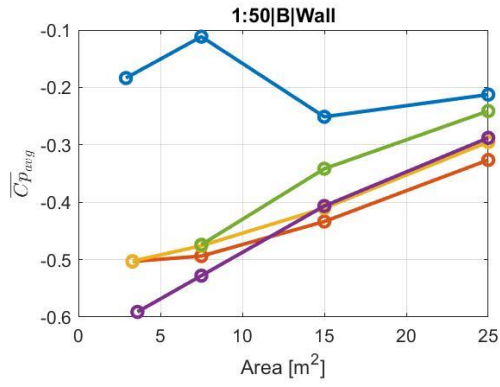
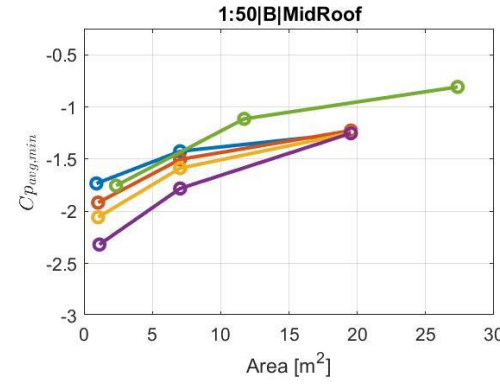
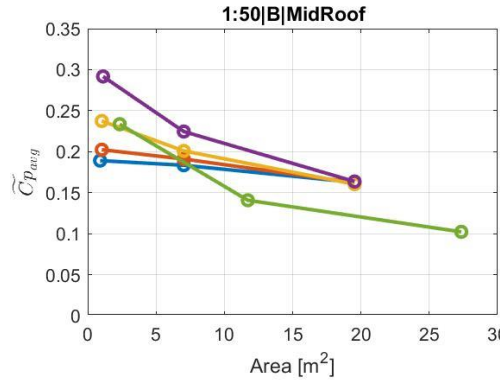
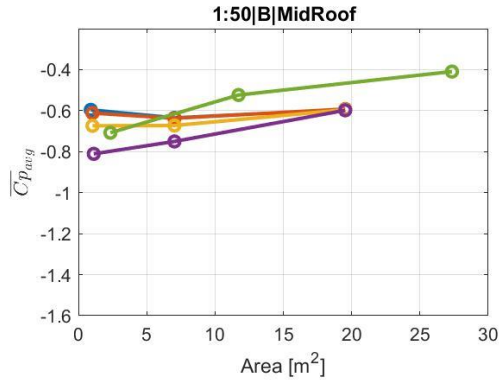
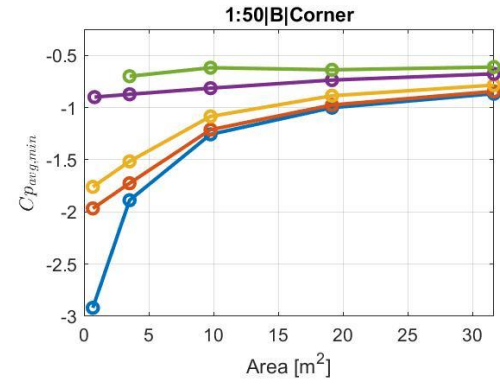
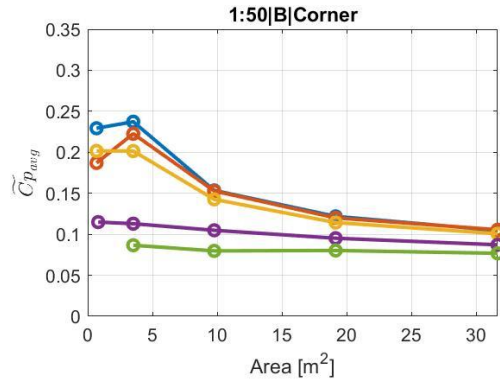
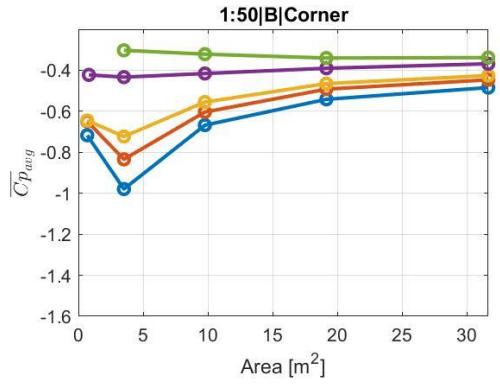


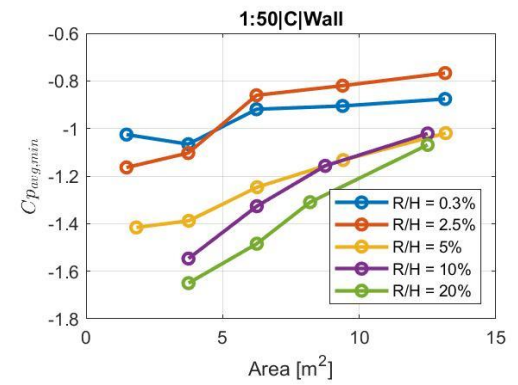
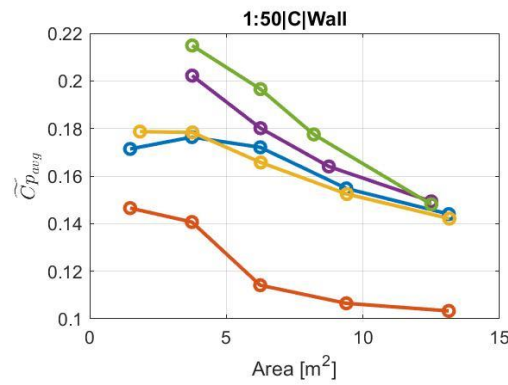
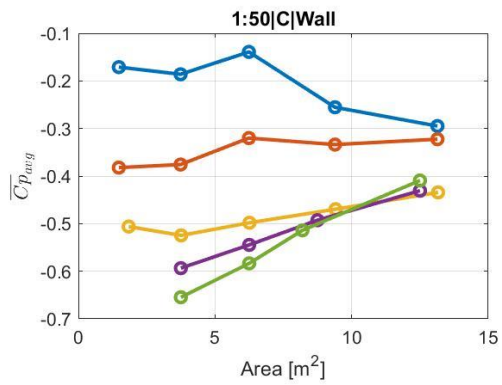
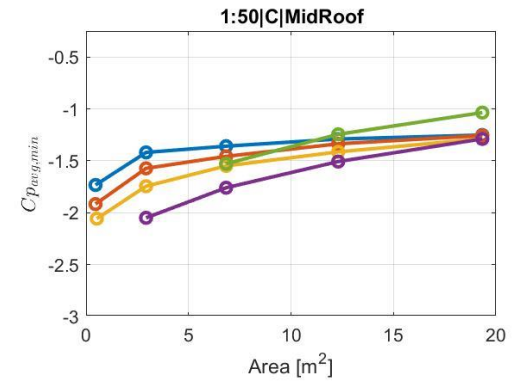
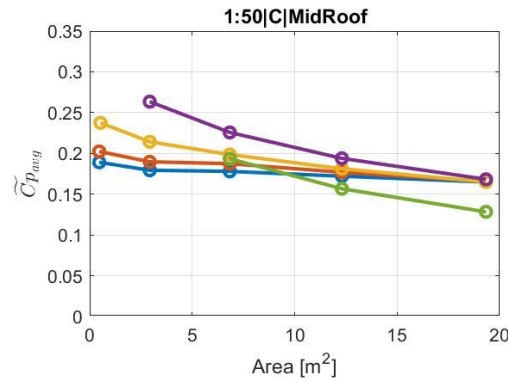
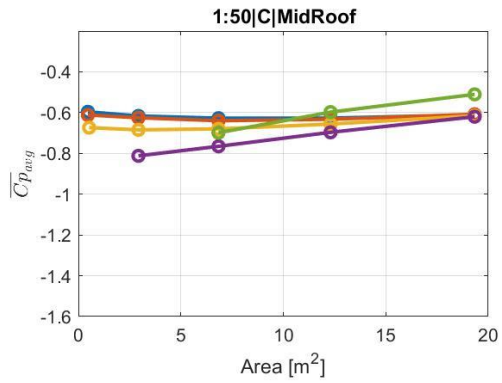
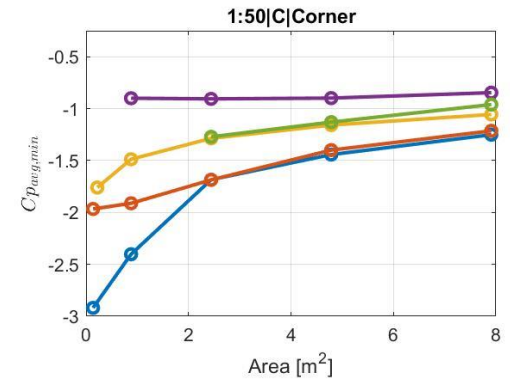
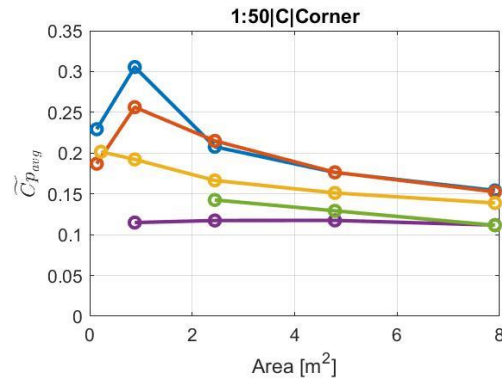
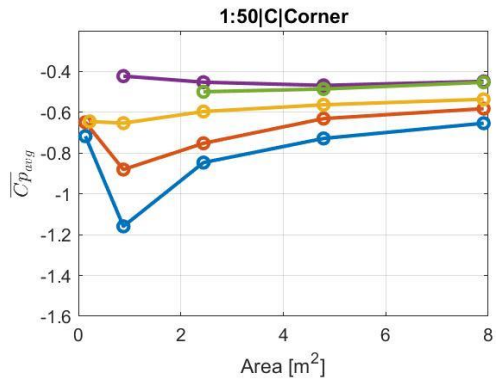


## Appendix I: Area-averaged pressure coefficients

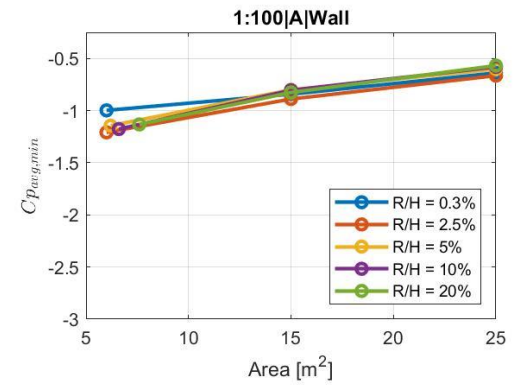
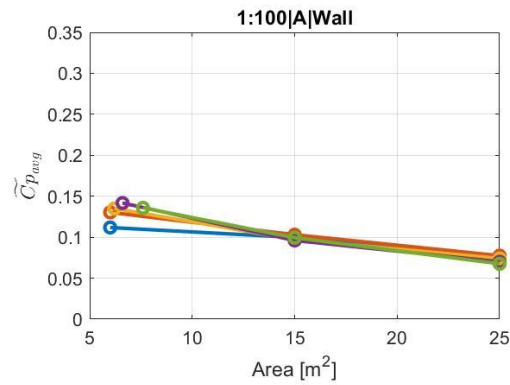
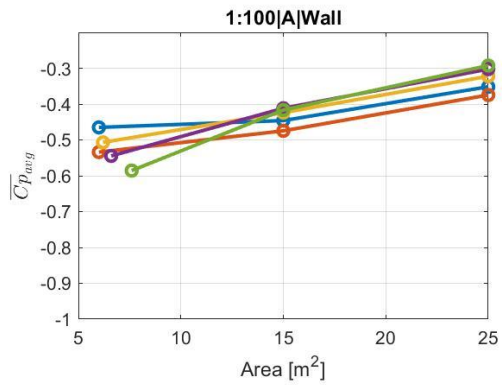
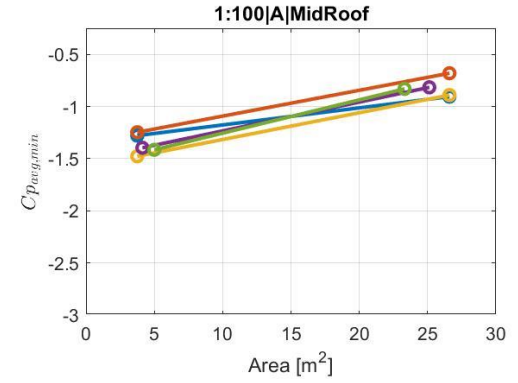
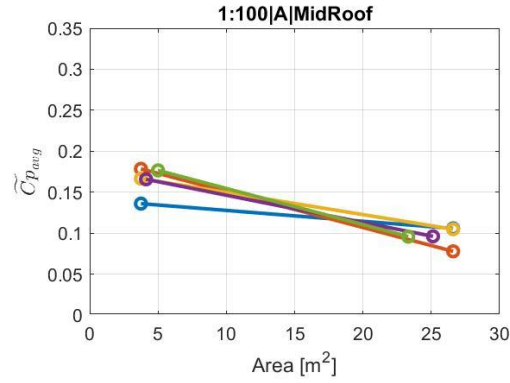
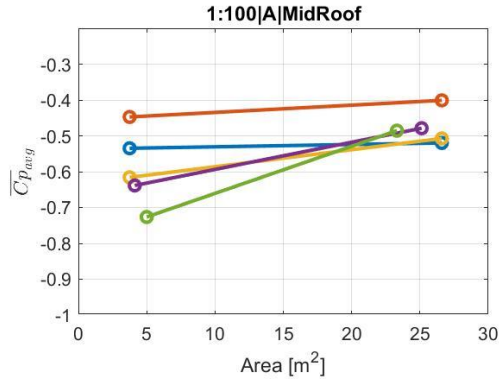
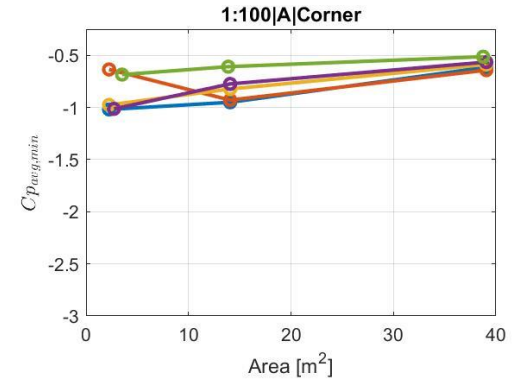
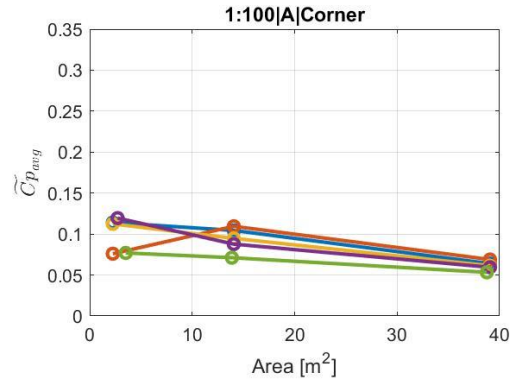
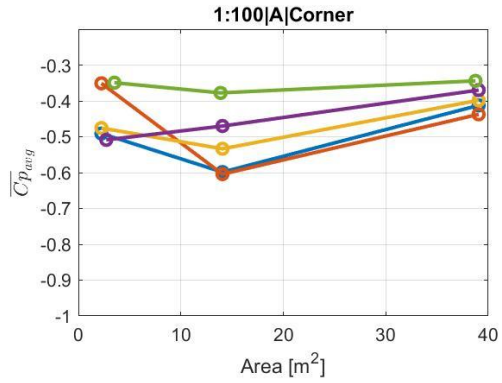


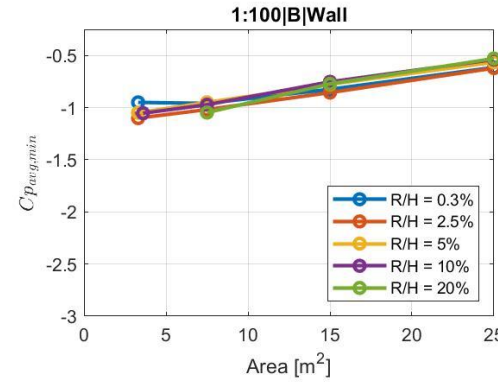
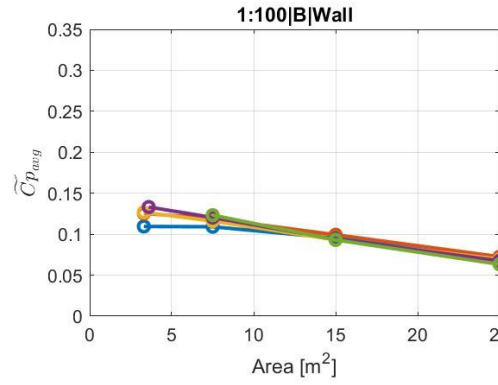
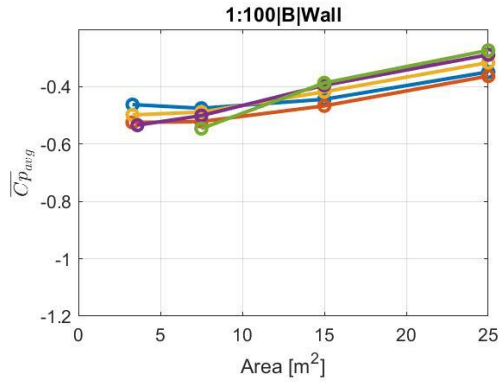
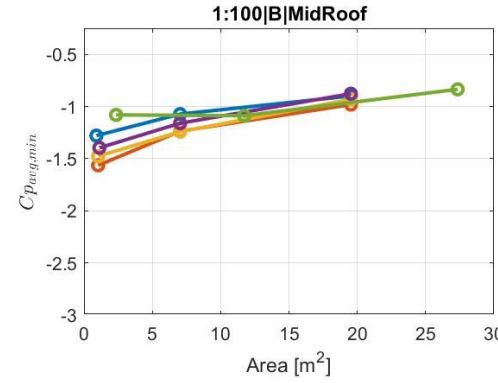
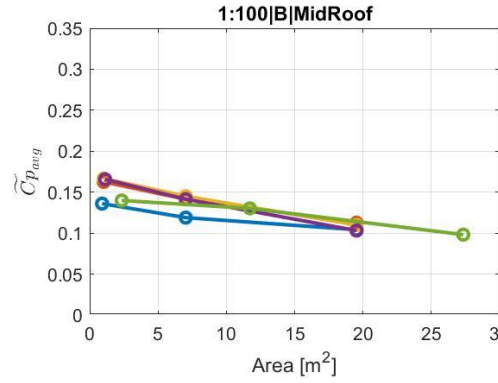
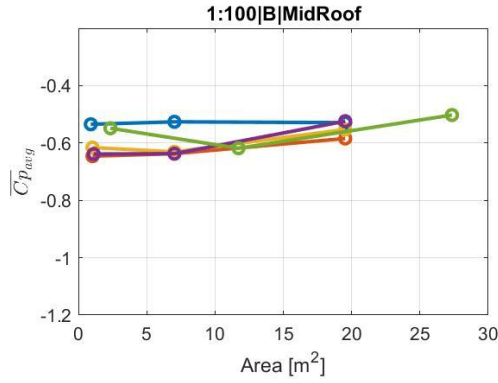
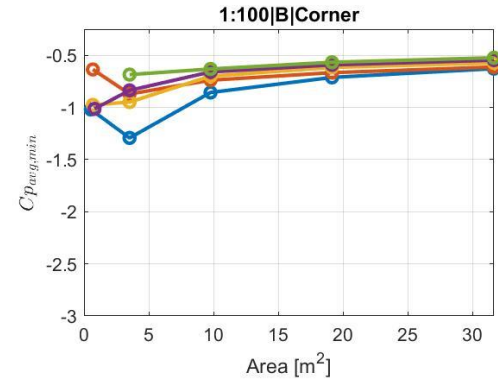
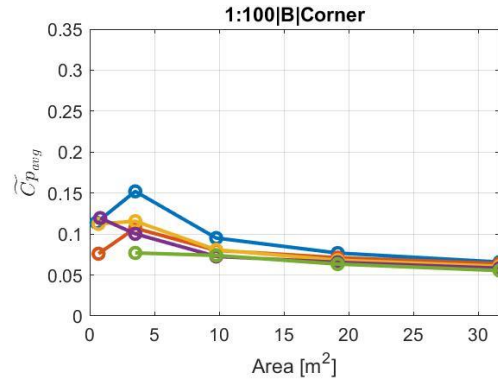
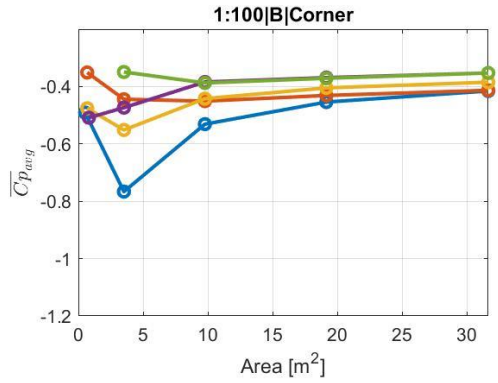


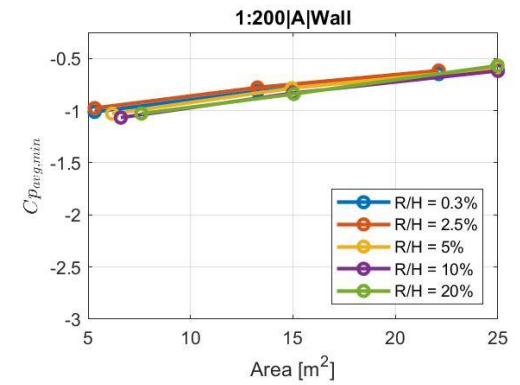
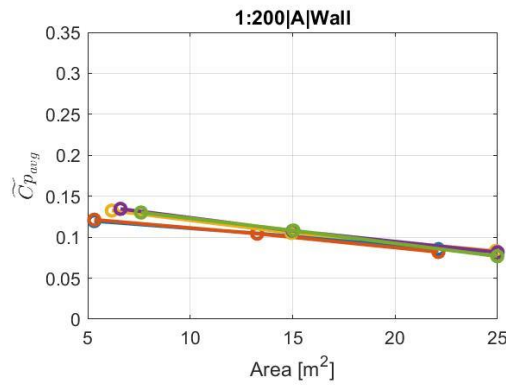
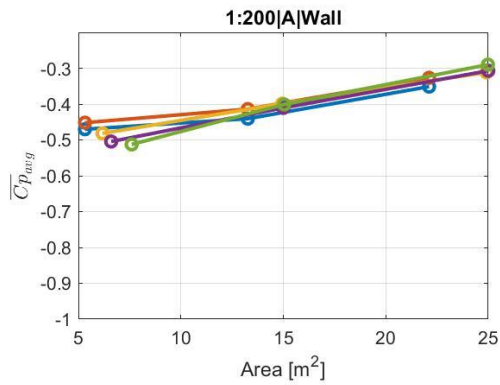
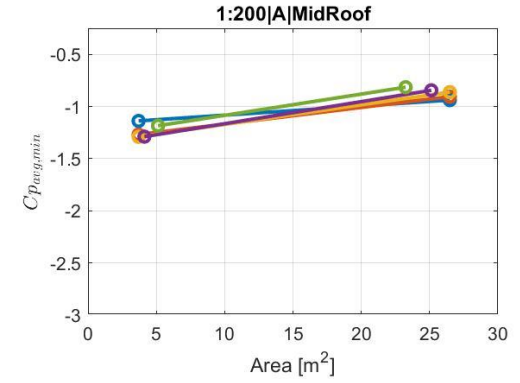
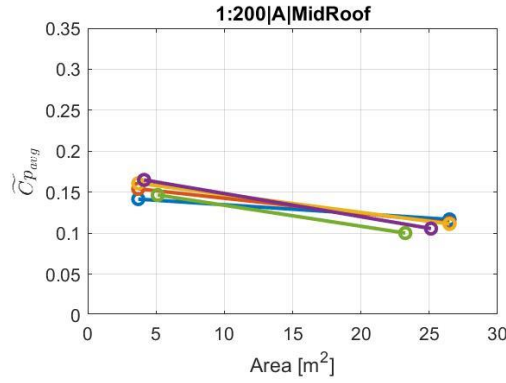
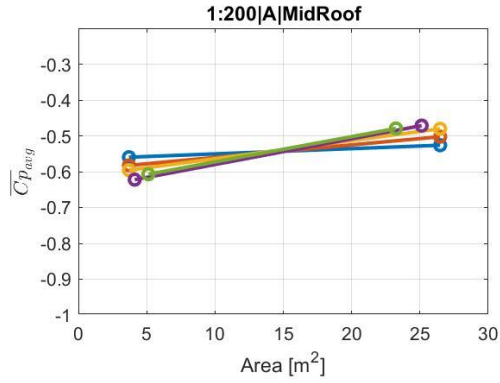
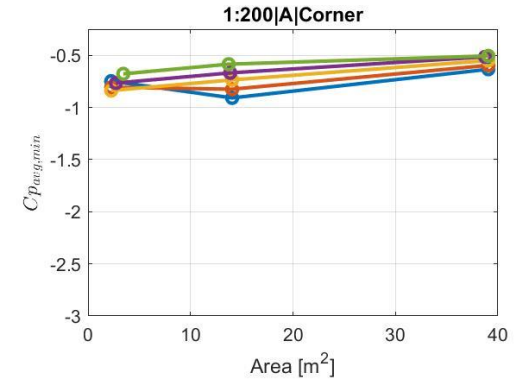
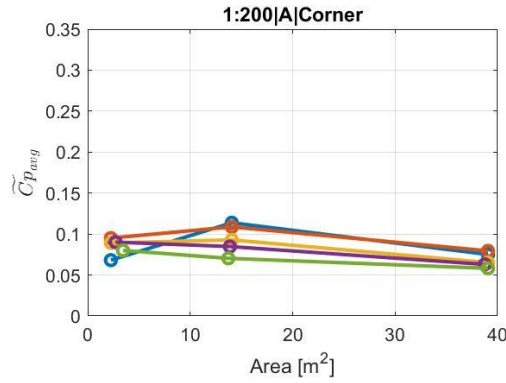
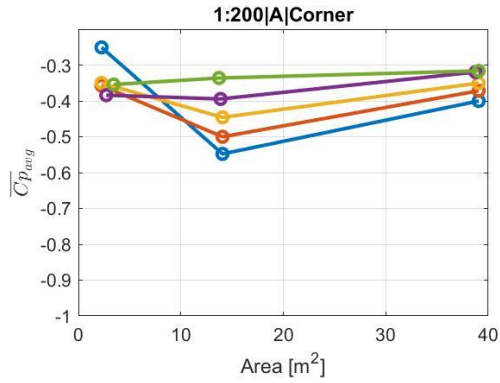






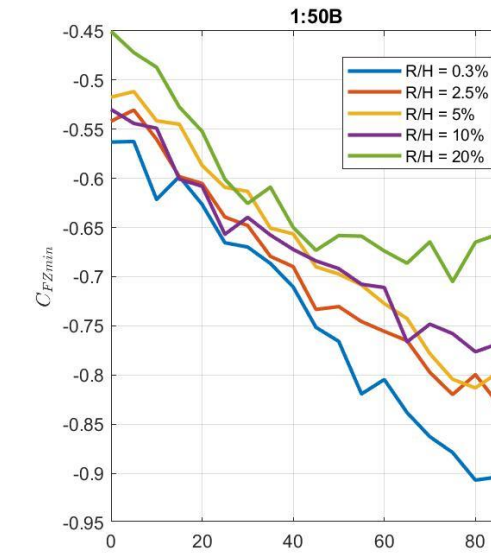
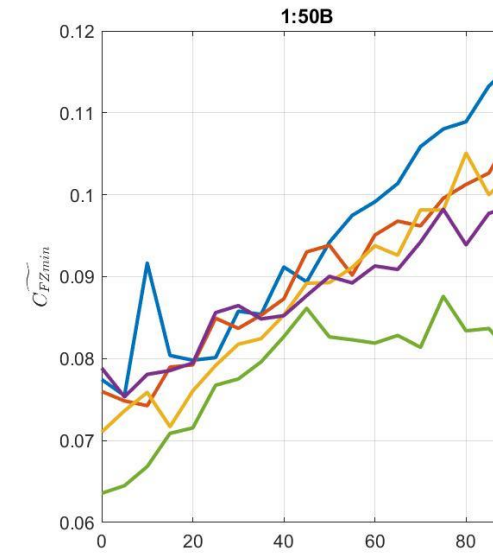
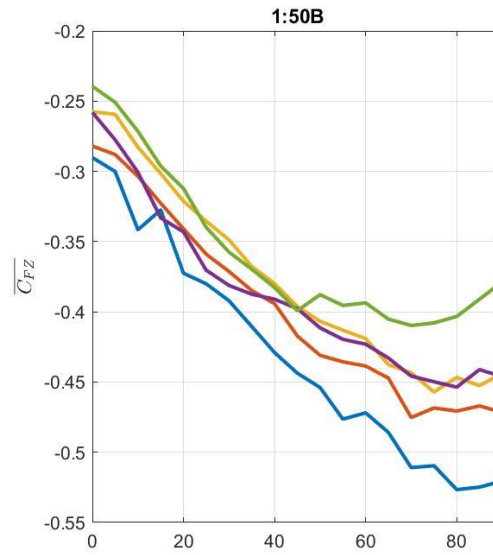
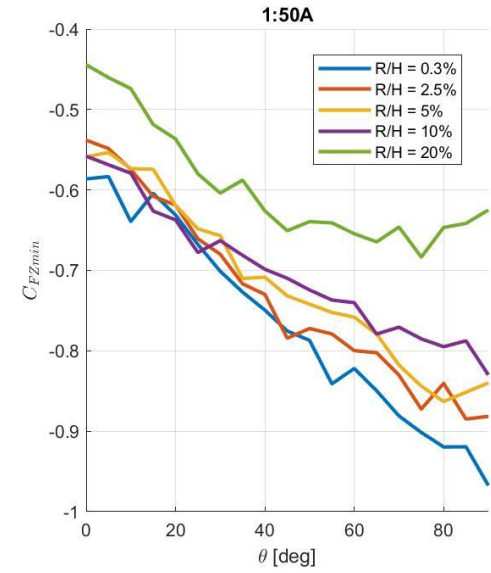
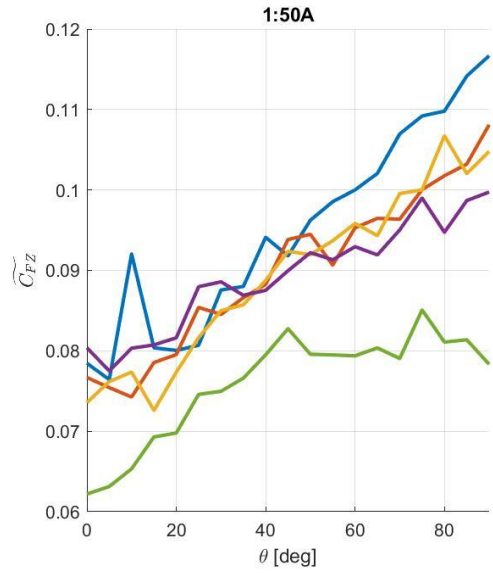
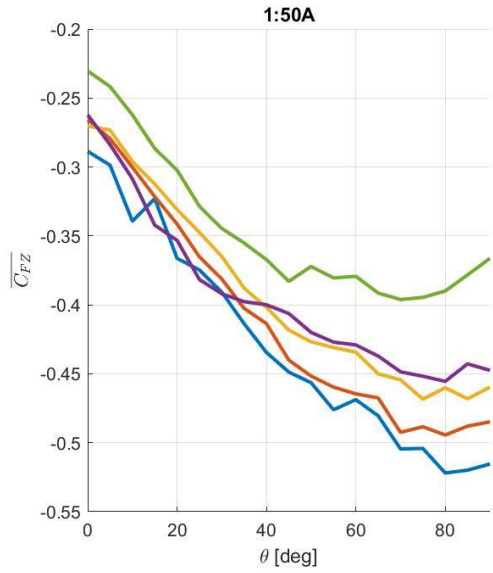


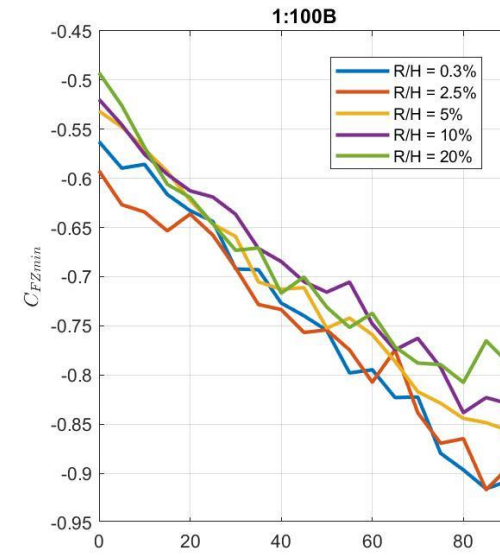
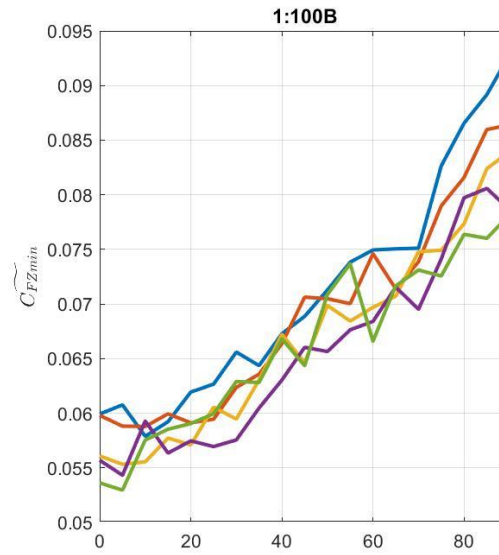
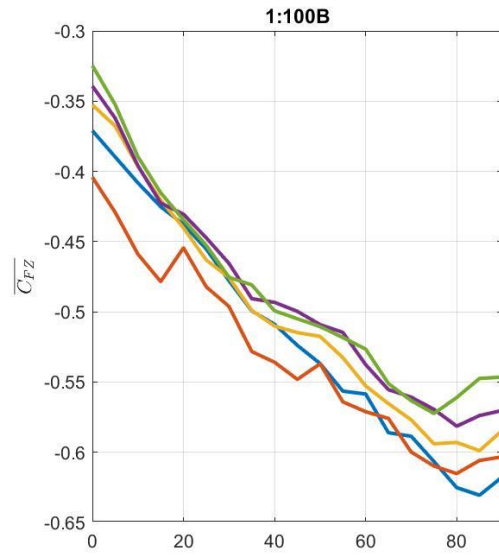
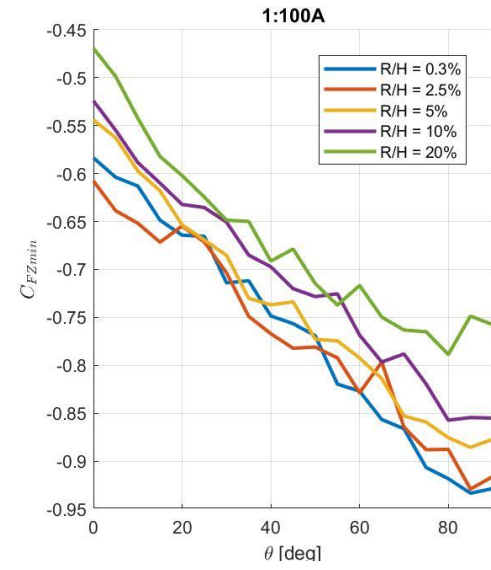
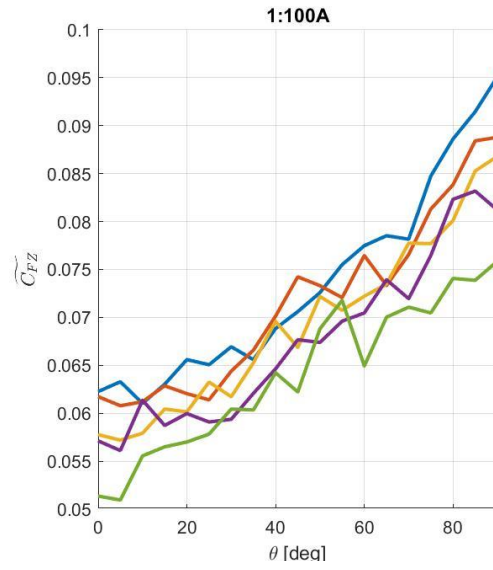
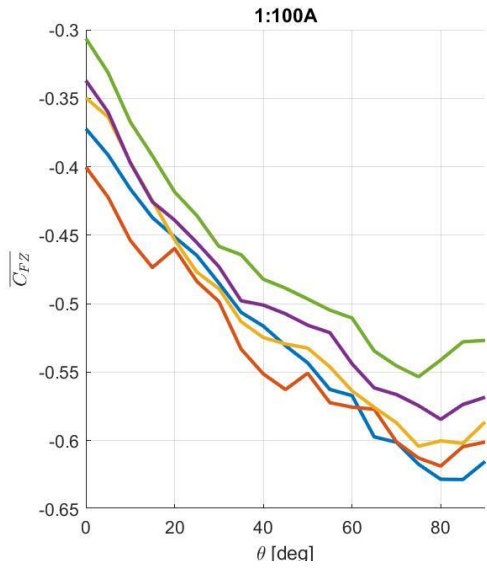


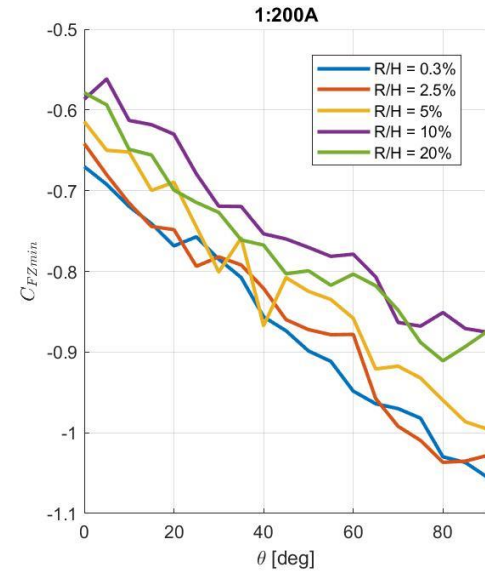
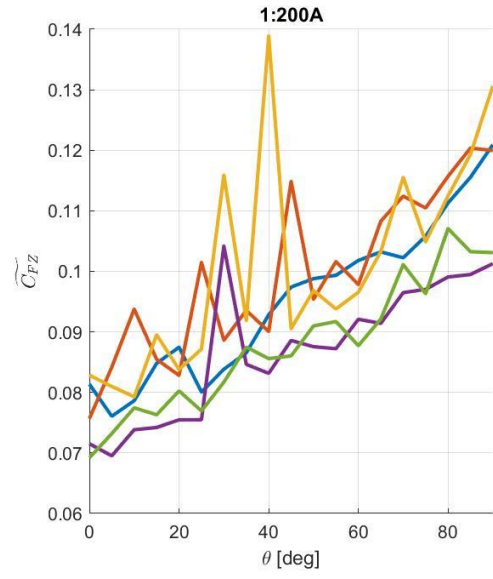
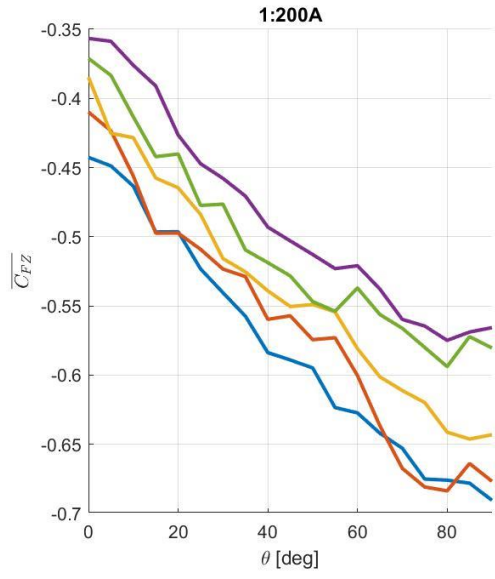




### Appendix J: Uplift coefficients







## Curriculum Vitae

**Name:** Kytin Kwan

**Post-secondary Education and Degrees:** University of Western Ontario  
London, Ontario, Canada  
2013-2018 B.E.Sc..

**Honours and Awards:** Ontario Graduate Scholarship  
2018-2019, 2019-2020

Advanced Materials and Biomaterials Interdisciplinary Research Award  
2015

**Related Work Experience** Teaching Assistant  
The University of Western Ontario  
2018-2020

Engineering Assistant  
The Boundary Layer Wind Tunnel Laboratory  
2017-2018